Modeling bone regeneration around endosseous implants

PROEFSCHRIFT

ter verkrijging van de graad van doctor
aan de Technische Universiteit Delft,
op gezag van de Rector Magnificus prof.ir. K.C.A.M. Luyben,
voorzitter van het College voor Promoties, in het openbaar te verdedigen
op 13 november 2012 om 15:00 uur

door

Pavel Aliaksandravich PROKHARAU
Mechanical Engineer, Applied Mathematician, Belarusian State University

geboren te Minsk, Belarus

Dit proefschrift is goedgekeurd door de promotor:
Prof.dr.ir. C. Vuik

Copromotor Dr.ir. F.J. Vermolen

Samenstelling promotiecommissie:

Rector Magnificus,	voorzitter
Prof.dr.ir. C. Vuik,	Technische Universiteit Delft, promotor
Dr.ir. F.J. Vermolen,	Technische Universiteit Delft, copromotor
Prof.Dr. J.M. García-Aznar,	Universidad de Zaragoza
Prof.Dr. M.A. Zhuravkov,	Belarusian State University
Prof.dr.ir. H.H. Weinans,	Technische Universiteit Delft
Dr. A. Madzvamuse,	University of Sussex
Dr. L. Geris,	Katholieke Universiteit Leuven
Prof.dr.ir. C.W. Oosterlee,	Technische Universiteit Delft, reservelid

Modeling bone regeneration around endosseous implants.
Dissertation at Delft University of Technology.

TU Delft

The work described in this thesis was financially supported by the Delft Institute of Applied Mathematics (DIAM) of the Delft University of Technology.

ISBN 978-94-6203-171-5

Cover design by Maxim Molokov and Pavel Prokharau. Painting by Maryja Prokharava.

Printed in the Netherlands by Wöhrmann Print Service.

to my parents, Masha and Paulinka

Summary

Modeling bone regeneration around endosseous implants

Pavel A. Prokharau

The present work is focused on mathematical modeling of bone regeneration. Various aspects of modeling are considered. In Chapter 2, a classical system of partial differential equations (PDE's) is analyzed, which is constructed to simulate bone healing around endosseous implants. The present system is of the diffusion-advection-reaction type and is typical for mathematical models for bone regeneration. The need of analyzing the PDE's follows from the appearance of the wave-like profiles, that are found in the numerical solutions for the distribution of cells and of growth factors and, consequently, of newly formed bone matrix. Such predictions of the model contradict experimental observations. Hence it is critically important to understand why these wave-like patterns appear and how the model may be modified in order to provide biologically relevant solutions. The linear stability analysis carried out around constant-state (i.e. homogeneous in the physical space) solutions provides the answers to the stated questions. Stability of the constant-state solutions is determined by the values of the model parameters. Explicit relations determining the stability region for the parameters are derived. It is concluded that if the model parameters have the values outside of the stability region, then the constant-state solution is unstable and the exact solution of the current system will not converge to it. Hence formation of stable patterns is likely. The analytical results are validated by finite element simulations.

Chapters 3 and 4 of the thesis are devoted to development of new approaches in modeling bone regeneration. In Chapter 3, the evolutionary differentiation model is introduced, that allows to incorporate the history into the differentiation of cells by defining an additional differentiation state variable $a \in [0, 1]$. During bone regeneration, mesenchymal stem cells differ-

entiate into other cell phenotypes. It is known from experiments [13, 60, 97] that cells obtain new properties gradually during a finite period of time. The differentiation state variable a allows to track a gradual evolution of cell states. Cell differentiation is simulated by an advection term in the governing equations, which is equivalent to modeling a certain velocity (differentiation rate) in the differentiation state space. Each cell is capable of changing its phenotype only after a *finite* (contrary to immediate) period of time. With the immediate differentiation approach, which is commonly used in classical models, it is only possible to consider just the initial and final states of differentiating cells. Cell differentiation is then modeled as an immediate change of the cell phenotype.

The advantage of the new evolutionary approach is that the differentiation history is employed, i.e. the current state of cells depends on how the cells evolved before. Therefore the new approach has a potential to describe cell differentiation more accurately, provided the model parameters are chosen correctly. The most important advantage related to the present approach is the concept of the *finite* time of differentiation. In experiments, new bone formation is observed within the healing site only after certain time after the implant placement (at the end of the first week according to Berglundh et al. [14] and Abrahamsson et al. [1]). With the evolutionary differentiation approach it is possible to calibrate the time of initiation of bone formation by setting the appropriate value for the differentiation rate u_b of osteogenic cells into osteoblasts. Initiation of new bone release is related to the time of appearance of secretorily active osteoblasts within the peri-implant region. If the rate u_b is equal, for example, to $1/4\ days^{-1}$, then the minimal time of differentiation of fully non-differentiated osteogenic cells (which are recruited from the old bone surface) into osteoblasts is equal to four days. For the classical immediate differentiation approach, differentiation always starts immediately. Hence classical models usually predict formation of new bone already during the first hours after the implant placement.

The present evolutionary approach is incorporated into another extended innovative model described in Chapter 4. The model is developed for early stages of peri-implant osseointegration. It is known from experiments that, during endosseous healing, bone forms through a direct apposition on a pre-existing solid surface [24]. Therewith the concept of the ossification front or of the bone forming surface is considered. The bone forming surface is dealt with directly in the present model, which is formulated as a moving boundary problem. The ossification front is modeled by the moving boundary of the computational domain containing the soft tissue. An explicit representation of the bone-forming surface is the main innovation of the proposed model, which distinguishes the current formalism from the classical models for peri-implant osseointegration. Due to the finite time of differentiation of osteogenic cells, no osteoblasts appear in the soft tissue region during first four days of simulation. New bone is not released and the initial geometry

is not changed within this time period. Hence during the first four days the sources of osteogenic cells and growth factors are modeled to be located at the old bone surface and at the implant surface. Therefore, the evolutionary differentiation approach is an essential part of the present model. The classical immediate differentiation formalism would lead to an immediate movement of the ossification front and to not being able to define the initial sources of cells and growth factors for the current moving boundary problem, since the old bone surface and the implant surface would not be the boundary of the physical (i.e. soft tissue) domain.

The numerical method for the present mathematical model is described in Chapter 5. The current problem has a number of characteristics which make the algorithm elaborate and complex. The constructed numerical method provides stable and *non-negative* solutions of the nonlinearly coupled system of the time dependent taxis-diffusion-reaction equations. The additional challenges, which are faced with at the stage of the construction of the algorithm, consist in the need to discretize the model equations within the irregular and time-evolving physical domain, and in the sensitivity of the mathematical model with respect to negative solutions. The presently proposed numerical approach is based on such methods as: the method of lines, finite volume method, level set method and the embedded boundary method. For coarse meshes, patterns are observed to develop. These patterns should not be there and result from numerical errors. Since we observe that convergence is only reached at high mesh resolutions, we think that further research should point into the direction of adaptive mesh refinement, improved time integration (operator splitting methods) and/or higher-order methods, such as spectral or DG-methods (however the requirement of the solution positivity is still essential for higher-order methods). The series of numerical simulations demonstrate the ability of the present osseointegration model to predict various paths of new bone formation depending on the chosen parameter values.

Samenvatting

Modelleren van botregeneratie rond enossale implantaten

Pavel A. Prokharau

Het huidige werk is gericht op de wiskundige modellering van botregeneratie. Een aantal aspecten van het modelleren worden beschouwd. In Hoofdstuk 2, wordt een klassiek stelsel partiële differentiaalvergelijkingen (pdv's) geanalyseerd, dat ontwikkeld is voor de simulatie van botingroei in enossale implantaten. Dit stelsel is van het diffusie-advectie-reactietype en is kenmerkend voor de wiskundige modellen voor botregeneratie. De noodzaak van de analyse van pdv's volgt uit het optreden van de golfachtige profielen die in de numerieke oplossingen voor de distributie van cellen en groeifactoren en derhalve voor nieuw gevormd bot matrix waargenomen worden. Dergelijke voorspellingen van het model spreken experimentele waarnemingen tegen. Daarom is het zeer belangrijk om te begrijpen, hoe deze golfachtige patronen verschijnen en hoe het model moet worden gewijzigd om biologisch zinvolle oplossingen te verkrijgen. De lineaire stabiliteitsanalyse die uitgevoerd rond een constante oplossing (dat wil zeggen in de ruimte homogene evenwichtsoplossingen) beantwoordt deze vraagstelling. Of de constante oplossingen stabiel zijn, wordt bepaald door de waarden van de modelparameters. Expliciete relaties, die het stabiliteitsgebied voor de parameters bepalen, worden in dit proefschrift afgeleid. Er wordt geconcludeerd, dat als de waarden van de modelparameters buiten het stabiliteitsgebied liggen, dat dan de constante oplossing instabiel is en dat de exacte oplossing van het huidige systeem niet convergeert. Hierdoor is de vorming van stabiele patronen zeer waarschijnlijk. De analytische resultaten zijn gevalideerd door middel van eindige elementen simulaties.

Hoofdstukken 3 en 4 van het proefschrift gaan over de ontwikkeling van nieuwe aanpakken in het modelleren van botregeneratie. In Hoofdstuk 3 is het evolutionaire differentiatie-model ingevoerd, waardoor het mogelijk

is om de voorgeschiedenis van de cellen mee te nemen door het definiëren van een extra differentiatie-variabele $a \in [0, 1]$. Tijdens de regeneratie van bot, differentiëren mesenchyme stamcellen naar andere cel fenotypes. Het is bekend uit experimenten [13, 60, 97] dat de cellen nieuwe eigenschappen geleidelijk in een eindige periode van tijd verkrijgen. De differentiatie-variabele a maakt het mogelijk om een geleidelijke evolutie van de cel te volgen. Celdifferentiatie wordt gesimuleerd door een advectie term in de beschrijvende vergelijkingen die een zekere snelheid (differentiatie-snelheid) in de differentiatie toestandsruimte modelleert. Elke cel is in staat zijn fenotype pas na een *eindig* (in tegenstelling tot onmiddellijk) tijdsbestek te veranderen. Met de aanpak waarin differentiatie onmiddellijk optreedt, die meestal in de klassieke modellen gebruikt wordt, is het slechts mogelijk de initiële en finale staat van differentiërende cellen te beschouwen. Celdifferentiatie wordt dan gemodelleerd als een instantane wijziging van het fenotype van de cel.

Het voordeel van de nieuwe evolutionaire aanpak is dat de differentiatie geschiedenis wordt gebruikt, dat wil zeggen de huidige stand van de cellen hangt af van hoe de cellen zich daarvoor ontwikkelden. Daarom biedt de nieuwe aanpak een mogelijkheid om celdifferentiatie nauwkeuriger te beschrijven, op voorwaarde dat de model parameters correct gekozen worden. De belangrijkste innovatie omtrent de huidige aanpak is het concept van de *eindige* tijd van differentiatie. In experimenten wordt de vorming van nieuw bot slechts na een bepaalde tijd na plaatsing van het implantaat in de genezende regio waargenomen (aan het einde van de eerste week volgens Berglundh et al. [14] en Abrahamsson et al. [1]). Met de geleidelijke differentiatie aanpak is het mogelijk om de aanvangstijd van botvorming te kalibreren door de juiste waarde voor de differentiatiesnelheid u_b van osteogene cellen in osteoblasten te kiezen. Initiatie van de aanmaak van nieuw bot hangt af van het moment van ontstaan van botvormende osteoblasten binnen het peri-implantaat gebied. Als de snelheid u_b, bijvoorbeeld, gelijk is aan $1/4$ $dagen^{-1}$, dan is de minimale tijd van differentiatie van volledig niet-gedifferentieerde osteogene cellen (die worden gerekruteerd uit het oorspronkelijke botoppervlak) naar osteoblasten gelijk aan vier dagen. Voor de klassieke instantane differentiatie aanpak is de minimale differentiatie tijd altijd gelijk aan nul. Daardoor voorspellen klassieke modellen vaak de vorming van bot al gedurende de eerste uren na de plaatsing van het implantaat.

De huidige evolutionaire aanpak is opgenomen in een ander uitgebreid innovatief model, dat in Hoofdstuk 4 beschreven is. Het model is ontwikkeld voor de vroege stadia van peri-implantaat osseo-integratie. Het is bekend uit experimenten dat tijdens de botgenezing bot vormt door middel van een direct bijstelling op een reeds bestaande stevige ondergrond [24]. Daarmee wordt het concept van ossificatiefront of botvormend oppervlak beschouwd. Het botvormende oppervlak wordt direct meegenomen in dit model, dat als een bewegend randwaardeprobleem geformuleerd wordt. Het ossifica-

tiefront wordt gemodelleerd door de bewegende grens van het rekengebied dat zacht weefsel bevat. Een expliciete representatie van het botvormende oppervlak is de belangrijkste innovatie van het voorgestelde model en hetgeen dat het huidige formalisme onderscheidt van de klassieke modellen voor de peri-implantaat osseo-integratie. Door het eindige tijdsbestek van differentiatie van osteogene cellen, verschijnen er geen osteoblasten in het zachte weefselgebied gedurende de eerste vier dagen van simulatie. Nieuw bot wordt niet aangemaakt en de begingeometrie niet veranderd tijdens deze periode. Dus worden in de modellen tijdens de eerste vier dagen de bronnen van osteogene cellen en groeifactoren aan het oude botoppervlak en bij het implantaatoppervlak meegenomen. Daarom is de evolutionaire differentiatie aanpak een essentieel onderdeel van het huidige model. Het klassieke instantane differentiatie formalisme zou leiden tot onmiddellijke beweging van het botvormende oppervlak en tot het niet kunnen definiëren van aanvankelijke bronnen van cellen en groeifactoren voor het huidige bewegend randwaardeprobleem, omdat het oorspronkelijke botoppervlak en het implantaatoppervlak niet de grens van het fysische (dat wil zeggen zachte weefsel) gebied zou zijn.

De numerieke methode voor het huidige wiskundige model wordt beschreven in Hoofdstuk 5. Het huidige probleem heeft een aantal kenmerken waardoor het algoritme ingewikkeld en complex is. De geconstrueerde numerieke methode zorgt voor stabiele en *niet-negatieve* oplossingen van het niet-lineair gekoppelde stelsel van tijdsafhankelijke taxis-diffusie-reactievergelijkingen. De verdere uitdagingen die men in het stadium van de constructie van het algoritme tegenkomt, bestaan uit de noodzaak om de model vergelijkingen binnen het irreguliere en tijdsveranderlijke fysieke domein te discretiseren en uit gevoeligheid van het wiskundige model ten aanzien van negatieve oplossingen. De huidige voorgestelde numerieke aanpak is gebaseerd op methoden als: de Methode der Lijnen, de eindige- volumenmethode, de Level-Set methode en de ingebedde-grensmethode (embedded boundary method). Omdat we waargenomen hebben dat convergentie enkel voor hoge gridresoluties bereikt wordt, denken we dat verder onderzoek zich zou moeten richten op adaptieve maasverfijning, verbeterde tijdsintegratie (operator-splitting) en/of hogere orde methoden, zoals spectrale of Discontinue Galerkin methoden (echter de eis van positiviteit van de oplossing blijft zeer belangrijk). De reeks van de numerieke simulaties tonen het vermogen van het huidige osseo-integratie model om afhankelijk van de gekozen parameterwaarden verschillende paden van nieuw botvorming te voorspellen.

CONTENTS

Summary **v**

Samenvatting **ix**

1 Introduction **1**
1.1 Bone regeneration 1
1.2 Study motivation 2
1.3 Review of mathematical models for bone regeneration 4
1.4 Structure and subjects of the thesis 9

2 Linear stability analysis **13**
2.1 Introduction 14
2.2 Biological model 15
2.3 Stability analysis 18
2.3.1 The simplified biological model 18
2.3.2 Non-homogeneous perturbations 22
2.3.3 Stability of the system of two equations 25
2.3.4 Correspondence between the systems of two and three equations 33
2.3.5 Stability of the system of three equations 37
2.3.6 Parameter choice and stability 39
2.4 Numerical results 41
2.5 Conclusions 44

3 Evolutionary cell differentiation **47**
3.1 Introduction 47
3.2 Differentiation model 49
3.2.1 Flow of non-differentiated cells 51

3.3 Peri-implant osseointegration 54
3.3.1 Mathematical model 54
3.3.2 Differentiation rates and tissue formation 59
3.4 Numerical simulations 64
3.4.1 Model parameters and numerical method 65
3.4.2 Numerical results 67
3.5 Discussion and conclusions 75

4 Moving boundary model for endosseous healing 79
4.1 Introduction 79
4.2 Recent mathematical models 81
4.3 Moving boundary model 83
4.3.1 Mature and immature cells 83
4.3.2 Modeling approach 84
4.4 Model validation 92
4.4.1 Numerical simulations 92
4.4.2 Model parameters 93
4.4.3 Sensitivity analysis 98
4.4.3.1 Numerical solutions for various mesh resolution 108
4.4.3.2 Convergence against the mesh resolution . . 117
4.5 Results and discussion 124
4.6 Conclusions 128

5 Numerical algorithm 131
5.1 Introduction 131
5.2 Mathematical model 132
5.3 Numerical method 134
5.3.1 Positivity of the solution 134
5.3.2 Definitions of cells and vertices in the grid 136
5.3.2.1 Domain evolution 137
5.3.2.2 Treatment and reconstruction of active cells 137
5.3.3 Level set equation 139
5.3.4 PDE discretization in space 140
5.3.5 Advection-diffusion discretization 145
5.3.5.1 Linear flux due to cell differentiation 145
5.3.5.2 Fluxes due to cell migration 148
5.3.5.3 Gradient approximation at cell edges 153
5.3.6 Nonlinear system of conservation laws 158
5.3.6.1 The strictly hyperbolic case 162
5.3.6.2 Nonconvex flux function 166
5.3.6.3 Nonstrictly hyperbolic system 170
5.3.6.4 Weakly hyperbolic system 172
5.3.6.5 Summary 176

5.3.7 Treatment of the reaction term . . . 178
5.3.8 Boundary conditions . . . 179
5.3.9 Time integration . . . 180
5.4 Discussion and conclusions . . . 183

6 Conclusions and outlook **185**
6.1 Conclusions . . . 185
6.2 Recommendations . . . 186

Appendices

A Notes to the moving boundary model for endosseous healing **189**
A.1 Cell source at the old bone surface . . . 189
A.2 Fluxes at the moving boundary . . . 190

B Notes to the numerical algorithm **193**
B.1 Determinant of the linear system . . . 193
B.2 Number of adjacent cells . . . 194

Acknowledgment **197**

Curriculum vitae **199**

Bibliography **201**

List of publications **211**

CHAPTER 1

Introduction

1.1 Bone regeneration

One of the most remarkable properties of bone tissue is its regenerative capacity. Bone regeneration is a complex biological process, which occurs starting from the skeletal development and continuing in the form of bone remodeling and in the form of response to bone injuries, throughout the entire lifetime of organisms. In contrast to other tissues, damaged bone regenerates without formation of a scar tissue. The newly formed bone is usually remodeled to such a state, that its properties are almost indistinguishable from the properties of surrounding old bone, and a bone geometry in the healing site is usually restored to its initial shape [26, 31].

Bone regeneration consists of a series of well-regulated biological processes, taking places in a certain pathway. Several cell types are involved in these processes. Activity of cells is regulated by biological, chemical and mechanical environments around them. Fracture healing is one of the most common cases of bone regeneration in a clinical setting. This process includes both mechanisms, in which new bone can form: intramembranous ossification and endochondral ossification [87]. The following three main stages of bone healing can be distinguished: the inflammatory phase, bone repair and bone remodeling [42].

At the first stage, immidiately after the injury, blood, which leaks from the damaged blood vessels, coagulates and a blood clot is formed in the wound region. Platelets, which are found within the blood clot, become activated and start to release growth factors, which regulate the processes of bone healing. Since the blood vessels are ruptured, the supply of nutrients and oxygen to osteocytes, which are the living cells, situated within the bone matrix, ceases. The lack of nutrients and oxygen makes the cells die.

Necrotic processes initiate inflammation. Inflammatory cells (macrophages, phagocytes, leukocytes) arrive in the wound site and remove a necrotic tissue. After this process, fibroblasts, mesenchymal stem cells (MSC's) and endothelial cells, which originate from the periosteum (the vascularity-rich external tissue layer of bone), from the marrow channel of the bone and from the soft tissues, which surround the bone including the muscles, migrate into the healing region [11]. One of the mechanisms regulating cellular processes during bone healing, is the influence of growth factors, which are released by activated platelets and by the aforementioned cells.

MSC's differentiate into osteoblasts, chondrocytes and fibroblasts under the influence of different stimuli, for example, growth factors and the local mechanical environment in the tissue. Differentiated osteoblasts can synthesize new bone matrix directly on a pre-existing surface without the mediation of the cartilage phase [87]. Such type of bone formation is called *intramembranous ossification*. In this case, the apposition of new bone matrix on a solid surface takes place [24], and an ossification front or a bone-forming surface is observed [1, 14]. Therefore, intramembranous ossification can be described by a moving-boundary type of bone formation.

The second mode of bone formation is referred to as *endochondral ossification*. During fracture healing, this type of ossification occurs in the middle of the fracture area, in which MSC's differentiate into chondrocytes. Chondrocytes proliferate and form cartilage tissue. Maturation of chondrocytes towards the hypertrophic chondrocytes is followed by the calcification of cartilage. Chondrocytes undergo apoptosis and blood vessels grow into the cavities, which were initially occupied by the chondrocytes. Osteoprogenitor cells are delivered into the cavities through a vascular network, and they differentiate into osteoblasts. The mineralized extracellular matrix of the cartilage tissue serves as a scaffold, on which osteoblasts release new bone [11].

Therefore during a reparation stage, new woven bone is synthesized within the healing site. Right after the formation of new bone, a remodeling phase begins. A patch of newly formed woven bone is remodeled into mature lamellar bone, through its resorption by osteoclasts and through new bone synthesis by osteoblasts.

1.2 Study motivation

Despite regenerative properties of bone, there is a large number of related clinical problems, which are not solved at the present time. One of them is an impaired bone regeneration during fracture healing. For example, Einhorn [30] refers to Praemer et al. [76], when he notes, that "the healing of 5 to 10 per cent of the estimated 5.6 million fractures occurring annually in the United States is delayed or impaired". Another representative number is

given by Audigé et al. [10]. They have done an observational study of the treatment of 416 patients with tibial shaft fractures, and reported 52 (13%) cases of delayed healing or nonunion.

The natural regenerative capacity of bone tissue is not sufficient in certain situations, which appear in orthopaedic, oral and maxillofacial surgery, such as skeletal reconstruction of large bone defects created by trauma, infection, tumor resection and skeletal abnormalities, or cases in which bone regeneration is compromised due to diseases, like osteoporosis or avascular necrosis [26]. For example, 3.79 million osteoporosis fractures were estimated in the European Union in 2000, and direct medical cost for their treatment were around 32 billion euros [82].

Einhorn [30] and Dimitriou et al. [26] review temporary treatment methods, which are aimed at promoting natural bone regeneration in situations, where this process is impaired or simply insufficient. Among the treatment techniques, which are often applied in clinical practice, the authors mention distraction osteogenesis and bone transport; bone-grafting methods, such as autologous bone grafts, allografts, and bone-graft substitutes or growth factors; non-invasive methods of biophysical stimulation, such as low-intensity pulsed ultrasound and pulsed electromagnetic fields; mechanical stimulation. These methods can be used separately or in combinations. However, the efficiency and the applicability of the considered techniques are still limited.

In order to improve existing methods and to develop new approaches, a better understanding of the processes, taking place during regeneration of bone, is needed. A large number of experimental works is devoted to the investigation of the influence of various factors on the course of bone healing.

In *in-vivo* experiments, the biological processes are observed in natural conditions. However, obtaining temporal and spatial experimental data often becomes technically complicated. Contemporary non-invasive methods such as various imaging techniques can sufficiently enhance the acquisition of the qualitative and quantitative information about the biology of bone regeneration. Molecular imaging techniques, which are reviewed in Mayer-Kuckuk and Boskey [64], can be used for real-time biology studies of bone regeneration in living tissues. These techniques are classified into three groups: nuclear imaging (among which are single photon computed tomography (SPECT) and positron emission tomography (PET)), optical imaging methods (in particular fluorescence reflectance imaging (FRI) and bioluminescence imaging (BLI)) and magnetic resonance imaging (MRI).

An alternative to *in-vivo* experiments is *in-vitro* studies. In these studies, it is possible to obtain a highly controllable and measurable environment, in which biological processes are observed. The disadvantage of this approach is that tissues and cells are separated from their natural environment. Some special attention should be paid to make the experimental settings correspond to natural conditions, in which bone regeneration takes place in real

organisms.

As the examples of various directions of the experimental studies of bone regeneration, the following references can be mentioned. Abrahamsson et al. [1], Berglundh et al. [14] studied paths of bone formation around smooth and micro-rough endosseous implants, which were installed into the dog mandibles. A review of *in-vivo* experiments on the influence of mechanical stimulation on bone healing is presented by Epari et al. [31]. The effect of a different micro-structure of an endosseous implant and of a mechanical stimulation on bone ingrowth into the implant within an experimental chamber, which was installed into a rabbit tibia, was investigated by Duyck et al. [28, 29], Vandamme et al. [92, 93, 94]. The experimental works, in which the influence of growth factors on bone regeneration was studied, are reviewed in Lind [61]. *In-vitro* studies, related to bone regeneration, can be found, for example, in Gabbay et al. [33], Kasper et al. [54], Weinand et al. [96]. The aforementioned list of references does not give a full picture of the experimental studies in the considered field. This list should be considered just as a short introduction into the topic.

Study of bone regeneration with use of *in-vivo* or *in-vitro* experiments can be very expensive, time-demanding or even impossible from ethical point of view. Qualitative and quantitative data, which are possible to obtain from the experiments, are often limited. In this situation, a mathematical model can deliver additional insight into various aspects of bone regeneration. Mathematical models and numerical simulations are valuable tools for representation and analysis of complex multi-scale biochemical and biomechanical processes. Simulations allow to investigate these cases, which are prohibitively difficult or impossible to consider in experiments. This makes mathematical modeling extremely valuable for, for example, the development of new treatment techniques and strategies.

1.3 Review of mathematical models for bone regeneration

Currently there is a large number of mathematical models, which were developed to study different aspects of bone regeneration. The models are based on various concepts and approaches and they differ in the types of the problems, for which they can be used. Therefore, several criteria can be employed for the classification of the models for bone regeneration. The models can be related to various forms of bone regeneration, for example, models for fracture healing, for bone regeneration around endosseous implants and/or for distraction osteogenesis. Another way to classify the models, is to look at the basic mathematical approaches used (continuous deterministic models and fuzzy-logic models). Other characteristics, in which models differ from each other, are, for example:

- representation of biological tissues as linear elastic, visco-elastic or poro-elastic (biphasic) media;
- choice of the mechanical stimulus (strain energy, hydrostatic stress, deviatoric strain, fluid flow etc.);
- representation of the considered cellular processes (random diffusion, chemotaxis and haptotaxis for cell migration, immediate and evolutionary cell differentiation, etc.);
- phases of bone regeneration represented (reparation phase and/or remodeling phase).

The focus of this manuscript is on the processes taking place during the reparation phase of bone regeneration. In this work, bone remodeling is not considered in detail. Bone remodels constantly throughout the entire life of an organism. The time scale of this process is much larger than the time scale of the reparation processes [24]. For extended mathematical models for bone remodeling see Doblaré and García-Aznar [27], García-Aznar et al. [34], Pivonka et al. [75], Ryser et al. [85] and references therein. Bone remodeling is out of the scope of the current work. Therefore, a detailed review of the models, mainly developed for the reparation phase of bone regeneration, is given in the remainder of this section.

Geris et al. [42] divide the models into three classes with respect to the essential mechanisms regulating the bone regeneration process. They distinguish *mechanoregulatory models, bioregulatory models and mechanobioregulatory models*. Such a classification has the advantage, that it reflects the chronological perspective of the mathematical modeling of bone regeneration. In mechanoregulatory models, the local mechanical environment is considered as the only factor that influences the path of bone regeneration. On the contrary, in bioregulatory models only biochemical factors, like the influence of growth factors on various cell processes, are considered. Mechanobioregulatory models employ mechanical and biological effects simultaneously.

An extended review of mathematical models for bone regeneration is presented in Geris et al. [42]. The authors track the history of the development of several mathematical approaches to bone regeneration. Further, they outline the connections between various theoretical works and they list some references to the original model formulations and to the numerical studies carried out to verify applicability and to evaluate and compare the performance of various approaches.

First theoretical studies of bone regeneration were related to mechanoregulation of bone healing. Pauwels [72] defined a model for tissue differentiation depending on local stresses and strains. Pauwels assumed, that deviatoric strains promote formation of fibrous tissue and a hydrostatic pressure

enhances formation of cartilage. Perren [73] and Perren & Cordey [74] presented the interfragmentary strain approach by defining the limiting (maximum) strains, which can be experienced by various tissues forming within the fracture site without rupturing.

The aforementioned pioneering models were followed by two mechanoregulatory models, developed by Carter et al. [17, 18] and by Claes and Heigele [19]. In these models, biological tissues were considered as linear elastic materials, and the formation of bone, cartilage, fibrous tissue and fibrocartilage was related to a hydrostatic stress and to principal strains. In the approach by Carter et al. [17, 18], the history of a cyclic mechanical loading was considered. Another tissue differentiation model was proposed by Prendergast et al. [77], who considered the biological tissues as *poroelastic materials* and who related differentiation into bone, cartilage or fibrous tissue to different levels of a fluid flow and of a distortional strain. Huiskes et al. [47] estimated the numerical limits for qualitative relations, defined in Prendergast et al. [77]. A fuzzy-logic theoretical model was constructed by Ament and Hofer [4], in which the mechanical stimulus was evaluated by means of a strain energy.

The considered mechanoregulatory models were used in numerical simulations, in which various situations of bone regeneration were considered. The obtained results were usually compared to experiments. The mechanoregulatory models were used in numerical studies of fracture healing [15, 36, 50, 51] , of bone regeneration near endosseous implants [8, 37, 38, 39] and of distraction osteogenesis [49, 52, 68].

Purely mechanoregulatory models do not represent any biological processes, which take place during bone regeneration. Hence, these models are applicable to studies, where only mechanical loading conditions are investigated.

Another class of formalisms is represented by the bioregulatory models, which focus on representation of various biochemical and cell processes. In a simple approach by Adam [2, 3], a critical size defect in fracture healing was determined from the the solution of a partial differential equation (PDE) defined for a growth factor concentration. More extended biological model for fracture healing was constructed by Bailon-Plaza and van der Meulen [11]. In this approach, a system of PDE's was defined for seven variables: densities of MSC's, of osteoblasts, of chondrocytes, concentrations of chondrogenic and osteogenic growth factors, and densities of connective/cartilage extracellular matrix and bone extracellular matrix. The authors represented the processes of cell differentiation, proliferation, migration and death, synthesis and resorption of tissues. Some conclusions about a regulatory role of growth factors in bone healing were drawn from numerical simulations.

The model of Bailon-Plaza and van der Meulen [11] is rather popular due to its generality. The derivation of several other bioregulatory models is based on the approach due to Bailon-Plaza and van der Meulen [11].

Geris et al. [40] extended the model of Bailon-Plaza and van der Meulen [11] by considering angiogenesis, by separating fibrous tissue and cartilage densities, and by defining additional chemotactic and haptotactic terms for cell migration in the governing equations. This approach was applied to model fracture healing, including issues of atrophic nonunions [41, 45].

Amor et al. [5, 6] adapted the model of Bailon-Plaza and van der Meulen [11] for peri-implant osseointegration. They disregarded chondrogenic growth factors, chondrocytes and cartilage, since the intermediate cartilaginous phase was not observed experimentally in bone healing occurring near implants [1, 14, 16, 21]. Chemotaxis of MSC's was represented in equations and a density of activated platelets was introduced as an additional model variable.

A similar biological model was developed by Moreo et al. [67]. Though the models of Amor et al. and Moreo et al. have several differences, a general representation of the main biological and cellular processes is very similar. The considered models allow to simulate bone regeneration around implants with a different surface microstructure, which is represented implicitly through the values of model parameters and through initial and boundary conditions. A detailed comparison of the current two models is given in Chapter 4, in which a new moving boundary bioregulatory model for endosseous bone healing is derived.

In contrast to purely mechano- and bioregulatory models, more complex mechanobioregulatory models allow to consider coupled effects of mechanoregulation and of biochemical factors on bone regeneration, in general. Further, an influence of a mechanical environment on cellular and biochemical processes can be studied.

This class of models is often derived from the bioregulatory and/or mechanoregulatory models, which were mentioned above. For example, a simple mechanobioregulatory model for normal fracture healing was developed by Lacroix et al. [58] and by Lacroix and Prendergast [57]. This formalism was derived from the mechanoregulatory model of Prendergast et al. [77] and Huiskes et al. [47]. The authors made a first step to consider cellular processes together with mechanical factors by incorporating the random walk of MSC's in their model.

Bailon-Plaza and van der Meulen [12] introduced some mechanoregulatory relations into the coefficients of their previous model [11]. With a new model, the authors predicted beneficial effects of moderate, early loading and adverse effects of delayed or excessive loading on bone healing. Mechanoregulatory approaches by Claes and Heigele [19] and Ament and Hofer [4] were used in a fuzzy logic model of Simon et al. [89] and Shefelbine et al. [88], in which such processes as vascularization, tissue destruction, intramembraneous and endochondral ossification, cartilage formation and bone remodeling were represented by a set of fuzzy logic rules, defined for the various states of a mechanical environment within the healing cite.

Gómez-Benito et al. [46] and García-Aznar et al. [35] constructed a mechanobioregulatory model in terms of a system of PDE's, defined for densities of MSC's, osteoblasts, fibroblasts and cartilage cells, and for volume fractions of the debris tissue, granulation tissue, fibrous tissue, bone and cartilage. Migration, differentiation, proliferation and death of cells, synthesis and damage of various tissues, and remodeling of bone were represented in the model. These processes were assumed to depend on the second invariant of the deviatoric strain tensor. The authors applied their model to study the influence of the intrafragmentary movement on the callus growth during fracture healing.

This approach was adapted by Reina-Romo et al. [83] to simulate distraction osteogenesis. One of the innovations introduced by Reina-Romo et al. [83], is that cell differentiation was determined by a *history* of mechanical loading. A concept of cell plasticity, which was presented in Röder [84], was incorporated into the model through the introduction of a maturation level of MSC's.

The mechanoregulatory approach proposed by Prendergast et al. [77] was used in the models of Andreykiv et al. [9] and Isaksson et al. [53], which were developed for fracture healing. The biological processes, such as migration, proliferation, differentiation and apoptosis of cells and production and resorption of fibrous tissue, bone, and cartilage were assumed to be related to the mechanical state of the tissues.

Geris et al. [43] extended their previous bioregulatory model [40], by defining dependencies for model parameters on mechanical stimuli, which were chosen according to Prendergast et al. [77]. This model was applied to study impaired fracture healing. The authors checked predictions of the model for various mechanoregulatory relations. They concluded that, if a mechanical environment was assumed to influence angiogenesis alone, then it was not possible to predict the formation of overload-induced nonunions. However, if both angiogenesis and osteogenesis were assumed to be effected by the mechanical loading, then the overload-induced nonunion formation was successfully predicted.

The combined mechanobioregulatory models allow to consider test cases of both mechanical and biological approaches in the treatment of bone defects. For example, to investigate the effects of a mechanical stimulation and of the addition of growth factors. By use of these models it is also possible to check the hypotheses for the influence of mechanical factors on various biological processes [42]. Mechanobioregulatory models are more general, compared to mechanoregulatory and bioregulatory approaches, and at the same time, they are more complicated, due to a larger number of assumptions, involved in their formulation. The necessary effort to validate a model increases with the level of complexity of a model and the number of model parameters therein. Therefore, it is not possible to choose the 'best' model or the 'best' approach. The choice of a theoretical model should be deter-

mined by the most important characteristics of the considered problem, i.e. by a form of bone regeneration (for example, fracture healing or implant osseointegration), by a subject of the research, by available experimental data, etc.

The issue of a proper model verification is even more critical in the case of a poor cooperation between experimental researchers and developers of theoretical models. Contemporary mathematical approaches are developed to accommodate the most important features in various applications of bone regeneration, which are known from experiments. Theoretical models allow to make some predictions, for example, about advanced treatment techniques. As it is reported by Geris et al. [44], there are no experimental studies on treatment strategies that were designed and optimized by using mathematical models. In other words, an advance in bone regeneration research depends on the connection established between experiments and theoretical modeling both on the stage of model construction and on the stage of model verification. The models have to be validated against experimental settings, that are different from the ones used on the stage of model formulation [42].

Bone regeneration is a multiscale process. In recent theoretical models a single time and space scale are considered. Cellular processes are represented on a tissue-level by means of a continuous approach. For example, random walk of cells is represented by a diffusion term in the governing equations. Development of multiscale models is another crucial issue of bone regeneration research [42]. It is important to understand the mechanisms, in which experimental and theoretical knowledge can be transferred between the various levels. For instance, how to derive a proper representation of cell haptotaxis on tissue level from the knowledge of this process at the cellular level. Mechanical stresses and strains, which are often considered as the main regulation factors, are represented in the recent models on the tissue-level. In reality, tissue strains and stresses can differ from mechanical stimulation, experienced by cells [98]. Therefore, an advanced representation of the mechanical behavior of biological tissues, i.e. more accurate models than linear elasticity or poroelasticity, and consideration of mechanical stimuli on various levels (the tissue-level, the cellular level, the intracellular level) is another possible direction for the future research in modeling bone regeneration [42].

1.4 Structure and subjects of the thesis

As it follows from Section 1.3, a large number of various approaches was developed in the field of mathematical modeling of bone regeneration. In the present work, various mathematical and numerical methods are used to study several areas of modeling bone regeneration. In Chapter 2, a

stability analysis is performed to study some characteristics of the behavior of diffusion-taxis systems that are considered in the most of the recent (mechano)bioregulatory models. An advanced representation of gradually evolving cell differentiation is presented in Chapter 3. This differentiation approach is implemented into a new moving boundary model for intramembraneous ossification, which is described in Chapter 4. A numerical algorithm for the solution of this model in two dimensional spatial domain is defined in Chapter 5. Further in this section, the mentioned subjects of the thesis are introduced in more detail.

In most of the considered models, a continuous approach is employed and a governing system of PDE's is defined for a number of unknowns, which can represent cell densities, growth factor concentrations, tissue volume fractions, mechanical stimuli, etc. Cell migration (if it is considered for a certain cell phenotype) is assumed to be caused by random walk of cells, by chemotaxis and/or by haptotaxis. Random walk is represented by parabolic diffusion terms, and the cell flux due to chemo- or haptotaxis is represented by hyperbolic taxis terms. Other cellular processes, like proliferation, differentiation and death are usually introduced by reaction terms. The equations defined for the evolution of the growth factor concentrations contain diffusion and reaction terms, which model, respectively, diffusion, and production and decay. Synthesis and resorption of various tissues are represented by reaction equations. Therefore, the systems of PDE's that constitute continuous models for the reparation phase of bone regeneration are usually of taxis-diffusion-reaction type.

Remark 1.1. In this work, the term "advection-diffusion-reaction system" is used to denote the equations, which contain taxis, diffusion and reaction terms. This terminology is adopted from Hundsdorfer and Verwer [48], which is a fundamental work about the numerical methods for the systems of the considered type. In various systems, the advection terms represent a flux of some quantity caused by an advection mechanism, i.e. the flux driven, for example, by the fluid velocity. In the case of chemotaxis, the flux of cells is driven by a growth factor gradient. Therefore, advection can be related to a taxis mechanism in a certain way.

Some important characteristics of such systems, such as a stability of the solution and a formation of 'wave-like' profiles in the spatial distribution of cell densities and growth factor concentrations, are studied in Chapter 2. Such wave-like profiles obtained in the solutions for bone regeneration models are unphysical and contradict experimental observations. Therefore, it is important to understand the reason of the appearance of these profiles.

Remark 1.2. 'Wave-like' patterns are also observed in solutions of advection-diffusion-reaction equations, defined in the models for bacteria colonies [66, 69, 91].

As a particular example, a bioregulatory model by Moreo et al. [67]

is chosen, due to its sufficient simplicity and generality. First of all, the considered model contains diffusion and advection (taxis) terms, which are responsible for the appearance of a wave-like profile in the solution. Such terms are also included in similar bioregulatory models, developed by [5, 11]. At the same time, the model of Moreo et al. [67] is simpler than another bioregulatory approach proposed by Geris et al. [40], in which angiogenesis was represented. Mechanobioregulatory models are not mentioned here, since consideration of mechanical stimuli only complicate models and has no added value for the present analysis.

Some conditions for the formation of wave-like profiles are determined from a linear stability analysis. These conditions are expressed in terms of several quantitative relations for the model parameters. The linear stability analysis, which is described in Chapter 2, provides some insight into the characteristic behavior of the bioregulatory models for bone regeneration, in which a diffusion-taxis mechanism of cell migration is incorporated.

Another cellular process, which is of great importance for bone regeneration, is cell differentiation. In all continuous models, excluding the model of Reina-Romo et al. [83], differentiation is represented by reactive terms, which correspond to immediate switch of cell phenotype. Reina-Romo et al. [83] considered the dependence of cell migration on the loading history by introducing a maturation level of cells. The idea of a temporal transformation of cells into another phenotype is elaborated in Chapter 3, in which a general mathematical formalism is developed for the evolutionary cell differentiation. The considered approach can be applied to an arbitrary number of cell types and to any set of factors influencing cell differentiation. The evolutionary model allows to consider a cell differentiation path, determined by a *history* of mechanical and/or biochemical stimulation. The present approach results into a final time of differentiation, which can be important in some applications. For instance, the boundary conditions for the peri-implant osseointegration model, which is described in Chapter 4, can be applied, only if the time of differentiation of MSC's into osteoblasts is final. An example of the application of the evolutionary approach for differentiation of MSC's regulated by the mechanical environment, is given by a simple peri-implant osseointegration model described in Section 3.3. Numerical simulations are carried out and results are compared with experimental data in Section 3.4.

In Chapter 4, a new moving boundary model for bone healing around endosseous implants is presented. The model is derived to accommodate the fact, that synthesis of bone within a peri-implant region occurs in the form of intramembraneous ossification [1, 14]. Davies [24] describes this process as a direct apposition of new bone matrix on a pre-existing rigid surface. The evolution of the bone forming surface (ossification front) is incorporated in the model directly through a movement of the boundary of the soft tissue region, which is considered as a physical domain, where various cellular

and biochemical processes are considered. The present approach conceptually differs from the recent continuous models for endosseous bone healing mentioned in Section 1.3, in which bone tissue is represented by its volume fraction defined within the stationary physical domain. The moving boundary model is formulated in terms of the system of time-dependent nonlinear advection-diffusion-reaction equations, defined within the physical domain that evolves in time. The numerical algorithm, used to solve this challenging mathematical problem in two dimensional physical domain, is described in Chapter 5. The solution procedure involves some methods, which are the finite volume method, which is applied on an unstructured two dimensional grid, the embedded boundary or Cartesian boundary method and the level set method, which is used to track the movement of the boundary of the irregular physical domain. In Chapter 6, final conclusions are drawn and some directions for future research are given.

CHAPTER 2

Linear stability analysis

In this chapter the stability of the solution of a system of advection-diffusion equations is studied. This class of equations is used in models for bone regeneration. Diffusion and advection (taxis) terms in the equations for the evolution of cell densities represent the fluxes due to random walk of cells and due to chemo- and/or haptotaxis, respectively. A bioregulatory model developed by Moreo et al. [67] is considered as a particular example of such a system. For certain parameter values, the solution of the considered equations has a wave-like profile, which appears in the distribution of osteogenic cells, osteoblasts, growth factor and bone matrix. This wave-like profile contradicts experimental observations. The conditions, under which such profile appears in the solution, are derived. Those conditions are determined in terms of model parameters, by means of a linear stability analysis, carried out around one of the constant-state solutions of the simplified system. The stability analysis was performed for a reduced system of PDE's. It is proved in this chapter, that the stability properties of constant solutions for the reduced and original systems are equivalent. Conclusions, derived from the linear stability analysis, are extended for the case of large perturbations. Analytical results are validated with finite element simulations. The simulations show, that the stability of a constant solution can determine the behavior of the solution of the whole system, if certain initial conditions are considered. If the constant solution is unstable, then the solution of the system never converges to this constant solution. The material, presented in the current chapter, was published in Prokharau and Vermolen [78].

2.1 Introduction

A stability analysis is performed for a biological model for peri-implant osseointegration, which was proposed in Moreo et al. [67]. This model allows to take into account an implant surface microtopography. The results presented in Moreo et al. [67] were in agreement with experiments. The authors reported, that model can predict contact and distance osteogenesis modes of bone formation [24].

From the numerical simulations, which were performed for a different geometry of the healing site, it was found that the system of equations, proposed in Moreo et al. [67], is characterized by appearance of a wave-like profile in the solution for a certain range of parameters. This profile was initially recognized in the solution of the model equations for the 1D domain of length $2.5mm$ (Figure 2.1b). This domain was chosen for the simulations of bone formation near the cylindrical implant, located within the bone chamber, used in the experiments by Duyck et al. [29], Vandamme et al. [92, 93, 94]. The authors reported that in experiments, new bone was formed at all distances from the host bone, and integration of bone and implant was achieved. That wave-like profile has not been noticed by Moreo et al. [67], since for the geometry used in his simulations, in which the distance from host bone to implant was $0.6mm$, only a part of 'wave' is visible in the solution (Figure 2.1a), and a wave-like profile is not distinguishable. For larger domains, more 'waves' appear in the solution. The solution for the domain of length $5mm$ is shown in Figure 2.1c.

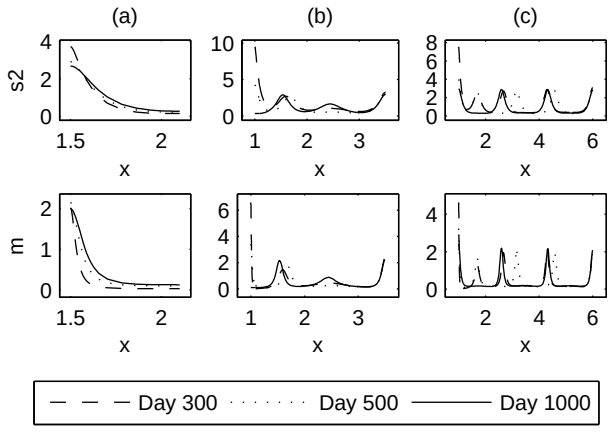

Figure 2.1: Osteogenic cell m and growth factor 2 s_2 distributions at different time moments, obtained from the numerical solution of model equations, defined in Moreo et al. [67], for 1D axisymmetric domain with length (a) $L = 0.6\,mm$ and (b) $L = 5\,mm$

The conditions, under which a wave-like profile appears, are studied in

this chapter. Such a wave-like profile in the solution for cell densities and growth factor concentrations is not realistic. In some cases it also leads to a wave-like distribution of bone matrix inside the peri-implant region. This distribution is in contradiction with experimental observations, from which it follows, that bone forms by deposition on the preexisting bone matrix, and no isolated bone regions appear [1, 14]. Thus, it is important to learn, under which conditions the model shows this unphysical behavior.

The proposed approach is to study the linear stability of the constant solutions of the system. As the full system of equations is large and extremely complicated for analytic derivations, an equivalent simplified system with similar properties will be defined.

The phenomenon of a wave-like profile in the solution can be related to the appearance of bacterial patterns in a liquid medium, described mathematically by similar systems of partial differential equations. The formation of bacterial patterns is studied in Miyata and Sasaki [66], Myerscough and Murray [69], Tyson et al. [91].

In Section 2.2 the system of equations proposed in Moreo et al. [67] is reviewed. The linear stability analysis of the system is carried out in Section 2.3. In Section 2.4 analysis results are validated with a series of numerical simulations. Finally, in Section 2.5 some conclusions are drawn.

2.2 Biological model

The original model proposed in Moreo et al. [67] consists of eight equations, defined for eight variables, representing densities of platelets c, osteogenic cells m, osteoblasts b, concentrations of two generic growth factor types s_1 and s_2, and volume fractions of fibrin network v_{fn}, woven bone v_w, and lamellar bone v_l. The above notations are introduced for non-dimensional cell densities and growth factor concentrations, i.e. for those, related to some characteristic values. If $\hat{f}$ and f_c are notations of a dimensional variable and of its characteristic value, then a non-dimensional variable f is defined as $f = \hat{f}/f_c$, $f = c, m, b, s_1, s_2$. The following characteristic values are proposed: $c_c = 10^8$ $platelets/ml$, $m_c = 10^6$ $cells/ml$, $b_c = 10^6$ $cells/ml$, $s_{1_c} = 100$ ng/ml, $s_{2_c} = 100$ ng/ml. The model equations are:

$$\frac{\partial c}{\partial t} = \nabla \cdot [D_c \nabla c - H_c c \nabla p] - A_c c, \tag{2.1}$$

where D_m and A_c are the coefficients of random migration and death of platelets. The term $\nabla \cdot [H_c c \nabla p]$ represents a "linear taxis". It accounts for the transport of platelets towards the gradient of the adsorbed proteins p, which is a predefined function of the distance from the implant surface d.

According to Moreo et al. [67], it is defined as

$$p(d) = \begin{cases} 0.5(1 - \frac{d}{0.1}), & if\ 0 \leq d < 0.1 \\ 0, & if\ d \geq 0.1 \end{cases}.$$

$$\begin{aligned} &\frac{\partial m}{\partial t} = \nabla \cdot [D_m \nabla m - m(B_{m1} \nabla s_1 + B_{m2} \nabla s_2)] \\ &+ \Big(\alpha_{m0} + \frac{\alpha_m s_1}{\beta_m + s_1} + \frac{\alpha_m s_2}{\beta_m + s_2}\Big) m(1 - m) - (\alpha_{p0} + \frac{\alpha_{mb} s_1}{\beta_{mb} + s_1}) m - A_m m, \end{aligned} \tag{2.2}$$

where the terms in the right-hand side represent random migration, chemotaxis, cell proliferation, differentiation into osteoblasts, and death respectively;

$$\frac{\partial b}{\partial t} = (\alpha_{p0} + \frac{\alpha_{mb} s_1}{\beta_{mb} + s_1}) m - A_b b, \tag{2.3}$$

where A_b is the rate of osteoblast death;

$$\frac{\partial s_1}{\partial t} = \nabla \cdot [D_{s1} \nabla s_1] + \Big(\frac{\alpha_{c1} p}{\beta_{c1} + p} + \frac{\alpha_{c2} s_1}{\beta_{c2} + s_1}\Big) c - A_{s1} s_1, \tag{2.4}$$

where the terms in the right-hand side model random migration, growth factor secretion and decay respectively;

$$\frac{\partial s_2}{\partial t} = \nabla \cdot [D_{s2} \nabla s_2] + \frac{\alpha_{m2} s_2}{\beta_{m2} + s_2} m + \frac{\alpha_{b2} s_2}{\beta_{b2} + s_2} b - A_{s2} s_2, \tag{2.5}$$

where the first term in the right-hand side determines random migration, the second and the third ones – growth factor secretion, and the last one – decay;

$$\frac{\partial v_{fn}}{\partial t} = -\frac{\alpha_w s_2}{\beta_w + s_2} b v_{fn} (1 - v_w), \tag{2.6}$$

$$\frac{\partial v_w}{\partial t} = \frac{\alpha_w s_2}{\beta_w + s_2} b v_{fn} (1 - v_w) - \gamma v_w (1 - v_l), \tag{2.7}$$

$$\frac{\partial v_l}{\partial t} = \gamma v_w (1 - v_l), \tag{2.8}$$

where terms containing coefficients α_w, β_w and γ model the substitution of the fibrin network by woven bone and the remodeling of woven bone into lamellar bone.

Moreo et al. [67] proposed the following initial and boundary conditions for this equation set. Let Ω be a problem domain with the boundary $\partial\Omega$,

and $\partial\Omega_b$ is a part of boundary, corresponding to bone surface, and $\vec{n}$ is an outward unit normal. Then,

$$\begin{cases} c(\vec{x},0)=0.25, & m(\vec{x},0)=0.001, & b(\vec{x},0)=0.001, & s_1(\vec{x},0)=0.01, \\ s_2(\vec{x},0)=0.01, & v_{fn}(\vec{x},0)=1, & v_w(\vec{x},0)=0, & v_l(\vec{x},0)=0, \end{cases} \tag{2.9}$$

where $\vec{x}\in\Omega$, and

$$\begin{cases} (D_c\nabla c - H_c c\nabla p)\cdot\vec{n}=0, \\ D_{s1}\nabla s_1\cdot\vec{n}=0, \quad D_{s2}\nabla s_2\cdot\vec{n}=0, \\ m=0.2, \\ (D_m\nabla m - m(B_{m1}\nabla s_1 \\ \qquad + B_{m2}\nabla s_2))\cdot\vec{n}=0, \end{cases} \quad \begin{array}{l} \vec{x}\in\partial\Omega,\ t\in(0,\infty) \\ \\ \vec{x}\in\partial\Omega_b,\ t\in(0,14]\ [days] \\ \left[\begin{array}{l} \vec{x}\in\partial\Omega\backslash\partial\Omega_b,\ t\in(0,14]\ [days], \\ \vec{x}\in\partial\Omega,\ t\in(14,\infty)\ [days]. \end{array}\right. \end{array} \tag{2.10}$$

According to Moreo et al. [67] the following parameters values are proposed:

$$\begin{array}{lll} D_c=1.365\cdot10^{-2}\,mm^2/day, & \alpha_{m0}=0.25\,day^{-1}, & \alpha_{b2}=25\,day^{-1}, \\ A_c=0.067\,day^{-1}, & \alpha_m=0.25\,day^{-1}, & \alpha_{m2}=25\,day^{-1}, \\ H_c=0.333\,mm^4/(day\cdot mg), & \beta_{mb}=0.1, & \beta_{c1}=0.1, \\ D_m=0.133\,mm^2/day, & \beta_m=0.1, & \beta_{c2}=0.1, \\ B_{m1}=0.667\,mm^2/day, & A_b=6.67\cdot10^{-3}\,day^{-1}, & \beta_{m2}=0.1, \\ B_{m2}=0.167\,mm^2/day, & A_{s1}=10\,day^{-1}, & \beta_{b2}=0.1, \\ D_{s1}=0.3\,mm^2/day, & A_{s2}=10\,day^{-1}, & \alpha_w=0.1\,day^{-1}, \\ D_{s2}=0.1\,mm^2/day, & \alpha_{c1}=66.7\,day^{-1}, & \beta_w=0.1, \\ A_m=2\cdot10^{-3}\,day^{-1}, & \alpha_{c2}=10\,day^{-1} & \gamma=0.06\,day^{-1}. \end{array} \tag{2.11}$$

Remark 2.1. Growth factor 1 s_1 is assumed to stimulate the differentiation of osteogenic cells into osteoblasts. In Moreo et al. [67] originally, the differentiation term in equations (2.2) and (2.3) was given in the form $\frac{\alpha_{mb}s_1}{\beta_{mb}+s_1}m$. In this paper, a more general representation for differentiation is proposed, which is given by $(\alpha_{p0}+\frac{\alpha_{mb}s_1}{\beta_{mb}+s_1})m$. Parameter α_{p0} implies, that differentiation can take place, if the growth factor 1 concentration s_1 is zero. This assumption is not in contradiction with experimental observations [25, 62], and can be useful, in order to get a more realistic simulation results for different problems. The profit of this representation for differentiation will be demonstrated in Remark 2.3 in Section 2.3.1.

The general form of the differentiation term is reduced to its original representation, proposed by Moreo et al. [67], if

$$\alpha_{mb}=0.5\ day^{-1}, \quad \alpha_{p0}=0\ day^{-1}. \tag{2.12}$$

The assumption, that differentiation also takes place without a presence of growth factors, is represented by the following parameter values:

$$\alpha_{mb} = \frac{2}{3} \cdot 0.5 \; day^{-1}, \quad \alpha_{p0} = \frac{1}{3} \cdot 0.5 \; day^{-1}. \tag{2.13}$$

In this study, both sets of parameter values in equations (2.12) and (2.13) are considered.

2.3 Stability analysis

2.3.1 The simplified biological model

The present aim is to study the conditions, that give the appearance of a wave-like profile. Simulations, performed for the full system, show that the wave-like profile can appear in the solution for the densities of osteogenic cells m and osteoblasts b, for the concentration s_2 of growth factor 2, and for the volume fractions of fibrin network v_{fn}, woven bone v_w and lamellar bone v_l, if the computational domain is sufficiently large. The equations for the variables m, b and s_2 (2.2), (2.5), (2.3) are coupled and can be solved, after the solution for c and s_1 is obtained from the equations (2.1) and (2.4). The equations for variables v_{fn}, v_w and v_l (2.6), (2.7), (2.8) contain only reaction terms in their right-hand side. The wave-like profile in the solution for these variables appears due to the wave-like profile in the solution for osteoblasts and growth factor 2.

Therefore, the phenomenon of the wave-like profile in the solution for variables m, b and s_2 is studied. The solution for m, b and s_2 is determined by the system of equations (2.1)–(2.5).

It is assumed, that the profile appearance can be related to the stability of the constant solutions of the system. Zero solutions $c = 0$, $s_1 = 0$ are the only constant solutions of system (2.1)– (2.5) for variables c and s_1.

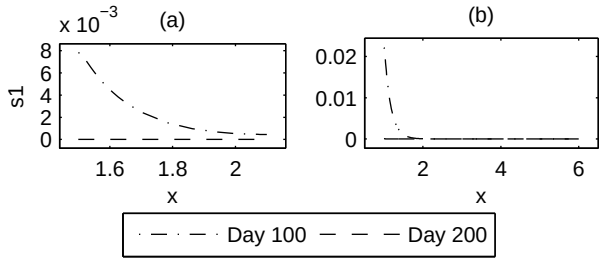

Figure 2.2: Growth factor 1 $s1$ distribution at different time moments, obtained from the numerical solution of the model equations (2.1)–(2.8), for 1D axisymmetric domain with length (a) $L = 0.6\,mm$, (b) $L = 5\,mm$

The equations for platelets c and growth factor 1 s_1 (2.1) and (2.4), can be solved separately from the other equations. That means, that the evolution of the platelet density $c(x,t)$ and growth factor 1 concentration $s_1(x,t)$ does not depend on the evolution of other biological and chemical species involved in the model. Equation (2.1) contains a term, corresponding to the death of platelets, but it does not contain a term, corresponding to the production of platelets. Therefore, the total amount of platelets decays to zero with time. The production of growth factor 1 s_1 is proportional to platelets concentration, and thus the production of s_1 also decays with time, while death rate A_{s1} is constant in time. It can be proved, that the integrals of platelet density and growth factor 1 concentration over the problem domain tend to zero with time, if zero flux on the boundaries is considered. If negative values in the solution for $c(x,t)$ and $s_1(x,t)$ are avoided (otherwise the solution becomes biologically irrelevant), then it follows, that these functions tend to zero almost everywhere in the problem domain. Numerical simulations confirm (Figure 2.2), that for a large time t the solution $s_1(x,t)$ is very close to zero.

The stability analysis deals with the asymptotic behavior of the system, that is with the behavior of the solution for long time periods. Therefore, the simplified system is derived from equations (2.2), (2.5) and (2.3), and from assumption $s_1(x,t) \equiv 0$ in the following form:

$$\frac{\partial m}{\partial t} = \nabla\cdot[D_m\nabla m - B_{m2}m\nabla s_2)]+\Big(\alpha_{m0}+\frac{\alpha_m s_2}{\beta_m + s_2}\Big)m(1-m)-(\alpha_{p0}+A_m)m, \tag{2.14}$$

$$\frac{\partial s_2}{\partial t} = \nabla\cdot[D_{s2}\nabla s_2] + \frac{\alpha_{m2}s_2}{\beta_{m2}+s_2}(m+b) - A_{s2}s_2, \tag{2.15}$$

$$\frac{\partial b}{\partial t} = \alpha_{p0}m - A_b b. \tag{2.16}$$

Remark 2.2. In derivation of (2.15) it was assumed, that $\alpha_{b2} = \alpha_{m2}$ and $\beta_{b2} = \beta_{m2}$. These simplifying assumptions are in line with the values for α_{b2}, α_{m2}, β_{b2} and β_{m2}, proposed by Moreo et al. [67], which were introduced in (2.11).

Remark 2.3. As it was mentioned, the concentration of s_1 becomes close to zero after a certain period of time. Then, differentiation of osteogenic cells into osteoblasts is roughly described by the term $\alpha_{p0}m$, as this is done in equations (2.14), (2.16). This term turns to zero, if $\alpha_{p0} = 0$, as was proposed by Moreo et al. [67]. The solution of (2.16), defined as $b(x,t) = b_0(x)e^{-A_b t}$, converges to zero with time. From a biological point of view, this means, that osteogenic cells stop to differentiate after a certain time period. There is no source of newly formed osteoblasts, and their amount decreases to zero, due to cell death.

If $\alpha_{p0} \neq 0$, then differentiation takes place also when s_1 is zero. This allows to obtain the solution for osteoblasts, which does not converge to zero, and hence, is more realistic from biological point of view. For this reason, the parameter values in equation (2.12), as proposed by Moreo et al. [67], and the alternative values in equation (2.13) are considered.

Moreo et al. [67] investigated the linear stability of the constant solutions of the system, which is similar to system (2.14)–(2.16), against purely temporal perturbations. In this paper, the system stability with respect to arbitrary perturbations (including non-homogeneous perturbations) is studied.

Constant solutions $z' = (m', s', b')$ of system (2.14)–(2.16) are derived from the algebraic system:

$$\begin{cases} \Big(\alpha_{m0} + \dfrac{\alpha_m s_2'}{\beta_m + s_2'}\Big) m'(1 - m') - (\alpha_{p0} + A_m) m' = 0, \\ \dfrac{\alpha_{m2} s_2'}{\beta_{m2} + s_2'}(m' + b') - A_{s2} s_2' = 0, \\ \alpha_{p0} m' - A_b b' = 0. \end{cases} \tag{2.17}$$

Two solutions of the above system have been denoted by Moreo et al. [67] as:

- "Chronic non healing state": $z_t = (0, 0, 0)$,
- "Low density state": $z_0 = (m_0, 0, b_0)$,

where

$$m_0 = 1 - \frac{\alpha_{p0} + A_m}{\alpha_{m0}}, \quad b_0 = \frac{\alpha_{p0}}{A_b} m_0. \tag{2.18}$$

From system (2.17), it follows, that root s_2' can not be equal to $-\beta_m < 0$ or to $-\beta_{m2} < 0$. Vectors $z_- = (m_-, s_{2-}, b_-)$ and $z_+ = (m_+, s_{2+}, b_+)$ are defined as

$$s_{2\pm} = \frac{-a_1 \pm \sqrt{a_1^2 - 4a_2 a_0}}{2a_2}, \tag{2.19}$$

$$m_\pm = \frac{A_b A_{s2}(s_{2\pm} + \beta_{m2})}{\alpha_{m2}(A_b + \alpha_{p0})} = \frac{A_{s2}(s_{2\pm} + \beta_{m2})}{\chi}, \quad b_\pm = \frac{\alpha_{p0}}{A_b} m_\pm, \tag{2.20}$$

where

$$\begin{cases} a_2 = A_{s_2}\left(1 + \dfrac{\alpha_m}{\alpha_{m0}}\right), \\ a_1 = \left(1 + \dfrac{\alpha_m}{\alpha_{m0}}\right)(\beta_{m2} A_{s_2} - \chi m_0) + \dfrac{\alpha_m}{\alpha_{m0}} \chi (m_0 - 1) + \beta_m A_{s_2}, \\ a_0 = \beta_m (\beta_{m2} A_{s_2} - \chi m_0), \end{cases} \tag{2.21}$$

$$\chi = \alpha_{m2}\left(1 + \alpha_{p0}/A_b\right), \tag{2.22}$$

and m_0 is defined in equation (2.18). They are the solutions of system (2.17), if $s_{2\pm} \notin \{-\beta_m; -\beta_{m2}\}$. Therefore, depending on the values of model parameters, system (2.17) can have two, three or four solutions.

Remark 2.4. From the derivation of the expression (2.19), which is not given here, it follows, that at least one of the roots s_{2+} and s_{2-} is equal to $-\beta_m$, if and only if $A_{s2}(\beta_{m2} - \beta_m) = \chi$. And at least one of the roots s_{2+} and s_{2-} is equal to $-\beta_{m2}$, if and only if $(\alpha_{m0} - \alpha_{p0} - A_m)(\beta_m - \beta_{m2}) = \alpha_m\beta_{m2}$. For the chosen parameter values in equations (2.11), (2.12), (2.13), $\beta_{m2} = \beta_m > 0$, $\alpha_m > 0$, $\chi = \alpha_{m2}\left(1 + \alpha_{p0}/A_b\right) > 0$. Hence, $s_{2\pm} \neq -\beta_m$ and $s_{2\pm} \neq -\beta_{m2}$ for the considered parameter values, and system (2.14)–(2.16) has four constant solutions z_t, z_0, z_+ and z_-.

It should be mentioned here, that for the existence of real $s_{2\pm}$ the necessary condition is:

$$a_1^2 - 4a_2a_0 \geq 0. \tag{2.23}$$

This necessary condition is written in terms of the model parameters as:

$$\begin{aligned}
a_1^2 - 4a_2a_0 &= \left(\chi\left(m_0 + \frac{\alpha_m}{\alpha_{m0}}\right) - A_{s2}\left(\beta_m + \beta_{m2}\left(1 + \frac{\alpha_m}{\alpha_{m0}}\right)\right)\right)^2 \\
&- 4A_{s2}\beta_m\left(1 + \frac{\alpha_m}{\alpha_{m0}}\right)(\beta_{m2}A_{s2} - \chi m_0) = \left(\chi\left(m_0 + \frac{\alpha_m}{\alpha_{m0}}\right) - \xi\right)^2 \\
&+ \chi\left(m_0 + \frac{\alpha_m}{\alpha_{m0}}\right)\eta - \eta\left(\beta_{m2}A_{s2} + \chi\frac{\alpha_m}{\alpha_{m0}}\right) = \left(\chi\left(m_0 + \frac{\alpha_m}{\alpha_{m0}}\right)\right)^2 \\
&+ \chi\left(m_0 + \frac{\alpha_m}{\alpha_{m0}}\right)(\eta - 2\xi) + \xi^2 - \eta\left(\beta_{m2}A_{s2} + \chi\frac{\alpha_m}{\alpha_{m0}}\right) \geq 0,
\end{aligned} \tag{2.24}$$

where

$$\xi = A_{s2}\left(\beta_m + \beta_{m2}\left(1 + \frac{\alpha_m}{\alpha_{m0}}\right)\right), \quad \eta = 4A_{s2}\beta_m\left(1 + \frac{\alpha_m}{\alpha_{m0}}\right). \tag{2.25}$$

From (2.24) it is derived, that (2.23) is equivalent to:

$$\left[\begin{array}{l}
\chi\left(m_0 + \frac{\alpha_m}{\alpha_{m0}}\right) \geq -A_{s2}\beta_m\frac{\alpha_m}{\alpha_{m0}} + \sqrt{\eta\frac{\alpha_m}{\alpha_{m0}}\chi}, \\
\chi\left(m_0 + \frac{\alpha_m}{\alpha_{m0}}\right) \leq -A_{s2}\beta_m\frac{\alpha_m}{\alpha_{m0}} - \sqrt{\eta\frac{\alpha_m}{\alpha_{m0}}\chi}.
\end{array}\right. \tag{2.26}$$

The sign of $s_{2\pm}$ depends on the sign of coefficients a_1 and a_0 (coefficient a_2 is larger than zero, which follows from its definition). Both roots will be positive if $a_1 < 0$ and $a_0 > 0$ and if inequality (2.23) holds.

For the parameter values in equations (2.11), (2.12) the constant solutions have values: $m_0 \approx 0.9920$, $b_0 = 0$; $m_- \approx 0.0201$, $s_{2-} \approx -0.0498$,

$b_- = 0$; $m_+ \approx 0.9959$, $s_{2+} \approx 2.3898$, $b_+ = 0$; and for parameter values (2.11), (2.13): $m_0 \approx 0.3253$, $b_0 \approx 8.1293$; $m_- \approx 0.0012$, $s_{2-} \approx -0.0245$, $b_- \approx 0.0290$; $m_+ \approx 0.6623$, $s_{2+} \approx 42.9271$, $b_+ \approx 16.5486$.

Remark 2.5. For the chosen parameter sets (2.11), (2.12) and (2.11), (2.13), growth factor 2 concentration s_{2-} is negative, which is unphysical. It is desirable to avoid such a negative concentration of growth factor 2 in the solution of the problem (2.14)–(2.16). Calculations show, that for the chosen parameter values there are two positive eigenvalues of the Jacobean of the equation system, linearized for the case of small purely temporal perturbations near the constant solution z_-. Hence, the constant solution z_- is unstable against temporal perturbations. It is possible to obtain non-negative values in the numerical solution for s_2, provided a sufficiently small time step and mesh size are chosen and positive initial values for concentrations of cells and growth factor are considered.

2.3.2 Non-homogeneous perturbations

In this section, the stability of constant-state solutions of system (2.14)–(2.16) is analyzed. The present approach is valid for a domain in any coordinate system, for which eigenfunctions of Laplace operator can be found. In this paper, the examples of the eigenfunctions are given for domains in 1D Cartesian coordinates and in 1D axisymmetric coordinates. The independent space coordinate is denoted by x for both coordinate systems. Suppose that non-homogeneous perturbations $m_p(x,t)$, $s_{2p}(x,t)$ and $b_p(x,t)$ are imposed on the constant solution (m', s_2', b'). Then the solution is given in the form:

$$\begin{cases} m(x,t) = m' + \varepsilon m_p(x,t), \\ s_2(x,t) = s_2' + \varepsilon s_{2p}(x,t), \\ b(x,t) = b' + \varepsilon b_p(x,t), \end{cases} \tag{2.27}$$

where $|\varepsilon| \ll 1$. Then, equations (2.27) are substituted into (2.14)–(2.16), and linearized with respect to small ε:

$$\begin{cases} \dfrac{\partial m_p}{\partial t} = D_m \nabla^2 m_p - m' B_{m2} \nabla^2 s_{2p} + \Big[\Big(\alpha_{m0} + \dfrac{\alpha_m s_2'}{\beta_m + s_2'} \Big)(1 - 2m') \\ \qquad\qquad - (\alpha_{p0} + A_m) \Big] m_p + \dfrac{\alpha_m \beta_m}{(\beta_m + s_2')^2} m'(1 - m') s_{2p}, \\ \dfrac{\partial s_{2p}}{\partial t} = D_{s2} \nabla^2 s_{2p} + \dfrac{\alpha_{m2} s_2'}{\beta_{m2} + s_2'}(m_p + b_p) \\ \qquad\qquad + \Big[\dfrac{\alpha_{m2} \beta_{m2}}{(\beta_{m2} + s_2')^2}(m' + b') - A_{s2} \Big] s_{2p}, \\ \dfrac{\partial b_p}{\partial t} = \alpha_{p0} m_p - A_b b_p. \end{cases} \tag{2.28}$$

Let us denote the problem domain as $[x_0, x_0 + L]$. Assume, that on the boundaries the flux of cells and of growth factors is zero. Then, perturbations are considered in the form:

$$\begin{cases} m_p(x,t) = C_0^m(t) + \sum_{n=1}^{\infty} C_n^m(t)\phi_n(x), \\ s_{2p}(x,t) = C_0^{s2}(t) + \sum_{n=1}^{\infty} C_n^{s2}(t)\phi_n(x), \\ b_p(x,t) = C_0^b(t) + \sum_{n=1}^{\infty} C_n^b(t)\phi_n(x). \end{cases} \tag{2.29}$$

Functions $C_0^m(t)$, $C_0^{s2}(t)$, $C_0^b(t)$ represent purely temporal perturbations. Eigenfunctions $\phi_n(x)$ satisfy equation $\nabla^2\phi_n(x) = -k_n^2\phi_n(x)$ and considered boundary conditions, i.e. zero flux on the boundaries: $\nabla\phi_n(x_0) = \nabla\phi_n(x_0 + L) = \vec{0}$.

If Cartesian coordinates are considered, then the function $\phi_n(x)$ is given as $\phi_n^C(x) = \cos(k_n(x - x_0))$, where $k_n = \frac{\pi n}{L}$, $n = 1, 2, \ldots$. In this case k_n is a wavenumber.

In the case of axisymmetric coordinates functions $\phi_n(x)$ have the form $\phi_n^a(x) = Y_0'(k_n x_0)J_0(k_n x) - J_0'(k_n x_0)Y_0(k_n x)$, where $J_0(k_n x)$ and $Y_0(k_n x)$ are Bessel functions, $k_n = \frac{w_n}{x_0+L}$ and w_n, $n = 1, 2, \ldots$ are positive real zeros of the function $\Phi(w) = -Y_0'(k_n x_0)J_1(w) + J_0'(k_n x_0)Y_1(w)$. Functions $\phi_n^a(x)$, $n = 1, 2, \ldots$ are not periodic. They can be roughly described as "waves" with variable in space wavelength and magnitude. For simplicity, k_n will be referred to as 'wavenumber', also if it is introduced in functions $\phi_n^a(x)$.

Remark 2.6. Perturbation modes $\phi_n(x)$, $n = 1, 2, \ldots$ by their definition have positive wavenumbers $k_n > 0$. For the sake of generality, purely temporal perturbations are considered as perturbations of mode $n = 0$ with zero wavenumber $k_0 = 0$ and $\phi_0(x) \equiv 1$.

Substitution of equations (2.29) into system (2.28) yields:

$$\vec{C}_n'(t) = \mathbf{A}_{k_n}\vec{C}_n(t), \quad n = 0, 1, \ldots, \tag{2.30}$$

where

$$\vec{C}_n(t) = \begin{bmatrix} C_n^m(t) \\ C_n^{s2}(t) \\ C_n^b(t) \end{bmatrix}, \quad n = 0, 1, \ldots, \tag{2.31}$$

$$\mathbf{A}_{k_n} = \begin{pmatrix} \mathbf{A}_{k_n(1,1)} & \mathbf{A}_{k_n(1,2)} & 0 \\ \dfrac{\alpha_{m2}s_2'}{\beta_{m2} + s_2'} & \mathbf{A}_{k_n(2,2)} & \dfrac{\alpha_{m2}s_2'}{\beta_{m2} + s_2'} \\ \alpha_{p0} & 0 & -A_b \end{pmatrix}, \tag{2.32}$$

where

$$\mathbf{A}_{k_n(1,1)} = \Big(\alpha_{m0} + \frac{\alpha_m s_2'}{\beta_m + s_2'}\Big)(1-2m') - (\alpha_{p0} + A_m) - k_n^2 D_m,$$
$$\mathbf{A}_{k_n(1,2)} = \frac{\alpha_m \beta_m}{(\beta_m + s_2')^2} m'(1-m') + k_n^2 B_{m2} m',$$
$$\mathbf{A}_{k_n(2,2)} = \frac{\alpha_{m2}\beta_{m2}}{(\beta_{m2} + s_2')^2}\big(1 + \frac{\alpha_{p0}}{A_b}\big)m' - A_{s2} - k_n^2 D_{s2}.$$

Then from (2.30):

$$\vec{C}_n(t) = e^{\mathbf{A}_{k_n} t}\vec{C}_n^0, \quad n = 0, 1, \ldots, \tag{2.33}$$

where $\vec{C}_n^0$ define the perturbations imposed on the constant solution of the system initially at time $t = 0$:

$$\begin{bmatrix} m_p(x,0) \\ s_{2p}(x,0) \\ b_p(x,0) \end{bmatrix} = \sum_{n=0}^{\infty} \vec{C}_n^0 \phi_n(x).$$

Thus the solution of (2.28) is written as:

$$\begin{bmatrix} m_p(x,t) \\ s_{2p}(x,t) \\ b_p(x,t) \end{bmatrix} = \sum_{n=0}^{\infty} e^{\mathbf{A}_{k_n} t}\vec{C}_n^0 \phi_n(x). \tag{2.34}$$

The magnitude of perturbations $\|\vec{C}_n(t)\| = \|e^{\mathbf{A}_{k_n} t}\vec{C}_n^0\|$ of mode n, will grow in time, if at least one of the eigenvalues of the matrix $\mathbf{A}_{k_n}$ is a positive real number or a complex number with a positive real part. And $\|\vec{C}_n(t)\|$ will converge to zero, if all the eigenvalues of $\mathbf{A}_{k_n}$ are real negative, or complex numbers with the real part less than zero. If the matrix $\mathbf{A}_{k_n}$ has precisely one zero eigenvalue, and other eigenvalues are real negative or complex with a negative real part, then small perturbations remain small for infinite time period.

It is not complicated to find expressions for the eigenvalues of $\mathbf{A}_{k_n}$, evaluated at the 'chronic non healing state' $z_t = (0, 0, 0)$ and 'low density state' $z_0 = (m_0, 0, b_0)$. For the constant solution z_t eigenvalues of $\mathbf{A}_{k_n}$ are:

$$\begin{aligned} &\lambda_{1t}(k_n^2) = \alpha_{m0} m_0 - k_n^2 D_m > 0, \ \text{ if } \ 0 \le k_n^2 < \frac{\alpha_{m0} m_0}{D_m}, \\ &\lambda_{2t}(k_n^2) = -A_{s2} - k_n^2 D_{s2} < 0, \quad \lambda_{3t}(k_n^2) = -A_b < 0. \end{aligned} \tag{2.35}$$

Therefore, if m_0 is positive, constant solution z_t is unstable against purely temporal perturbations and perturbations with a small wavenumber $0 < k_n < \sqrt{\frac{\alpha_{m0} m_0}{D_m}}$. The first eigenvalue $\lambda_{1t}(k_n^2)$ takes the largest positive value for the wavenumber k_0, i.e. for the purely temporal perturbation mode.

Remark 2.7. For negative m_0, 'chronic non-healing state' z_t will become stable against perturbations with any wavenumber. Further the constant solution z_0 will contain an unphysical negative concentration for osteogenic cells. Inequality $m_0 = 1 - \frac{\alpha_{p0}+A_m}{\alpha_{m0}} < 0$ implies, that differentiation and death of osteogenic cell dominate over their production. Therefore, this situation is not relevant for the considered model of bone formation, and further $m_0 > 0$ is assumed a priori.

For the constant solution $z_0 = (m_0, 0, b_0)$ matrix $\mathbf{A}_{k_n}$ eigenvalues are:

$$\begin{gathered}\lambda_{10}(k_n^2) = -\alpha_{m0}m_0 - k_n^2 D_m < 0,\\ \lambda_{20}(k_n^2) = \frac{\alpha_{m2}}{\beta_{m2}}m_0(1+\frac{\alpha_{p0}}{A_b}) - A_{s2} - k_n^2 D_{s2}, \quad \lambda_{30}(k_n^2) = -A_b < 0.\end{gathered} \tag{2.36}$$

If expression $\frac{\alpha_{m2}}{\beta_{m2}}m_0(1+\frac{\alpha_{p0}}{A_b}) - A_{s2}$ takes a positive value, which is true for the current parameter values in equations (2.11), (2.12) and (2.13), then the constant solution z_0 is unstable against perturbations with the wavenumbers $k_n^2 < \left(\frac{\alpha_{m2}}{\beta_{m2}}m_0(1+\frac{\alpha_{p0}}{A_b}) - A_{s2}\right)/D_{s2}$. The largest eigenvalue λ_{20} corresponds to zero wavenumber k_0, i.e. to the purely temporal mode of perturbation.

The eigenvalues of the matrix $\mathbf{A}_{k_n}$ defined at points z_- and z_+ can not be found in such a trivial manner, as for the constant solutions z_t and z_0. They are obtained from the characteristic equation, which is a non-trivial cubic algebraic equation. Therefore, instead of analyzing the expressions for the eigenvalues, which are extremely complicated in this case, a different approach is proposed, which based on a reduction of the considered system of equations to two equations with similar stability properties.

Remark 2.8. For the chosen parameter values, see expressions (2.11), (2.12) and (2.11), (2.13), s_{2-} is negative, hence the constant solution z_- is biologically irrelevant in this case. Therefore, only the stability of the constant solution z_+ and not of z_- is analyzed. The stability analysis, being introduced for z_+, is not valid for the constant solution z_-, if it contains the negative value of growth factor concentration. Calculations also show, that for parameter values (2.11), (2.12) and (2.13), the constant solution z_- is unstable against at least purely temporal perturbations.

2.3.3 Stability of the system of two equations

To simplify the stability analysis, system (2.14)–(2.16) is reduced to a system of two equations. For this reduced system the assumption

$$b(x,t) = \frac{\alpha_{p0}}{A_b}m(x,t) \tag{2.37}$$

is made, instead of equation (2.16). The system is defined as:

$$\begin{cases} \dfrac{\partial m}{\partial t} = \nabla \cdot [D_m \nabla m - B_{m2} m \nabla s_2)] \\ \qquad\qquad + \Big(\alpha_{m0} + \dfrac{\alpha_m s_2}{\beta_m + s_2}\Big) m(1-m) - (\alpha_{p0} + A_m) m, \\ \dfrac{\partial s_2}{\partial t} = \nabla \cdot [D_{s2} \nabla s_2] + \dfrac{\alpha_{m2} s_2}{\beta_{m2} + s_2}(1 + \dfrac{\alpha_{p0}}{A_b}) m - A_{s2} s_2. \end{cases} \tag{2.38}$$

Substitution of (2.37) into equation (2.16), yields the condition $\frac{\partial b}{\partial t} = 0$, which is not true in general case. Therefore, system (2.14)–(2.16) and system (2.38) are not equivalent, and their stability properties are different in general. However, it will be shown in Section 2.3.4, that there is a certain similarity (or correspondence) between the stability properties of the two systems. This similarity is sufficient, to transfer important results, obtained from the stability analysis for the system of two equations (2.38), onto the system of three equations (2.14)–(2.16).

System (2.38) has constant solutions, that are analogous to those of system (2.14)–(2.16). They are: $\tilde{z}_t = (0,0)$, $\tilde{z}_0 = (m_0, 0)$, $\tilde{z}_+ = (m_+, s_{2+})$, $\tilde{z}_- = (m_-, s_{2-})$. Linearizing the system near the point (m', s_2'), with $m(x,t) = m' + \varepsilon m_p(x,t)$ and $s_2(x,t) = s_2' + \varepsilon s_{2p}(x,t)$, yields:

$$\begin{cases} \dfrac{\partial m_p}{\partial t} = D_m \nabla^2 m_p - m' B_{m2} \nabla^2 s_{2p} + \Big[\Big(\alpha_{m0} + \dfrac{\alpha_m s_2'}{\beta_m + s_2'}\Big)(1 - 2m') \\ \qquad\qquad - (\alpha_{p0} + A_m)\Big] m_p + \dfrac{\alpha_m \beta_m}{(\beta_m + s_2')^2} m'(1-m') s_{2p}, \\ \dfrac{\partial s_{2p}}{\partial t} = D_{s2} \nabla^2 s_{2p} + \dfrac{\alpha_{m2} s_2'}{\beta_{m2} + s_2'}(1 + \dfrac{\alpha_{p0}}{A_b}) m_p \\ \qquad\qquad + \left[\dfrac{\alpha_{m2}\beta_{m2}}{(\beta_{m2} + s_2')^2}(1 + \dfrac{\alpha_{p0}}{A_b}) m' - A_{s2}\right] s_{2p}. \end{cases} \tag{2.39}$$

Considering solutions of the form

$$\begin{cases} m_p(x,t) = \displaystyle\sum_{n=0}^{\infty} C_n^m(t) \phi_n(x), \\ s_{2p}(x,t) = \displaystyle\sum_{n=0}^{\infty} C_n^{s2}(t) \phi_n(x), \end{cases}$$

and substituting them into system (2.39), for each $n = 0, 1, \ldots$ we arrive at:

$$\begin{bmatrix} \dfrac{dC_n^m(t)}{dt} \\ \dfrac{dC_n^{s2}(t)}{dt} \end{bmatrix} = \widetilde{\mathbf{A}}_{k_n} \begin{bmatrix} C_n^m(t) \\ C_n^{s2}(t) \end{bmatrix},$$

where

$$\widetilde{\mathbf{A}}_{k_n} = \begin{pmatrix} \tilde{\mathbf{A}}_{k_n(1,1)} & \tilde{\mathbf{A}}_{k_n(1,2)} \\ \dfrac{\alpha_{m2} s_2'}{\beta_{m2} + s_2'} \left(1 + \dfrac{\alpha_{p0}}{A_b}\right) & \tilde{\mathbf{A}}_{k_n(2,2)} \end{pmatrix},$$

$$\begin{aligned}
\tilde{\mathbf{A}}_{k_n(1,1)} &= \Big(\alpha_{m0} + \frac{\alpha_m s_2'}{\beta_m + s_2'}\Big)(1 - 2m') - (\alpha_{p0} + A_m) - k_n^2 D_m, \\
\tilde{\mathbf{A}}_{k_n(1,2)} &= \frac{\alpha_m \beta_m}{(\beta_m + s_2')^2} m'(1 - m') + k_n^2 B_{m2} m', \\
\tilde{\mathbf{A}}_{k_n(2,2)} &= \frac{\alpha_{m2} \beta_{m2}}{(\beta_{m2} + s_2')^2} \big(1 + \frac{\alpha_{p0}}{A_b}\big) m' - A_{s2} - k_n^2 D_{s2}.
\end{aligned}$$

First the stability properties of system (2.39) are studied, and then it is determined, how they are related to the stability properties of the system of three equations (2.28). Since $s_{2+} \neq -\beta_{m2}$, then from relation (2.20) it follows that $m_+ \neq 0$. Therefore, the matrix $\widetilde{\mathbf{A}}_{k_n}$ evaluated in the point (m_+, s_{2+}), can be simplified. From the first equation of system (2.17) it follows:

$$\Big(\alpha_{m0} + \frac{\alpha_m s_{2+}}{\beta_m + s_{2+}}\Big)(1 - m_+) - (\alpha_{p0} + A_m) = 0. \tag{2.40}$$

Then:

$$\begin{aligned}
\widetilde{\mathbf{A}}_{k_n(1,1)}(m_+, s_{2+}) =& \Big(\alpha_{m0} + \frac{\alpha_m s_{2+}}{\beta_m + s_{2+}}\Big)(1 - 2m_+) - (\alpha_{p0} + A_m) - k_n^2 D_m \\
=& 2\left(\Big(\alpha_{m0} + \frac{\alpha_m s_{2+}}{\beta_m + s_{2+}}\Big)(1 - m_+) - (\alpha_{p0} + A_m)\right) \\
& - \left(\Big(\alpha_{m0} + \frac{\alpha_m s_{2+}}{\beta_m + s_{2+}}\Big) - (\alpha_{p0} + A_m)\right) - k_n^2 D_m \\
=& -\alpha_{m0} m_0 - \frac{\alpha_m s_{2+}}{\beta_m + s_{2+}} - k_n^2 D_m, \\
\widetilde{\mathbf{A}}_{k_n(2,1)}(m_+, s_{2+}) =& \frac{\alpha_{m2} s_{2+}}{\beta_{m2} + s_{2+}} (1 + \frac{\alpha_{p0}}{A_b}) = \chi \frac{s_{2+}}{\beta_{m2} + s_{2+}},
\end{aligned}$$

where χ is defined in (2.22). From equation (2.20), it follows that

$$\begin{aligned}
\widetilde{\mathbf{A}}_{k_n(1,2)}(m_+, s_{2+}) =& \frac{\alpha_m \beta_m}{(\beta_m + s_{2+})^2} m_+(1 - m_+) + k_n^2 B_{m2} m_+ \\
=& \frac{A_{s2} \alpha_m \beta_m}{\chi(\beta_m + s_{2+})} \frac{\beta_{m2} + s_{2+}}{\beta_m + s_{2+}} (1 - m_+) + k_n^2 B_{m2} m_+.
\end{aligned}$$

Everywhere in the calculations, presented in Moreo et al. [67] and in this paper, the same values are used for the parameters β_m and β_{m2}. So both notations β_m and β_{m2} is used, though $\beta_{m2} = \beta_m$ is supposed below. Then

$$\widetilde{\mathbf{A}}_{k_n(1,2)}(m_+, s_{2+}) = \frac{A_{s2} \alpha_m \beta_m}{\chi(\beta_m + s_{2+})} (1 - m_+) + k_n^2 B_{m2} m_+,$$

$$\widetilde{\mathbf{A}}_{k_n(2,2)}(m_+, s_{2+}) = \frac{\alpha_{m2}\beta_{m2}}{(\beta_{m2}+s_{2+})^2}(1+\frac{\alpha_{p0}}{A_b})m_+ - A_{s2} - k_n^2 D_{s2}$$
$$= A_{s2}(\frac{\beta_{m2}}{\beta_{m2}+s_{2+}} - 1) - k_n^2 D_{s2} = -A_{s2}\frac{s_{2+}}{\beta_{m2}+s_{2+}} - k_n^2 D_{s2}.$$

Therefore,

$$\widetilde{\mathbf{A}}_{k_n}(m_+, s_{2+})$$
$$= \begin{pmatrix} -\alpha_{m0}m_0 - \frac{\alpha_m s_{2+}}{\beta_m+s_{2+}} - k_n^2 D_m & \frac{A_{s2}\alpha_m\beta_m}{\chi(\beta_m+s_{2+})}(1-m_+) + k_n^2 B_{m2}m_+ \\ \chi\frac{s_{2+}}{\beta_{m2}+s_{2+}} & -A_{s2}\frac{s_{2+}}{\beta_{m2}+s_{2+}} - k_n^2 D_{s2} \end{pmatrix}.$$

Then the characteristic equation for the matrix $\widetilde{\mathbf{A}}_{k_n}$, evaluated at point (m_+, s_{2+}), is given by:

$$\lambda^2(k_n^2) + b(k_n^2)\lambda(k_n^2) + c(k_n^2) = 0, \tag{2.41}$$

where

$$\begin{aligned} b(k_n^2) &= -(\widetilde{\mathbf{A}}_{k_n(1,1)}(m_+, s_{2+}) + \widetilde{\mathbf{A}}_{k_n(2,2)}(m_+, s_{2+})) \\ &= k_n^2 D_m + \alpha_{m0}m_0 + \frac{\alpha_m s_{2+}}{\beta_m + s_{2+}} + k_n^2 D_{s2} + A_{s2}\frac{s_{2+}}{\beta_{m2}+s_{2+}} \\ &= k_n^2(D_m + D_{s2}) + \alpha_{m0}m_0 + (\alpha_m + A_{s2})\frac{s_{2+}}{\beta_m + s_{2+}}, \end{aligned}$$

$$\begin{aligned} c(k_n^2) =& \widetilde{\mathbf{A}}_{k_n(1,1)}(m_+, s_{2+})\widetilde{\mathbf{A}}_{k_n(2,2)}(m_+, s_{2+}) \\ &- \widetilde{\mathbf{A}}_{k_n(1,2)}(m_+, s_{2+})\widetilde{\mathbf{A}}_{k_n(2,1)}(m_+, s_{2+}) \\ =& \left(k_n^2 D_m + \alpha_{m0}m_0 + \frac{\alpha_m s_{2+}}{\beta_m + s_{2+}}\right)\left(k_n^2 D_{s2} + A_{s2}\frac{s_{2+}}{\beta_{m2}+s_{2+}}\right) \\ &- \left(k_n^2 B_{m2}m_+ + \frac{A_{s2}\alpha_m\beta_m}{\chi(\beta_m+s_{2+})}(1-m_+)\right)\chi\frac{s_{2+}}{\beta_{m2}+s_{2+}}. \end{aligned}$$

From equation (2.41) the eigenvalues of $\widetilde{\mathbf{A}}_{k_n}(m_+, s_{2+})$ are determined as:

$$\lambda_{1,2}(k_n^2) = -\frac{b(k_n^2)}{2} \pm \frac{1}{2}\sqrt{b^2(k_n^2) - 4c(k_n^2)}. \tag{2.42}$$

It should be mentioned that

$$\begin{cases} s_{2+} > 0, \\ m_0 > 0 \end{cases} \quad \Rightarrow \quad b(k_n^2) > 0. \tag{2.43}$$

Thus, the following lemma can be formulated.

Lemma 2.1. *Suppose, that for the chosen parameter values, m_0 defined in* (2.18) *is positive, $\beta_m = \beta_{m2}$ and that there exists a real positive s_{2+} defined in* (2.19)*. Then the nature of eigenvalues of the matrix $\widetilde{\mathbf{A}}_{k_n}(m_+, s_{2+})$ is determined by the sign of $c(k_n^2)$:*

- *if $c(k_n^2) < 0$, then one of the eigenvalues is positive and the other is negative,*
- *if $c(k_n^2) = 0$, then the matrix $\widetilde{\mathbf{A}}_{k_n}(m_+, s_{2+})$ has one zero eigenvalue and one negative.*
- *if $c(k_n^2) > 0$ then both eigenvalues are either negative, or complex with a negative real part.*

The wavenumbers which lead to growing perturbations are determined by inequality $c(k_n^2) < 0$. $c(k_n^2)$ can be written in the form:

$$c(k_n^2) = \gamma_2 k_n^4 + \gamma_1 k_n^2 + \gamma_0, \tag{2.44}$$

where

$$\gamma_2 = D_m D_{s2}, \tag{2.45}$$

$$\gamma_1 = (D_m A_{s2} + D_{s2}\alpha_m - \chi m_+ B_{m2})\frac{s_{2+}}{\beta_{m2} + s_{2+}} + D_{s2}\alpha_{m0} m_0, \tag{2.46}$$

$$\gamma_0 = A_{s2}\frac{s_{2+}}{\beta_{m2} + s_{2+}}\left(\alpha_{m0} m_0 + \alpha_m \frac{s_{2+}}{\beta_m + s_{2+}}(2 - m_+) + \alpha_m(m_+ - 1)\right). \tag{2.47}$$

Lemma 2.2. *Suppose, that for the chosen parameter values, m_0 defined in* (2.18) *is positive, and that $\beta_{m2} = \beta_m$. Then if there exists a real positive s_{2+} defined in* (2.19)*, then γ_0 defined in* (2.47) *is non-negative.*

Proof. Since $s_{2+} > 0$, then it is necessary to prove, that

$$\alpha_{m0} m_0 + \alpha_m \frac{s_{2+}}{\beta_m + s_{2+}}(2 - m_+) + \alpha_m(m_+ - 1) \geq 0.$$

The previous inequality is simplified with use of equations(2.40) and (2.18):

$$\begin{aligned}
&\alpha_{m0} m_0 + \alpha_m \frac{s_{2+}}{\beta_m + s_{2+}}(2 - m_+) + \alpha_m(m_+ - 1) \\
&\quad = \left(\alpha_{m0} m_0 + \alpha_m \frac{s_{2+}}{\beta_m + s_{2+}}(1 - m_+) - \alpha_{m0} m_+\right) + \alpha_m \frac{s_{2+}}{\beta_m + s_{2+}} \\
&+ \alpha_{m0} m_+ + \alpha_m(m_+ - 1) = m_+(\alpha_{m0} + \alpha_m) + \alpha_m\left(\frac{s_{2+}}{\beta_m + s_{2+}} - 1\right) \geq 0.
\end{aligned}$$

That is equivalent to $m_+(\alpha_{m0} + \alpha_m) \geq \left(\frac{\alpha_m \beta_m}{\beta_m + s_{2+}}\right)$. Considering (2.20), this transforms to

$$(\beta_m + s_{2+})^2 \geq \frac{\alpha_m \beta_m \chi}{A_{s2}(\alpha_{m0} + \alpha_m)}, \tag{2.48}$$

where χ is defined in (2.22). Next, it is proved, that inequality (2.48) holds. From equation (2.19) and assumption $\beta_{m2} = \beta_m$ it follows, that

$$\begin{aligned} s_{2+} + \beta_m &= \frac{-a_1 + \sqrt{a_1^2 - 4a_2a_0}}{2a_2} + \beta_m \geq -\frac{a_1}{2a_2} + \beta_m \\ &= -\frac{(\alpha_{m0} + \alpha_m)(\beta_m A_{s_2} - \chi m_0) + \alpha_m \chi (m_0 - 1) + \alpha_{m0}\beta_m A_{s_2}}{2A_{s2}(\alpha_{m0} + \alpha_m)} \\ &\quad + \frac{2\beta_m A_{s2}(\alpha_{m0} + \alpha_m)}{2A_{s2}(\alpha_{m0} + \alpha_m)} = \frac{\alpha_m \beta_m A_{s2} + \chi(\alpha_m + \alpha_{m0} m_0)}{2A_{s2}(\alpha_{m0} + \alpha_m)}, \end{aligned} \tag{2.49}$$

where a_2, a_1, a_0 are defined in (2.21). Since $\chi = \alpha_{m2}\,(1 + \alpha_{p0}/A_b) > 0$ and m_0 is supposed to be positive, then from (2.26) it is derived that:

$$\chi \left(m_0 + \frac{\alpha_m}{\alpha_{m0}} \right) \geq -A_{s2}\beta_m \frac{\alpha_m}{\alpha_{m0}} + \sqrt{\eta \frac{\alpha_m}{\alpha_{m0}} \chi}. \tag{2.50}$$

where η is defined in (2.25). Thus from (2.49) and (2.50) it follows:

$$\begin{aligned} \beta_m + s_{2+} \geq & \frac{\alpha_m \beta_m A_{s2} + \chi(\alpha_m + \alpha_{m0} m_0)}{2A_{s2}(\alpha_{m0} + \alpha_m)} \\ \geq & \frac{\alpha_m \beta_m A_{s2} - \alpha_m \beta_m A_{s2} + \sqrt{\eta \alpha_m \alpha_{m0} \chi}}{2A_{s2}(\alpha_{m0} + \alpha_m)} \\ = & \frac{\sqrt{\eta \alpha_m \alpha_{m0} \chi}}{2A_{s2}(\alpha_{m0} + \alpha_m)} = \sqrt{\frac{\alpha_m \beta_m \chi}{A_{s2}(\alpha_{m0} + \alpha_m)}} \end{aligned}$$

Thus inequality (2.48) holds, and consequently $\gamma_0 \geq 0$. □

Remark 2.9. From the proof of Lemma 2.2 it follows, that $\gamma_0 = 0$, if and only if $a_1^2 - 4a_2a_0 = 0$ which is equivalent for $m_0 > 0$ to

$$\chi \left(m_0 + \frac{\alpha_m}{\alpha_{m0}} \right) = -A_{s2}\beta_m \frac{\alpha_m}{\alpha_{m0}} + \sqrt{\eta \frac{\alpha_m}{\alpha_{m0}} \chi}. \tag{2.51}$$

where η is defined in (2.25). In this case two constant solutions $\tilde{z}_-$ and $\tilde{z}_+$ coincide, since $s_{2-} = s_{2+} = -\frac{a_1}{2a_0}$.

It should be mentioned here, that under the assumptions of Lemma 2.2, $c(0) = \gamma_0 \geq 0$. Then, Lemma 2.3 follows from Lemma 2.1.

Lemma 2.3. *If, for the chosen parameter values, m_0 defined in* (2.18) *is positive, $\beta_{m2} = \beta_m$ and there exists a real positive s_{2+} defined in* (2.19)*, then for zero wavenumber k_0, the matrix $\widetilde{\mathbf{A}}_{k_n}(m_+, s_{2+})$ has either one zero eigenvalue and one negative, or two negative eigenvalues, or two complex eigenvalues with a negative real part; and the constant solution (m_+, s_{2+}) of system* (2.38) *is stable against the purely temporal perturbations.*

Since $k_n \in [0, \infty)$, then $c(k_n^2)$ given in (2.44) can be considered as a real function of a real non-negative argument. It is a quadratic polynomial. The interval, where $c(k_n^2) < 0$, is defined by the roots of the polynomial. If this polynomial has no roots among non-negative real numbers, then for $\forall k_n \in [0, \infty)$, $c(k_n^2) > 0$, since γ_2 defined (2.45) is positive. Thus, it is necessary to find the conditions, for which the polynomial defined in (2.44) has at least one non-negative real root. The general formula for the roots of the polynomial is:

$$\kappa_{1,2}^2 = \frac{-\gamma_1 \pm \sqrt{\gamma_1^2 - 4\gamma_2\gamma_0}}{2\gamma_2}. \tag{2.52}$$

The discriminant of the polynomial is:

$$\mathscr{D}_\gamma = \gamma_1^2 - 4\gamma_0\gamma_2. \tag{2.53}$$

Since $\gamma_2 > 0$ and $\gamma_0 \geq 0$ under the conditions of Lemma 2.2, the polynomial $c(k_n^2)$ has either two real roots of the same sign as $-\gamma_1$, which are different if $\mathscr{D}_\gamma > 0$, and coincident if $\mathscr{D}_\gamma = 0$; or two complex roots with real part $-\frac{\gamma_1}{2\gamma_2}$, if $\mathscr{D}_\gamma < 0$.

Theorem 2.1. *Suppose, that for the chosen parameter values m_0 defined in* (2.18) *is positive, $\beta_m = \beta_{m2}$ and there exists a real positive s_{2+} defined in* (2.19)*. Then if $\mathscr{D}_\gamma$ defined in* (2.55) *is positive, and γ_1 defined in* (2.54) *is negative, then $\exists \kappa_1, \kappa_2 \in \mathbb{R}$ defined by expression* (2.52)*, such that $0 \leq \kappa_1 < \kappa_2$, and the constant solution solution $\tilde{z}_+ = (m_+, s_{2+})$ of system* (2.38) *is unstable with respect to the perturbations with the wavenumbers $k_n \in (\kappa_1, \kappa_2)$. Otherwise, the constant solution $\tilde{z}_+$ is stable.*

Proof. Let $\lambda_1(k_n^2)$ and $\lambda_2(k_n^2)$ be the eigenvalues of the matrix $\widetilde{\mathbf{A}}_{k_n}(m_+, s_{2+})$ defined in (2.42) and $c(k_n^2)$ be defined in (2.44). Then:

1. If $\mathscr{D}_\gamma > 0$, and
   (a) if $\gamma_1 < 0$, then $\exists \kappa_1, \kappa_2 \in \mathbb{R}$ defined from expression (2.52), such that $0 \leq \kappa_1 < \kappa_2$ and:
      - for $k_n \in (\kappa_1, \kappa_2)$: $c(k_n^2) < 0$, hence $\lambda_1(k_n^2) < 0$ and $\lambda_2(k_n^2) > 0$;
      - for $k_n \in \{\kappa_1; \kappa_2\}$: $c(k_n^2) = 0$, and $\lambda_1(k_n^2) < 0$ and $\lambda_2(k_n^2) = 0$;
      - for $k_n \in [0, \infty)/[\kappa_1, \kappa_2]$: $c(k_n^2) > 0$, and $\lambda_1(k_n^2)$, $\lambda_2(k_n^2)$ are either real and negative, or complex with a negative real part;

   (b) if $\gamma_1 > 0$, then:
      i. if $\gamma_0 > 0$, then for $\forall k_n \in [0, \infty)$: $c(k_n^2) > 0$ and $\lambda_1(k_n^2)$, $\lambda_2(k_n^2)$ are either real and negative, or complex with a negative real part;
      ii. if $\gamma_0 = 0$, then

- for $\forall k_n \in (0,\infty)$: $c(k_n^2) > 0$ and $\lambda_1(k_n^2)$, $\lambda_2(k_n^2)$ are either real and negative, or complex with a negative real part;
- $c(0) = 0$ and $\lambda_1(0) < 0$ and $\lambda_2(0) = 0$.

2. If $\mathscr{D}_\gamma = 0$, and

   (a) if $\gamma_1 \leq 0$, then $\exists \kappa_1 = \kappa_2 = \sqrt{-\frac{\gamma_1}{2\gamma_2}} \geq 0$, such that

   - $c(\kappa_1^2) = 0$, and $\lambda_1(\kappa_1^2) < 0$ and $\lambda_2(\kappa_1^2) = 0$;
   - for $k_n \in [0,\infty)/\{\kappa_1^2\}$: $c(k_n^2) > 0$ and $\lambda_1(k_n^2)$, $\lambda_2(k_n^2)$ are either real and negative, or complex with a negative real part;

   (b) if $\gamma_1 > 0$, then for $\forall k_n \in [0,\infty)$: $c(k_n^2) > 0$ and $\lambda_1(k_n^2)$, $\lambda_2(k_n^2)$ are either real and negative, or complex with a negative real part.

3. If $\mathscr{D}_\gamma < 0$, then for $\forall k_n \in [0,\infty)$: $c(k_n^2) > 0$ and $\lambda_1(k_n^2)$, $\lambda_2(k_n^2)$ are either real and negative, or complex with a negative real part.

Therefore, if $\mathscr{D}_\gamma > 0$, and $\gamma_1 < 0$, then $\lambda_2(k_n^2) > 0$, if $k_n \in (\kappa_1, \kappa_2)$, and the magnitude of the perturbation modes having wavenumbers $k_n \in (\kappa_1, \kappa_2)$ grows monotonically after a certain period of time. Hence, the constant solution $\tilde{z}_+ = (m_+, s_{2+})$ is unstable with respect to these perturbation modes.

Otherwise, $\forall k_n \in [0,\infty)$ the eigenvalues of the matrix $\widetilde{\mathbf{A}}_{k_n}$ are either real non-positive numbers (the matrix $\widetilde{\mathbf{A}}_{k_n}$ can not have more than one zero eigenvalue) or complex numbers with a negative real part. Hence, initially small perturbations remain small during any period of time, or even disappear when $t \to \infty$, and the constant solution $\tilde{z}_+$ is stable in this case. □

The parameters γ_1 and $\mathscr{D}_\gamma$, can be written in terms of the model parameters as

$$\gamma_1 = (D_m A_{s2} + D_{s2}\alpha_m - \chi m_+ B_{m2})\frac{s_{2+}}{\beta_{m2} + s_{2+}} + D_{s2}\alpha_{m0} m_0, \tag{2.54}$$

$$\begin{aligned}\mathscr{D}_\gamma =& \Big((D_m A_{s2} + D_{s2}\alpha_m - \chi m_+ B_{m2})\frac{s_{2+}}{\beta_{m2} + s_{2+}} + D_{s2}\alpha_{m0} m_0\Big)^2 \\ & - 4 D_m D_{s2} A_{s2}\frac{s_{2+}}{\beta_{m2} + s_{2+}}\left(\alpha_{m0} m_0 + \alpha_m \frac{s_{2+}}{\beta_{m2} + s_{2+}}(2 - m_+)\right. \\ & \left. + \alpha_m (m_+ - 1)\right).\end{aligned} \tag{2.55}$$

2.3.4 Correspondence between the systems of two and three equations

Next, the relation between the eigenvalues of the matrices $\widetilde{\mathbf{A}}_{k_n}(m_+, s_{2+})$ and $\mathbf{A}_{k_n}(m_+, s_{2+}, b_+)$ is determined, and the similarity between the stability properties of systems (2.14)–(2.16) and (2.38), with respect to perturbations about the equilibria (m_+, s_{2+}, b_+) and (m_+, s_{2+}), respectively, is demonstrated. Let us define a matrix $\mathbf{M}_{k_n}$:

$$\mathbf{M}_{k_n} = \begin{bmatrix} \mathbf{A}_{k_n(1,1)} - \lambda & \mathbf{A}_{k_n(1,2)} \\ \mathbf{A}_{k_n(2,1)} & \mathbf{A}_{k_n(2,2)} - \lambda \end{bmatrix}.$$

From the definition of $\mathbf{A}_{k_n}$ it follows, that $\mathbf{A}_{k_n(2,3)} = \mathbf{A}_{k_n(2,1)}$. Then

$$\mathbf{A}_{k_n} - \lambda \mathbf{I}_3 = \begin{bmatrix} \mathbf{A}_{k_n(1,1)} - \lambda & \mathbf{A}_{k_n(1,2)} & 0 \\ \mathbf{A}_{k_n(2,1)} & \mathbf{A}_{k_n(2,2)} - \lambda & \mathbf{A}_{k_n(2,1)} \\ \alpha_{p0} & 0 & -A_b - \lambda \end{bmatrix}$$

$$= \begin{bmatrix} \begin{bmatrix} \\ \mathbf{M}_{k_n} \\ \\ \end{bmatrix} & \begin{matrix} 0 \\ \\ \mathbf{A}_{k_n(2,1)} \end{matrix} \\ \begin{matrix} \\ \alpha_{p0} \end{matrix} \quad \begin{matrix} \\ 0 \end{matrix} & \begin{matrix} \\ -A_b - \lambda \end{matrix} \end{bmatrix}.$$

The determinant of this matrix is the characteristic polynomial of $\mathbf{A}_{k_n}$:

$$\det(\mathbf{A}_{k_n} - \lambda \mathbf{I}_3) = \big(-A_b - \lambda\big) \det(\mathbf{M}_{k_n}) + \alpha_{p0} \mathbf{A}_{k_n(1,2)} \mathbf{A}_{k_n(2,1)}. \tag{2.56}$$

From the definition of the matrices $\widetilde{\mathbf{A}}_{k_n}$ and $\mathbf{A}_{k_n}$, it follows that

$$\widetilde{\mathbf{A}}_{k_n(1,1)} = \mathbf{A}_{k_n(1,1)}, \quad \widetilde{\mathbf{A}}_{k_n(1,2)} = \mathbf{A}_{k_n(1,2)},$$
$$\widetilde{\mathbf{A}}_{k_n(2,1)} = \left(1 + \frac{\alpha_{p0}}{A_b}\right) \mathbf{A}_{k_n(2,1)}, \quad \widetilde{\mathbf{A}}_{k_n(2,2)} = \mathbf{A}_{k_n(2,2)}.$$

Therefore, the determinant of the matrix $\widetilde{\mathbf{A}}_{k_n} - \lambda \mathbf{I}_2$ and the characteristic polynomial of the matrix $\widetilde{\mathbf{A}}_{k_n}$ is

$$det\left(\widetilde{\mathbf{A}}_{k_n} - \lambda \mathbf{I}_2\right) = det\left(\begin{bmatrix} \mathbf{A}_{k_n(1,1)} - \lambda & \mathbf{A}_{k_n(1,2)} \\ \mathbf{A}_{k_n(2,1)} + \frac{\alpha_{p0}}{A_b} \mathbf{A}_{k_n(2,1)} & \mathbf{A}_{k_n(2,2)} - \lambda \end{bmatrix}\right)$$

$$= det(\mathbf{M}_{k_n}) - \frac{\alpha_{p0}}{A_b} \mathbf{A}_{k_n(1,2)} \mathbf{A}_{k_n(2,1)}. \tag{2.57}$$

From (2.56) and (2.57) it is derived that

$$det(\mathbf{A}_{k_n} - \lambda \mathbf{I}_3) = \big(-A_b - \lambda\big) det\left(\widetilde{\mathbf{A}}_{k_n} - \lambda \mathbf{I}_2\right) - \lambda \frac{\alpha_{p0}}{A_b} \mathbf{A}_{k_n(1,2)} \mathbf{A}_{k_n(2,1)}. \tag{2.58}$$

Then, the characteristic polynomials of the matrices $\mathbf{A}_{k_n}$ and $\widetilde{\mathbf{A}}_{k_n}$, which are evaluated at the constant solutions (m_+, s_{2+}, b_+) and (m_+, s_{2+}), respectively, are denoted by a cubic polynomial $P_3(\lambda)$ and a quadratic polynomial $P_2(\lambda)$ with respect to λ:

$$P_3(\lambda) = det(\mathbf{A}_{k_n}(m_+, s_{2+}, b_+) - \lambda \mathbf{I}_3);\ P_2(\lambda) = det(\widetilde{\mathbf{A}}_{k_n}(m_+, s_{2+}, b_+) - \lambda \mathbf{I}_2).$$

Equation (2.58) can be written as:

$$P_3(\lambda) = \big(- A_b - \lambda \big) P_2(\lambda) - C(k_n^2)\lambda, \tag{2.59}$$

where

$$\begin{aligned} C(k_n^2) =& \frac{\alpha_{p0}}{A_b} \mathbf{A}_{k_n(1,2)}(m_+, s_{2+}, b_+) \mathbf{A}_{k_n(2,1)}(m_+, s_{2+}, b_+) \\ =& \frac{\alpha_{p0}}{A_b} \frac{\alpha_{m2} s_{2+}}{\beta_{m2} + s_{2+}} \left(\frac{\alpha_m \beta_m}{(\beta_m + s_{2+})^2} m_+ (1 - m_+) + k_n^2 B_{m2} m_+ \right). \end{aligned} \tag{2.60}$$

If $s_{2+} > 0$, it follows from (2.20) that $m_+ > 0$, and equation (2.40) yields: $m_+ = 1 - \frac{\alpha_{p0} + A_m}{\alpha_{m0} + \frac{\alpha_m s_{2+}}{\beta_m + s_{2+}}} < 1$. Thus,

$$s_{2+} > 0 \ \Rightarrow\ 0 < m_+ < 1 \ \Rightarrow\ C(k_n^2) > 0,\ \forall k_n^2 \in [0, \infty). \tag{2.61}$$

Lemma 2.4. *Suppose, that for the chosen parameter values m_0 defined in* (2.18) *is positive, and that there exists a real positive s_{2+} defined in* (2.19). *If the matrix $\widetilde{\mathbf{A}}_{k_n}(m_+, s_{2+})$ has one real negative eigenvalue $\tilde{\lambda}_1 < 0$ and one real positive eigenvalue $\tilde{\lambda}_2 > 0$, then $\mathbf{A}_{k_n}(m_+, s_{2+}, b_+)$ has one real positive eigenvalue and either two real negative eigenvalues, or two complex conjugated eigenvalues with a negative real part.*

Proof. From the assumption of the lemma and from (2.61) it follows, that $C(k_n^2) > 0$. Let $\widetilde{\mathbf{A}}_{k_n}(m_+, s_{2+})$ have one real negative eigenvalue $\tilde{\lambda}_1 < 0$ and one real positive eigenvalue $\tilde{\lambda}_2 > 0$. The characteristic polynomial can be written as $P_2(\lambda) = (\lambda - \tilde{\lambda}_1)(\lambda - \tilde{\lambda}_2)$. Then from equation (2.59)

$$\begin{aligned} P_3(\lambda) = \big(- A_b - \lambda \big)(\lambda - \tilde{\lambda}_1)(\lambda - \tilde{\lambda}_2) - C(k_n^2)\lambda = -\lambda^3 + (\tilde{\lambda}_1 + \tilde{\lambda}_2 - A_b)\lambda^2 \\ + (-\tilde{\lambda}_1 \tilde{\lambda}_2 + A_b(\tilde{\lambda}_1 + \tilde{\lambda}_2) - C(k_n^2))\lambda - A_b \tilde{\lambda}_1 \tilde{\lambda}_2. \end{aligned} \tag{2.62}$$

From (2.62) it follows:

$$P_3(0) = -\tilde{\lambda}_1 \tilde{\lambda}_2 A_b > 0 \quad \text{and} \quad P_3(\tilde{\lambda}_2) = -\tilde{\lambda}_2 C(k_n^2) < 0. \tag{2.63}$$

Since $P_3(\lambda)$ is continuous, it follows from relation (2.63), that the polynomial $P_3(\lambda)$ has at least one real positive root λ_1 on the interval $(0, \tilde{\lambda}_2)$.

The other two eigenvalues λ_2 and λ_3 of $\mathbf{A}_{k_n}(m_+, s_{2+}, b_+)$ can be real (negative or positive) or complex conjugated numbers (as the coefficients of the polynomial are real). Then,

$$P_3(\lambda) = -\lambda^3 + (\lambda_1 + \lambda_2 + \lambda_3)\lambda^2 - (\lambda_1\lambda_2 + \lambda_1\lambda_3 + \lambda_2\lambda_3)\lambda + \lambda_1\lambda_2\lambda_3, \tag{2.64}$$

since this polynomial has λ_1, λ_2, λ_3 as its roots. As the coefficients at the second degree of λ in the two expressions for $P_3(\lambda)$ from (2.62) and (2.64) should be equal, it follows that $\lambda_2 + \lambda_3 = \tilde{\lambda}_1 + \tilde{\lambda}_2 - A_b - \lambda_1$. From (2.42) it is derived:

$$\lambda_2 + \lambda_3 = -b(k_n^2) - A_b - \lambda_1 < 0. \tag{2.65}$$

The above inequality holds, since it was mentioned in (2.43), that $b(k_n^2) > 0$, if $m_0 > 0$ and $s_+ > 0$. Thus, if two other eigenvalues are real, then from (2.65) it follows, that at least one of them is negative. Let us suppose $\lambda_2 < 0$. Then

$$\lim_{\lambda \to -\infty} P_3(\lambda) = \infty,$$

and $P_3(0) = -\tilde{\lambda}_1\tilde{\lambda}_2 A_b > 0$. That means that on the interval $(-\infty, 0)$ the polynomial $P_3(\lambda)$ does not change its sign, or changes it twice. Since $P_3(\lambda)$ is continuous, it follows from $\lambda_2 < 0$ that λ_3 also is negative. In the case, when λ_2 and λ_3 are complex conjugated, their real part is $\lambda_{re} = (\lambda_2 + \lambda_3)/2 < 0$. □

Lemma 2.5. *Suppose, that for the chosen parameter values there exists a real positive s_{2+} defined in* (2.19)*. If $\widetilde{\mathbf{A}}_{k_n}(m_+, s_{2+})$ has one zero eigenvalue and one real negative eigenvalue, then $\mathbf{A}_{k_n}(m_+, s_{2+}, b_+)$ has one zero eigenvalue and either two real negative eigenvalues, or two complex conjugated eigenvalues with a negative real part.*

Proof. From the assumption of the lemma and from (2.61) it follows, that $C(k_n^2) > 0$. Let $\widetilde{\mathbf{A}}_{k_n}(m_+, s_{2+})$ have one zero eigenvalue and one real negative eigenvalue, $\tilde{\lambda}_1 < \tilde{\lambda}_2 = 0$. Then the characteristic polynomial $P_2(\lambda)$ has the form $P_2(\lambda) = \lambda(\lambda - \tilde{\lambda}_1)$. Then equation (2.59) implies

$$\begin{aligned} P_3(\lambda) &= \big(-A_b - \lambda\big)\lambda(\lambda - \tilde{\lambda}_1) - C(k_n^2)\lambda \\ &= -\lambda(\lambda^2 + (A_b - \tilde{\lambda}_1)\lambda + (C(k_n^2) - \tilde{\lambda}_1 A_b)). \end{aligned} \tag{2.66}$$

And eigenvalues of $\mathbf{A}_{k_n}(m_+, s_{2+}, b_+)$ are following:

$$\lambda_1 = 0, \quad \lambda_{2,3} = \frac{-A_b + \tilde{\lambda}_1 \pm \sqrt{(A_b - \tilde{\lambda}_1)^2 - 4(C(k_n^2) - \tilde{\lambda}_1 A_b)}}{2}. \tag{2.67}$$

Since $C(k_n^2) - \tilde{\lambda}_1 A_b > 0$ and $A_b - \tilde{\lambda}_1 > 0$, then from (2.67) it follows, that eigenvalues $\lambda_{2,3}$ are either real and negative (possible coincident), or complex with a negative real part. □

Lemma 2.6. *Suppose, that for the chosen parameter values there exists a real positive s_{2+} defined in* (2.19)*. If $\widetilde{\mathbf{A}}_{k_n}(m_+, s_{2+})$ has two real negative eigenvalues, then $\mathbf{A}_{k_n}(m_+, s_{2+}, b_+)$ has either three real negative eigenvalues, or one real negative eigenvalue, and two complex eigenvalues with a negative real part.*

Proof. From the assumption of the lemma and from (2.61) it follows, that $C(k_n^2) > 0$. Let $\widetilde{\mathbf{A}}_{k_n}(m_+, s_{2+})$ have two real negative eigenvalues $\tilde{\lambda}_1 \leq \tilde{\lambda}_2 < 0$. Then the characteristic polynomial $P_2(\lambda)$ has the form $P_2(\lambda) = (\lambda - \tilde{\lambda}_1)(\lambda - \tilde{\lambda}_2)$. Then from equation (2.59)

$$P_3(\lambda) = \big(- A_b - \lambda\big)(\lambda - \tilde{\lambda}_1)(\lambda - \tilde{\lambda}_2) - C(k_n^2)\lambda = -\lambda^3 + (\tilde{\lambda}_1 + \tilde{\lambda}_2 - A_b)\lambda^2 + (-\tilde{\lambda}_1\tilde{\lambda}_2 + A_b(\tilde{\lambda}_1 + \tilde{\lambda}_2) - C(k_n^2))\lambda - A_b\tilde{\lambda}_1\tilde{\lambda}_2. \quad (2.68)$$

From (2.68) it follows:

$$P_3(-A_b) = C(k_n^2)A_b > 0 \quad \text{and} \quad P_3(0) = -\tilde{\lambda}_1\tilde{\lambda}_2 A_b < 0. \quad (2.69)$$

Since $P_3(\lambda)$ is continuous, it follows from (2.69), that the polynomial $P_3(\lambda)$ has at least one root on the interval $(-A_b, 0)$. Thus it can be supposed, that $-A_b < \lambda_1 < 0$. From (2.68) it follows, that for $\lambda \geq 0$ the polynomial $P_3(\lambda)$ only takes values less than zero. That means, that $P_3(\lambda)$ has no non-negative real roots $P_3(\lambda)$. Thus, if two other eigenvalues of $\mathbf{A}_{k_n}(m_+, s_{2+}, b_+)$ are real, they are also negative. Though it is possible, that the polynomial $P_3(\lambda)$ has two complex conjugated roots. Let us denote them as $\lambda_{2,3} = \lambda_{re} \pm i\lambda_{im}$. Then:

$$\begin{aligned} P_3(\lambda) &= -(\lambda - \lambda_1)(\lambda^2 - 2\lambda_{re}\lambda + \lambda_{re}^2 + \lambda_{im}^2) \\ &= -\lambda^3 + (\lambda_1 + 2\lambda_{re})\lambda^2 - (2\lambda_1\lambda_{re} + \lambda_{re}^2 + \lambda_{im}^2)\lambda + \lambda_1(\lambda_{re}^2 + \lambda_{im}^2). \end{aligned} \quad (2.70)$$

Since the coefficients at the second degree of λ in two expressions for $P_3(\lambda)$ (2.68) and (2.70) should be equal, it is derived that $2\lambda_{re} = \tilde{\lambda}_1 + \tilde{\lambda}_2 - A_b - \lambda_1$. As $\tilde{\lambda}_1 \leq \tilde{\lambda}_2 < 0$ and $-A_b - \lambda_1 < 0$, then $\lambda_{re} < 0$. That is, if two eigenvalues of $\mathbf{A}_{k_n}(m_+, s_{2+}, b_+)$ are complex, then their real part is less than zero. □

Lemma 2.7. *Suppose, that for the chosen parameter values there exists a real positive s_{2+} defined in* (2.19)*. If $\widetilde{\mathbf{A}}_{k_n}(m_+, s_{2+})$ has two complex conjugated eigenvalues with a negative real part, then $\mathbf{A}_{k_n}(m_+, s_{2+}, b_+)$ has either three real negative eigenvalues, or one real negative eigenvalue, and two complex eigenvalues with a negative real part.*

Proof. From the assumption of the lemma and from (2.61) it follows, that $C(k_n^2) > 0$. Let $\widetilde{\mathbf{A}}_{k_n}(m_+, s_{2+})$ have the complex conjugated eigenvalues with a negative real part: $\tilde{\lambda}_{1,2} = \tilde{\lambda}_{re} \pm i\tilde{\lambda}_{im}$, $\tilde{\lambda}_{re} < 0$. Then the characteristic

polynomial $P_2(\lambda)$ takes positive values for $\forall\lambda \in \mathbb{R}$ and has the form $P_2(\lambda) = (\lambda^2 - 2\tilde{\lambda}_{re}\lambda + \tilde{\lambda}_{re}^2 + \tilde{\lambda}_{im}^2)$. Then from equation (2.59), if follows

$$P_3(\lambda) = \big(-A_b-\lambda\big)(\lambda^2-2\tilde{\lambda}_{re}\lambda+\tilde{\lambda}_{re}^2+\tilde{\lambda}_{im}^2)-C(k_n^2)\lambda = -\lambda^3+(2\tilde{\lambda}_{re}-A_b)\lambda^2 + (-\tilde{\lambda}_{re}^2 - \tilde{\lambda}_{im}^2 + 2A_b\tilde{\lambda}_{re} - C(k_n^2))\lambda - A_b(\tilde{\lambda}_{re}^2 + \tilde{\lambda}_{im}^2). \quad (2.71)$$

Equation (2.71) yields

$$P_3(-A_b) = C(k_n^2)A_b > 0 \quad \text{and} \quad P_3(0) = -A_b(\tilde{\lambda}_{re}^2 + \tilde{\lambda}_{im}^2) < 0. \quad (2.72)$$

Since $P_3(\lambda)$ is continuous, it follows from (2.72), that the polynomial $P_3(\lambda)$ has at least one root on the interval $(-A_b, 0)$. Thus it can be supposed, that $-A_b < \lambda_1 < 0$.

From (2.71) it follows, that for $\lambda \geq 0$ the polynomial $P_3(\lambda)$ takes values less than zero. That means, that $P_3(\lambda)$ has no non-negative real roots $P_3(\lambda)$. Therefore, if the two other roots of $P_3(\lambda)$ are real, they are also negative.

Next, the possibility, that the polynomial $P_3(\lambda)$ has two complex conjugated roots, is considered. The roots are denoted as $\lambda_{2,3} = \lambda_{re} \pm i\lambda_{im}$. Then:

$$\begin{aligned} P_3(\lambda) &= -(\lambda - \lambda_1)(\lambda^2 - 2\lambda_{re}\lambda + \lambda_{re}^2 + \lambda_{im}^2) \\ &= -\lambda^3 + (\lambda_1 + 2\lambda_{re})\lambda^2 - (2\lambda_1\lambda_{re} + \lambda_{re}^2 + \lambda_{im}^2)\lambda + \lambda_1(\lambda_{re}^2 + \lambda_{im}^2). \end{aligned} \quad (2.73)$$

Since the coefficients of λ^2 in two expressions for $P_3(\lambda)$ (2.71) and (2.73) should be equal, then $2\lambda_{re} = 2\tilde{\lambda}_{re} - A_b - \lambda_1$. As $\tilde{\lambda}_{re} < 0$ and $-A_b - \lambda_1 < 0$, it follows that $\lambda_{re} < 0$. That is, if two eigenvalues of $\mathbf{A}_{k_n}(m_+, s_{2+}, b_+)$ are complex, then their real part is less than zero. □

2.3.5 Stability of the system of three equations

Lemma 2.8. *Suppose, that for the chosen parameter values, m_0 defined in* (2.18) *is positive, $\beta_m = \beta_{m2}$ and there exists a real positive s_{2+} defined in* (2.19). *Then the constant solution $z_+ = (m_+, s_{2+}, b_+)$ of system* (2.14)–(2.16) *is stable against purely temporal perturbations.*

Proof. From Lemma 2.3, 2.5, 2.6 and 2.7, it follows, that for zero wavenumber k_0, the matrix $\mathbf{A}_{k_n}$, evaluated at the constant solution z_+, has either two negative eigenvalues and one zero eigenvalue, or three real negative eigenvalues, or one real non-positive eigenvalue, and two complex eigenvalues with a negative real part. □

Theorem 2.2. *Suppose, that for the chosen parameter values m_0 defined in* (2.18) *is positive, $\beta_m = \beta_{m2}$ and there exists a real positive s_{2+} defined in* (2.19). *Then if $\mathscr{D}_\gamma$ defined in* (2.55) *is positive, and γ_1 defined in* (2.54) *is negative, then $\exists\kappa_1, \kappa_2 \in \mathbb{R}$ defined by expression* (2.52), *such that $0 \leq \kappa_1 <$*

κ_2, and the constant solution z_+ of system (2.14)–(2.16) *is unstable with respect to the perturbations having wavenumbers $k_n \in (\kappa_1, \kappa_2)$. Otherwise, the constant solution z_+ is stable.*

Proof. The theorem is proved, by analogy with the proof of Theorem 2.1. In that proof all possible cases for the signs of the parameters $\mathscr{D}_\gamma$ and γ_1 are considered, and the relations between the eigenvalues of the matrix $\widetilde{\mathbf{A}}_{k_n}$ and the wavenumber k_n are determined for each case. From these relations, and from the relations between the eigenvalues of the matrices $\widetilde{\mathbf{A}}_{k_n}$ and $\mathbf{A}_{k_n}$, stated in Lemma 2.4–2.7, it is possible to determine the correspondence between the eigenvalues of the matrix $\mathbf{A}_{k_n}$ and the wavenumber k_n for the sets of signs of the parameters $\mathscr{D}_\gamma$ and γ_1.

Therefore, it is obtained, that if $\mathscr{D}_\gamma > 0$, and $\gamma_1 < 0$, then $\exists \kappa_1, \kappa_2 \in \mathbb{R}$ defined by expression (2.52), such that $0 \leq \kappa_1 < \kappa_2$, and the magnitude of the perturbation modes having wavenumbers $k_n \in (\kappa_1, \kappa_2)$ grow monotonically after a certain period of time, since one of the eigenvalues of $\mathbf{A}_{k_n}$ is positive. Hence, the constant solution $z_+ = (m_+, s_{2+}, b_+)$ is unstable with respect to these perturbation modes.

Otherwise, $\forall k_n \in [0, \infty)$ the eigenvalues of the matrix $\mathbf{A}_{k_n}$ are either real non-positive numbers (the matrix $\mathbf{A}_{k_n}$ can not have more than one zero eigenvalue) or complex numbers with a negative real part. Hence, initially small perturbations remain small during any period of time, or even disappear when $t \to \infty$, and the constant solution z_+ is stable in this case. □

The conditions on the parameters, stated in Theorem 2.2, can be formulated in a compact form:

$$\begin{cases} \gamma_1 < 0, \\ \mathscr{D}_\gamma = \gamma_1^2 - 4\gamma_0\gamma_2 > 0 \end{cases} \Leftrightarrow \gamma_1 < -2\sqrt{\gamma_2\gamma_0}. \tag{2.74}$$

From the proof of the theorem, it follows, that condition (2.74) is a necessary condition for the instability of the solution z_+, since it is equivalent to the existence of the real positive numbers κ_1 and κ_2. The necessary and sufficient condition holds, if there exist wavenumbers $k_n \in (\kappa_1, \kappa_2)$. From (2.52) it follows, that the length of the interval (κ_1, κ_2) is equal to $\frac{\mathscr{D}_\gamma}{D_m D_{s2}}$. If $\mathscr{D}_\gamma$ is small enough, then it is possible, that no wavenumber k_n will lie inside the interval (κ_1, κ_2), and perturbations will not grow. In this case, the necessary condition for the instability holds, but the solution is stable.

The necessary instability condition (2.74), can be transformed into the sufficient stability condition by the substitution of the sign in inequality (2.74) by the opposite one:

$$\gamma_1 \geq -2\sqrt{\gamma_2\gamma_0}. \tag{2.75}$$

This condition is formulated in terms of model parameters and does not depend on the problem statement. This means, that a general instruction on the choice of the parameter values, which guaranties the stability of the constant solution z_+, can be formulated.

The necessary and sufficient stability condition is opposite to the the necessary and sufficient instability condition, which depends on the the wavenumbers k_n. The set of the wavenumbers k_n contains infinite number of elements, and is determined by the domain size, by the coordinate system and by the boundary conditions. Therefore, it is not possible to state the necessary and sufficient condition in terms of the model parameters for the general case. For different boundary conditions, coordinate systems or domain sizes, these conditions have to be reformulated.

2.3.6 Parameter choice and stability

In this subsection the choice of parameter values, providing stability of the constant solution $z_+ = (m_+, s_{2+}, b_+)$ of the system of three equations, is discussed.

For the parameter values in equations (2.11), (2.12) and (2.13), the constant solutions $z_t = (0, 0, 0)$, $z_0 = (m_0, 0, b_0)$ and $z_- = (m_-, s_{2-}, b_-)$ are unstable, and the solution will not converge to these constant solutions. From a biological point of view, this is a favorable situation. Since, the 'non-healing state' z_t contains zero concentrations of osteogenic cells and osteoblasts, the 'low density state' z_0 corresponds to much lower concentrations of osteogenic cells and osteoblasts, compared to those for z_+, and the constant solution z_- contains unphysical negative concentrations of cells.

For the chosen parameter value sets in equations (2.11), (2.12) and (2.11), (2.13), the sufficient condition (2.75) for the stability of z_+ does not hold. It is necessary to change the values of parameters, to guaranty the stability of the constant solution z_+ in general. It is proposed here, to vary values of parameters B_{m2} and D_m. These two particular parameters are chosen, since:

- their variation does not cause change of the values of the constant solutions z_t, z_0, z_- and z_+ (see equations (2.18),(2.19), (2.20));
- from (2.35) and (2.36) it follows, that parameters B_{m2} and D_m do not influence the stability of the constant solutions z_t and z_0 against purely temporal perturbations. The stability of the constant solution z_- against purely temporal perturbations is determined from the eigenvalues of the matrix $A_{k_0}(m_-, s_{2-}, b_-)$, see equation (2.32). As $k_0 = 0$, this matrix does not depend on parameters B_{m2} and D_m. For the considered parameter values in equations (2.11), (2.12) and (2.13), and for any B_{m2} and D_m, z_- is unstable against purely temporal perturbations. Therefore, variation of B_{m2} and D_m, can provide

the stability of the constant solution z_+, while the constant solutions z_t, z_0 and z_- remain unstable;

- calculations showed, that stability condition (2.75) is most sensitive with respect to the parameters B_{m2} and D_m. That is, the ratio of the initial parameter value and the ultimate value of the parameter, which satisfies condition (2.75), is much smaller for B_{m2} and D_m, compared to the rest of the model parameters.

The first quadrant of the plane (D_m, B_{m2}), which contains all possible non-negative values D_m and B_{m2}, can be divided into three regions, with respect to the stability of the solution z_+:

region R_1: sufficient stability condition (2.75) holds, solution z_+ is stable;

region R_2: condition (2.75) does not hold, no wavenumbers k_n lie in the interval (κ_1, κ_2), solution z_+ is stable;

region R_3: condition (2.75) does not hold, some of the wavenumbers k_n lie in the interval (κ_1, κ_2), solution z_+ is unstable.

Configuration of regions R_2 and R_3 depend on the specified boundary conditions, on the coordinate system and on the domain length. In Figure 2.3 these regions were plotted for the case of zero flux of m and s_2 on the boundaries, 1D Cartesian coordinates, and the domain with length $0.6mm$. This length is equal to the width of the domain, used in the numerical simulations by Moreo et al. [67]. The values of the model parameters, given in (2.11), (2.12) (Figure 2.3a), and in (2.11), (2.13) (Figure 2.3b), were chosen.

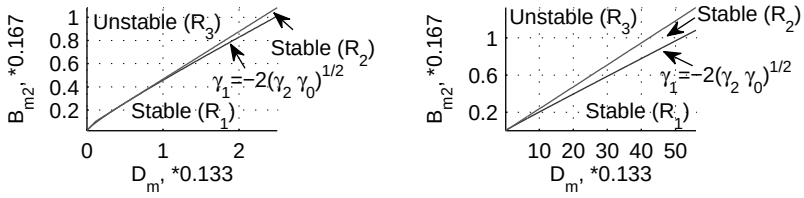

Figure 2.3: Plot of the regions in the first quadrant of the plane (D_m, B_{m2}), where the constant solution z_+ is stable (R_1, R_2) and unstable (R_3), for the case of a zero flux of m and s_2 on the boundaries, 1D Cartesian coordinates, and the domain of the length $0.6mm$. The rest of the model parameters are initialized: (a) as in (2.11), (2.12), and (b) as in (2.11), (2.13).

With use of (2.45), (2.46) and (2.47), sufficient stability condition (2.75) can be rewritten as follows:

$$B_{m2} \leq \frac{1}{s_{2+} + \beta_{m2}} \left(D_m + G_1 + \frac{2}{G_0} \sqrt{D_m D_{s2} \gamma_0} \right), \tag{2.76}$$

or in the form

$$\begin{cases} D_m \geq 0, \quad \text{if } B_{m2} \leq \dfrac{G_1}{s_{2+}+\beta_{m2}}, \\ D_m \geq B_{m2}(s_{2+}+\beta_{m2}) - G_1 + 2\dfrac{\gamma_0 D_{s2}}{G_0^2} \\ \quad -2\sqrt{\dfrac{\gamma_0 D_{s2}}{G_0^2}\left(B_{m2}(s_{2+}+\beta_{m2}) - G_1 + \dfrac{\gamma_0 D_{s2}}{G_0^2}\right)}, \text{if } B_{m2} > \dfrac{G_1}{s_{2+}+\beta_{m2}}, \end{cases} \tag{2.77}$$

where $G_0 = \frac{A_{s2}s_{2+}}{s_{2+}+\beta_{m2}}$, $G_1 = \frac{D_{s2}}{A_{s2}}\left(\alpha_m + \alpha_{m0}m_0\frac{s_{2+}+\beta_{m2}}{s_{2+}}\right)$, and γ_0 is defined in (2.47). Inequalities (2.76) and (2.77) determine the values of B_{m2} and D_m, which ensure the stability of the solution z_+.

The following remark can be helpful for the solution of practical problems. Suppose, that initial values of model parameters do not satisfy sufficient condition (2.75) for the stability of the solution z_+. Then, it is possible to guaranty the stability of z_+ in general case (i.e. for any set of wavenumbers, which are determined by problem statement), by decreasing the value of B_{m2}, or increasing D_m, until condition (2.76) or condition (2.77) is satisfied, respectively.

2.4 Numerical results

The predictions from the linear stability analysis are validated against a sequence of numerical simulations. The sufficient stability condition is considered in the form of equation (2.76) and the parameter B_{m2} is varied.

If the values of all parameters, except B_{m2}, are fixed, then the right part of inequality (2.76) can be denoted as the ultimate value B_{m2}^{lim}, such that for $B_{m2} \leq B_{m2}^{lim}$ small perturbations near (m_+, s_{2+}, b_+) are predicted not to grow with time. For $B_{m2} > B_{m2}^{lim}$ small perturbations of mode $\phi_n(x)$ will grow, if $\kappa_1 < k_n < \kappa_2$. If B_{m2} is close to ultimate value B_{m2}^{lim}, then the interval (κ_1, κ_2) is small, and it can happen, that no wavenumber k_n lies inside this interval. In this case perturbations near the constant solution will not grow, in spite of the fact, that sufficient stability condition (2.76) does not hold.

For the cases when the model parameters are initialized as in (2.11), (2.12) and (2.11), (2.13), the ultimate values are $B_{m2}^{lim} \approx 0.45716 \cdot 0.167$ mm^2/day and $B_{m2}^{lim} \approx 0.02481 \cdot 0.167\, mm^2/day$.

First, the parameter values (2.11), (2.12) are considered. If the problem domain is a 1D interval $x \in [1, 6]$ in Cartesian coordinates, and if a zero flux of osteogenic cells m and growth factor s_2 is supposed, then the wavenumbers are determined as $k_n = \pi n/5\, mm^{-1}$, $n = 0, 1, 2, \ldots$. Then for $B_{m2} = 0.4572 \cdot 0.167\, mm^2/day$, which is larger than the ultimate value, still no wavenumber lies between $\kappa_1 \approx 4.2805 mm^{-1}$ and $\kappa_2 \approx 4.3838 mm^{-1}$. Though, for $B_{m2} =$

$0.4573 \cdot 0.167\, mm^2/day$, the wavenumber $k_7 \approx 4.3982 mm^{-1} \in (\kappa_1, \kappa_2) = (\approx 4.2322 mm^{-1}, \approx 4.4339 mm^{-1})$. If the parameter values (2.11), (2.13) are chosen, then for $B_{m2} = 0.0249 \cdot 0.167\, mm^2/day$, the wavenumber

$$k_6 \approx 3.7699 mm^{-1} \in (\kappa_1, \kappa_2) = (\approx 3.6417 mm^{-1}, \approx 4.324 mm^{-1}).$$

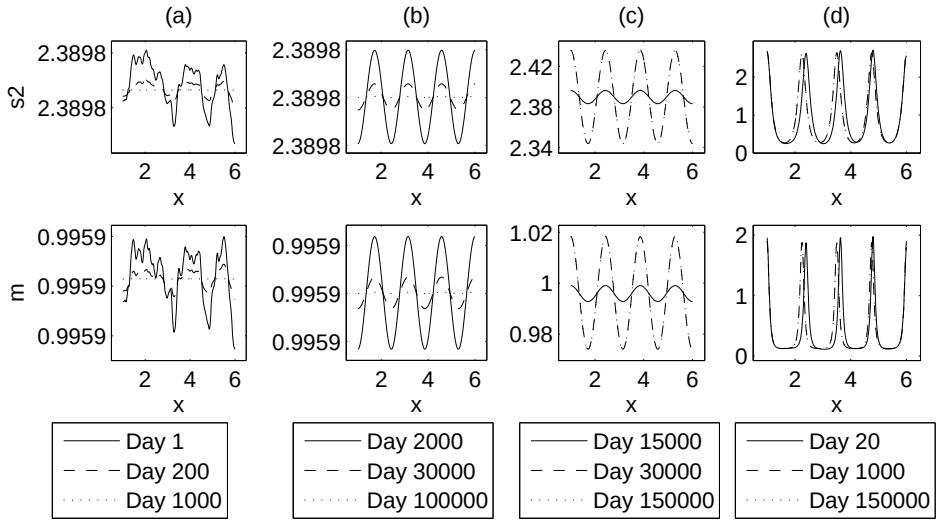

Figure 2.4: Solution of equations (2.14)–(2.16) in Cartesian coordinates at different time moments. Small random initial perturbations near the constant solution (m_+, s_{2+}, b_+) are considered. Zero fluxes of m, $s2$ on the boundaries are taken as the boundary conditions. Parameter B_{m2} takes different values: $B_{m2} = k \cdot 0.167\ mm^2/day$, (a) $k = 0.3$, (b) $k = 0.4572$, (c) $k = 0.4573$, (d) $k = 1$. The rest of parameters are initialized as in (2.11), (2.12).

In Figure 2.4 the results of the numerical simulations are shown. The solutions were obtained with use of the finite element method. Linear 1D elements of size $0.02mm$ were used for the discretization in space. The implicit backward Euler method, to prevent instabilities due to numerical time integration, and adaptive time stepping were used for time integration. Zero flux of m, $s2$ on the boundaries was specified as the boundary conditions. To introduce the perturbations in the initial solution during simulations, the corresponding constant solution value plus a small random number were assigned to every degree of freedom at time $t = 0$. From Figure 2.4 it follows, that for the values of B_{m2} less than the ultimate value, the numerical solution tends to the constant solution (m_+, s_{2+}, b_+) with time (Figure 2.4a). And if the parameter B_{m2} is larger than B_{m2}^{lim} and such, that $\exists k_n \in (\kappa_1, \kappa_2)$, then there is no convergence to the constant solution, and a wave-like profile occurs in the solution (Figure 2.4c, d). However, if B_{m2} is larger than B_{m2}^{lim},

but such that no wave number lies inside (κ_1, κ_2) yet, then the numerical solution again converges to the constant solution (m_+, s_{2+}, b_+) (Figure 2.4b). Thus, the predictions of the linear stability analysis are fully confirmed by the numerical simulations.

The linear stability analysis allows to assess the stability of the considered constant solution. From its stability it can be concluded, whether or not small perturbations grow with time. The important conclusion can be made, for cases in which perturbations are large: if the constant solution is not stable, then the solution of the problem will never converge to that constant solution. Hence, the introduced linear analysis provides important results also for the case of large perturbations, since it allows to determine the situation, in which the solution, which is constant in time and in space, can never be reached. However, if the constant solution is stable, it is still unknown, how large initial perturbations behave, whether they disappear or prevail, or even grow.

In reality, the deviations from the constant solution are large. The initial and boundary conditions, proposed by Moreo et al. [67] for the full system (2.1)–(2.8), were given in Section 2.2. When adapted to the simplified system of three equations, initial and boundary conditions (2.9), (2.10) are rewritten as:

$$m(\vec{x},0) = 0.001, \quad b(\vec{x},0) = 0.001, \quad s_2(\vec{x},0) = 0.01, \qquad \vec{x} \in \Omega. \tag{2.78}$$

$$\begin{cases} D_{s1}\nabla s_1 \cdot \vec{n} = 0, \quad D_{s2}\nabla s_2 \cdot \vec{n} = 0, & \vec{x} \in \partial\Omega,\ t \in (0,\infty) \\ \qquad\qquad\qquad\qquad m = 0.2, & \vec{x} \in \partial\Omega_b,\ t \in (0,14]\ [days] \\ (D_m\nabla m - mB_{m2}\nabla s_2)\cdot\vec{n} = 0, & \left[\begin{array}{l} \vec{x} \in \partial\Omega\backslash\partial\Omega_b,\ t \in (0,14]\ [days], \\ \vec{x} \in \partial\Omega,\ t \in (14,\infty)\ [days]. \end{array}\right. \end{cases} \tag{2.79}$$

Initial conditions (2.78) are far from small perturbations near the constant solution (m_+, s_{2+}, b_+).

The simplified system (2.14)–(2.16), and the full system (2.1)–(2.8) were solved numerically for initial and boundary conditions (2.9), (2.10) and (2.78), (2.79) respectively, and for several sets of parameter values. Some of the solutions for the full system (2.1)–(2.8) are plotted in Figure 2.5. The numerical simulations show, that if the parameter values are such, that the constant solution (m_+, s_{2+}, b_+) is stable, then the numerical solutions of both systems for the unknowns $m(x,t)$, $s_2(x,t)$, $b(x,t)$ converge to this constant solution after a certain period of time (Figure 2.5a). Though, if the constant solution (m_+, s_{2+}, b_+) is not stable, then a wave-like profile develops in the solution for osteogenic cells and growth factor 2 and for parameter values (2.11), (2.13) also in the solution for osteoblasts. For some values of the parameter B_{m2} the wave-like profile is steady (Figure 2.5b).

Though, if B_{m2} is much larger than the ultimate value, then the waves in the numerical solution are not steady, but moving (Figure 2.5c, d). This is in agreement with the stability analysis presented in Section 2.4.

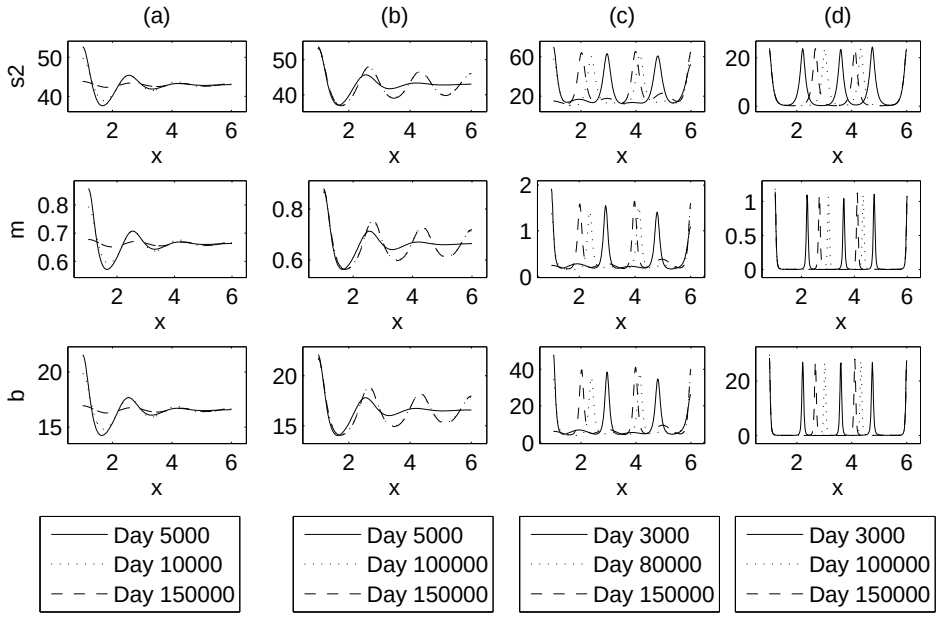

Figure 2.5: Solution of equations (2.1)–(2.8) in axisymmetric coordinates at different time moments. Initial and boundary conditions are chosen in the form (2.9), (2.10), according to Moreo et al. [67]. Parameter B_{m2} takes different values: $B_{m2} = k \cdot 0.167\ mm^2/day$, (a) $k = 0.0248$, (b) $k = 0.0249$, (c) $k = 0.04$, (d) $k = 0.2$. The rest of parameters are initialized as in (2.11), (2.13).

2.5 Conclusions

A simplified system of three equations is defined, which is characterized by the appearance of a wave-like profile in the solution under the same conditions, as for the solution of the full system of eight equations. For the considered parameter values the simplified system has four constant solutions. The sufficient stability condition for one of the constant solutions, denoted as $z_+ = (m_+, s_{2+}, b_+)$, is derived in terms of model parameters, by means of the linear stability analysis. If all constant solutions are unstable, then by changing the values of the model parameters B_{m2} and D_m, it is possible to make the solution z_+ stable, while three other constant solutions z_t, z_0 and z_- remain unstable. The analytical predictions on the stability of the constant solution z_+ for various parameter sets are confirmed by numer-

ical simulations, when starting from small perturbations near the constant solution.

In real simulations for the peri-implant osseointegration, initial conditions correspond to the large deviations from the constant solution. However, linear stability analysis provides important results also in this case. It allows to avoid such values of model parameters, for which all constant solutions are unstable, and consequently, can not be reached. Linear stability analysis makes it possible to determine parameter values, for which the solution of the problem will never converge to the solution, which is constant in time and in space. This conclusion is confirmed by the numerical simulations, which evidence, that a wave-like profile appears in the solution, if all the constant solutions are unstable. The numerical simulations also show, that if the solution z_+ is stable and z_t, z_0, z_- are unstable, then numerical solutions for unknowns $m(x,t)$, $s_2(x,t)$, $b(x,t)$ of the full and the simplified system converge to the constant solution (m_+, s_{2+}, b_+) after a certain period of time, when starting with initial conditions proposed in Moreo et al. [67].

Therefore, the numerical simulations demonstrate, that if the constant solutions z_t, z_0, z_- are unstable, then the stability of the constant solution z_+ can determine the behavior of the solution of the whole system. That makes it possible to determine the values of model parameters, for which biologically irrelevant solutions with a wave-like profile can be obtained.

CHAPTER 3

Evolutionary cell differentiation

In this chapter an approach is developed, which allows to introduce the concept of cell plasticity into the models for tissue regeneration. Opposed to most of the recent models for tissue regeneration, cell differentiation is considered as a process, which evolves in time, and which is regulated by an arbitrary number of parameters. In the current approach, cell differentiation is modeled by means of a differentiation state variable. Cells are assumed to differentiate into an arbitrary number of cell types. The differentiation path is considered as reversible, unless differentiation has fully completed.

Cell differentiation is incorporated into the partial differential equations (PDE's), which model the tissue regeneration process, by means of an advection term in the differentiation state space. This allows to consider the differentiation path of cells, which is not possible, if a reaction-like term is used for differentiation.

The boundary conditions, which should be specified for the general PDE's, are derived from the flux of the fully non-differentiated cells, and from the irreversibility of the fully completed differentiation.

An application of the proposed model for peri-implant osseointegration is considered. Numerical results are compared with experimental data. Potential lines of further development of the present approach are proposed. The current evolutionary approach also is presented in Prokharau et al. [79].

3.1 Introduction

Cell differentiation, along with proliferation and migration, plays an important role at the early stages of the tissue regeneration process. A lot of studies have been devoted to the phenomenon of bone regeneration recently. In a number of studies various theoretical models were developed for frac-

ture healing, peri-implant osseointegration and bone distraction (see Section 1.3). In these models cell differentiation is considered as a crucial process in regulating the course of bone healing. In most of the mentioned works, the differentiation process is introduced into the constitutive equations by means of a logistic term. Such an approach corresponds to the situation, when a particular cell changes its type immediately.

A more enhanced representation of cell differentiation is introduced in the model by Reina-Romo et al. [83]. The differentiation process is assumed to depend on the mechanical stimulus and *time*. The differentiation evolution is introduced by means of maturation state m_i of the cells, being reversible if $m_i < 1$. Full differentiation into another cell type corresponds to the value $m_i = 1$, and is assumed to be irreversible.

In the first part of this chapter the conceptual mathematical model for the evolutionary cell differentiation is derived. The basic assumptions for this model are in line with those, proposed in Reina-Romo et al. [83]. Due to the generality of the current model, it can be adapted and used for various applications.

The main idea, characterizing the current approach, is that in the course of differentiation, a cell of a certain type gains the properties of another cell type gradually. Therefore, differentiation is considered as a process, which evolves in time, or in other words, the path of cell differentiation is incorporated into the model. The particular trajectory of the path can be determined by an arbitrary number of parameters, e.g. by biochemical and mechanical factors, by the level of differentiation of the cell at the current moment or by a random variable etc. The phenomenon, when cells change their differentiation path, depending on some parameters, is known as *cell (or tissue) plasticity* (see e.g. Röder [84]).

In Section 3.2, the differentiation of mesenchymal stem cells (MSC's) into osteoblasts, fibroblasts and chondrocytes is considered. Due to the generic nature of the proposed approach, the present model can be modified for the case of evolutionary differentiation of arbitrary cells into *any number* of cell types.

In Section 3.3, an example of the application of the current approach is given. A peri-implant osseointegration is modeled. The mechanical state in the interface tissue is chosen to be the main factor, which influences the mesenchymal stem cell (MSC) differentiation. The series of numerical simulations are carried out for the constructed model. The numerical method is described and simulations results are presented and discussed in Section 3.4. Conclusions are drawn in Section 3.5.

The present study is inspired by the work of Röder [84], where the complete differentiation of a stem cell is considered as attainment of a certain value by some cell property a. The path of variation of property a is assumed to depend on the changing growth environment, to which the cell belongs.

3.2 Differentiation model

In this section a new modeling approach for the differentiation of MSC's is developed. MSC's are supposed to differentiate into osteoblasts, fibroblasts and chondrocytes. The most important innovating assumption of the current approach, is that cells are supposed to gain the properties of another cell type *gradually*, in the course of time, until a complete differentiation of MSC's takes place. Therefore, a certain *finite* time of differentiation can be related to each MSC. The variation of the differentiation time is represented by means of the differentiation rate, which is assumed to depend on the state of the environment, in which cells are situated. The proposed approach allows to consider the differentiation of MSC's as partially stochastic process. However, for the numerical simulations, presented in this chapter, the MSC differentiation process is modeled only in a deterministic way.

The model for cell differentiation is presented in two successive steps. First, the current stage of differentiation of MSC's into a certain cell type i, where $i \in \{b, f, c\}$, is represented via a differentiation property a_i. The value b of the sub-index i corresponds to osteoblasts, f – to fibroblasts, c – to chondrocytes. The variables a_b, a_f, a_c take values from 0 to 1. The value 1 implies, that a MSC has completely differentiated into the respective cell type, and the value 0 corresponds to the initial state of a MSC, which has not yet started to differentiate. The region, in which the variables a_b, a_f, a_c take their values, is referred to as the differentiation state domain Ω_a. The concept of differentiation properties a_i is implemented in the model, by considering the MSC density c as a function of location in physical space $\vec{x}$, of time t and of differentiation state coordinates a_b, a_f, a_c. The process of differentiation corresponds to the variation of the value of the differentiation property a_i, and it can be considered as a movement of the MSC within the region Ω_a. This movement is determined by velocity $\underline{u}$ (the underlined symbol denotes a vector in the differentiation state space), which is assumed to depend on a number of parameters, being $\psi_1, \ldots, \psi_p$, $p \in \mathbb{N}$, and also on the differentiation state variables a_i. Parameters $\psi_1, \ldots, \psi_p$ can be defined, for example, as mechanical stimuli, biochemical factors or as a random variable, and they are functions of location in physical space $\vec{x}$ and time t. For conciseness, the set of parameters is denoted as vector $\Psi(\vec{x}, t) = (\psi_1, \ldots, \psi_p) \in \Omega_p \subset \mathbb{R}^p$, where p is the number of parameters. Therefore, $\underline{u} = \underline{u}(\Psi(\vec{x}, t), a_b, a_f, a_c)$.

If no additional conditions on variables a_i, $i \in \{b, f, c\}$ are applied, then the differentiation state domain $\Omega_a = [0, 1]^3$ is a unit cube. In general case, when a cell is able to differentiate into n various types, Ω_a is the n-dimensional unit cube. For the considered model, the unknown function $c(\vec{x}, t, a_b, a_f, a_c)$ is defined within the domain $Q = \Omega \times \mathbb{R}^+ \times \Omega_a$, which is a 6-dimensional region in the case of a two-dimensional domain Ω in the physical space, and a 7-dimensional region, for a three-dimensional domain Ω. For

the numerical simulations this can lead to extremely large computation time and size of solution data.

In the second step, the current model is modified, so that it becomes more useful for the practical applications. Certain constraints on variables a_i are imposed, which allow to reduce the dimensionality of the problem domain by $n-1$, where n is the number of cell types, into which the considered cells can differentiate ($n = 3$ for the particular model for MSC's differentiation). This restriction is formulated as follows.

Assumption 3.1. *A cell cannot have characteristics of the differentiation into several cell types simultaneously. In other words, each cell can have only one non-zero differentiation property a_i.*

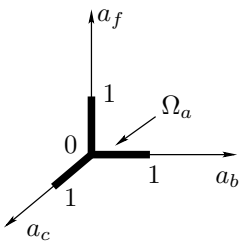

Figure 3.1: Plot of the differentiation state domain Ω_a, as defined in equation (3.1)

The differentiation state domain Ω_a is then defined as:

$$\Omega_a = \{(a_b, 0, 0), (0, a_f, 0), (0, 0, a_c) : \ a_i \in [0, 1], \ i = b, f, c\} . \tag{3.1}$$

The region Ω_a, given in (3.1), is depicted in Figure 3.1. This region can be considered as a set of three one dimensional unit intervals situated on the axes of Cartesian coordinates in a three-dimensional space, which have one common point in the origin. The region Ω_a lies in $\mathbb{R}^3$ and it has a zero measure. In order to get a one-dimensional differentiation state domain, the following technique is used. Instead of one unknown c, depending on three differentiation state variables a_i, $i \in \{b, f, c\}$, three unknowns c_i, $i \in \{b, f, c\}$, depending on one differentiation state variable a are defined for the MSC density. The correspondence between c and c_i can be determined in the following way:

$$c_b(\vec{x}, t, a) = c(\vec{x}, t, a, 0, 0), \quad c_f(\vec{x}, t, a) = c(\vec{x}, t, 0, a, 0),$$
$$c_c(\vec{x}, t, a) = c(\vec{x}, t, 0, 0, a), \quad \text{for } a \in \Omega_a^1 = [0, 1], \ \vec{x} \in \Omega, \ t > 0,$$

where the one-dimensional differentiation state domain is denoted as Ω_a^1. Unknowns $c_i(\vec{x}, t, a)$, $i \in \{b, c, f\}$, denote the density of the MSC's at the point $\vec{x}$ at the time moment t, differentiating into osteoblasts, fibroblasts or

chondrocytes, respectively, at the differentiation level a. These unknowns have the dimension of number of cells per unit volume, per unit of differentiation level. The differentiation path is determined by functions u_i, which denote the velocity of cell "motion" in the differentiation state domain, or the rate, at which a cell changes the value of its differentiation level a. In other words, if a fixed cell is considered, which differentiates into the cell type $i \in \{b, f, c\}$, and if its differentiation level is denoted as $a_{cell}(t)$, then $u_i = \frac{da_{cell}}{dt}$. The velocities u_i depend on the parameters $\Psi(\vec{x}, t) = (\psi_1(\vec{x}, t), \ldots, \psi_p(\vec{x}, t)) \in R^p$, on the differentiation level a, and on the specific phenotype $i \in \{b, f, c\}$ the cell is differentiating to, i.e. $u_i = u_i(\Psi(\vec{x}, t), a)$.

The flux of MSC's in the differentiation state domain is denoted as

$$q_i(\vec{x}, t, a) = u_i(\Psi(\vec{x}, t), a)\, c_i(\vec{x}, t, a).$$

A positive value of the flux q_i and of the velocity u_i corresponds to the positive direction of axis a. From a biological point of view, a positive velocity $u_i(\vec{x}, t, a)$, $i \in \{b, c, f\}$ implies, that cells $c_i(\vec{x}, t, a)$ are gaining the properties of the phenotype i, and a negative rate $u_i(\vec{x}, t, a)$ means, that MSC's are losing the properties of the cell type i. The process of differentiation is assumed to be reversible, except if the cell has achieved the maximum level of differentiation $a = 1$, i.e. if the MSC has completely differentiated into another cell type. In this case the differentiation is irreversible, since a fully differentiated cell cannot become a MSC again [83]. Hence, the influx of MSC's at the boundary $\Gamma_a^1 = \{(\vec{x}, a) : \vec{x} \in \Omega, a = 1\}$ should be zero. From this it follows:

Proposition 3.1. *If* $u_i(\Psi(\vec{x}, t), 1) < 0$, *where* $\vec{x} \in \Omega$, $t > 0$, $i \in \{b, f, c\}$, *then*

$$c_i(\vec{x}, t, 1) = 0. \tag{3.2}$$

Otherwise, reverse differentiation of cells of the type $i \in \{b, c, f\}$ into MSC's would take place.

3.2.1 Flow of non-differentiated cells

The density of the fully non-differentiated MSC's at the point $(\vec{x}, t)$ is determined by $\sum_i c_i(\vec{x}, t, 0)$. The "location" of the non-differentiated cells is the part of the domain $\Omega \times \Omega_a^1$ boundary, where $a = 0$:

$$\Gamma_a^0 = \{(\vec{x}, a) : \vec{x} \in \Omega, a = 0\}.$$

The magnitude of the flux $\|q_i\| = \|u_i c_i\|$, $i \in \{b, f, c\}$ at Γ_a^0 denotes either the inflow or the outflow of c_i, depending on the sign of the velocity u_i. A positive velocity u_i at Γ_a^0, corresponds to the inflow of c_i, and negative – to the outflow.

Suppose, that at a certain location $\vec{x}_0$ and at the given time moment t_0 the environment in the tissue is such, that non-differentiated MSC's differentiate into osteoblasts at a rate $u_1 > 0$. Hence, $u_b(\Psi_0, 0) = u_1 > 0$, where $\Psi_0 = \Psi(\vec{x}_0, t_0)$. Fully non-differentiated MSC's are not biologically distinguishable, though they can be related to different densities c_i. This means, that non-differentiated MSC's, related to $c_f(\vec{x}_0, t_0, 0)$, also will differentiate into osteoblasts with rate u_1. They gain the properties of osteoblasts, and consequently will become related to c_b. This implies, that the outflow of density c_f, equal to $u_1 c_f$, will take place at the point $(\vec{x}_0, t_0, 0)$. Since outflow at $a = 0$ corresponds to the negative differentiation rate, then

$$u_1 c_f(\vec{x}_0, t_0, 0) = \|q_f(\vec{x}_0, t_0, 0)\| = \|u_f(\Psi_0, 0) c_f(\vec{x}_0, t_0, 0)\| \\ = -u_f(\Psi_0, 0) c_f(\vec{x}_0, t_0, 0).$$

Hence,

$$u_f(\Psi_0, 0) = -u_1 = -u_b(\Psi_0, 0). \tag{3.3}$$

By analogy, it is derived, that

$$u_c(\Psi_0, 0) = -u_b(\Psi_0, 0). \tag{3.4}$$

From this example, it follows, that the negative differentiation rate $u_i(\Psi, 0)$, $i \in \{b, f, c\}$, $\Psi \in \Omega_p$, corresponds to the situation, when non-differentiated MSC's are stimulated to differentiate into the cell type j, different from the cell type i.

The path of cell differentiation is determined by the parameter vector $\Psi \in \Omega_p$ and the maturation level a. It is supposed, that each value of $\Psi \in \Omega_p$ corresponds to a certain state, for which non-differentiated MSC's differentiate into a particular cell type $i \in \{b, f, c\}$ and do not differentiate into any other cell type.

Remark 3.1. Randomness of the differentiation process, if needed, can be taken into account by considering one or more random variables ψ_j, included in the parameter set Ψ.

The situation, when the non-differentiated MSC's do not differentiate at all, is also allowed. From this, the following statement can be made.

Proposition 3.2. *For any $\Psi \in \Omega_p$,*

- *there exists exactly one $i \in \{b, c, f\}$, such that $u_i(\Psi, 0) > 0$, and $u_j(\Psi, 0) = -u_i(\Psi, 0) < 0$ for $j \in \{b, c, f\}, j \neq i$; or*
- *$u_i(\Psi, 0) = 0$ for all $\forall i \in \{b, f, c\}$.*

Suppose that $u_b(\Psi(\vec{x}_0, t_0), 0) > 0$, then the inflow of the density c_i takes place at the point $(\vec{x}_0, t_0)$. From Proposition 3.2, it follows, that

$$u_f(\Psi(\vec{x}_0, t_0), 0) = u_c(\Psi(\vec{x}_0, t_0), 0) = -u_b(\Psi(\vec{x}_0, t_0), 0) < 0.$$

If there is no external source of MSC's, then this inflow can be formed only by the outflow of densities c_f and c_c. That means, that

$$\|q_b(\vec{x}_0, t_0, 0)\| = \|q_f(\vec{x}_0, t_0, 0)\| + \|q_c(\vec{x}_0, t_0, 0)\|.$$

Hence,

$$\begin{aligned}\|u_b(\Psi_0, 0)c_b(\vec{x}_0, t_0, 0)\| &= u_b(\Psi_0, 0)c_b(\vec{x}_0, t_0, 0) \\ &= \|u_f(\Psi_0, 0)c_f(\vec{x}_0, t_0, 0)\| + \|u_c(\Psi_0, 0)c_c(\vec{x}_0, t_0, 0)\| \\ &= -u_f(\Psi_0, 0)c_f(\vec{x}_0, t_0, 0) - u_c(\Psi_0, 0)c_c(\vec{x}_0, t_0, 0),\end{aligned}$$

$$\Rightarrow \quad c_b(\vec{x}_0, t_0, 0) = c_f(\vec{x}_0, t_0, 0) + c_c(\vec{x}_0, t_0, 0). \tag{3.5}$$

In general case, if $u_i(\Psi(\vec{x}, t), 0) > 0$ for a certain $i \in \{b, f, c\}$, then the inflow of c_i occurs at the point $(\vec{x}, t, 0)$, which is supposed to be equal to the total outflow of c_j, $j \in \{b, c, f; j \neq i\}$. Hence, the proposition can be formulated.

Proposition 3.3. *If* $u_i(\Psi(\vec{x}, t), 0) > 0$, *where* $\vec{x} \in \Omega$, $t > 0$, $i \in \{b, f, c\}$, *then*

$$c_i(\vec{x}, t, 0) = \sum_{j \neq i} c_j(\vec{x}, t, 0). \tag{3.6}$$

To motivate the use of the boundary and initial conditions for c_i due to the differentiation state dimension, the following simple partial differential equation (PDE) is considered:

$$\frac{\partial c_i}{\partial t} + \frac{\partial (u_i c_i)}{\partial a} = 0. \tag{3.7}$$

The above equation describes the dynamics of the differentiation of MSC's at a certain point in the physical space. Here, motility and proliferation of the cells are not considered. The equation illustrates, which boundary conditions with respect to a should be specified, due to the presence of the term $\frac{\partial(u_i c_i)}{\partial a}$, which represents cell differentiation. Consider the case when u_i is constant. Then, the lines in the (a, t)-plane are considered, over which c_i is constant, that is

$$0 = \frac{d}{dt} c_i(\vec{x}, t, a(t)) = \frac{\partial c_i}{\partial t} + \frac{\partial c_i}{\partial a} a'(t).$$

From equation (3.7) and from the assumption $u_i = const$, it follows that $a'(t) = u_i$. Hence $a(t) = u_i(t - t_0) + a_0$ is the equation of the characteristic lines, over which $c_i(\vec{x}, t, a(t)) = const$. Plots of the characteristics $a(t)$ in the plane (a, t) are shown in Figure 3.2. It follows, that the solution c_i at any point $(t, a) \in [0, \infty) \times [0, 1]$ is determined by the initial condition $c_i(0, a) = g_0(a)$, and by the condition $c_i(t, 0) = g_{b0}(t)$ on the boundary

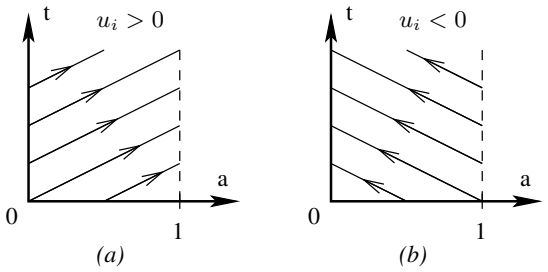

Figure 3.2: Projections of characteristics of the equation (3.7) on the plane (a, t) for different signs of velocity $u_i = u_i(\Psi, a)$

$(t, 0)$, if $u_i > 0$ (Figure 3.2a), or by the condition $c_i(t, 1) = g_{b1}(t)$ on the boundary $(t, 1)$, if $u_i < 0$ (Figure 3.2b). In general case, i.e. if $u_i \neq const$, the condition will be required on the part of the boundary, where the influx takes place, and no boundary condition should be specified on the outflow boundary (see e.g. LeVeque [59]). Therefore, for the existence and the uniqueness of the solution of (3.7):

1. initial conditions at $t = 0$ should be specified;
2. (a) if $u_i(\Psi, 0) > 0$ (Figure 3.2a), then boundary conditions for c_i, defined in Proposition 3.3, are required on the boundary $a = 0$;
   (b) if $u_i(\Psi, 0) \leq 0$ (Figure 3.2b), then no boundary conditions for c_i should be prescribed on the boundary $a = 0$;
3. (a) $u_i(\Psi, 1) < 0$, then boundary conditions, defined in Proposition 3.1, are required on the boundary $a = 1$;
   (b) if $u_i(\Psi, 1) \geq 0$, then no boundary conditions should be specified on the boundary $a = 1$.

Therefore, in Propositions 3.1, 3.3, the boundary conditions are defined, which are necessary for the existence and the uniqueness of the solution of partial differential equations, which contain the advection term $\frac{\partial(u_i c_i)}{\partial a}$, representing evolutionary cell differentiation. This differentiation term is included in the equations to model the evolution of the MSC densities, that are derived in Section 3.3.

3.3 Peri-implant osseointegration

3.3.1 Mathematical model

In Section 3.2, the generic mathematical representation of evolutionary cell differentiation is described. Further, the validation of this approach is presented, and its advantages over the commonly used model for immediate cell differentiation are highlighted.

In order to look at the applicability of the current differentiation approach, it is incorporated in the simulations of bone regeneration during peri-implant osseointegration. This specific example of an application is chosen due to the following reasons:

1. In the current model, differentiation of MSC's into osteoblasts and fibroblasts is considered, which is determined by the level of the mechanical loading. Then, the ability of the model to represent evolutionary differentiation into several cell types under the influence the external factors can be demonstrated .

2. Furthermore, a number of experimental and numerical studies have been devoted to the bone regeneration process. Hence, it will be possible to compare the results of simulations with the available data.

Further, the mathematical model for the peri-implant osseointegration will be derived. Bone regeneration is represented in the model as a series of biological events, such as:

- migration and proliferation of MSC's,
- differentiation of MSC's into osteoblasts and fibroblasts,
- migration and proliferation of fibroblasts,
- proliferation of osteoblasts,
- fibrin network substitution by woven bone, and fibrous tissue,
- woven bone remodeling into lamellar bone.

Three cell types are considered: MSC's, osteoblasts and fibroblasts. The density of MSC's, differentiating into chondrocytes, and the density of chondrocytes are not included into the model, since formation of cartilage tissue is not observed in the experiments for the peri-implant osseointegration within the bone chamber [28, 29, 92, 93, 94].

MSC's are introduced into the model by variables c_f, c_b, which denote the densities of MSC's per unit of volume and per unit of differentiation level, normalized with respect to the limit density C of cells per unit volume. The unknowns c_f, c_b have dimension *(unit of differentiation level)*$^{-1}$. The variables c_f, c_b are functions of the space coordinate $\vec{x} \in \Omega$, of time $t \in \mathbb{R}^+$ and of the differentiation level $a \in [0, 1]$. Non-dimensional model variables b, f denote the densities of osteoblasts and fibroblasts per unit volume, normalized with respect to the limit density C. Unknown variables v_n, v_w, v_l, v_f denote the volume fractions of fibrin network, woven bone, lamellar bone and fibrous tissue, respectively. They are functions of the physical space coordinates and of time.

It is assumed, that MSC's tend to differentiate into cells of a certain type, depending on the mechanical environment. Cells, originated from the differentiated MSC's, provide the substitution of a fibrin network by the respective tissue type. Mechanoregulation of differentiation is introduced in terms of the mechanical stimulus ψ. The stimulus ψ is evaluated, after the mechanical environment in the interface tissue is determined. It is assumed that the interface tissue is loaded at a low or moderate frequency and that deformations appearing in the peri-implant region are small. Therefore fluid motion is neglected, and the interface tissue is modeled as an isotropic linear elastic medium. The elasticity properties of the medium are determined by the mixture rule, using the volume fractions of various tissue types. The mechanical stimulus ψ is assumed to be defined by the octahedral shear strain γ_{oct} [50]:

$$\psi = \gamma_{oct} = \frac{1}{3}\sqrt{(\varepsilon_1 - \varepsilon_2)^2 + (\varepsilon_2 - \varepsilon_3)^2 + (\varepsilon_1 - \varepsilon_3)^2}. \tag{3.8}$$

Assumption 3.2. *It is assumed here, that within the regions with a low and moderate level of mechanical stimulus, bone formation is promoted, whereas high values of mechanical stimulus lead to the formation of fibrous tissue [18, 19, 77].*

The dynamics of the MSC densities c_i, $i \in \{b, f\}$ is described by the equation:

$$\frac{\partial c_i}{\partial t} = \nabla_s \cdot (D_c \nabla_s c_i) - \frac{\partial}{\partial a}(u_i c_i) + A_c(1 - c_{tot} - f - b)c_i, \quad i \in \{b, f\}, \tag{3.9}$$

where $c_{tot}(\vec{x}, t)$ is the total density of MSC's, normalized with respect to the limit cell density C per unit volume, at the point $(\vec{x}, t)$:

$$c_{tot}(\vec{x}, t) = \int_0^1 (c_b(\vec{x}, t, a) + c_f(\vec{x}, t, a))da. \tag{3.10}$$

The first term in the right-hand side of equation (3.9) represents random walk of MSC's in the physical space. The symbol ∇_s denotes the nabla operator in physical space, and the constant D_c is the mobility coefficient. Proliferation of MSC's is represented by the last term in the right-hand side of equation (3.9). The constant A_c is the rate of proliferation. Proliferation stops, if the normalized total cell density reaches its limit value, which is equal to one.

The term $-\frac{\partial}{\partial a}(u_i c_i)$ in equation (3.9) corresponds to the change of MSC density due to the flux $u_i c_i$ in the differentiation state domain Ω_a^1. The functions $u_i = u_i(\psi(\vec{x}, t), a)$ denote the differentiation rates. Mechanoregulation of the cell and tissue processes is introduced in the current model through

the functions u_i. This is done, by assuming a certain relation between the mechanical stimulus ψ and differentiation rates u_i. A relation should be chosen, such that the results, predicted by the model, are in agreement with Assumption 3.2 concerning the mechanoregulation of tissue formation within the peri-implant interface. The choice of the functions $u_i(\psi, a)$ will be described in the Section 3.3.2.

Remark 3.2. In most of the recent models for bone regeneration, for example in [6, 7, 11, 12, 35, 43, 46, 67], the process of differentiation of MSC's is introduced into the model equations by means of the reaction term, which can be written in the general form as $-\alpha_i c$. The variable c denotes the density of MSC's per unit volume, and α_i is the rate of differentiation of MSC's into cell type i, which can depend on a number of variables, such as chemical or mechanical stimuli. This representation implies, that the number of MSC's, differentiating into cell type i within the volume V during time period $[t_0, t_0 + dt]$, is equal to $\left(\int_V \alpha_i c(x, t_0)\, dx\right) dt$. The rate of differentiation of MSC's is determined by the total MSC density c *at the current time moment* t_0, and not by the path of differentiation of cells, opposed to what is done in the current work. In the classical models, there is always a nonzero portion of MSC's that will differentiate, even in the case of MSC's that did not yet inherit any property of the phenotype they are differentiating to. Further, the entire differentiation is formally never completed within a finite time frame. The present evolutionary approach corresponds to a final, bounded, time of cell differentiation, and further if the MSC's would have no property of the phenotype they are differentiating to, then differentiation is no longer immediate in the current approach. These are the main distinctions of the current model from the mentioned models, which results from the consideration of MSC differentiation as an evolutionary process (see also the discussion in Section 3.5).

A zero density of MSC's is assumed within the peri-implant interface at time $t = 0$ [6]:

$$c_i(\vec{x}, 0, a) = 0 \quad \vec{x} \in \Omega, i \in \{b, f\}. \tag{3.11}$$

Suppose, that $\partial\Omega$ is the boundary of Ω, $\partial\Omega_b$ is the part of $\partial\Omega$, corresponding to the bone surface, and $\vec{n}$ is an outward unit normal of $\partial\Omega$. It is assumed, that there is a source of MSC's, with the differentiation level $a \in [0, \delta]$, on the bone surface $\partial\Omega_b$ during the first two weeks [67]. This source is introduced into the model by specifying the influx $h(t, a) \geq 0$ of the densities c_i, $i \in \{f, b\}$, on $\vec{x} \in \partial\Omega_b$, $a \in [0, \delta]$. On the rest of the boundary $\vec{x} \in \partial\Omega$, $a \in [0, 1]$ a zero flux is assumed. Therefore, the boundary

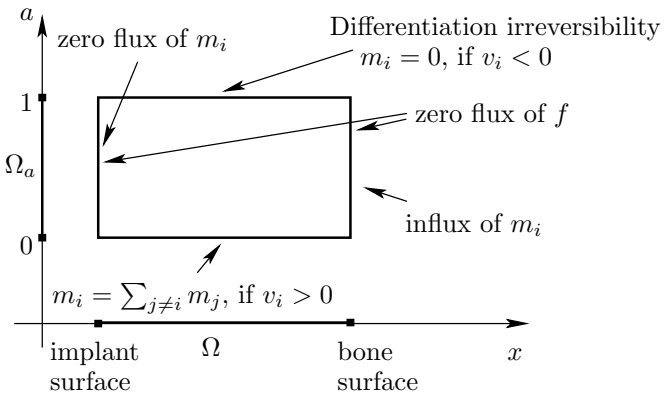

Figure 3.3: Boundary conditions for the case of a one dimensional physical domain Ω. Additional source of MSC's is shown at the bone surface

conditions for the MSC densities c_i, $i \in \{b, f\}$ are defined as:

$$\begin{cases} c_i(\vec{x}, t, 0) = \sum\limits_{j \neq i} c_j(\vec{x}, t, 0), & \text{if } u_i(\psi(\vec{x}, t), 0) > 0,\ \vec{x} \in \bar{\Omega}, t > 0, \\ c_i(\vec{x}, t, 1) = 0, & \text{if } u_i(\psi(\vec{x}, t), 1) < 0,\ \vec{x} \in \bar{\Omega}, t > 0, \\ -D_c \nabla_s c_i \cdot \vec{n}_s = \begin{cases} -h(t, a), & \vec{x} \in \partial\Omega_b, \\ 0, & \vec{x} \in \partial\Omega / \partial\Omega_b, \end{cases} & t > 0, a \in [0, 1], \end{cases} \tag{3.12}$$

$$h(t, a) = \begin{cases} 0.01 \cdot \frac{1}{\delta}(1 - \frac{a}{\delta}), & \text{if } t \in (0, 14),\ a \in [0, \delta], \\ 0, & \text{otherwise,} \end{cases}$$

where $\nabla_s(\cdot)$ denotes the gradient in the physical space and $h(t, a)$ corresponds to the source of MSC's on the bone surface. The parameter δ should be related to the size of computational grid within the differentiation state space. Therefore, in the current study, it is assumed, that $\delta = 0.1$. In Figure 3.3, the boundary conditions, defined in equation (3.12), are depicted for the case of the one dimensional physical domain Ω.

For conciseness, the fluxes of fully differentiated MSC's are denoted via functions

$$Q_i(\vec{x}, t) = u_i(\psi(\vec{x}, t), 1) c_i(\vec{x}, t, 1),\ \vec{x} \in \Omega, t > 0, i \in \{b, f\}. \tag{3.13}$$

They determine the increment of the density of osteoblasts and fibroblasts per unit of time, caused by the differentiation of MSC's. The equations for the dynamics of osteoblasts and fibroblasts are given as:

$$\frac{\partial b}{\partial t} = Q_b + A_b(1 - c_{tot} - f - b)b, \tag{3.14}$$

$$\frac{\partial f}{\partial t} = \nabla_s \cdot (D_f \nabla_s f) + Q_f + A_f(1 - c_{tot} - f - b)f, \tag{3.15}$$

where D_f is the coefficient of the fibroblast motility in the physical space, A_b and A_f are the proliferation rates of osteoblasts and fibroblasts, respectively.

It is straightforward, that the sum of all considered tissue volume fractions is equal to one. Hence, the volume fraction of the fibrin network is determined by:

$$v_n = 1 - (v_w + v_l + v_f). \tag{3.16}$$

The evolution of the volume fractions of woven bone v_w, lamellar bone v_l and fibrous tissue v_f is described by the equations:

$$\frac{\partial v_w}{\partial t} = \alpha_w b v_n (1 - v_w) - \gamma v_w (1 - v_l), \tag{3.17}$$

$$\frac{\partial v_l}{\partial t} = \gamma v_w (1 - v_l), \tag{3.18}$$

$$\frac{\partial v_f}{\partial t} = \alpha_f f v_n (1 - v_f), \tag{3.19}$$

where terms, containing coefficients α_w and α_f, correspond to the substitution of the fibrin network by woven bone and fibrous tissue, respectively. The coefficient γ is the rate of the remodeling of woven bone into lamellar bone.

The boundary and initial conditions for PDE (3.14), and the initial conditions for ordinary differential equations (3.15), (3.17)–(3.19) are given by:

$$-D_f \nabla_s f \cdot \vec{n}_s = 0, \quad \vec{x} \in \partial\Omega,\ t > 0 \tag{3.20}$$

$$\begin{cases} b(\vec{x}, 0) = 0,\ f(\vec{x}, 0) = 0, \\ v_w(\vec{x}, 0) = 0,\ v_f(\vec{x}, 0) = 0,\ v_l(\vec{x}, 0) = 0, \end{cases} \quad \vec{x} \in \Omega. \tag{3.21}$$

3.3.2 Differentiation rates and tissue formation

In this section the particular expressions for the differentiation rates u_i, $i \in \{b, f\}$, as a function of the mechanical stimulus ψ are defined in line with Assumption 3.2 on mechanoregulation.

First, it is investigated, how the magnitudes of the differentiation rates influence tissue formation, described by the proposed model. It is assumed, that the differentiation rates u_i, $i \in \{b, f\}$, do not depend on the level of differentiation a. Hence,

$$u_i = U_i(\psi),\ i \in \{b, f\}. \tag{3.22}$$

The following assumption is derived from the hypotheses in Proposition 3.2:

$$U_b(\psi) = U(\psi) = -U_f(\psi),\ \psi \in [0, \infty). \tag{3.23}$$

A simplified problem is considered, that is derived from the full model by assuming the mechanical stimulus $\psi(\vec{x}, t)$ to be constant in the physical

space Ω and in time. The problem is defined by equations (3.9), (3.14)–(3.19) and by the initial and boundary conditions in equations (3.11), (3.12), (3.21),(3.20). The functions $U_b(\psi)$, $U(\psi)$, $U_f(\psi)$ can be considered as constant parameters, denoted as U_b, U, U_f. From condition (3.23), it follows that $U_b = U = -U_f$. The behavior of the solution of the simplified problem with respect to the value of U is studied. The parameter U is assumed to take a range of values $\{U_{max} - i\Delta U;\ i = 0, 1, \ldots, N,\ \Delta U = 2U_{max}/N\}$. The problem is solved numerically for each value of U. As a measure of formation of bone and of fibrous tissue, the average volume fraction of woven and lamellar bone, v_b^{avg}, and the average volume fraction of fibrous tissue v_f^{avg} in the bone-implant interface at the time moment $t = 63$ *days* is chosen, respectively. Time $t = 63$ *days* is chosen according to the experiments by Vandamme et al. [94]. A one dimensional axisymmetric physical domain $\Omega = [1, 3.5]$ mm is considered, in order to reduce the calculation time. A source of MSC's is assumed at the point $r = 3.5$ mm. A uniform rectangular grid of 40 by 40 control volumes is constructed within the domain $\Omega \times [0, 1]$. The governing equations are solved with the finite volume method and with the explicit modified Euler time integration scheme. The considered parameter values are described in Section 3.4.1.

The relations between the average tissue volume fractions v_b^{avg} and v_f^{avg}, and the values of differentiation rates U_b and U_f are denoted as $v_b^{avg} = V_b^u(U_b)$, $v_f^{avg} = V_f^u(U_f)$. Their plots are given in Figure 3.4.

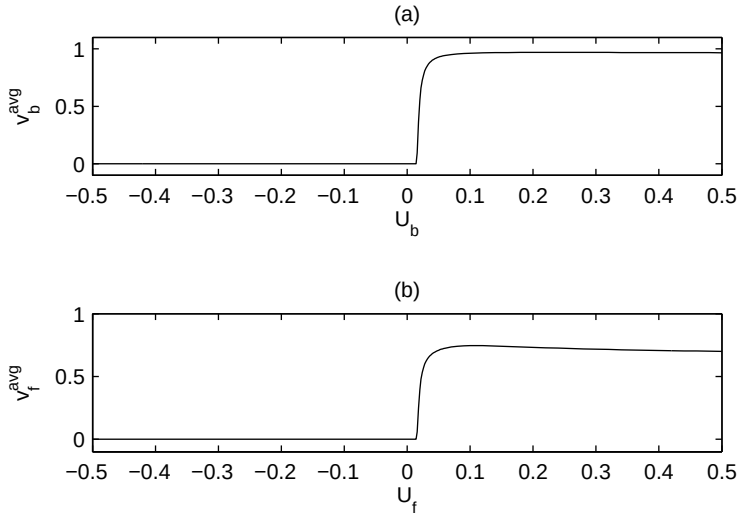

Figure 3.4: Plot of the average volume fraction of *(a)* woven and lamellar bone v_b^{avg} and *(b)* of fibrous tissue v_f^{avg} in the peri-implant interface at the time moment $t = 63$ *days* against the value of differentiation rate (a) U_b and (b) U_f, respectively

MSC's do not differentiate into osteoblasts, if $u_b < 0$. Hence, for negative values of the parameter U_b, the osteoblast density b is zero, and from equation (3.17) it follows, that no bone forms in the peri-implant interface and $v_b^{avg} = 0$ (Figure 3.4*a*). According to the boundary condition, defined in equation (3.12), any MSC originated from the old bone surface has a differentiation level lower than $\delta = 0.1$. Hence, some of the MSC's will reach the differentiation level $a = 1$ at time $t = 63$ $days$, and consequently differentiate into osteoblasts completely, only if the differentiation rate U_b is larger than $U^{min} = \frac{1-\delta}{63} \approx 0.0143$ $days^{-1}$. For $U_b \in [0, U^{min}]$ no osteoblasts and no bone tissue will appear in the peri-implant region within 63 days. For the values $U_b > U^{min}$, the amount of the bone, formed within the bone-implant interface, grows with the increase of the parameter U_b up to a certain extremum point $U_b^{extr} \approx 0.24$ $days^{-1}$, which follows from Figure 3.4*a*. Further increase of U_b leads to a bit smaller amount of bone in the interface.

The relation between the parameter U_f and the amount of fibrous tissue v_f^{avg} is plotted in Figure 3.4*b*. For negative U_f and for $U_f \in [0, U^{min}]$, no fibroblasts appear within the peri-implant interface ($f = 0$), and no fibrous tissue forms, i.e. $v_f^{avg} = 0$. The fibrous tissue volume fraction v_f^{avg} increases with an increase of U_f on the interval $U_f \in [U^{min}, U_f^{extr}]$ and decreases for $U_f > U_f^{extr}$, $U_f^{extr} \approx 0.1$ $days^{-1}$.

The decrease in volume fraction of bone and fibrous tissue, when the differentiation rates exceed the limits U_b^{extr} and U_f^{extr}, respectively, can be explained by a coupled effect of cell migration, proliferation and differentiation. The inverse proportionality is more recognizable for the fibrous tissue dependence on the differentiation rate U_f (Figure 3.4*b*). As it follows from the values of the motility and proliferation coefficients D_c, D_f, A_c and A_f (see Section 3.4.1), MSC's migrate and proliferate within the healing site faster than fibroblasts. On the one hand, for smaller differentiation rates U_f, each cell remains a MSC for a longer time period. In this state, the cell migrates towards the implant surface and proliferates faster, that if it were a fibroblast. This can lead to a higher total density of MSC's within the peri-implant region for smaller U_b after some time. On the other hand, if the supply of MSC's is sufficient, then the larger the value of the differentiation rate U_f, the more MSC's differentiate into fibroblasts per unit of time. For high rates $U_f > U_f^{extr}$, the first effect prevails. However, for slow differentiation, $U_f < U_f^{extr}$, the second effect becomes more important.

Next, the following functions are defined: $v_i^{avg} = V_i^{\psi}(\psi)$, $i \in \{b, f\}$, where

$$V_i^{\psi}(\psi) = V_i^{u}(U_i(\psi)),\ \psi \in [0, \infty). \tag{3.24}$$

A certain expression for the function $U : [0, \infty) \to \mathcal{U} \subset \mathbb{R}$ should be determined, such that $U_b(\psi) = U(\psi) = -U_f(\psi)$, and such that the dependencies $v_b^{avg} = V_b^{\psi}(\psi)$, $v_f^{avg} = V_f^{\psi}(\psi)$ will be in agreement with the Assumption 3.2

about mechanoregulation of tissue formation. The following relation is proposed (see Figure 3.5):

$$U(\psi) = \begin{cases} (U_b^{max} - U_b^0)\sin\left(\dfrac{\psi\pi}{2\psi_1}\right) + U_b^0, & 0 \le \psi < \psi_1, \\ (U_b^{max} - U^{min})\cos\left(\dfrac{(\psi-\psi_1)\pi}{2(\psi_2-\psi_1-\delta\psi)}\right) + U^{min}, & \\ & \psi_1 \le \psi < \psi_2 - \delta\psi, \\ \dfrac{U^{min}}{\delta\psi}(\psi_2 - \psi), & \psi_2 - \delta\psi \le \psi < \psi_2 + \delta\psi, \\ (U^{min} - U_f^{max})\sin\left(\dfrac{(\psi-\psi_2-\delta\psi)\pi}{2(\psi_3-\psi_2-\delta\psi)}\right) - U^{min}, & \\ & \psi_2 + \delta\psi \le \psi < \psi_3, \\ -U_f^{max}, & \psi_3 \le \psi. \end{cases} \tag{3.25}$$

From the plot of the function $U(\psi)$ (Figure 3.5) and from equations (3.22)–(3.23), (3.25), it follows, that the line of non-negative values of the mechanical stimulus ψ is divided into five characteristic intervals. On the first interval $[0, \psi_1]$, the rate of MSC differentiation into osteoblasts increases from the value U_b^0, which corresponds to a zero mechanical stimulus, to the value U_b^{max}. Abrahamsson et al. [1] and Berglundh et al. [14] observed formation of bone within the peri-implant region at the end of the first week. The value 0.2 $days^{-1}$ is estimated for U_{max}, so that osteoblasts, releasing bone matrix, will appear at the end of the first week. It is assumed, that $U_b^0 = 0.1\ days^{-1}$. The threshold ψ_1, corresponding to the maximal rate of differentiation of MSC's into osteoblast U_b^{max}, is assumed to be equal to 0.008. On the interval $[\psi_1, \psi_2 - \delta\psi]$, the differentiation rate into osteoblasts decreases monotonically to the value U^{min}, for which no osteoblasts will be formed within 63 *days*. This time period is chosen for the numerical simulations, in line with Vandamme et al. [94]. The region $[\psi_2 - \delta, \psi_2 + \delta\psi]$ is a 'transition region'. The function $U(\psi)$ changes its sign at the point $\psi = \psi_2$, and MSC's stop differentiating into osteoblasts, and start differentiating into fibroblasts for $\psi > \psi_2$. In other words, within the transition region, MSC's change the 'direction' of differentiation. The value of 0.05 is estimated for the threshold ψ_2 [50]. Note, that for $\psi \in [\psi_2 - \delta, \psi_2 + \delta\psi]$, $U_b \le U^{min}$, $U_f \le U^{min}$, no osteoblasts and fibroblasts, and hence, no bone and fibrous tissue will appear after 63 *days*. This situation is biologically irrelevant. Therefore, the size of the transition region is chosen to be very small, and the following parameter value is used $\delta\psi = 10^{-4}$. The function $U(\psi)$ is very steep within the transition region, since it changes its value from U_{min} to $-U_{min}$ over a very small interval. For $\psi \in [\psi_2 + \delta\psi, \psi_3]$, the rate of MSC differentiation into fibroblasts increases to its maximum value $U_f^{max} = 0.1\ days^{-1}$, and then remains constant for $\psi > \psi_3$. It is assumed,

that $\psi_3 = 0.07$.

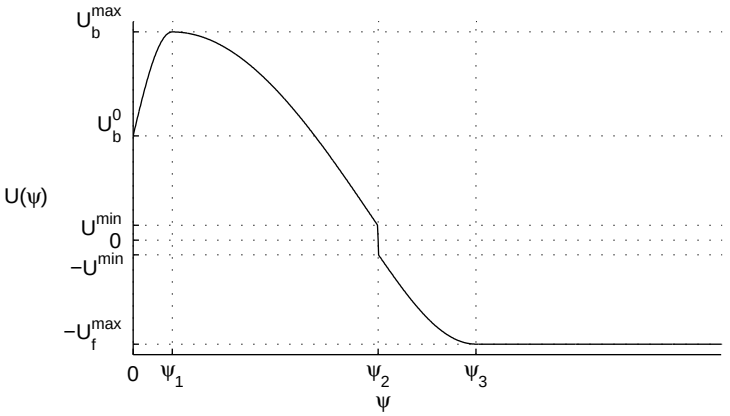

Figure 3.5: Plot of the function $U(\psi)$, related to the differentiation rate magnitude, versus mechanical stimulus ψ, defined in equation (3.25)

Equation (3.24) yields, that $V_b^{\psi\prime}(\psi) = V_b^{u\prime}(U_i(\psi))U_b'(\psi)$. The derivative $V_b^{\psi\prime}(\psi)$ has the same sign as the derivative $U_b'(\psi)$, if $V_b^{u\prime}(U_i(\psi)) > 0$. From Figure 3.5 it follows, that $U_i(\psi) \in [U^{min}, U_b^{max}]$, for $\psi \in [0, \psi_2 - \delta\psi]$. It is mentioned in this Section 3.3.2, that the function $v_b^{avg} = V_b^u(U)$ increases for $U \in [U^{min}, U_b^{extr}]$ (see Figure 3.4a). The value for U_b^{max} was defined earlier, which was smaller than U_b^{extr}. Hence, $[U^{min}, U_b^{max}] \subset [U^{min}, U_b^{extr}]$, and $V_b^{u\prime}(U_i(\psi)) > 0$ for $\psi \in [0, \psi_2 - \delta\psi]$. This means, that the function V_b^{ψ} behaves similarly to the function $U_b(\psi)$ on interval $\psi \in [0, \psi_2 - \delta\psi]$: V_b^{ψ} increases on $\psi = [0, \psi_1]$, has its maximum at $\psi = \psi_1$, and monotonically decreases to zero on the interval $\psi \in [\psi_1, \psi_2 - \delta\psi]$. For $\psi > \psi_2 - \delta\psi$, $U_b(\psi) < U^{min}$. As it is mentioned earlier, no osteoblasts will be formed till day 63 for such values of the differentiation rate U_b. Consequently, for these values of ψ, $V_b^{\psi}(\psi) = V_b^u(U_b(\psi)) = 0$.

Let us consider the behavior of the function $v_f^{avg} = V_f^{\psi}(\psi)$. For $\psi \in [0, \psi_2 + \delta\psi]$, $U_f(\psi) = -U(\psi) < U^{min}$ (see Figure 3.5). Hence, no fibroblasts will appear at day 63, and $V_f^{\psi}(\psi) = V_f^u(U_f(\psi)) = 0$. From equation (3.24) it is derived, that the derivative $V_f^{\psi\prime}(\psi)$ is equal to $V_f^{u\prime}(U_f(\psi))U_f'(\psi)$. On the interval $\psi \in [\psi_2 + \delta\psi, \infty)$ the function $U_f(\psi) = -U(\psi)$ takes values, which lie inside the interval

$$[U^{min}, U_f^{max}] \subset [U^{min}, U_f^{extr}].$$

For such values of $U_f(\psi)$, the derivative $V_f^{u\prime}(U_f(\psi))$ is positive, which follows from Figure 3.4b. Consequently, the function $V_f^{\psi\prime}(\psi)$ behaves similarly to the function $U_f(\psi) = -U(\psi)$ for $\psi > \psi_2 + \delta\psi$. It increases on the interval $\psi \in [\psi_2 + \delta\psi, \psi_3)$, and stays constant for $\psi \geq \psi_3$.

The functions $v_b^{avg} = V_b^{\psi}(\psi)$ and $v_f^{avg} = V_f^{\psi}(\psi)$ can be derived from the dependencies $v_b^{avg} = V_b^{u}(u)$, $v_f^{avg} = V_f^{u}(u)$, obtained from numerical solutions, and from the function $U(\psi)$, defined in equation (3.25). These functions are plotted in Figure 3.6. These plots are in line with the expec-

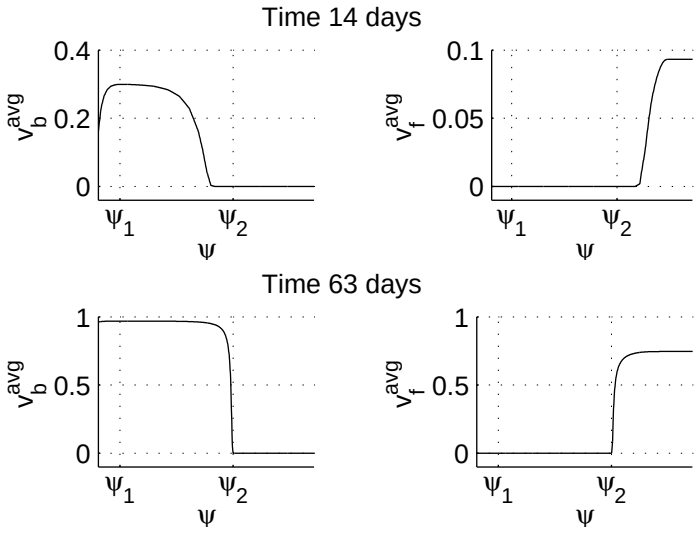

Figure 3.6: Plots of the functions $v_b^{avg} = V_b^{\psi}(\psi)$ and $v_f^{avg} = V_f^{\psi}(\psi)$ versus the mechanical stimulus ψ for time $t = 14$ *days* and $t = 63$ *days*. The functions are derived from the functions $V_b^u(u)$, $V_f^u(u)$, and $U(\psi)$, which were obtained earlier

tations. For the values of the mechanical stimulus ψ, lying in the interval $[0, \psi_2)$, bone formation takes place, and for $\psi \in (\psi_2, \infty)$, fibrous tissue forms. The largest amount of bone is expected for $\psi = \psi_1$. The promoting role of mechanical stimulation of the level ψ_1, if compared with no loading conditions $\psi = 0$, is more recognizable at early periods of bone regeneration. It is shown in Figure 3.6, that the amount of bone, corresponding to the stimulus value ψ_1 is by $\approx 50\%$ larger than for a zero mechanical stimulus at time $t = 14$ *days*.

3.4 Numerical simulations

A series of numerical simulations is carried out for the developed mechano-biological model. The chosen configuration of the bone-implant interface and the mechanical loading scheme correspond to those from the experiments by [94]. In the experiments, a perforated chamber is installed into the bone. The cylindrical implant is situated in the middle of the chamber. The perforations in the chamber allowed blood inflow and tissue growth from the surrounding area into the cavity of the chamber. The mechanical

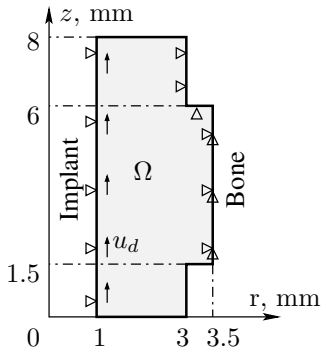

Figure 3.7: The axisymmetric physical domain Ω, and the boundary conditions for the displacements u_r and u_z, which determine the distribution of the mechanical stimulus within Ω

loading is applied by means of the axial movement of the implant inside the chamber.

This experimental study is chosen for the verification of the current mathematical model, due to the well controlled mechanical environment, achieved within the chamber. This is important for the present approach, since the field of the mechanical stimulus within the bone-implant interface is calculated, since it determines cell differentiation.

3.4.1 Model parameters and numerical method

The axisymmetric physical domain Ω, used for the present simulations, is sketched in Figure 3.7. The computational model is defined by the elastostatic equations in Navier-Cauchy's formulation and by equations (3.9), (3.14)–(3.19). Boundary conditions for the mechanical part of the model are shown in Figure 3.7. Constant vertical displacements of the magnitude u_d are specified on the surface, attached to the implant. Initial conditions for the cell densities and the tissue fractions are defined in (3.11), (3.21), and the boundary conditions are taken from (3.12) and (3.20). The following values for model parameters are chosen (according to [a]Moreo et al. [67] and [b]Andreykiv [7]):

$$D_c = 0.133\,\frac{1}{day}\,^{a},\quad D_f = 0.5\,\frac{1}{day}\,^{b},\quad A_c = 0.5\,\frac{1}{day}\,^{a},\quad A_b = 0.5\,\frac{1}{day}\,^{b},$$
$$A_f = 0.1\,\frac{1}{day}\,^{b},\quad \alpha_w = 0.1\,\frac{1}{day}\,^{a},\quad \gamma = 0.06\,\frac{1}{day}\,^{a},\quad \alpha_f = 0.06\,\frac{1}{day}\,^{b}.$$

For the limit cell density C the value of $10^6 cells/mm^3$ is chosen [11]. The procedure of obtaining the numerical solution is outlined in Figure 3.8. Mechanical properties of the interface tissue are determined by the mixture rule, according to the distribution of the various tissue fractions at time t_0.

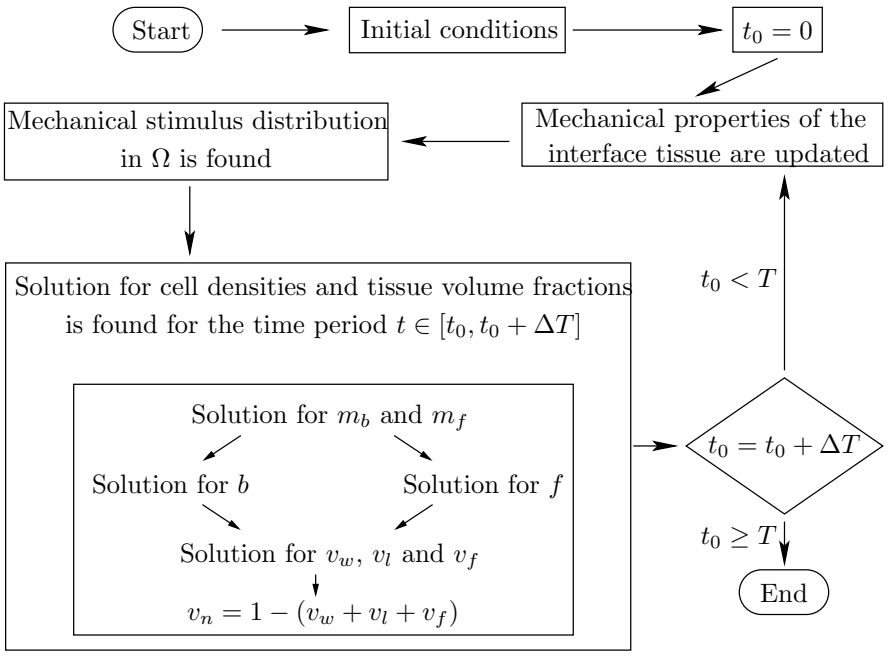

Figure 3.8: Outline of the method of the numerical solution

Elastic properties for the considered tissue types are given in Table 3.1 [39]. The mechanical stimulus field is found from the solution of the elastostatic

Table 3.1: Elasticity properties for the considered tissue types [39]

	Fibrin network	Woven bone	Lamellar bone	Fibrous tissue
Young's modulus (MPa)	0.2	1000	6000	1
Poisson's ratio	0.17	0.3	0.3	0.17

equations for the updated properties. Then, the solution for the biological part of the model is obtained. After time period ΔT, the mechanical properties are updated again. The cycle repeats, until $t_0 = T$. For the current simulations $\Delta T = 1$ *day* and $T = 63$ *days*.

The linear elasticity equations are solved by use of the finite element method. The equations for the evolution of MSC and fibroblasts densities contain advection terms. The finite volume method with the Koren flux limiter is used to discretize the partial differential equations (3.9) and (3.15) in the physical space and in the differentiation state domain [48]. This method provides a converging non-oscillating non-negative numerical solution. The positiveness of the numerical approximation for the cell densities is critical for the present model. Negative densities could lead to negative tissue frac-

tions and, consequently, to negative mechanical properties and, finally, to the non-convergence of the solution. The Koren limiter for the flux at the cell interfaces is equivalent to the third-order upwind-biased discretization scheme for smooth solutions. Time integration is performed with use of the second order modified Euler's method.

The physical domain Ω is meshed with rectangular cells (i.e. finite elements or control volumes), with edge lengths $dx = 0.125\ mm$ and $dy = 0.25\ mm$. Twenty layers of the corresponding cuboid cells, with edge $da = 0.05$ along the a axis, constitute the grid in the domain $\Omega \times [0, 1]$. Axial symmetry of the physical domain Ω is considered. The configuration of the region Ω is sketched in Figure 3.7. The discretized ordinary differential equations are integrated by means of the second-order explicit modified Euler's method.

3.4.2 Numerical results

The numerical simulations are carried out for different loading regimes, which are applied by specifying constant vertical displacements u_d on the implant surface (see Figure 3.7). Four levels of the displacements are considered: $u_d = 0\ mm$, $u_d = 0.03\ mm$, $u_d = 0.09\ mm$ and $u_d = 0.24\ mm$. The spatial distribution of new bone matrix differs for the four considered cases, as it follows from Figure 3.9.

First, the numerical solutions for the displacements $u_d = 0\ mm$ and $u_d = 0.03\ mm$ are considered. Due to the chosen relations for the differentiation rates of MSC's, no displacements imply a zero mechanical stimulus and a uniform value 0.1 day^{-1} of the differentiation rate u_b within the entire bone-implant interface. The tissue deformations, corresponding to the displacements of the implant with magnitude $0.03\ mm$, are small enough throughout the whole simulation period, so that the differentiation rate u_b is always positive (see Figure 3.10). This means, that in the considered cases, all MSC's differentiate only into osteoblasts. Hence, no fibrous tissue is formed in the peri-implant interface for the implant displacements $u_d = 0\ mm$ and $u_d = 0.03\ mm$. In the present model it is assumed, that a low level mechanical loading enhances differentiation into osteoblasts. Therefore the differentiation rate u_b for the case $u_d = 0.03\ mm$ is in general higher than in the case $u_d = 0\ mm$, when $u_b = 0.1\ day^{-1}$ (Figure 3.10). This leads to an earlier appearance of osteoblasts within the bone-implant interface for the displacements of the magnitude $0.03\ mm$. Hence, bone formation starts earlier in the case $u_d = 0.03\ mm$ compared with no loading conditions (see Figure 3.9). Another difference between the two considered levels of the loading, is the spatial distribution of new bone matrix. For the zero implant displacement case, the volume fraction of bone is larger near the implant surface than near the old bone surface for $t \geq 12\ days$, and the bone volume fraction is larger near the old bone surface for the displace-

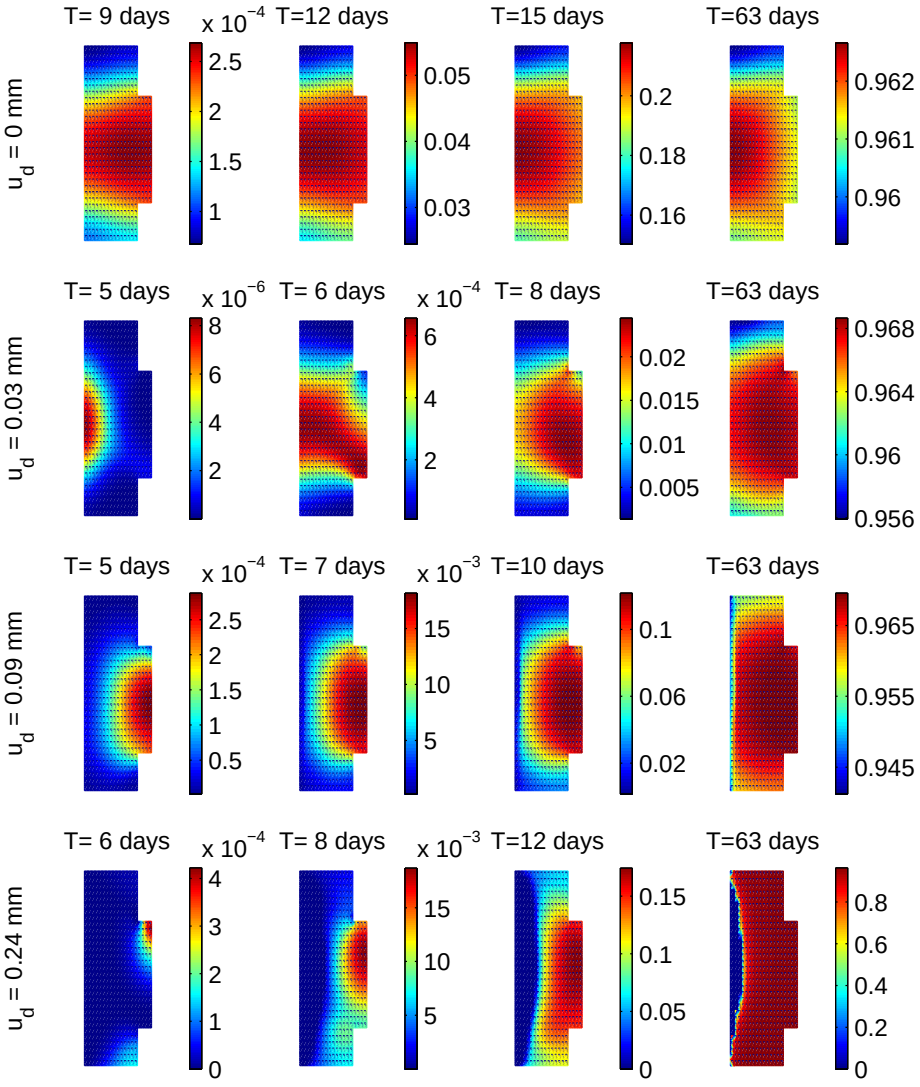

Figure 3.9: Plots of the volume fraction of woven and lamellar bone $v_w + v_l$ in the peri-implant interface at different time moments for the implant displacements of the magnitude u_d equal to 0 mm, 0.03 mm, 0.09 mm and 0.24 mm

ments $u_d = 0.03\ mm$ for $t \geq 7\ days$. The different spatial distribution of bone results from the respective behavior of cells.

At the first place, it should be mentioned, that the MSC's originating from the bone surface initially have a differentiation level close to zero. These cells start to differentiate into osteoblasts and, simultaneously, migrate towards the implant. The migration of MSC's takes place due to the higher MSC density at the bone surface at a low maturation level, which is provided by the inflow of MSC's, specified at this boundary (see Figure 3.11). While MSC's approach the implant surface, their maturation level increases. Hence, the average maturation level a_{avg} of the MSC's is higher near the implant surface, than near the old bone surface (Figure 3.12). Due to a lower total cell density at the implant interface, MSC's proliferate faster in this region, since the proliferation rate is assumed to be equal to $A_c(1-c_{tot})$. The maturation level of daughter cells is assumed to be equal to the maturation level of their mother cell. Therefore, it is possible, that at some time moment a number of MSC's with a high maturation level becomes larger near the implant surface than near the old bone surface. This results in a higher density of osteoblasts and in a faster formation of bone near the implant. Such a behavior is predicted for the case $u_d = 0\ mm$.

As it was mentioned earlier, the differentiation rate u_b is higher for the displacements $u_d = 0.03\ mm$, compared with no mechanical loading conditions. Therefore, MSC's undergo fewer divisions till the moment, when osteoblasts appear within the healing site and active bone formation starts. Despite the fact, that the average maturation level a_{avg} is lower at the old bone surface (Figure 3.12), the total number of MSC's with high maturation level will be larger, due to a much larger total density of MSC's in the considered region compared with the area close to the implant surface (Figure 3.11). The effect of the MSC source at the old bone surface prevails over the effect of a higher proliferation rate near the implant surface. As a result, the volume fraction of bone is higher near the old bone in the case $u_d = 0.03\ mm$.

In a similar way, the bone volume fraction is larger near the old bone surface for the implant displacements of the magnitude $0.09\ mm$. However, in this case a delayed bone formation on the implant surface is predicted. As it follows from Figure 3.9, new bone matrix starts to form approximately at day 5 predominantly in the region adjacent to the old bone surface. The effective tissue stiffness increases significantly in this region. The gradient of the tissue stiffness leads to the localization of deformations near the implant surface. Thereby, high values of the mechanical stimulus appear near the implant surface at day 6 (Figure 3.13). These values correspond to negative values of the differentiation rate u_b. This means that MSC's start to differentiate into fibroblasts, i.e. $u_f > 0$. The number of osteoblasts grows slowly, compared with the neighboring region, where $u_b > 0$ and a large source of osteoblasts is provided by differentiating MSC's. This leads to a

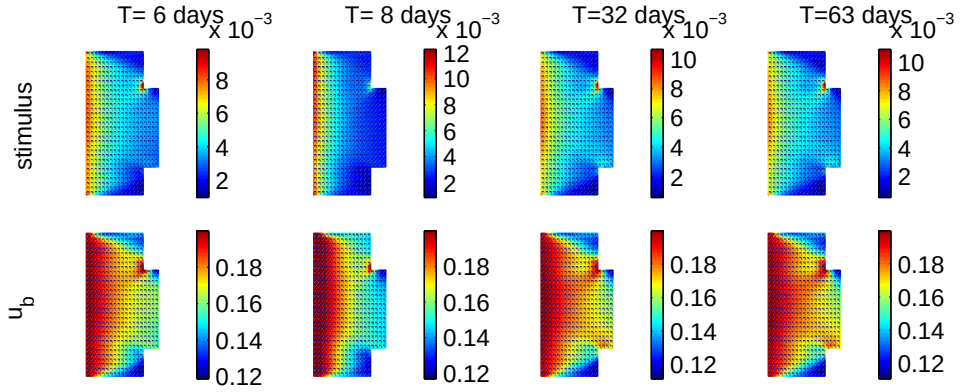

Figure 3.10: Plots of the mechanical stimulus and of the differentiation rate u_b in the peri-implant interface at different time moments for the implant displacements of the magnitude u_d equal to 0.03 mm

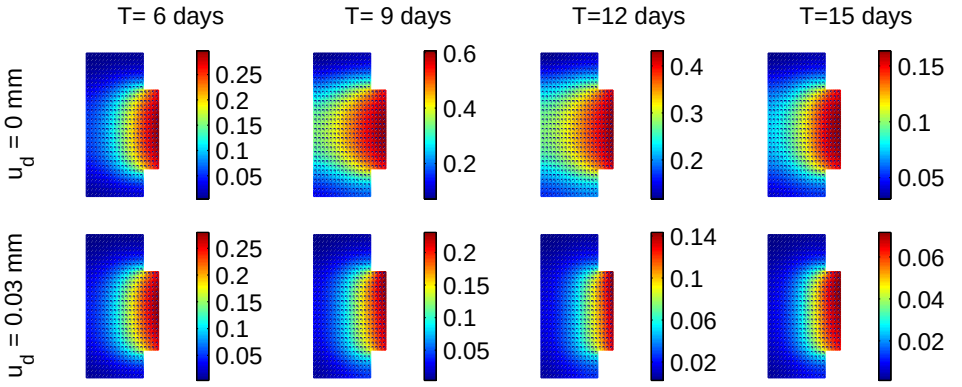

Figure 3.11: Plots of the total density of MSC's, which is calculated as $\int_0^1 (c_b + c_f) da$, in the peri-implant interface at different time moments for the implant displacements of the magnitude u_d equal to 0 mm and 0.03 mm

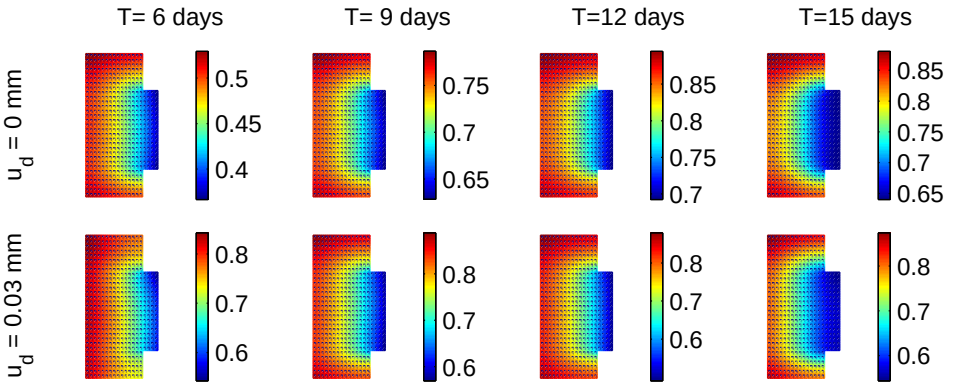

Figure 3.12: Plots of the average maturation level a_{avg} of MSC's, which is calculated as $a_{avg} = \left(\int_0^1 c_f\ (-a)\ da + \int_0^1 c_b\ a\ da\right) / \int_0^1 (c_b + c_f)\ da$, in the peri-implant interface at different time moments for the implant displacements of the magnitude u_d equal to 0 mm and 0.03 mm

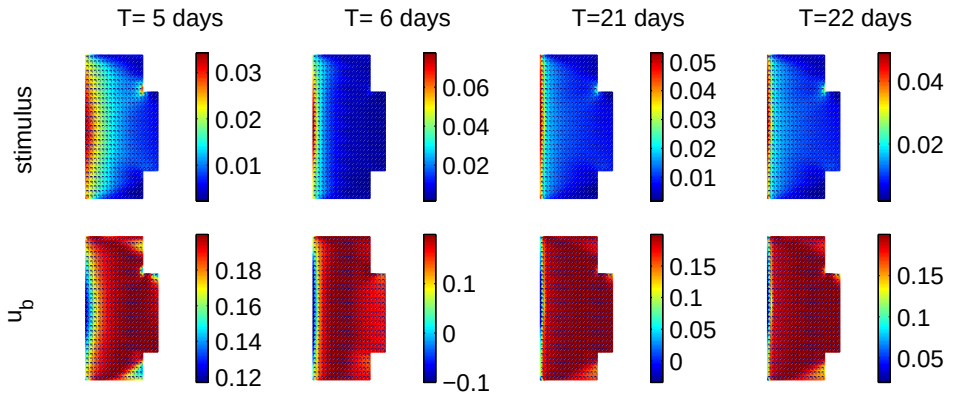

Figure 3.13: Plots of the mechanical stimulus and of the differentiation rate u_b in the peri-implant interface at different time moments for the implant displacements of the magnitude u_d equal to 0.09 mm

narrow zone next to the implant surface with a lower volume fraction of bone, which is well recognizable in Figure 3.9.

The zone, where $u_f > 0$, which is equivalent to $u_b < 0$, and where MSC's differentiate into fibroblasts, is narrow. Due to random walk of cells, this region is densely populated by the MSC's with a high level of differentiation into osteoblasts, which migrate from the neighboring part of the peri-implant interface, where $u_b > 0$ (see Figure 3.14). MSC's, which differ-

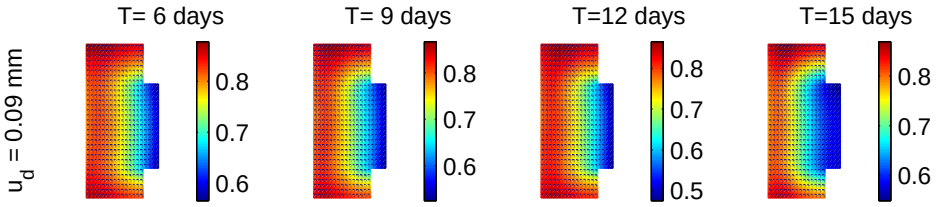

Figure 3.14: Plots of the average maturation level a_{avg} of MSC's, which is calculated as $a_{avg} = \left(\int_0^1 c_f\ (-a)\ da + \int_0^1 c_b\ a\ da\right) / \int_0^1 (c_b + c_f)\ da$, in the peri-implant interface at different time moments for the implant displacements of the magnitude u_d equal to 0.09 mm

entiate into fibroblasts within this narrow zone, migrate in their turn into the neighboring region, and the direction of their differentiation is reversed to osteoblasts again. Active cell diffusion and a limited time period (approximately 16 days), when $u_f > 0$ at the implant surface, lead to that no fibroblasts are derived from MSC's near the implant surface and no fibrous tissue is formed for the displacements of the magnitude $u_d = 0.09\ mm$.

Large implant displacements of the magnitude $u_d = 0.24\ mm$ lead to high values of the mechanical stimulus near the implant surface, which correspond to a positive differentiation rate u_f (Figure 3.15). The region, where $u_f > 0$ is larger compared with the analogous region, which appears for 0.09 mm displacements. A larger size of the region leads to smaller values of the gradient of the density of MSC's differentiating into fibroblasts. Hence fewer MSC's migrate away from this region and more MSC's differentiate continuously into fibroblasts. As a result, a non-zero density of fibroblasts is predicted in the middle of the implant interface at day 15 (Figure 3.15). Therefore, fibrous tissue is produced by fibroblasts and no bone formation is predicted near the implant surface for the displacements $u_d = 0.24\ mm$. In the rest of the peri-implant interface the volume fraction of bone is close to one at day 63 (Figure 3.9). It should be noted, that the calculated density of fibroblasts is much lower than the density of osteoblasts. From Figure 3.16a it follows that the average density of osteoblasts is equal to 0.82 mm^{-3} at day 63. While the maximal density of fibroblasts is 0.024 mm^{-3} at the same time moment (Figure 3.15). The density f is low, since the region, where

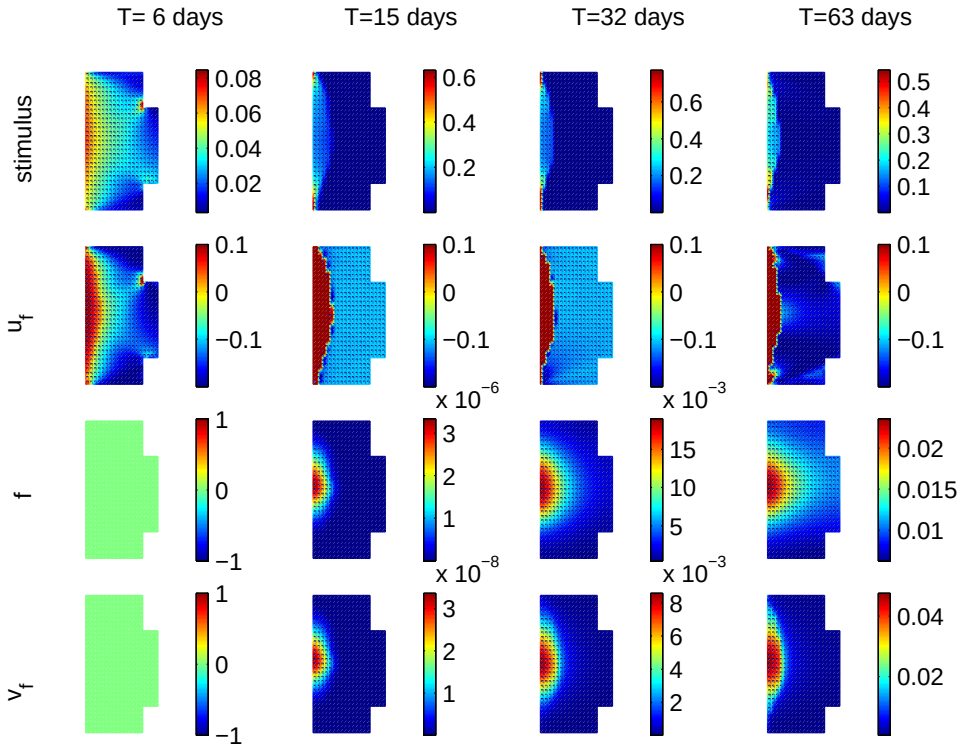

Figure 3.15: Plots of the mechanical stimulus, of the differentiation rate u_f, of the fibroblast density f and of the volume fraction of fibrous tissue v_f within the peri-implant interface at different time moments for the implant displacements of the magnitude $u_d = 0.24\ mm$

$u_b > 0$, occupies the most part of the peri-implant interface. It is even more important, that $u_b > 0$ near the old bone surface, where the total density of MSC's is the highest, due to the cell influx from the boundary surface during the first two weeks. This leads to a high proportion of MSC's differentiating into osteoblasts even in the regions, where $u_f > 0$ (Figure 3.14), and few MSC's differentiate into fibroblasts completely, as it is explained in the previous paragraph.

Therewith, the evolution of the average density of osteoblasts and of the bone volume fraction is shown in Figure 3.16. The average number of osteoblasts is maximal for the displacements $u_d = 0.03\ mm$ and $u_d = 0.09\ mm$ (Figure 3.16a), due to high differentiation rates of MSC's into osteoblasts within the entire bone-implant interface, excluding a very small area near the implant surface for $u_d = 0.09\ mm$ (see Figures 3.10 and 3.13). Hence, the average volume fractions of the bone tissue for this loading regimes are highest among the considered implant displacements (Figure 3.16b). At the end of the simulation period, the average amount of new bone tissue is comparable for the displacements $u_d = 0\ mm$, $u_d = 0.03\ mm$ and $u_d = 0.09\ mm$, and it is larger than for the large displacement conditions $u_d = 0.24\ mm$ (Figure 3.16b).

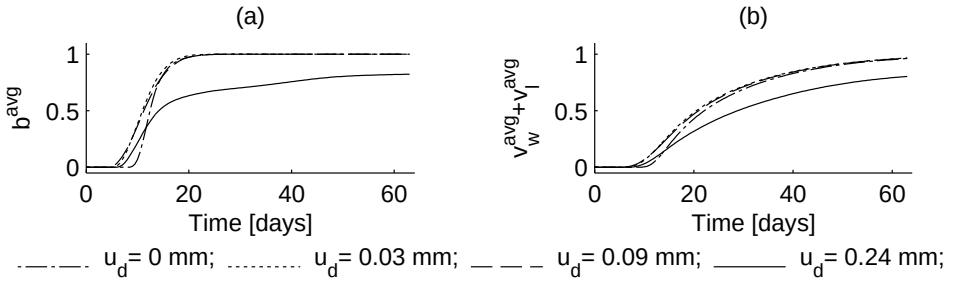

Figure 3.16: Plots of the average density of osteoblasts b^{avg} (a) and of the average volume fraction of woven and lamellar bone $v_w^{avg} + v_l^{avg}$ (b) against time. Averaging is introduced with respect to a spatial distribution

Vandamme et al. [94] determined the area fraction of bone tissue, averaged over the transverse sections, made at the level of the perforation in the bone chamber, after 9 weeks from the beginning of the experiments. In the experiments, where the implant was not loaded, they obtained the bone area fraction (BAF) of 0.6403 ± 0.2381 (mean value $\pm$ standard deviation). For the displacements of the implant of the magnitude $0.03\ mm$ and $0.09\ mm$, the measured values of BAF were 0.7509 ± 0.2149 and 0.7347 ± 0.2229, respectively. From the statistical analysis, Vandamme et al. [94] derived, that the bone area fraction was significantly higher for $0.09\ mm$ implant displacement compared with no displacement, and a significantly higher fraction of bone trabeculae was found for 0.03 and $0.09\ mm$ implant displacement

compared with the unloaded situation.

The calculated values of the bone volume fraction are higher than the values obtained in the experiments. The numerical simulations yield, that the average values of the volume fraction of woven and lamellar bone in the region of peri-implant interface, located at the level of the perforation, i.e. for $r \in [1, 3.5]$, $z \in [1.5, 6]$ (see Figure 3.7), are equal to 0.961, 0.968 and 0.967, for the implant displacements of the magnitude 0 mm, 0.03 mm and 0.09 mm, respectively. From Figure 3.17 it follows, that the average volume fraction of bone is lower for the displacements $u_d = 0$ mm compared with the displacements $u_d = 0.03$ mm and $u_d = 0.09$ mm. This difference is the largest at the initial period of bone formation (3-4 weeks). Therefore, the

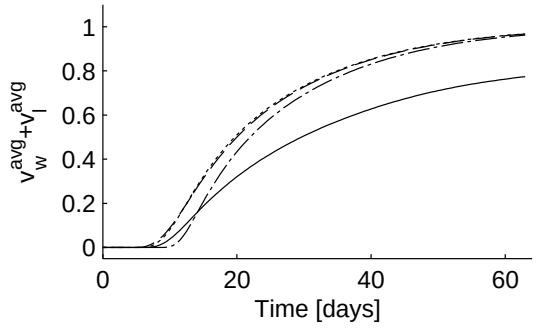

Figure 3.17: Plots of the average volume fraction of woven and lamellar bone $v_w^{avg} + v_l^{avg}$ in the region of peri-implant interface, located at the level of the perforation, against time

numerical and experimental results are in partial agreement qualitatively for the considered levels of the implant displacements. The displacements equal to 0.24 mm lead to the appearance of fibrous tissue. This is in line with Assumption 3.2 concerning the mechanoregulation of tissue regeneration. A weak quantitative correspondence of the model predictions to the experiments can be explained by the fact, that the current model is constructed in a rather simple form, since the main interest in this chapter, is the representation of cell differentiation as a gradually evolving process, although several over biological processes like proliferation, motility and bone formation are modeled using classical formalisms.

3.5 Discussion and conclusions

In this chapter a model for peri-implant osseointegration is proposed, in which MSC differentiation is considered as an evolutionary process that is

influenced by the mechanical state in the region of tissue formation. The main distinction of the current model for peri-implant osseointegration is in the description of the differentiation of cells. MSC's are distinguished with respect to their differentiation state. The differentiation state is evaluated through the variable a, which takes a value from zero to one. In the common approach, used in the most of the recent models for bone regeneration, the differentiation level of MSC's is not considered and cell differentiation is introduced into the constitutive equations by means of the reaction term. This can be interpreted, that only one state of the MSC's is considered. Therefore, the evolutionary differentiation approach can be considered as continuous, and the common immediate differentiation approach, as discrete. The continuous approach is likely to describe the process of cell differentiation more accurately, than the discrete model. It assigns a finite time of differentiation to each cell, which is in line with experimental observations [13, 60, 97], where cells gradually obtain the new properties in the course of time. The history of cell differentiation is incorporated, so that the current state of cells depends on how the cells evolved before. In the discrete approach the differentiation history or path cannot be modeled (see Remark 3.2).

Reina-Romo et al. [83] applied the concept of cell plasticity in the model for the bone distraction. However, in this chapter a *generic mathematical model* is defined, which allows to consider cell differentiation, as a process that evolves in time. The current approach can be extended to an *arbitrary* number of parameters, which determine the differentiation rates of MSC's, and to an arbitrary number of cell types, into which MSC's differentiate. The mathematical model for evolutionary cell differentiation is presented by means of a set of partial differential equations, boundary and initial conditions. The MSC differentiation is introduced into the model by adding one extra dimension to the problem domain. The differentiation rates are considered as functions of a number of parameters. A specific representation of the differentiation of fully non-differentiated MSC's poses some conditions on the differentiation rates.

Unfortunately, an example of an application, that is useful to directly validate the present model for the evolution of the differentiation level of cells, was not found. Instead, the present differentiation approach is incorporated into a model for peri-implant osseointegration. This model allows to demonstrate the main characteristics of the evolutionary approach. The history of MSC differentiation into two cell types is included in the model, and it is determined by the mechanical environment within the tissue. The present application example also shows, how the current differentiation approach can be used to represent cell differentiation, coupled with cell migration and proliferation, in one model.

It is assumed, that a low and moderate level of mechanical loading promotes bone formation, whereas a high level of loading leads to the appearance of the fibrous tissue within the bone-implant interface. On the basis

of these assumptions and on the basis of the numerical assessment for the 1D test problem, certain expressions for the differentiation rates of MSC's are specified (see equations (3.22)– (3.23), (3.25)). The essential feature of these relations, is that the differentiation rates u_b and u_f do not exceed certain thresholds U_b^{extr} and U_f^{extr}, which are determined in 1D simulations. This condition ensures, that the amount of a certain tissue type increases with the increment of the rate of differentiation of MSC's into a respective cell type. The simulations of peri-implant osseointegration within the bone chamber are carried out for four levels of loading.

The obtained results are in a partial correspondence with the experimental measurements, presented in Vandamme et al. [94]. Different paths of bone formation are obtained for different levels of displacements. For no loading conditions, new bone matrix is formed faster at the implant surface, while for the displacements of the magnitude 0.03 mm, 0.09 mm and 0.24 mm bone is released faster at the old bone surface. These two modes of bone formation are usually referred to as *contact* and *distance* osteogenesis. Moreo et al. [67] and Amor et al. [6] use their models for peri-implant osseointegration to study the situations, when contact and distance osteogenesis occur. They related the two different paths of bone regeneration to a micro-roughness of the implant surface. This assumption is in line with the experiments of Abrahamsson et al. [1]. The implant micro-roughness is represented into the models implicitly by means of various growth factor sources at the implant surface, that correspond to the growth factor release by activated platelets.

The predictions of the present model about different osseointegration modes follow from a coupled effect of MSC differentiation, migration and proliferation. The present model should be extended, in order to represent the conditions providing contact and distance osteogenesis in a more strict and clear way. This can be done, by adding a growth factor concentration variable into the model. A more complex model is not considered in the present chapter, since the focus of the current study is on evolutionary cell differentiation approach. The current peri-implant osseointegration model is used, to check the performance of the evolutionary approach as a part of a more general bone regeneration model.

As another potential direction of the model improvement, a variation of the mechanoregulatory relations for the differentiation rates, and a modification of the mechanical stimulus can be considered. For example, dynamical mechanical loading may be considered, and the tissue within the peri-implant interface may be introduced as a poro-elastic media. Another option, is to consider differentiation of cells as a partly stochastic process, for example, by introducing a random variable into the relations for the differentiation rate. In this chapter the evolution of the differentiation process is introduced. Considering cell proliferation as an evolutionary process, can also be a following step in improving the given model.

One feature of the evolutionary differentiation approach, which can be used to enhance the accuracy of the future models for bone regeneration, is the finite time of cell differentiation. In reality, new bone appears in the peri-implant interface after some time from the implant placement. For example, in the experiments of Berglundh et al. [14] and Abrahamsson et al. [1], bone matrix started forming on the pre-existing surfaces at the end of the first week. This fact can be modeled with use of the evolutionary differentiation approach. Due to a finite time of differentiation, osteoblasts, which release bone matrix, can be assumed to appear after some time from the implant placement. This issue cannot be modeled with the immediate differentiation approach, since for this approach, bone would appear immediately.

The present differentiation representation is incorporated into a moving boundary model, which is described in Chapter 4. For that model it is essential, that the time of differentiation of MSC's into osteoblasts is finite. This condition is satisfied by the present evolutionary approach.

CHAPTER 4

Moving boundary model for endosseous healing

In this section, a model for the early stages of peri-implant bone regeneration is developed. This model is able to capture some important characteristics of endosseous healing, which are not incorporated in the existing models. It is a well known fact, that during peri-implant osseointegration, bone forms only by apposition on a pre-existing rigid surface, which initially consists of the implant surface and the old bone surface. In order to track the movement of the front of the newly formed bone, a moving boundary problem is formulated. Another important feature of the current model, is that cell differentiation is considered as a gradual process, evolving in time and being influenced by the presence of growth factors. Hence the evolution of cell differentiation level is captured in the present approach.

Some of the model parameters are taken from the literature and the rest of them is estimated from numerical simulations. The numerical algorithm, developed for the solution of the model equations within a two dimensional physical domain, is described in Chapter 5. This algorithm allows to solve the model equations within an irregular domain, which evolves in time. In the current chapter, only some general features of the numerical method are outlined. A large number of numerical simulations is introduced, in order to estimate the values of the model parameters. Results of the numerical solutions are compared with experiments.

4.1 Introduction

Bone regeneration around implants and the ways of improving early mechanical stability of the implants have been investigated by many researchers

recently. A number of experimental in-vivo and in-vitro studies are available in the literature [1, 14, 65, 80, 92, 93, 94]. The peri-implant endosseous healing consists of the cascade of biological processes, which take place within the healing site after the implant placement [24, 63]. In Davies [24], the four stages of implant osseointegration are distinguished. At the first stage, *haemostasis*, right after the placement of the implant into the bone, the wound site is filled with blood and a blood clot forms. At this stage blood platelets attach to the implant surface, and after being activated they start to release cytokines and growth factors. The second stage, referred as *osteoconduction*, involves recruitment and migration of differentiating osteogenic cells to the implant surface. At the third stage, named *de novo bone formation*, osteogenic cells differentiate into osteoblasts, which start to release bone matrix at the implant surface. This bone formation occurs in the form of intramembranous ossification. New bone matrix is released by osteoblasts, attached to a rigid surface [1, 14, 65]. In other words, peri-implant ossification occurs through a direct apposition of new bone matrix on the pre-existing surface [24]. Hence the concept of the newly formed bone front or surface can be used. Due to the synthesis of bone, the bone front moves into the region of the non-ossified tissue. In the case of successful osseointegration, a direct structural and functional fixation of the implant within the new bone matrix is established.

Two modes of the bone front movement, called distance and contact osteogenesis, can be distinguished. For the first mode, bone forms initially at the old bone surface, and the bone front moves towards the implant surface. The contact osteogenesis corresponds to the situation, when new bone matrix is released by osteoblasts at the implant surface itself, and the front of newly formed bone moves from the implant towards the old bone surface. In this case, the implant surface turns to be in a direct contact with newly formed woven bone. Bone synthesis, taking place both at the old bone surface and at the implant surface, leads to a faster biological anchorage of the implant, compared to distance osteogenesis mode [1, 32]. Therefore, contact osteogenesis provides better mechanical stability of the implant at the early stages than distance osteogenesis.

The osteoconduction phase is critical for the contact osteogenesis mode. Synthesis of bone at the implant surface is possible, only if enough differentiating osteogenic cells are present near the implant, i.e. it is necessary, that osteogenic cells migrate constantly from the old bone surface towards the implant through the fibrin network, formed in the blood clot.

Therefore, the first three stages of osseointegration result in the formation of woven bone, which provide the biological fixation of the implant. The fourth stage in peri-implant osseointegration is remodeling of the woven bone into mature bone. The process of remodeling is slow, compared to the processes, involved in the first three stages. In the present work, the second (osteoconduction) and third (*de novo* bone formation) stages of

osseointegration are considered. Bone remodeling, which follows after the woven bone formation, is not considered in the current model. According to Davies [24], osteoconduction and *de novo* bone formation are the crucial stages of osseointegration, since exactly at these phases, the implant is anchored within the wound site by the newly formed bone matrix. Without such biological anchorage, successful osseointegration is impossible.

The structure of this chapter is as follows. A brief review of several recent mathematical models for the peri-implant osseointegration is given in Section 4.2.

The new model for the early stages of peri-implant bone regeneration is developed in Section 4.3. The main innovation of this model is the moving boundary approach, used to represent the movement of the bone-forming surface. It is derived to accommodate the aforementioned fact that bone only forms by apposition on the pre-existing rigid surface [24]. The peri-implant region is divided into two domains: the first domain is occupied by the soft tissue, and the second domain is filled with the new bone. The evolution of the osteogenic cell density and of the growth factor concentration within the first domain is modeled with partial differential equations. The number of mature osteogenic cells and the concentration of growth factor at the bone-forming surface, which is the boundary of the soft tissue domain, determines the rate of new bone matrix release, and consequently the velocity of the bone-forming surface. Within the region, filled with new bone, the process of bone remodeling takes place, which is not considered in this work. Cell differentiation is considered as a gradual process, which depends on the growth factors concentration. The approach, derived in Chapter 3, is used to model the evolution of the cell differentiation level.

Some basic features of the 2D numerical algorithm are outlined in Section 4.4.1. A model validation procedure and initialization of the parameters are described in Section 4.4.2. In Section 4.4.3, a sensitivity analysis based on the results of numerical simulations for various model parameters is presented. The main results of the numerical simulations are discussed in Section 4.5. Conclusions are drawn in Section 4.6.

4.2 Recent mathematical models

Mathematical modeling is a useful tool for the investigation of peri-implant osseointegration. It allows to study the role of various processes, which take place during bone regeneration under the influence of numerous external and internal factors. Mathematical models for bone regeneration around endosseous oral implants were developed by Amor et al. [5, 6], Moreo et al. [67]. Moreo et al. [67] reported that their model is able to predict different modes of bone regeneration (i.e. contact and distance osteogenesis), depending on the degree of adhesion and activation of the blood platelets at the

implant surface, which is related to the implant surface micro-structure.

Amor et al. [5] used the model by Bailon-Plaza and van der Meulen [11], initially created for bone fracture healing, and adapted it to model peri-implant osseointegration. An enhanced model was presented in [6], where the implant surface micro-structure is taken into account, which determines the mode of osteogenesis (distance or contact).

In the models by Amor et al. [6] and Moreo et al. [67], the platelet density, osteogenic cell and osteoblast densities, soft (fibrous) tissue and bone tissue volume fractions, and growth factor concentration are considered as unknown functions in space-time coordinates. Moreo et al. [67] defined two generic types of growth factors. The growth factors, related to the first type, are released by activated platelets (e.g. platelet-derived growth factor (PDGF), transforming growth factor beta (TGF-β), etc.). The growth factors, related to the second generic type, are released by osteogenic cells and osteoblasts (bone morphogenetic proteins (BMPs), TGF-β, etc.). Both growth factor types cause chemotaxis of osteogenic cells and promote proliferation of osteogenic cells, while the first one enables differentiation into osteoblasts, and the second one enables bone formation.

Amor et al. [6] consider both mentioned growth factor types through one unknown variable. In this model, growth factors cause chemotaxis of osteogenic cells. Osteoblast differentiation is assumed to take place only under the presence of growth factors.

Moreo et al. [67] distinguish woven and lamellar bone, while Amor et al. [6] consider just one variable for the bone tissue volume fraction. The model parameters, boundary and initial conditions, proposed for both models differ and some of them – even considerably. Nevertheless, these two models have much in common. In particular, they were constructed to study different paths of bone regeneration around endosseous implants, depending on the implant surface micro-structure. The models are capable to predict contact and distance osteogenesis mode. The switch mechanism between these two modes is introduced in the models by means of the activated platelet density. The adhesion of platelets is assumed to depend on the implant surface roughness. Platelets produce growth factors, and growth factor concentration determines osteoblast differentiation and bone tissue synthesis. Bone matrix release is proportional to the osteoblast density and ceases, if the volume fraction of bone tissue exceeds one. It follows that bone is synthesized by osteoblasts wherever these cells are found. It is also confirmed by the simulation results, that were reported in Amor et al. [6] and Moreo et al. [67], that bone forms throughout the whole interface region simultaneously. However, it is released faster in the vicinity of old bone and implant surface, under certain conditions.

4.3 Moving boundary model

The ideas and approaches, proposed by Moreo et al. [67] and Amor et al. [6], are used partially as the basis, on which the present model is built. The principal innovations are introduced in the current model, which allow to reflect some important characteristics of peri-implant osseointegration. These characteristics are taken from three basic principles, formulated by Davies [24], which are literally quoted.

Hypothesis 4.1. ***Principles for endosseous healing***

1. *"bone matrix is synthesized by only one cell: the osteoblast", and "the osteoblast is irrevocably attached to the bone-forming surface";*

2. *bone can only be deposited by laying down matrix on a pre-existing solid surface. ... the osteoblast is incapable of migration away from the bone surface, and the only method by which this surface can receive further additions (beyond the synthetic capacity of a single osteoblast) is by the recruitment of more osteogenic cells to the surface, which then differentiate into secretorily active osteoblasts;*

3. *bone matrix mineralizes and has no inherent capacity to "grow" . ... Thus, once bone formation has been initiated, the matrix and the cells that have synthesized that matrix have almost no ability to govern the ongoing pattern of bone growth on the implant surface.*

In line with the above hypotheses, the following variables for the new model are defined: the densities of immature and mature osteogenic cells (c_i and c_m, respectively), and the concentration of growth factor g.

4.3.1 Mature and immature cells

The concepts of immature and mature osteogenic cells are critical for the present model. First, it should be noted, that according to the stated principles for endosseous healing, the main characteristics of osteoblasts are that they are attached to the bone-forming surface and that they release bone matrix. Terms 'immature' and 'mature osteogenic cells' are used to introduce the differentiation of osteogenic cells in the model. Mature cells are these cells, which have reached such a level of maturation (differentiation threshold), that they are able to attach to the rigid surface and initiate bone matrix synthesis. In other words they are able to become osteoblasts. Mature osteogenic cells are mobile, until they become osteoblasts.

Immature cells have to undergo the differentiation path for some time, until they reach the differentiation threshold, and only after that they will

be able to become osteoblasts. The osteogenic cell differentiation is introduced in the model in the way it was proposed in Chapter 3. Immature osteogenic cells are distinguished according to their maturation level a (or 'differentiation level'), which ranges from 0 to 1, and which is considered as an additional independent coordinate in the problem domain. While an immature cell is differentiating into an osteoblast, its maturation level increases. If it reaches value 1, it is assumed that the cell has reached the differentiation threshold, and it becomes a mature osteogenic cell. This cell does not lose its mobility, as long as it has not become an osteoblast. Therewith, immature cell density c_i is defined as a number of cells per unit volume, per maturation level unit.

4.3.2 Modeling approach

Let the problem domain Ω be an approximation (e.g. in 1D, 2D or 3D) of the real geometry of a bone-implant interface. It is assumed that initially the whole peri-implant region is filled with soft connective tissue (fibrin network of blood clot). The domain boundary $\partial\Omega$ is composed of the implant surface $\partial\Omega_i$ and the old bone surface $\partial\Omega_b$, i.e. $\partial\Omega = \partial\Omega_i \cup \partial\Omega_b$. The initial density of osteogenic cells, and the initial growth factor concentration are equal to zero. A source of immature osteogenic cells and growth factors is assumed at the old bone surface $\partial\Omega_b$ (Figure 4.1). At the implant surface $\partial\Omega_i$, a source of

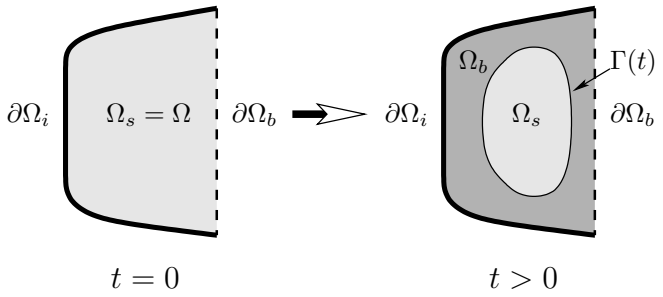

Figure 4.1: Sketch of the problem domain Ω. The old bone and implant surfaces are denoted by $\partial\Omega_b$ and $\partial\Omega_i$ respectively. Subdomains Ω_b and Ω_s correspond to regions within the healing site, filled with newly formed bone and soft tissue, respectively. They are separated by the bone-forming surface, denoted by $\Gamma(t)$. At $t = 0$, soft tissue occupies the whole peri-implant space $\Omega_s = \Omega$, and the bone-forming surface is composed of the implant interface and the old bone surface, i.e. $\Gamma(0) = \partial\Omega_i \cup \partial\Omega_b$

growth factor is considered, which corresponds to the release of growth factor by activated platelets, that are attached to the implant surface. Osteogenic cells, originating from the old bone surface, migrate into the peri-implant region, and differentiate into osteoblasts under the influence of growth factor.

Assume that at a certain time moment, there is a number of mature osteogenic cells within the healing site. Further, let some of them be situated at the rigid surface, which initially consists of the implant and old bone surface. It is assumed that these cells attach to the rigid surface and start releasing bone matrix. These cell functions are characteristic for osteoblasts. Hence it is assumed that mature osteogenic cells, situated near the rigid surface, immediately become osteoblasts. Due to bone production by the osteoblasts, the front of newly formed bone starts moving. This front forms the surface, onto which other mature cells can attach and synthesize bone matrix consequently, providing further bone front movement. The mobile bone-forming surface is the boundary between the soft tissue within the healing site and newly formed bone. In other words, the bone-forming interface, denoted as

$$\Gamma(t) \subset \overline{\Omega}, \quad t \geq 0, \qquad \text{and} \quad \Gamma(0) = \partial\Omega,$$

divides the computational domain Ω into two regions Ω_b and Ω_s, which are filled with bone tissue and soft tissue, respectively. Within region Ω_b, bone remodeling starts. This is a long term process, and the present model is developed for the second and third stages of bone regeneration. As it was mentioned before, bone remodeling is not considered in the current model. Therefore, no processes, which take place within subdomain Ω_b, are modeled. Though, it should be noted, that osteoblasts, trapped into the bone, become osteocytes.

According to the third principle for endosseous healing, the formation of new bone tissue within the peri-implant interface is governed by the processes, taking place within the region Ω_s. The following processes are considered in the present model:

1. osteogenic cell migration, caused by random walk and chemotaxis, directed towards the gradient of growth factor concentration;

2. osteogenic cell proliferation and differentiation;

3. growth factor diffusion and decay;

4. growth factor release by osteogenic cells and activated platelets.

The mathematical model consists of a set of partial differential equations (PDE's), boundary and initial conditions. The equations are specified for the unknown real-valued functions $c_i(\vec{x}, a, t)$, $c_m(\vec{x}, t)$ and $g(\vec{x}, t)$, defined for $\vec{x} \in \Omega_s$, $a \in [0, 1]$, $t \geq 0$, where $\vec{x}$ is the coordinate vector in physical space, a is the maturation level of the immature osteogenic cells, i.e. a is the coordinate in maturation or differentiation state domain, and t is time. The functions c_i, c_m and g represent densities of immature and mature osteogenic cells, and concentration of growth factor, respectively.

The evolution of unknown variables is determined by the following PDE's

$$\frac{\partial c_i}{\partial t} = \underbrace{-\nabla_s \cdot \left(-D_c \nabla_s c_i + \chi(g, c_{tot})\, c_i \nabla_s g\right)}_{Migration} - \underbrace{\frac{\partial}{\partial a}\left(u_b(g) c_i\right)}_{Differentiation} + \underbrace{A_c(g) c_i \left(1 - c_{tot}\right)}_{Proliferation}, \quad (4.1)$$

$$\frac{\partial c_m}{\partial t} = -\nabla_s \cdot \left(-D_c \nabla_s c_m + \chi(g, c_{tot})\, c_m \nabla_s g\right) + u_b(g) c_i(\vec{x}, 1, t) + A_c(g) c_m \left(1 - c_{tot}\right), \quad (4.2)$$

$$\frac{\partial g}{\partial t} = \underbrace{\nabla_s \cdot \left(D_g \nabla_s g\right)}_{Diffusion} + \underbrace{E_c(g)\left(c_m + \int_0^1 \gamma(a) c_i \, da\right)}_{Production} - \underbrace{d_g g}_{Degradation}, \quad (4.3)$$

where $c_{tot} = \int_0^1 c_i da + c_m$ is the total density of osteogenic cells per unit of volume. Equation (4.1) is defined for $(\vec{x}, a, t) \in \Omega_s \times [0,1] \times \mathbb{R}^+$, and equations (4.2), (4.3) for $(\vec{x}, t) \in \Omega_s \times \mathbb{R}^+$. Operator ∇_s is the nabla operator, defined in physical space, e.g. in 3D physical space

$$\nabla_s = \left(\frac{\partial}{\partial x_1}, \frac{\partial}{\partial x_2}, \frac{\partial}{\partial x_3}\right).$$

The parameter D_c is the diffusion coefficient of osteogenic cells. The terms $\chi(g, c_{tot}) c_i \nabla_s g$ and $\chi(g, c_{tot}) c_m \nabla_s g$ in equations (4.1) and (4.2) represent cell migration due to chemotaxis, where the coefficient $\chi(g, c_{tot})$ depends on the growth factor concentration and on the total density of osteogenic cells in the current location. Cell proliferation is introduced by the terms, that contain coefficient $A_c(g)$, which depends on growth factor concentration. It is assumed that a parent cell and the daughter cells, into which it divides, have the same level of maturation. The second term in the right-hand side of equation (4.1) represents the increase of maturation level of immature cells, due to cell differentiation (see also Chapter 3 for the derivation of this term). The parameter $u_b(g)$ is the differentiation rate (or maturation rate), and it depends on growth factor concentration. It can also be considered as the velocity of cell "motion" in the differentiation state domain. The term $u_b(g) c_i(\vec{x}, 1, t)$ in equation (4.2) corresponds to the increase of a number of the mature cells due to the differentiation of the immature cells. The terms in the right-hand side of equation (4.3) (in order from left to right) represent growth factor diffusion with constant coefficient D_g; growth factor production by cells with coefficient $E_c(g)$, depending on growth factor

concentration; and growth factor decay, respectively. It was assumed that growth factor is released by mature and immature osteogenic cells [25], and that its production depends on the maturation level of immature cells. The last mentioned assumption is introduced by the function $\gamma(a)$ under the integral sign.

The size and geometry of the subdomains change due to new bone formation. This process is introduced in the model by specifying the magnitude of the normal velocity v_n of the moving bone-forming surface $\Gamma(t)$. That is, the variable v_n denotes the normal component of the velocity of the points of the moving boundary, and is equal to the scalar product of the velocity vector and outward (with respect to domain Ω_s) unit normal of the boundary surface. The magnitude of the front normal velocity v_n is related to the amount of new bone matrix, produced locally per time unit. As it was mentioned, the new bone matrix is produced only by osteoblasts.

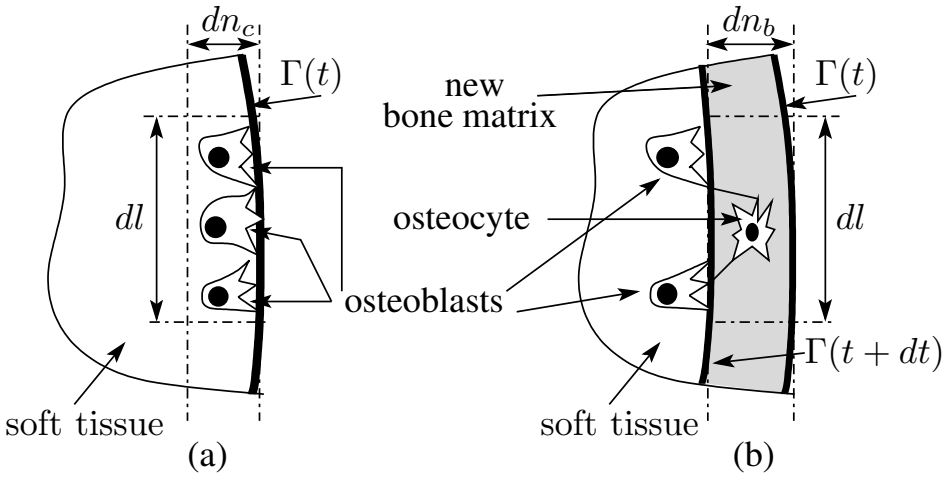

Figure 4.2: Sketch of the bone release by osteoblasts. First, mature osteogenic cells, situated within the distance dn_c from the boundary surface $\Gamma(t)$, attach to it and become osteoblasts (a). After that, osteoblasts release new bone matrix. Osteoblasts are trapped by the released bone matrix and become osteocytes (b). The width of the layer of new bone matrix, released in time dt, is denoted as dn_b

Let us consider a small segment of the boundary surface $\Gamma(t)$ of length dl (Figure 4.2a). Assume that mature osteogenic cells, situated within the distance dn_c from the boundary surface, attach to it and start to release bone matrix. In other words, these osteogenic cells become osteoblasts. A volume of bone matrix, produced by one osteoblast per unit of time, is denoted by parameter V_b. Then units of V_b is $\frac{volume\ units}{day \cdot cell}$. The number of osteoblasts, attached to the boundary segment dl is equal to $N_b = c_m\ dl\ dn_c$. These cells

will produce the bone matrix of the volume $dV = V_b\ N_b\ dt$ in time period dt. Since the new bone matrix is released, the bone-forming surface will change its location from $\Gamma(t)$ to $\Gamma(t + dt)$ (Figure 4.2b). The volume dV of new bone, laid down on the boundary segment dl, corresponds to the shift of the boundary element dl by distance $dn_b = \frac{dV}{dl}$ in normal direction, in time period dt. The normal velocity v_n is equal to the local shift of boundary in normal direction *per unit of time*. Hence

$$v_n = -\frac{dn_b}{dt} = -\frac{dV}{dl\ dt} = -\frac{V_b\ c_m\ dl\ dn_c\ dt}{dl\ dt} = -V_b\ dn_c\ c_m.$$

The minus sign appears, since the velocity v_n is considered along the *outer* normal, with respect to the region of soft tissue Ω_s, and quantity dn_b is the shift along the *inner* normal. A new parameter $P_b = V_b\ dn_c$ is defined, and the following relation for the normal velocity of the boundary is obtained:

$$v_n(\vec{X}, t) = -P_b\ c_m(\vec{X}, t), \quad \vec{X} \in \Gamma(t),\ t > 0, \tag{4.4}$$

where constant parameter P_b denotes the rate of the production of bone matrix by one osteoblast per unit of time, times the width of the layer of osteogenic cells, attached to the bone-forming surface. The parameter P_b has the units $\frac{[volume\ units]}{day \cdot cell}\ mm$. The expression (4.4) for the normal velocity of the moving boundary has been derived, in which the normal velocity is assumed to be proportional to the local density of the mature osteogenic cells.

Remark 4.1. The value of the parameter P_b will be estimated, based on the results of numerical simulations and on educated guesses. Parameters V_b and dn_c were used to explain the physical meaning of the parameter P_b and in the derivation of the relation (4.4) for velocity v_n. Further, parameters V_b and dn_c will not be used.

Remark 4.2. For convenience and computational efficiency, the considered cell densities and growth factor concentration are nondimensionalized with respect to a saturated cell density of $10^6\ \frac{cells}{ml}$, and typical growth factor concentration of $100\frac{ng}{ml}$ [11]. That is, variables c_i, c_m and g are dimensionless quantities. Consequently, the units of parameter P_b should be redefined as $\frac{mm}{day}$ (see equation (4.4)).

The initial position of the boundary is defined as:

$$\Gamma(0) = \partial\Omega_b \cup \partial\Omega_i. \tag{4.5}$$

The movement of the boundary is determined by its normal velocity, the expression for which is given in equation (4.4).

Remark 4.3. The term 'moving boundary problem' is used for the formulated equations, which constitute the present model. It is different from the

classical Stefan problem. The term 'moving boundary problem' is applied, since the partial differential equations within the evolving domain, which changes in time, are solved. The temporal evolution of the domain has to be determined as a part of the solution. Time-dependent problems of such type are called moving boundary problems (see for example the introduction to the monograph by Crank [22]).

The movement of the domain boundary, which corresponds to the ossification front, is given by equation (4.4). It is not derived from the principle of conservation of some quantity, as it is done in classical Stefan problems. Indeed, the ossification front moves due to the physical phenomenon, regulated by the osteogenic cells, in which these cells are located on the bone surface and deposit new bone matrix. Therefore, the domain boundary is gradually evolving due to the action of the cells. Some of these cells remain on the bone surface, whereas others are buried by the matrix as it is shown in Figure 4.2. Therefore, to describe accurately this phenomenon the temporal evolution of the bone surface is modeled. That is why it was assumed that the normal boundary velocity is proportional to the local concentration of mature osteogenic cells. The boundary motion is effected only by the local cell density at the boundary itself. Mature osteogenic cells do not release any bone matrix away from a rigid surface, and consequently, they do not have any influence on the movement of ossification front.

The idea of the limit concentration at the moving interface, which is often used in classical Stefan problems, is not applicable in the present model, since even a low concentration of cells will provide some slow advance of the ossification front.

As it was mentioned, the initial cell densities and growth factor concentration are assumed to be zero:

$$c_i(\vec{x}, a, 0) = 0,\ c_m(\vec{x}, 0) = 0,\ g(\vec{x}, 0) = 0, \quad \vec{x} \in \Omega,\ a \in [0, 1]. \tag{4.6}$$

The boundary conditions are derived from the following assumptions. The source of immature cells and of growth factor are considered at the old bone surface $\partial\Omega_b$ from $t = 0$ until time t_{cbone} and t_{gbone}, respectively. The time period t_{gbone} is set to 4 $days$ [6]. The other time parameter t_{cbone} is estimated from numerical simulations, based on sensitivity analysis, presented in Appendix A.1. The value $t_{cbone} = 1$ day is chosen. For $t > t_{cbone}$ and $t > t_{gbone}$, no source of osteogenic cells and of growth factor at the old bone boundary is assumed. As it was mentioned, during haemostasis phase, blood platelets attach to the implant surface, and after being activated, they start to release growth factors. This release of growth factor by activated platelets is represented in the current model by means of a boundary condition. The influx of growth factor is defined as a time-dependent function $g_{impl}(t)$. This function is supposed to decay exponentially [6]. Since it is assumed to decrease rapidly, the influx is set to zero for $\max(t_{cbone}, t_{gbone}) = 4$ $days$.

In the current model, the movement of the domain boundary is supposed to start after a certain time period, larger than $\max(t_{cbone}, t_{gbone}) = 4\ days$. Due to the boundary movement, a special treatment of the fluxes of the model variables is necessary. Mature osteogenic cells, adjacent to the bone-forming surface, are assumed to become osteoblast. Hence according to the principles for endosseous healing, they become immobile and are trapped by the newly formed bone. On the contrary, immature cells and growth factor are assumed to be pushed out by the moving surface, in a piston-like way (they are assumed not to be able to penetrate into the bone). According to these assumptions, the conditions for the fluxes of the model variables are set at the domain boundary. The derivation of the particular expressions is given in Appendix A.2.

Thereby, the boundary conditions are defined as follows:

$$\begin{cases} (-D_c\nabla_s c_i + \chi(g, c_{tot})c_i\nabla_s g)\,(\vec{X}, a, t)\cdot\vec{n}(\vec{X}, t) = 0, & \vec{X}\in\partial\Omega_i, \\ (-D_c\nabla_s c_i + \chi(g, c_{tot})c_i\nabla_s g)\,(\vec{X}, a, t)\cdot\vec{n}(\vec{X}, t) = -c_{bone}(a), & \vec{X}\in\partial\Omega_b, \end{cases} \tag{4.7}$$

for $a\in[0,1]$, $t\le t_{cbone}$;

$$(-D_c\nabla_s c_i + \chi(g, c_{tot})c_i\nabla_s g)\,(\vec{X}, a, t)\cdot\vec{n}(\vec{X}, t) = c_i(\vec{X}, a, t)\ v_n(\vec{X}, t), \tag{4.8}$$

for $a\in[0,1], \vec{X}\in\Gamma(t), t > t_{cbone}$;

$$(-D_c\nabla_s c_m + \chi(g, c_{tot})c_m\nabla_s g)\,(\vec{X}, t)\cdot\vec{n}(\vec{X}, t) = 0, \tag{4.9}$$

for $\vec{X}\in\Gamma(t), t > 0$;

$$-D_g\nabla_s g(\vec{X}, t)\cdot\vec{n}(\vec{X}, t) = -g_{impl}(t), \tag{4.10}$$

for $\vec{X}\in\partial\Omega_i$, $t\le\max(t_{cbone}, t_{gbone})$;

$$-D_g\nabla_s g(\vec{X}, t)\cdot\vec{n}(\vec{X}, t) = -g_{bone}, \qquad \vec{X}\in\partial\Omega_b,\ t\le t_{gbone}; \tag{4.11}$$

$$-D_g\nabla_s g(\vec{X}, t)\cdot\vec{n}(\vec{X}, t) = g(\vec{X}, t)\ v_n(\vec{X}, t), \qquad \vec{X}\in\Gamma(t), t > t_{gbone}. \tag{4.12}$$

In the above formulas, $\vec{n}(\vec{X}, t)$ is the unit outward normal of boundary $\Gamma(t)$ of subdomain Ω_s. The constant parameter g_{bone} and function $c_{bone}(a)$, respectively, represent the source of growth factor and of immature osteogenic cells at differentiation level a, both found at the old bone surface.

Let us denote the *total* influx of immature cells by parameter C_{bone}, i.e.

$$C_{bone} = \int_0^1 c_{bone}(a)\ da. \tag{4.13}$$

It is assumed first that the cells, which are recruited from the old bone surface, are completely non-differentiated (have maturation level equal to

zero). Then function $c_{bone}(a)$ should be defined through the Dirac delta function $\delta(a)$, i.e

$$c_{bone}(a) = C_{bone}\ \delta(a), \quad a \in [0,1].$$

The present mathematical model is constructed mainly to be used for the numerical simulations of the osseointegration process. Then it can be useful to smooth the Dirac delta function, so that the boundary condition (4.7) can be incorporated into the numerical scheme exactly. Therefore, let us consider some small parameter δ_a. Then the source of cells can be represented by smoothed function

$$c_{bone} = \begin{cases} C_{bone} \cdot \frac{2}{\delta_a}(1 - \frac{a}{\delta_a}), & a \in [0, \delta_a], \\ 0, & a \in [\delta_a, 1]. \end{cases} \tag{4.14}$$

This function satisfies condition (4.13). The parameter δ_a corresponds to the range of maturation level of cells, that are recruited from the surrounding bone tissue, and is introduced in the model, in order to make it more suitable for the numerical simulations.

External sources of osteogenic cells and of growth factor are introduced through boundary conditions (4.7), (4.10) and (4.11), which are defined at surfaces $\partial\Omega_i$, $\partial\Omega_b$ for time less than t_{cbone}, t_{gbone} and $\max(t_{cbone}, t_{gbone})$, respectively. That means, that the implant surface $\partial\Omega_i$ and the old bone surface $\partial\Omega_b$ should be a part of the boundary $\Gamma(t)$ of the physical domain Ω_s for $t \leq \max(t_{cbone}, t_{gbone})$. Otherwise, conditions (4.7), (4.10) and (4.11) make no sense. A new parameter is introduced:

$$t_0 = \max(t_{cbone}, t_{gbone}).$$

In order to obtain initiation of bone formation only after time t_0, we want our solution to satisfy the following relation for the movement of the interface

$$v_n(\vec{X}, t) = 0, \quad \vec{X} \in \Gamma(t), t \leq t_0 = \max(t_{cbone}, t_{gbone}). \tag{4.15}$$

The above equation is not imposed explicitly in the current simulations, however, the biological parameters are chosen in such a way, that equation (4.15) is satisfied *a posteriori*. From equations (4.5) and (4.15) it follows that $\Gamma(t) = \partial\Omega_i \cup \partial\Omega_b$, for $t \leq t_0$, i.e. the subdomain Ω_s will keep its initial geometry and occupy the whole peri-implant region at least until time t_0.

For the selected parameter values, time t_0 is equal to 4 *days*. Condition (4.15) means that bone does not start forming earlier than t_0 days. Value $t_0 = 4$ *days* is in line with experiments [1], in which newly formed bone was observed only at the end of the first week. Condition (4.15) is accomplished by an appropriate choice of the model parameters. In particular, an upper limit u_b^{lim} for the differentiation rate u_b is defined, i.e.

$$u_b \leq u_b^{lim}. \tag{4.16}$$

From condition (4.16), and since the initial density of immature and mature cells is zero, and since the maturation level of immature osteogenic cells, which originate from the source at the old bone surface, is not larger than δ_a (see equations (4.7) and (4.14)), it follows that no mature cells will derive from immature cells, at least until time

$$t_{lim} = \frac{1-\delta_a}{u_b^{lim}}. \tag{4.17}$$

That is

$$c_m(\vec{x},t) = 0, \quad \vec{x} \in \bar{\Omega}_s,\ t \leq t_{lim}. \tag{4.18}$$

If the following relation holds:

$$u_b^{lim} < \frac{1-\delta_a}{t_0} \tag{4.19}$$

then for time t_{lim}, defined in equation (4.17), it holds $t_{lim} = \frac{1-\delta_a}{u_b^{lim}} > t_0$, and from equations (4.18) and (4.4) it follows that $v_n(\vec{X},t) = 0$, for $\vec{X} \in \Gamma(t)$, $t \leq t_0 < t_{lim}$, and condition (4.15) holds.

Remark 4.4. Note that two types of boundary conditions have been defined. Boundary condition (4.4) determines the evolution of the domain boundary in time. Another set of boundary conditions, given by equations (4.7)–(4.12), is necessary for the uniqueness of the solution of governing equations (4.1)–(4.3), defined within the soft tissue region Ω_s. Hence all the requirements for well-posedness (in terms of existence and uniqueness) of the moving boundary problem are fulfilled.

4.4 Model validation

In this section, the present model is validated against experiments. Approximate solutions are obtained from numerical simulations. The values of the model parameters are taken from the literature and are estimated from numerical simulations. A parametric study is carried out, and some conclusions about the influence of various parameters on the model predictions are drawn.

4.4.1 Numerical simulations

Numerical simulations are performed for a 2D axisymmetric physical domain. A 1D physical domain makes calculations much faster and much simpler. However, some important solution characteristics can not be represented in 1D simulations. For example, bone front propagation from the corners, formed by the implant body and by the thread, has a large influence on the final state of osseointegration and can only be modeled for a 2D

geometry of the physical domain. To have a full picture of the model characteristics it is necessary to perform a parametric study for a 2D physical domain, despite it leads to a large computation time and to a complicated numerical algorithm. The solution of non-linearly coupled PDE's within an irregular 2D physical domain, which evolves in time, is a rather challenging task. A derivation of the numerical approach designed for the solution of the present problem is a separate subject of the research. Therefore, Chapter 5 as a whole is devoted to its description. At this moment it is only mentioned, that the governing advection-diffusion-reaction equations are solved with the use of the finite volume method. The embedded boundary method is used to capture an irregular geometry of a 2D physical domain and the level set method is applied to track the evolution of the physical domain. The explicit modified Euler method is used for time integration. More details about the solution technique are given in the Chapter 5.

An approximate geometry of the initial healing site, formed by the thread of the implant and by the old bone surface, is determined from the image of the endosseous implant given in Berglundh et al. [14] (Figure 4.3). The

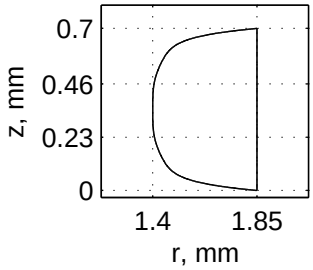

Figure 4.3: Initial geometry of the healing site, bounded by the thread of the implant from the left and the old bone surface from the right

sizes of the initial uniform rectangular control volumes along $r-$, $z-$ and $a-$ axes are chosen to be equal to $h_r = 0.0045\ mm$, $h_z = 0.005\ mm$ and $h_a = 0.05$, respectively.

4.4.2 Model parameters

The model parameters as such, and their magnitudes, determine the behavior of the model. The values of the parameters, which provide physical solutions, are found in this section. It is necessary to specify certain criteria to assess biologically relevant solutions. A focus of the numerical studies presented by Amor et al. [6] and Moreo et al. [67] is on the distance and contact osteogenesis modes, which are predicted by their osseointegration models for micro-rough and smooth implants, respectively. Therefore, a path of bone formation predicted by the present model for the implant surfaces with var-

ious magnitudes of the micro-roughness is the main criterion applied for the choice of the model parameters. In the experiments by Abrahamsson et al. [1], contact osteogenesis was observed near a rough implant surface, and distance osteogenesis occurred near smooth implants. The possibility to quantify the micro-roughness of the implant surface is incorporated into the present model implicitly through the boundary conditions for the growth factor concentration. The influx of growth factors at the implant surface corresponds to the release by activated platelets. It is known from experiments [56, 71] that the rate of adhesion of platelets, their activation and release of growth factors are higher near a micro-rough implant surface than near smooth surfaces. Two types of implants are considered in the present model: a micro-rough 'Sand-Blasted, Large Grit, Acid-Etched' (SLA) implant and a smooth 'turned' implant. A high value and a low value of the growth factor source are considered at the surfaces of a SLA implant and of a 'turned' implant, respectively. The micro-roughness of the implant is represented by the parameter E_{pl}, which is proportional to the influx of growth factors at the implant surface.

A large number of numerical simulations is introduced in order to determine relevant values of the model parameters. Due to a large number of the parameters a random selection of the parameters requires an enormous number of simulations. Therefore, random search is not efficient in the current case. The following approach is used to choose the values of the parameters. At the first step, the ability of the model to predict distance osteogenesis for smooth implants is tested. As a first approximation, the influx of growth factors at the smooth implant surface is assumed to be very small and is set to zero: $E_{pl} = 0$. The rest of the model parameters is estimated, such that a bone-forming front moves from the old bone surface towards the implant (distance osteogenesis mode).

Bone formation near the two different implant types is modeled by varying the value of E_{pl}, whereas all other model parameters are kept unchanged. Hence at the second stage, the value of E_{pl} corresponding to a micro-rough SLA implant surface is chosen, such that new bone starts forming directly at the implant surface (contact osteogenesis). If it is not possible to find such a value of E_{pl}, then the parameters, which were estimated at the first step, should be readjusted, until contact osteogenesis is implemented into the model as well as distance osteogenesis.

Finally, a limit value E_{pl}^{lim} for the source of growth factor E_{pl} near the surface of the smooth turned implant is found, such that distance osteogenesis mode is predicted for $E_{pl} \leq E_{pl}^{lim}$.

The expressions for the model parameters are given in Table 4.1. The values for the constant parameters of the model equations and of the boundary conditions are specified in Table 4.2. In the right column of the table, the references are noted, from which the values of the constant model parameters are taken. No reference is given next to the parameters, which are

Table 4.1: Expressions for the dependent model parameters

Dependent parameter expression	Description
$\chi(g, c_{tot}) = \begin{cases} \frac{\chi_0 g}{K_{ch}^2 + g^2}(1 - c_{tot}), & \text{if } c_{tot} < 1 \\ 0, & \text{if } c_{tot} \geq 1 \end{cases}$	Osteogenic cell chemotaxis
$A_c(g) = A_{c0}\left(1 + \frac{g}{K_p + g}\right)$	Osteogenic cell proliferation
$u_b(g) = u_b^{lim}\ \frac{g^2}{K_u^2 + g^2}$	Osteogenic cell differentiation
$E_c(g) = \frac{E_{c0}\ g}{K_g + g}$ $\gamma(a) = a^{\lambda_c}$	Growth factor release by osteogenic cells
$g_{impl}(t) = E_{pl} e^{-\lambda_{pl} t}$	Growth factor release by activated platelets

estimated from numerical simulations or based on educated guesses.

Further, an initialization of each model parameter is described in detail. In order to justify the choice of values for the parameters, which are estimated from simulations, and in order to demonstrate, how various parameters influence the model behavior, a sensitivity analysis is performed. The main results of the sensitivity analysis are presented in Section 4.4.3.

Remark 4.5. The model variables c_i, c_m and g are nondimensionalized (see Remark 4.2). This fact is taken into consideration, when the parameters of the model are defined. Appropriate scaling of parameter values is applied and suitable units of the parameters are chosen.

The chemotaxis coefficient $\chi(g, c_{tot})$ is defined as in [6] times the term $(1 - c_{tot})$, if the total cell density is less than saturation limit 1. Otherwise, chemotaxis is switched to zero. This switch prevents, that cells migrate towards regions, where the cell density has reached its saturation value. In the regions, where the saturation limit has been exceeded, no chemotaxis takes place, and cell migration is determined by cell diffusion. The value for the constant parameter K_{ch} is also taken from [6].

The values of the chemotaxis coefficient χ_0 and of the cell diffusivity coefficient D_c are estimated from numerical simulations. See Section 4.4.3 for a discussion on the choice of these parameters.

The expression for the proliferation coefficient $A_c(g)$, and the values of the parameters A_{c0} and K_p are taken from Moreo et al. [67].

It is reported in Linkhart et al. [62] and Dimitriou et al. [25] that growth factors enhance differentiation into osteoblasts. Therefore, it is assumed that the differentiation rate $u_b(g)$ depends on the growth factor concentration. For the proposed relation, $u_b(g) \approx 0$, if $g \ll K_u$, and it increases to the limit value u_b^{lim}, if the growth factor concentration g grows. The choices of values for the parameters u_b^{lim} and K_u are discussed in Section 4.4.3.

The expression for the growth factor release parameter $E_c(g)$ and the values of the parameters E_{c0} and K_g are taken from [6]. It is assumed according to Dimitriou et al. [25], that growth factors are released by immature and mature cells. Furthermore, it seems to be necessary to introduce the dependence of growth factor release on the level of maturation through the power function $\gamma(a)$. The exponent of this function is denoted by the parameter $\lambda_c \geq 0$. Various authors use different assumptions for growth factor release in their models. For example, Moreo et al. [67] define the same production rate for osteogenic cells (immature cells) and osteoblasts (mature cells). For the present approach, this assumption is equivalent to a zero value of the parameter λ_c. On the other hand, Amor et al. [6] assume that growth factor is produced only by osteoblasts. Then an option $\lambda_c \to +\infty$ will represent this situation in the present model. The choice of the value of exponent λ_c is discussed in Section 4.4.3.

As in [6], it is assumed that the number of platelets at the implant

Table 4.2: Values of the model parameters, and boundary condition parameters

Constant parameter values	Description	Ref.
$D_c = 0.0998\ mm^2/day$	Osteogenic cell diffusion coefficient	
$\chi_0 = 0.324\ mm^2/day$	Osteogenic cell chemotaxis coefficient	
$K_{ch} = 0.01$	Growth factor concentration, related to osteogenic cell chemotaxis coefficient	[6]
$A_{c0} = 0.25\ day^{-1}$	Half of the maximal proliferation coefficient	[67]
$K_p = 0.1$	Growth factor concentration, related to osteogenic cell proliferation coefficient	[67]
$u_b^{lim} = 0.2\ day^{-1}$	Maximum cell differentiation rate	
$K_u = 0.01$	Growth factor concentration, related to cell differentiation rate	
$D_g = 0.045\ mm^2/day$	Growth factor diffusion coefficient	[6]
$d_g = 100\ day^{-1}$	Growth factor decay rate	[6]
$E_{c0} = 570\ day^{-1}$	Growth factor production rate by osteogenic cells	[6]
$K_g = 1$	Growth factor concentration, related to growth factor production rate	[6]
$\lambda_c = 2$	Parameter, related to growth factor production rate by immature cells	
$g_{bone} = 0.6\ mm/day$	Influx of growth factors at the old bone surface	
$C_{bone} = 0.07\ mm/day$	Influx of cells at the old bone surface	
$\delta_a = 0.1$	Maximum maturation level of cells, recruited from the old bone surface	
$E_{pl} \leq E_{pl}^{lim} = 0.32\ mm/day$ $E_{pl} = 204.8\ mm/day$	Influx of growth factors, released by activated platelets – at the turned implant surface – at the SLA implant surface	
$\lambda_{pl} = 1\ day^{-1}$	Platelets degradation rate coefficient	[6]
$P_b = 0.01\ mm/day$	Bone-forming surface velocity coefficient	

surface decays exponentially with rate $\lambda_{pl} = 1\ day^{-1}$, which gives a half time of $\ln 2\ days$. Hence the release of growth factors decreases in the same way. The production rate E_{pl} at $t = 0$ is estimated in Section 4.4.3.

The value for the growth factor decay rate d_g is defined as in Amor et al. [6].

The maximum maturation level $\delta_a = 0.1$ of cells, recruited from the old bone surface, is chosen to be of order of the length of the grid spacing in the a-coordinate, used in the simulations.

The value of the parameter D_g is taken from Amor et al. [6]. The dependence of the solution on the value of D_g is discussed in Section 4.4.3.

4.4.3 Sensitivity analysis

As it is outlined in Section 4.4.2, at the first step of an estimation of the parameter values, a zero influx of growth factors is assumed at the implant surface, i.e. $E_{pl} = 0$. The values of the parameters are chosen, such that distance osteogenesis is predicted, i.e. a bone-forming front moves from the old bone surface towards the implant.

Remark 4.6. The numerical solutions presented in this section are obtained for a fine mesh resolution. The sizes of the initial uniform rectangular control volumes along $r-$, $z-$ and $a-$ axes are equal, respectively, to $h_r = 0.0045$ mm, $h_z = 0.005$ mm and $h_a = 0.05$, respectively.

The numerical solution of the model equations, which is obtained for the parameter values in Tables 4.1 and 4.2 and for $E_{pl} = 0$, is plotted in Figure 4.4. Distance osteogenesis is predicted by simulations, if a considerable amount of growth factors is only observed in the regions, situated close to the bone-forming surface. Suppose, that bone starts forming at the old bone surface and not at the implant surface. If the growth factors are able to spread far from the bone-forming surface, then they can reach the implant surface after a certain time. The growth factors cause cell differentiation and cell migration towards the implant due to chemotaxis. Mature osteogenic cells appear and bone formation is initiated near the implant. Hence distance osteogenesis cannot be modeled, unless the growth factor concentration is always low in the regions, which are not adjacent to the new bone surface.

Since the sources of cells and of growth factors are considered only on the old bone surface, a layer with a high cell density and a high growth factor concentration is formed near the old bone. The thickness of this layer depends on random walk and chemotaxis of the cells. Increasing the value of the cell diffusion coefficient D_c and/or decreasing the chemotaxis coefficient χ_0 lead to a faster spreading of cells towards the implant. The cells release growth factors and the width of the layer with a high cell density and a high growth factor concentration increases.

Remark 4.7. Further, the region of the soft tissue domain with a high cell

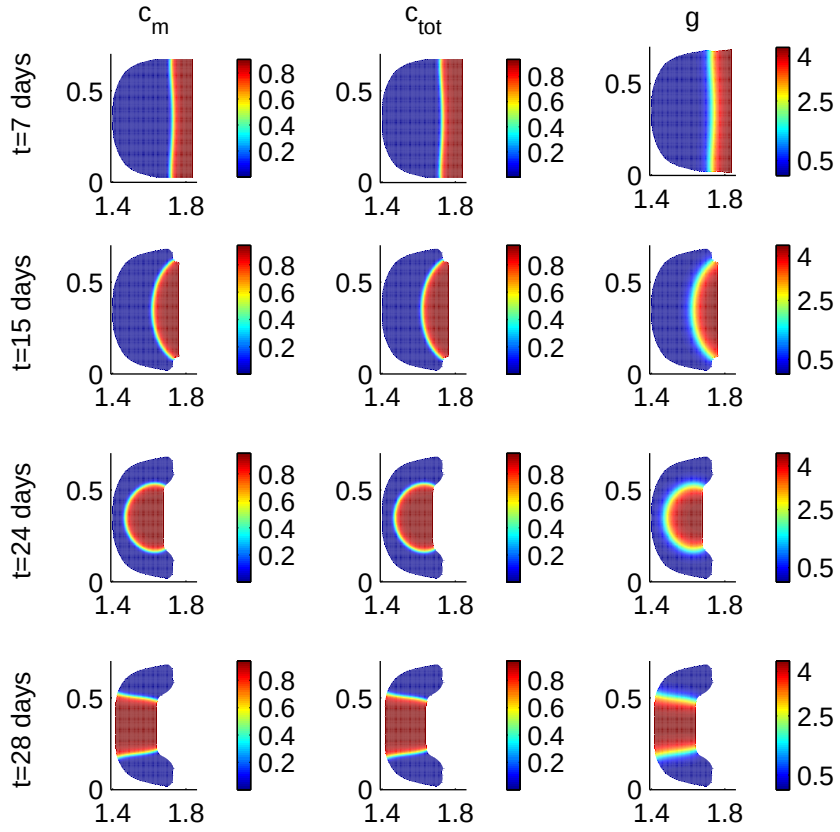

Figure 4.4: Plots of the mature cell density c_m, of the total cell density c_{tot} and of the growth factor concentration g at the time moments $t = 7$, 15, 24 and 28 *days* for the parameter values given in Tables 4.1 and 4.2 and for $E_{pl} = 0$. The bone-forming surface moves from the old bone surface towards the implant (distance osteogenesis)

density and a high growth factor concentration are referred to as "high density- high concentration layer". Such a region is usually adjacent to the boundary of the domain. The thickness and the length of the layer can be considered. The length of the layer corresponds to the length of the ossification front.

The value $0.75 \cdot 0.133 = 0.0998\ mm^2/day$ is assigned to the diffusion coefficient D_c in Table 4.2, whereas $0.133\ mm^2/day$ is the value for the cell diffusion coefficient defined in Moreo et al. [67]. The value $0.133\ mm^2/day$ yields a large width of the high density- high concentration layer, adjacent to the bone-forming surface, and mature osteogenic cells appear near the implant body, i.e. at the middle of the implant surface, at day 21 (Figure 4.5).

A similar effect is reached, if the reference value of the chemotaxis coefficient χ_0 is divided by two, i.e. if $\chi_0 = 0.5 \cdot 0.324\ mm^2/days = 0.162\ mm^2/days$. In this case, bone starts forming at the implant surface at time $t = 15\ days$ (Figure 4.6).

The growth factor diffusion coefficient D_g effects the width of the high density- high concentration layer to a smaller extent. Increasing the value of D_g by two times yields the appearance of mature osteogenic cells in the middle of the implant surface at day 24 (Figure 4.7).

Decrease of the diffusion D_g to the value $0.0225\ mm^2/days$ does not change the path of bone formation significantly.

Decrease of the value of the cell diffusion coefficient D_c to $0.5 \cdot 0.133 = 0.0665\ mm^2/days$, or increase of the reference value of the chemotaxis coefficient χ_0 by two times yield smaller length and width of the high density-high concentration layer compared with the solution for the reference values D_c and χ_0 (see Figures 4.4, 4.8 and 4.9). For the decreased D_c and increased χ_0, bone forms only from the old bone surface and the length of the ossification front decreases significantly at the end of the second week.

As it is mentioned in Section 4.3.2, the value of the maximum cell differentiation rate u_b^{lim} should be less than $\frac{1-\delta_a}{4}\ days^{-1} = 0.225\ days^{-1}$. Abrahamsson et al. [1] observed, that bone formation started at the end of the first week. Hence the differentiation rate should be larger than $\frac{1-\delta_a}{7}\ days^{-1} \approx 0.1285\ days^{-1}$. The estimated value of $0.2\ days^{-1}$ is assigned to u_b^{lim}. Simulations provide similar results for the rates $0.2\ days^{-1}$ and $0.224\ days^{-1}$. The smaller values 0.18 and $0.15\ days^{-1}$ of u_b^{lim} yield a delay of cell differentiation and, hence, of bone formation. A delay of bone formation is clearly observed in the numerical solutions. For example, the mature cell density is maximal near the old bone surface and it reaches the value 0.6 at the time moments 7.9, 6.7 and 6 *days* for the values 0.15, 0.18 and $0.2\ days^{-1}$ of u_b^{lim}, respectively, as it is illustrated in Figure 4.10.

The parameter K_u influences the cell differentiation in the regions with

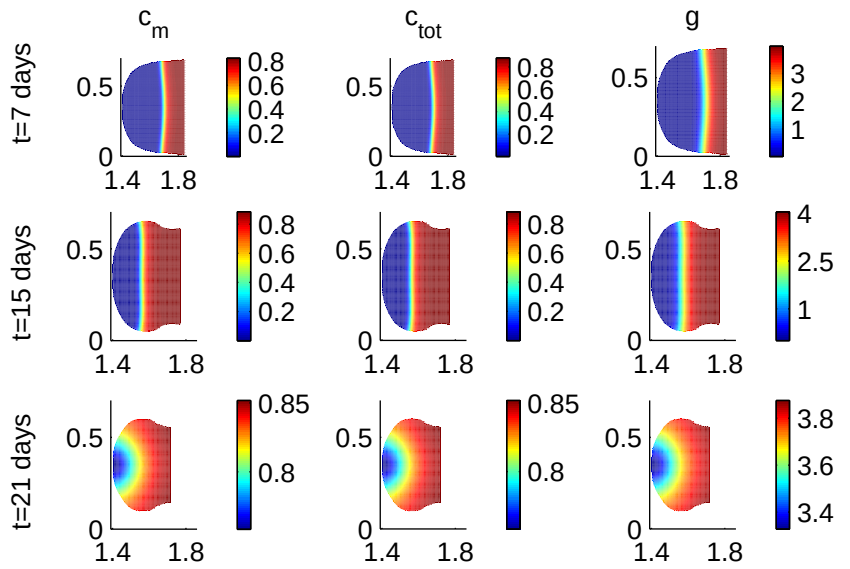

Figure 4.5: Plots of the mature cell density c_m, of the total cell density c_{tot} and of the growth factor concentration g at the time moments $t = 7$, 15 and 21 *days* for the parameter values given in Tables 4.1 and 4.2 and for $E_{pl} = 0$ and $D_c = 0.133\ mm^2/days$. New bone matrix starts forming at the implant body surface at time 21 *days*

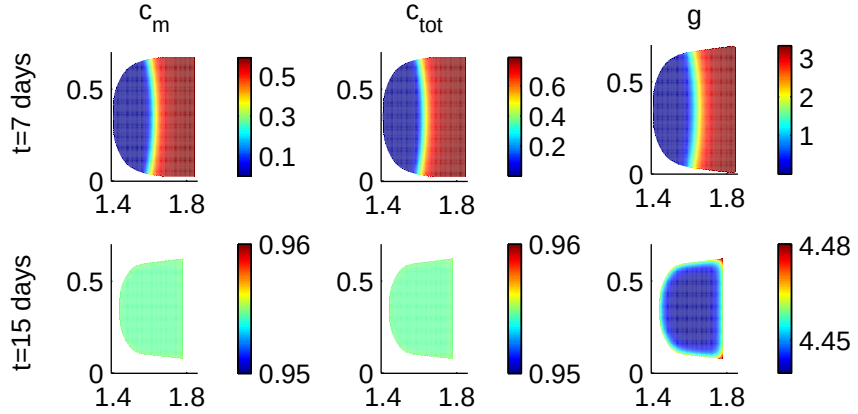

Figure 4.6: Plots of the mature cell density c_m, of the total cell density c_{tot} and of the growth factor concentration g at the time moments $t = 7$ and 15 *days* for the parameter values given in Tables 4.1 and 4.2 and for $E_{pl} = 0$ and $\chi_0 = 0.162\ mm^2/days$. New bone matrix starts forming at the implant body surface at time 15 *days*

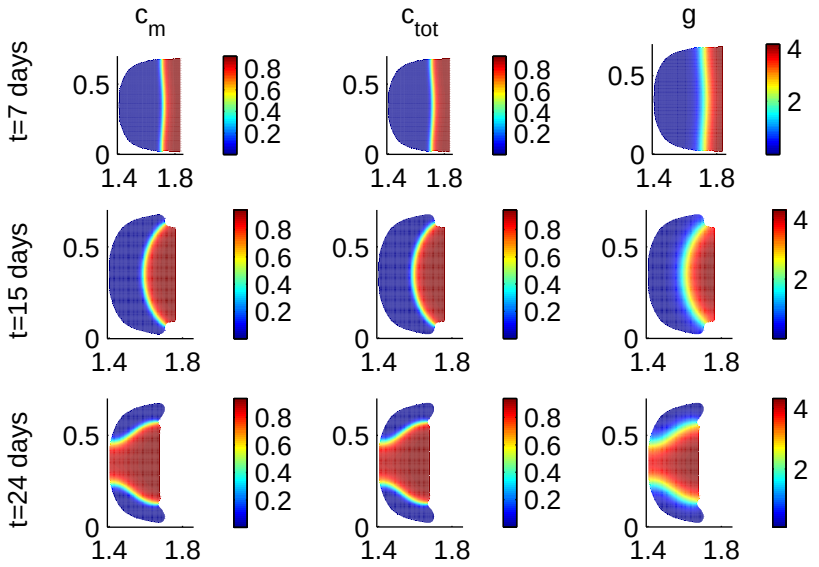

Figure 4.7: Plots of the mature cell density c_m, of the total cell density c_{tot} and of the growth factor concentration g at the time moments $t = 7$, 15 and 24 *days* for the parameter values given in Tables 4.1 and 4.2 and for $E_{pl} = 0$ and $D_g = 0.09\ mm^2/days$. Mature osteogenic cells appear in the middle of the implant surface at time $t = 24$ days

a low concentration of growth factors, since the differentiation rate u_b is defined as $u_b^{lim}\frac{g^2}{K_u^2+g^2}$ in Table 4.1. Small values of K_u yield a large differentiation rate of cells even in the regions, where the growth factor concentration g is considerably low. If K_u is large, then active cell differentiation occurs only in the regions, where g is high. Sensitivity analysis shows, that the numerical solutions are similar for the reference value 0.01 of K_u, defined in Table 4.2, and for the small value 0.001. Increasing K_u to the value 0.1 yields that no mature cells appear within the peri-implant region and no bone forms, due to deficiency of cell differentiation.

It follows from simulations that the values 1, 2 and 3 of the parameter λ_c provide similar numerical solutions. The value 2 is chosen as the reference value in Table 4.2.

The values of the parameters g_{bone} and C_{bone} are chosen in such a way, that bone formation is initiated at the old bone surface at the end of the first week. Numerical simulations provide similar solutions for the reference value 0.6 $mm/days$ of g_{bone} and for values twice as small and twice as large. Multiplication of the chosen value 0.07 $mm/days$ of C_{bone} by two leads to a large width of the layer with a high concentration of growth factors and a high density of cells at the bone-forming surface. Hence a larger influx of cells at the old bone surface leads to appearance of mature osteogenic cells

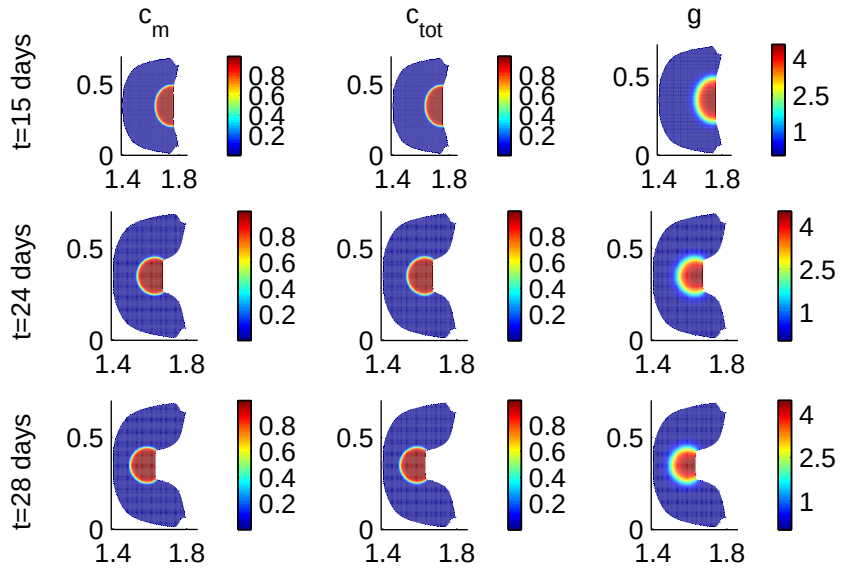

Figure 4.8: Plots of the mature cell density c_m, of the total cell density c_{tot} and of the growth factor concentration g at the time moments 15, 24 and 28 *days* for the parameter values given in Tables 4.1 and 4.2 and for $E_{pl} = 0$ and $D_c = 0.5 \cdot 0.133 = 0.0665\ mm^2/days$. The region, in which mature osteogenic cells are present is much smaller, compared to the case $D_c = 0.75 \cdot 0.133\ mm^2/days$, illustrated in Figure 4.4

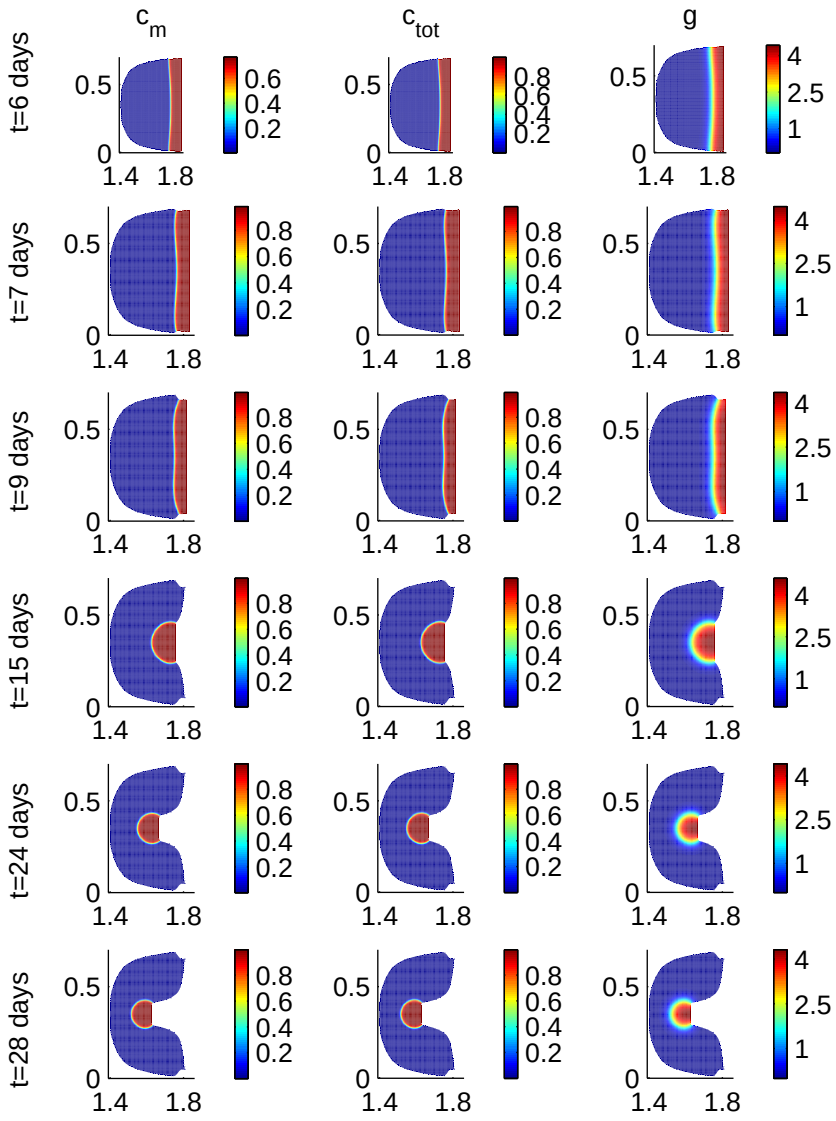

Figure 4.9: Plots of the mature cell density c_m, of the total cell density c_{tot} and of the growth factor concentration g at the time moments $t = 6$, 7, 9, 15, 24 and 28 *days* for the parameter values given in Tables 4.1 and 4.2 and for $E_{pl} = 0$ and $\chi_0 = 0.648\ mm^2/days$. The region, in which mature osteogenic cells are present is much smaller, compared to the case $\chi_0 = 0.324\ mm^2/days$, illustrated in Figure 4.4

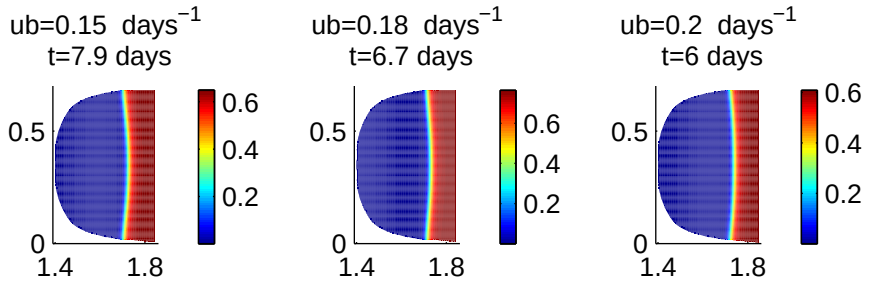

Figure 4.10: Plots of the mature cell density c_m for the parameter values given in Tables 4.1 and 4.2 and for $E_{pl} = 0$ and the values 0.15, 0.18 and 0.2 $days^{-1}$ of the differentiation rate limit u_b^{lim}. Smaller values u_b^{lim} yield a delay of cell differentiation and of bone formation, which are well observed in the present plots

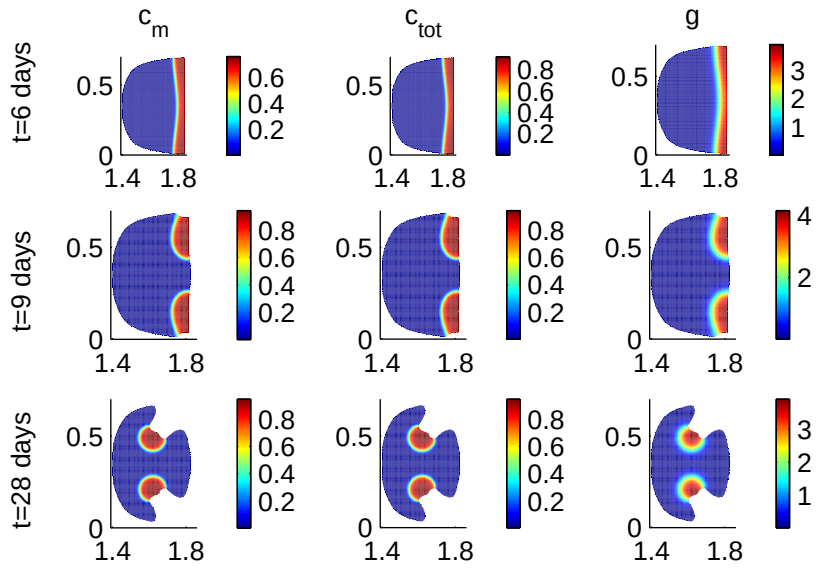

Figure 4.11: Plots of the mature cell density c_m, of the total cell density c_{tot} and of the growth factor concentration g at the time moments $t = 6$, 9 and 28 *days* for the parameter values given in Tables 4.1 and 4.2 and for $E_{pl} = 0$ and $C_{bone} = 0.035$ $mm/days$. The bone-forming surface moves from the corners formed by the implant thread and by the old bone surface

at the implant body surface at day 18. Hence distance osteogenesis is not predicted for a large value of C_{bone}.

Division of the reference value of C_{bone} by two yields that the ossification front advances from the corners formed by the implant thread and by the old bone surface (Figure 4.11). A similar path of bone formation is illustrated in Figure A.1 in Appendix A.1. The solutions plotted in the last figure are obtained for a small time span of the influx of osteogenic cells at the old bone surface $t_{cbone} = 0.5\ days$. Therefore, the current path of bone formation is related to a weak source of osteogenic cells at the old bone surface.

The value of the bone-forming surface velocity coefficient, P_b, is estimated in such a way that the amount of newly formed bone within the peri-implant region after four weeks of simulation is line with the experimental data of [1].

Up to this point a zero source of growth factors at the implant surface was assumed. This assumption is used in the numerical simulations, which are carried out to estimate all necessary parameter values, except the value of the parameter E_{pl} corresponding to a micro-rough SLA implant. For the SLA implant, a value for E_{pl} is chosen, such that bone formation is observed at the entire implant surface (contact osteogenesis) at the end of the first week. Depending on the value of E_{pl}, different paths are predicted by simulations, which are illustrated in Figures 4.12–4.15. In the case $E_{pl} = 3.2\ mm/days$ bone formation proceeds from the old bone surface and from the corners, formed by the implant body and by the thread (Figure 4.12).

The values $4 \cdot 3.2\ mm/days$ and $16 \cdot 3.2\ mm/days$ of E_{pl} yield the occurrence of bone formation at the lateral sides, i.e. at the thread surface (Figures 4.13 and 4.14).

For the reference value $64 * 3.2 = 204.8\ mm/days$ of E_{pl} in Table 4.2, the bone-forming surface starts moving from the entire implant surface including the thread. The high density- high concentration layer is moving to the left the first ten days and becomes aligned with the implant body surface at time 11 $days$ (Figure 4.15).

The limit value E_{pl}^{lim} is chosen is such a way, that for all $E_{pl} \leq E_{pl}^{lim}$ distance osteogenesis is predicted by the model. The value $0.32\ mm/days$ of the parameter E_{pl}^{lim} is determined from the simulations.

Therewith, more than half of the model parameters are estimated numerically. The rest of the parameters is taken from previous models, in which some of the parameters are also estimated. The choice of the parameter values is made in such a way, that the model solution is in line with the experimental studies mentioned in this work. There is no experimental evidence that the estimated parameter values correspond to their actual values. The biological relevance of the proposed model parameters and, probably, more accurate parameter values, should be determined from further experimental studies.

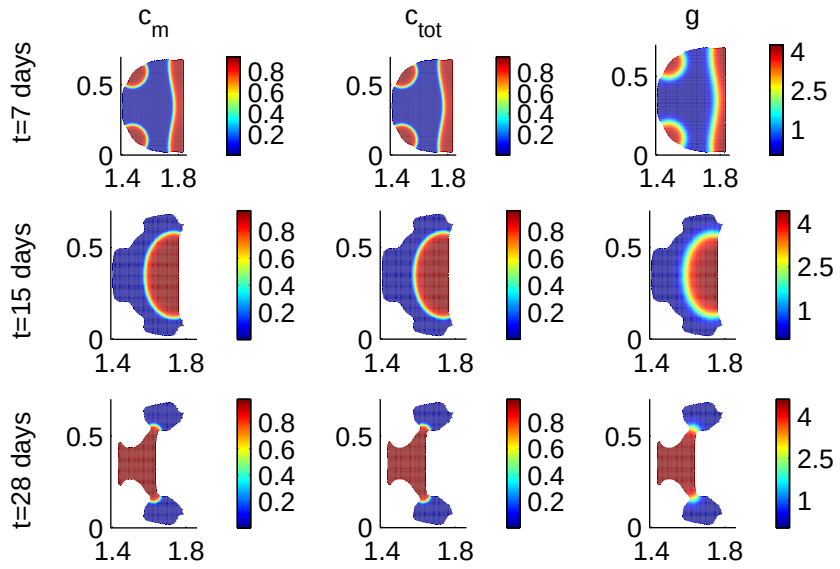

Figure 4.12: Plots of the mature cell density c_m, of the total cell density c_{tot} and of the growth factor concentration g at the time moments $t = 7$, 15 and 28 *days* for the parameter values given in Tables 4.1 and 4.2 and for $E_{pl} = 3.2$ *mm/days*. Bone formation occurs at the old bone surface and in the corners, formed by the implant body and by the thread

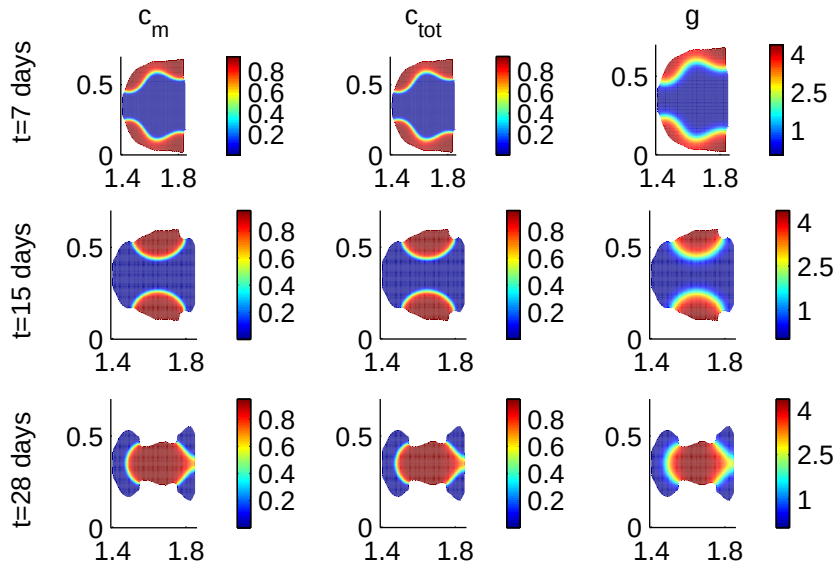

Figure 4.13: Plots of the mature cell density c_m, of the total cell density c_{tot} and of the growth factor concentration g at the time moments $t = 7$, 15 and 28 *days* for the parameter values given in Tables 4.1 and 4.2 and for $E_{pl} = 4 \cdot 3.2$ *mm/days*. Bone forms at the thread surface

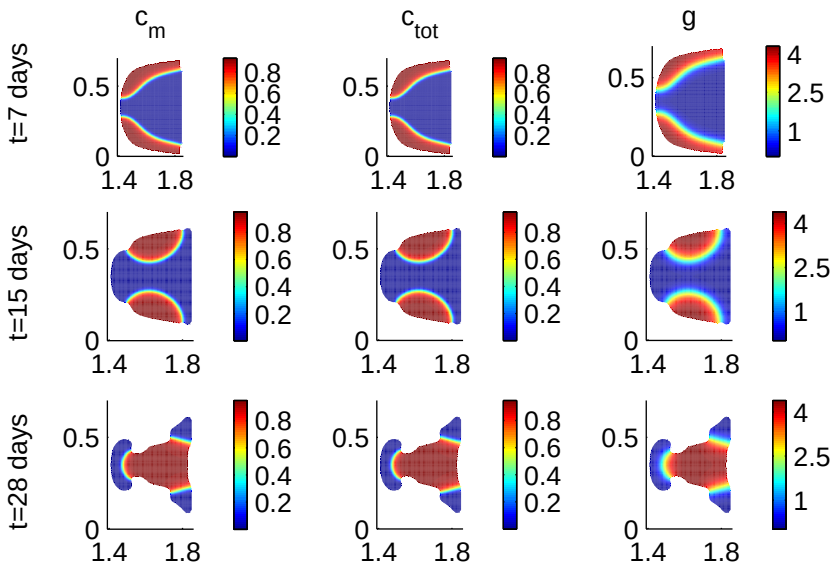

Figure 4.14: Plots of the mature cell density c_m, of the total cell density c_{tot} and of the growth factor concentration g at the time moments $t = 7$, 19, 22 and 28 *days* for the parameter values given in Tables 4.1 and 4.2 and for $E_{pl} = 16 \cdot 3.2$ $mm/days$. Bone forms at the thread surface

4.4.3.1 Numerical solutions for various mesh resolution

The results of numerical simulations presented in Section 4.4.3 are obtained for a fine mesh resolution. The sizes of the initial uniform rectangular control volumes along $r-$, $z-$ and $a-$ axes are equal, respectively, to $h_r = 0.0045$ mm, $h_z = 0.005$ mm and $h_a = 0.05$, respectively. For conciseness, the present mesh grid is denoted by Ω_h, where the subindex h refers to the chosen spatial resolution.

Some interesting features about convergence of the numerical solutions against the spatial resolution of the control volume grid are observed during simulations. Decrease of the mesh resolution within the physical space (r, z) can yield completely different path of bone formation predicted by the numerical solutions.

Consider the initial mesh Ω_{2h} with the following sizes of control volumes: $h_r = 0.009$ mm, $h_z = 0.01$ mm and $h_a = 0.05$; and the mesh Ω_{4h}, such that $h_r = 0.018$ mm, $h_z = 0.02$ mm and $h_a = 0.05$.

The numerical solutions for the parameter values in Tables 4.1 and 4.2 and for $E_{pl} = 0$ and $\chi_0 = 0.648$ $mm^2/days$, which are obtained on the meshes Ω_{2h} and Ω_{4h}, are shown in Figures 4.16 and 4.17, respectively. The layer of high cell densities and of a high growth factor concentration near the old bone surface takes a wave-like appearance at the end of the first week. The wave length is approximately equal to 0.35 mm and 0.7 mm

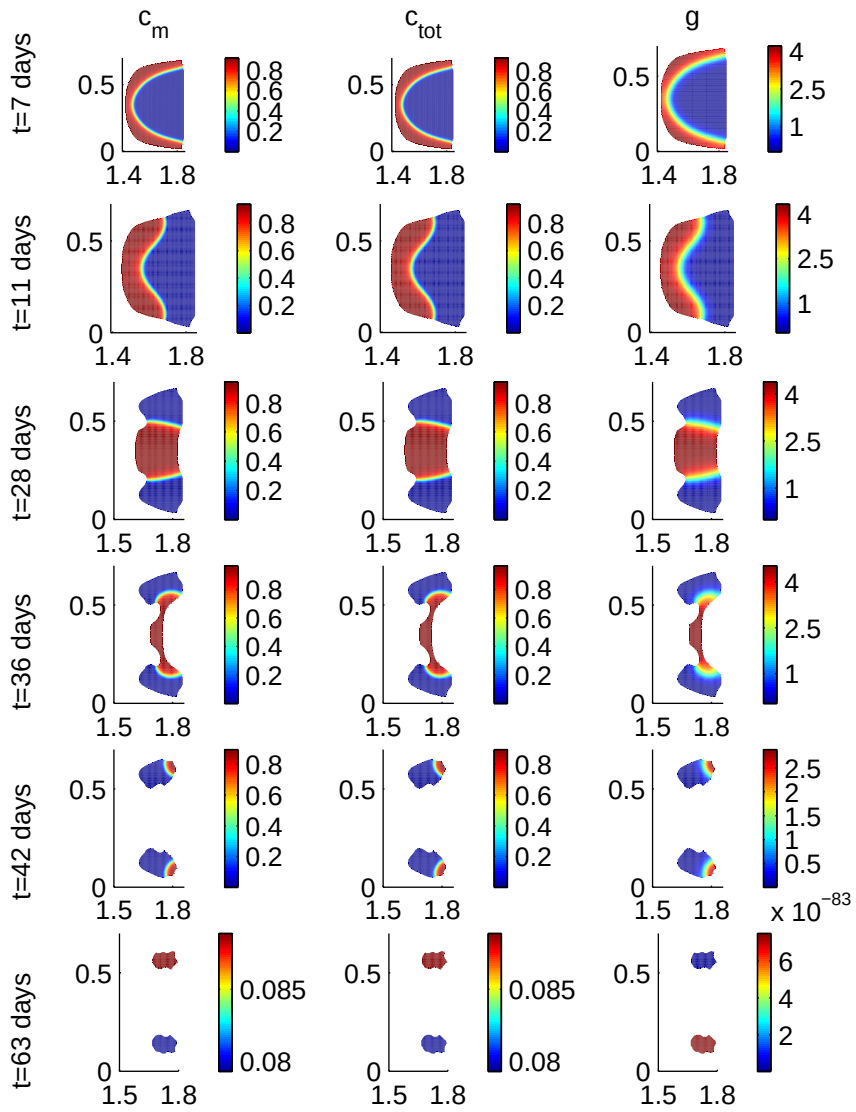

Figure 4.15: Plots of the mature cell density c_m, of the total cell density c_{tot} and of the growth factor concentration g at the time moments $t = 7$, 11, 28, 36, 42 and 63 *days* for the parameter values given in Tables 4.1 and 4.2 and for $E_{pl} = 64 \cdot 3.2$ $mm/days$. The high density- high concentration layer is moving to the left during the first ten days and becomes aligned with the implant body surface at time 11 *days*

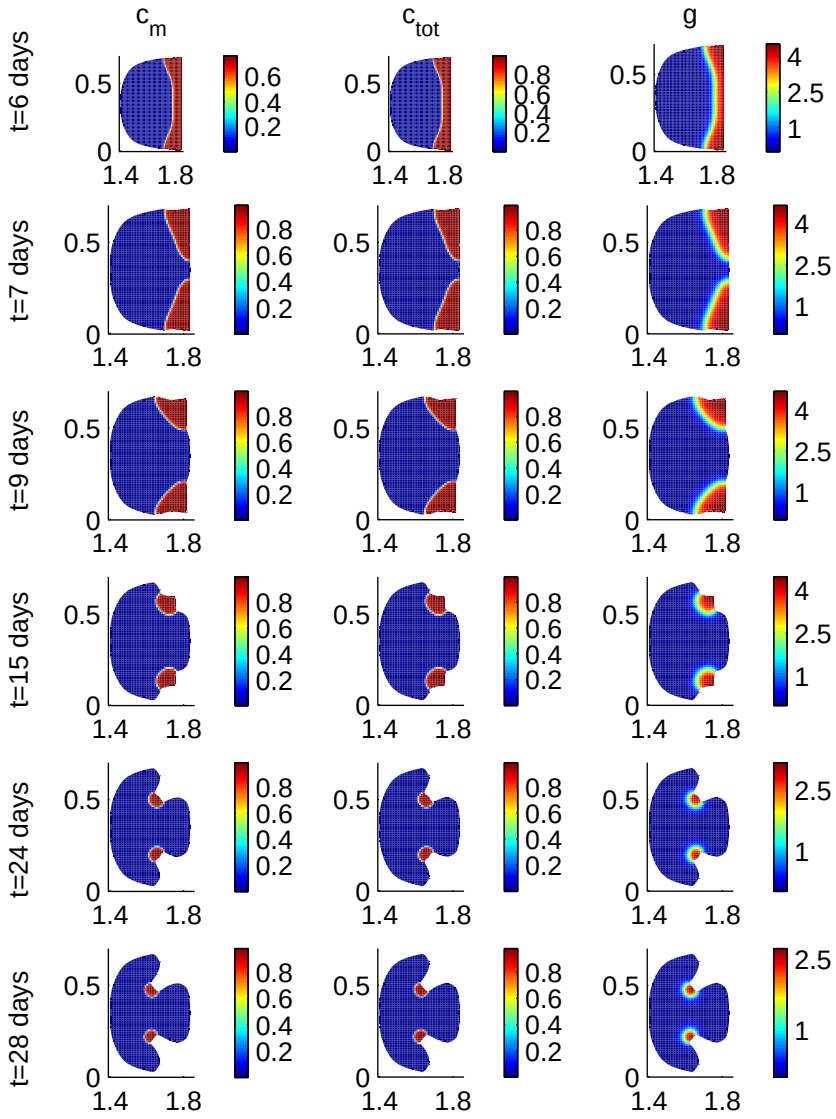

Figure 4.16: Plots of the mature cell density c_m, of the total cell density c_{tot} and of the growth factor concentration g at the time moments $t = 6$, 7, 9, 15, 24 and 28 *days* for the parameter values given in Tables 4.1 and 4.2 and for $E_{pl} = 0$ and $\chi_0 = 0.648\ mm^2/days$. The numerical solution is obtained on the mesh Ω_{2h} with the cell sizes $h_r = 0.009\ mm$, $h_z = 0.01\ mm$ and $h_a = 0.05$ along $r-$, $z-$ and $a-$ axes, respectively

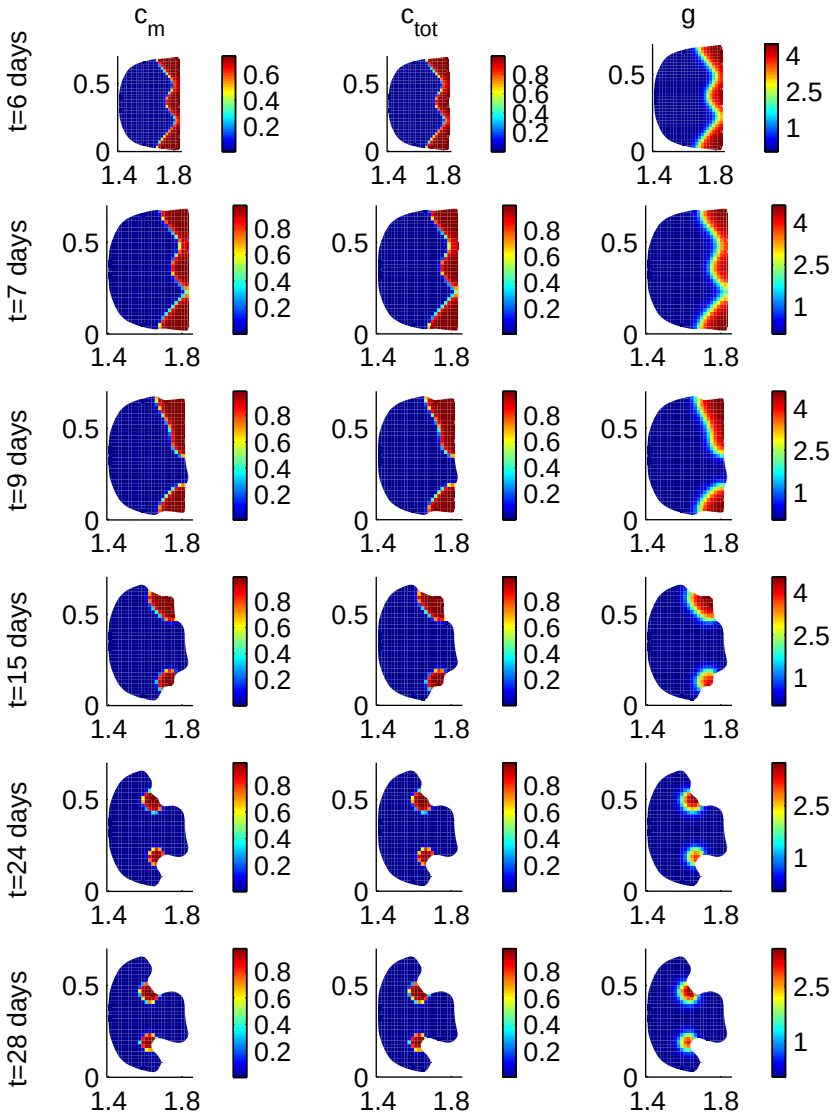

Figure 4.17: Plots of the mature cell density c_m, of the total cell density c_{tot} and of the growth factor concentration g at the time moments $t = 6$, 7, 9, 15, 24 and 28 *days* for the parameter values given in Tables 4.1 and 4.2 and for $E_{pl} = 0$ and $\chi_0 = 0.648\ mm^2/days$. The numerical solution is obtained on the mesh Ω_{4h} with the cell sizes $h_r = 0.018\ mm$, $h_z = 0.02\ mm$ and $h_a = 0.05$ along $r-$, $z-$ and $a-$ axes, respectively

for the meshes Ω_{2h} and Ω_{4h}, respectively. After that, the layer splits in its middle and shrinks towards the corners formed by the old bone surface and the implant thread. Consequently, the bone forming front moves from the corners to the center of the healing site. Such a path of the ossification front is completely different from the path predicted by simulations for the fine mesh Ω_h shown in Figure 4.9.

Formation of the wave-like high density - high concentration layer near the old bone surface and its splitting are also observed for some other parameter values and coarse meshes. Consider the values of the model parameters given in Tables 4.1 and 4.2 and the boundary condition $E_{pl} = 0$. The numerical solution obtained on the mesh Ω_{4h} is plotted in Figure 4.18. The

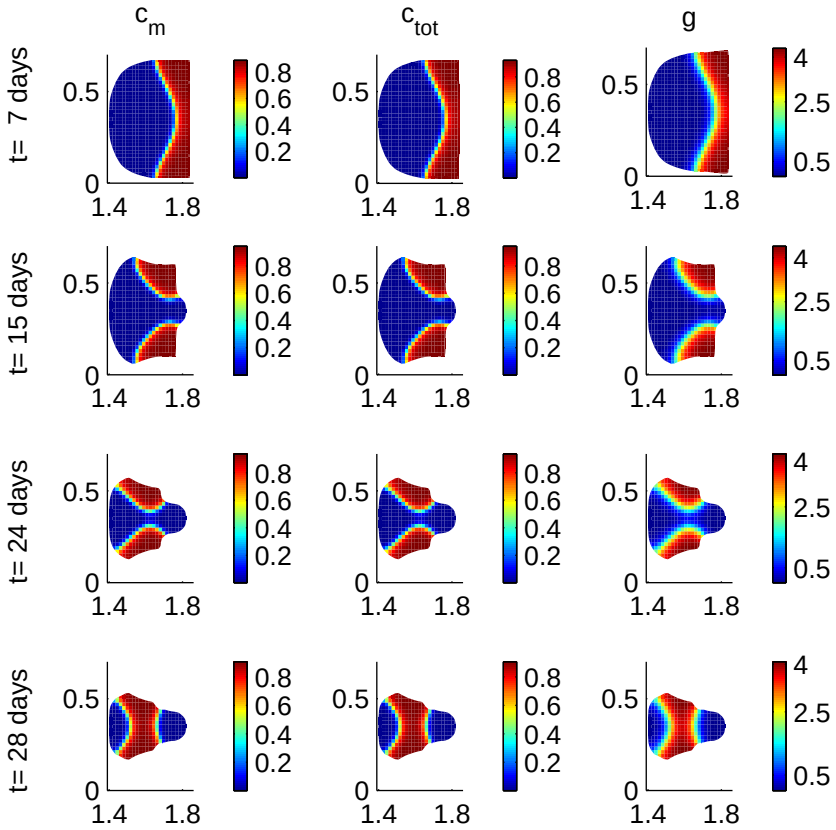

Figure 4.18: Plots of the mature cell density c_m, of the total cell density c_{tot} and of the growth factor concentration g at the time moments $t = 7$, 15, 24 and 28 *days* for the parameter values given in Tables 4.1 and 4.2 and for $E_{pl} = 0$. The numerical solution is obtained on the mesh Ω_{4h} with the cell sizes $h_r = 0.018$ mm, $h_z = 0.02$ mm and $h_a = 0.05$ along $r-$, $z-$ and $a-$ axes, respectively

wave-like layer forms at the old bone surface at the end of the first week. At

the end of the second week the layer splits and bone is predicted to form in the corners, which are formed by the old bone surface and by the implant thread, and then at the lateral surfaces, i.e. near the surface of the implant thread. The ossification path is different from the path obtained in the solution for the fine mesh Ω_h (see Figure 4.4). For the present parameter values, the solution for the mesh Ω_{2h} is close to the solution on the mesh Ω_h.

Therefore, it can be concluded that insufficient mesh resolution can give large errors in the numerical solutions. It is important to assess the convergence of the numerical solution against the mesh resolution. Therefore, a simplified problem is defined in order to study the convergence. The simplified problem is derived from the original model by setting the velocity of the boundary of the physical domain to zero. Considering a constant physical domain makes the comparison of numerical solutions more straightforward, compared to the situation when the solutions, which are obtained on the evolving in time domains, should be compared. In order to reduce computation time, the physical domain is simplified to the rectangular region $\bar{\Omega} = \{(r, z) \in [1.41, 1.85]\ mm \times [0, 0.35]\ mm\}$. The part of the domain boundary $(r, z) \in \{1.85\} \times [0, 0.35]$ is assumed to correspond to the old bone surface. The rest of the domain boundary is the implant surface.

It was found from the numerical simulations, that the appearance of a wave-like high density- high concentration layer is most sensitive with respect to the mesh resolution is the x-direction. Further in this subsection, the solutions of simplified problem are compared for meshes with various h_r sizes. The initial meshes $\bar{\Omega}_{4h}$, $\bar{\Omega}_{2h}$, $\bar{\Omega}_h$ and $\bar{\Omega}_{h/2}$ constructed within the simplified physical domain $\bar{\Omega}$ have the respective values 0.02 mm, 0.01 mm, 0.005 mm and 0.0025 mm of the linear size h_r. The lengths of the control volumes along the z- and a axes are kept constant for the present meshes, such that $h_z = 0.0175\ mm$ and $h_a = 0.025$.

Consider the numerical solution of the simplified problem for the parameter values in Tables 4.1 and 4.2, for $E_{pl} = 0$ and for $P_b = 0$. The appearance of wave patterns is studied. The patterns develop from initial perturbations or inhomogeneity of the solution in the $z-$ direction. For the full problem, perturbations appear due to irregular geometry of the physical domain Ω_s. In the simplified problem, an inhomogeneity in the $z-$ direction is imposed through perturbations of the boundary conditions at the old bone surface. The perturbations $\tilde{c}_{bone}$ and $\tilde{g}_{bone}$ are added to the original influx of cells $c_{bone}(a)$ and of growth factors g_{bone}, which are defined in Section 4.3.2 and in Table 4.2. Two modes of perturbations are considered. In the first case,

$$\tilde{c}_{bone} = 0.1 \cdot c_{bone}(a) \sin\left(\frac{\pi z}{0.8}\right), \qquad \tilde{g}_{bone} = 0.1 \cdot g_{bone} \sin\left(\frac{\pi z}{0.8}\right). \tag{4.20}$$

For the second type of perturbations, a random value of the magnitude from 0 to $0.1 \cdot c_{bone}(a)$ and from 0 to $0.1 \cdot g_{bone}$, respectively, is assigned to $\tilde{c}_{bone}$ and $\tilde{g}_{bone}$ at each boundary edge of control volumes, which coincides with

the old bone surface.

Numerical solutions obtained for the mesh $\bar{\Omega}_{4h}$ predict formation of a high density-high concentration layer, which increases in width from the bottom to the top for the both types of perturbations (Figure 4.19). The left boundary of the considered layer has the form of a half wave with the wave-length approximately 0.7 mm. The wave mode is the same for the random perturbations and for the 'sine' perturbations. Therefore, it can be concluded that the form of the initial perturbations does not directly determine the mode of the current pattern in the high density - high concentration layer.

Increase of the mesh resolution in the x-direction yields uniform width of the considered layer near the old bone surface. The distribution of the growth factor concentration at time 9 $days$ obtained for the meshes $\bar{\Omega}_{2h}$, $\bar{\Omega}_h$, $\bar{\Omega}_{h/2}$ and for the perturbations defined in equation (4.20) is shown in Figure 4.20. The layers of high cell densities have the same width as the layers of a high growth factor concentration plotted in Figure 4.20.

For a twice as large value of the chemotaxis parameter χ_0, i.e. for $\chi_0 = 0.648\ mm^2/days$, the boundary layer with nonuniform width is obtained at day 7 for the meshes $\bar{\Omega}_{4h}$ and $\bar{\Omega}_{2h}$, if the perturbations defined in equation (4.20) are added to the boundary conditions. The meshes $\bar{\Omega}_h$ and $\bar{\Omega}_{h/2}$ with a finer resolution provide uniform solutions along the $z-$ axis (see Figure 4.21).

Therefore, at this point the following conclusions can be made:
Clause 1. If the parameter values in Tables 4.1 and 4.2 and $E_{pl} = 0$ are considered, then

- The solution of the full problem is characterized by the appearance of the wave-like high density- high concentration layer with the wave length $\approx 0.7\ mm$ at the end of the first week, if the size of control volumes h_r in r-direction is equal to 0.018 mm (Figure 4.18). If the mesh resolution in the physical space is increased two times, then the high density- high concentration layer has almost a uniform length at day 7 (Figure 4.4).

- The high density- high concentration layer in the solution of the perturbed simplified problem has a wave-like profile with wave length $\approx 0.7\ mm$, if $h_r = 0.02\ mm$ at day 9 (Figure 4.19). The considered layer is uniform for the mesh with the resolution increased two, four and eight times (Figure 4.20).

Clause 2. If the chemotaxis coefficient is increased two times, i.e. $\chi_0 = 0.648\ mm^2/days$, then

- The wave-like layer at the old bone surface appears in the solution of the full problem at the end of the first week for the meshes Ω_{4h}

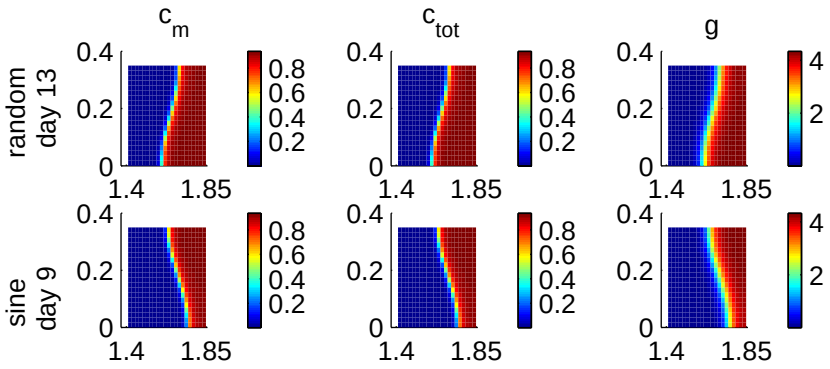

Figure 4.19: Plots of the mature cell density c_m, of the total cell density c_{tot} and of the growth factor concentration g for the parameter values given in Tables 4.1 and 4.2 and for $E_{pl} = 0$, $P_b = 0$ and for the two modes of perturbations: random perturbations (upper row) and 'sine' perturbations defined in equation (4.20) (lower row). The solutions are plotted at time $t = 13$ *days* for random perturbations and at time $t = 9$ *days* for the 'sine' perturbations. The numerical solution is obtained on the mesh $\bar{\Omega}_{4h}$

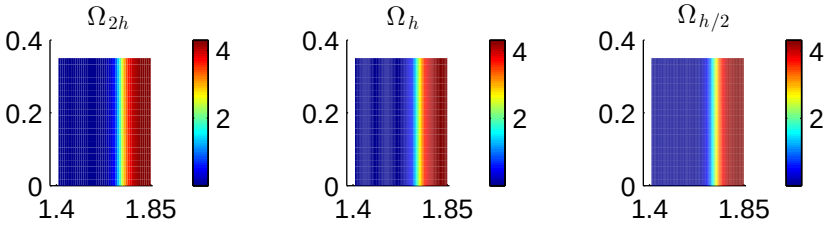

Figure 4.20: Plots of the growth factor concentration g at the time moment $t = 9$ *days* for the parameter values given in Tables 4.1 and 4.2, for $E_{pl} = 0$, $P_b = 0$ and for the 'sine' perturbations defined in (4.20). The numerical solution is obtained on the meshes $\bar{\Omega}_{2h}$, $\bar{\Omega}_h$, $\bar{\Omega}_{h/2}$

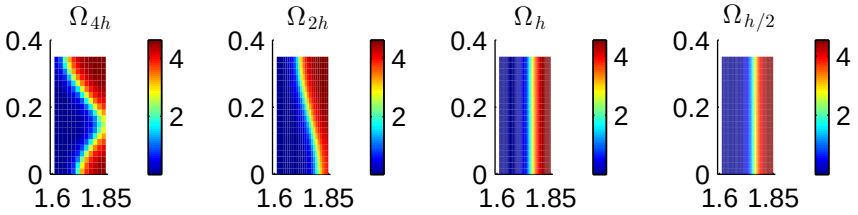

Figure 4.21: Plots of the growth factor concentration g at the time moment $t = 7$ *days* for the parameter values given in Tables 4.1 and 4.2 and for $E_{pl} = 0$, $P_b = 0$, $\chi_0 = 0.648$ $mm^2/days$ and for the 'sine' perturbations defined in (4.20). The numerical solution is obtained on the meshes $\bar{\Omega}_{4h}$, $\bar{\Omega}_{2h}$, $\bar{\Omega}_h$, $\bar{\Omega}_{h/2}$

($h_r = 0.018\ mm$) and Ω_{2h} ($h_r = 0.009\ mm$). The wave length of the left boundary of the layer is $\approx 0.35\ mm$ for Ω_{4h} and $\approx 0.7\ mm$ for Ω_{2h}. The layer is uniform along the z-axis in the solution for the mesh Ω_h with the size $h_r = 0.0045\ mm$.

- The wave-like layer at the old bone surface appears in the solution of the perturbed simplified problem at day 7 for the meshes $\bar{\Omega}_{4h}$ ($h_r = 0.02\ mm$) and $\bar{\Omega}_{2h}$ ($h_r = 0.01\ mm$). The wave length of the left boundary of the layer is $\approx 0.35\ mm$ for $\bar{\Omega}_{4h}$ and $\approx 0.7\ mm$ for $\bar{\Omega}_{2h}$. The layer is uniform along the z-axis in the solution for the meshes $\bar{\Omega}_h$ and $\bar{\Omega}_{h/2}$ with the sizes $h_r = 0.05\ mm$ and $h_r = 0.025\ mm$, respectively.

Clause 3. From Clauses 1 and 2 it follows that the parameter values and the mesh resolution in the x-direction, for which the present phenomenon is observed in the solutions of the full and the perturbed simplified models, perfectly correspond to each other. The wave characteristics of the left boundary of the high density- high concentration layer in the solution of the full problem are fully reflected by the solutions for the perturbed simplified model. Hence the perturbed simplified problem, which is derived in this section, is suitable to study the phenomenon of the appearance of a wave-like high density- high concentration layer near the old bone surface.

Clause 4. Formation of the high density- high concentration layer with a nonuniform width is likely to be related to large errors in the numerical solutions obtained for a coarse mesh. Meshes with a fine enough resolution provide solutions with a uniform distribution of the cells densities and of the growth factor concentration along the old bone surface. The order of convergence of numerical solutions is studied in Section 4.4.3.2.

Clause 5. Values of model parameters influence the appearance of a wave-like high density- high concentration layer. Such a layer is observed, for example, in the numerical simulation for a large value of the chemotaxis parameter χ_0 for the mesh Ω_{2h}. For a twice as small parameter χ_0, the non-uniform layer forms in the solution on the coarser mesh Ω_{4h} but not on Ω_{2h}.

Clause 6. A wave-like pattern formation and splitting of the high density-high concentration layer is observed in the solutions plotted in Figures 4.11 and A.1, which are obtained on the finest mesh that can be afforded for simulations at the present moment. The parameter values are defined in Tables 4.1 and 4.2 and the parameters C_{bone} and t_{cbone} are decreased two times, respectively. Therefore, it is not clear, whether such a solution behavior is characteristic for the exact solution, or whether the numerical solution does not converge to the exact solution for the chosen mesh resolution.

4.4.3.2 Convergence against the mesh resolution

The numerical errors and the order of convergence are estimated by comparing the numerical solutions obtained for various meshes. Convergence is considered against the mesh resolution in each of the r-, z- and a-directions separately. In the series of simulations, the mesh resolution in one direction is varied, and the resolution in the other two dimensions is the same. The simulations considered in this section are performed for the parameter values defined in Tables 4.1 and 4.2 and for $E_{pl} = 0$ and $P_b = 0$.

The order of convergence with respect to the mesh resolution in the z-direction is obtained in the following way. Three meshes with various numbers n_z of control volumes along the z-axis are considered. The sizes of control volumes along the r- and a-axes are fixed and are equal to 0.0025 mm and 0.025, respectively. The sizes h_r and h_a are chosen to be as small as possible, in order to make the error due to discretization in the r- and a- axes comparatively small. On the other hand, the considered sizes should provide a reasonable computation time. The considered three meshes, referred to as $\bar{\Omega}_{nz=10}$, $\bar{\Omega}_{nz=20}$ and $\bar{\Omega}_{nz=40}$, have 10, 20 and 40 control volumes along the z-axis, respectively. The length of the physical domain $\bar{\Omega}$ in the z-direction is 0.7 mm. Hence, the present meshes are characterized by the respective sizes $h_z = 0.035\ mm$, $h_z = 0.0175\ mm$ and $h_z = 0.00875\ mm$.

Remark 4.8. The positivity and stability requirements impose severe restrictions on the time step size. Therefore, the time steps used for the simulations presented in this section are very small. Comparison of the numerical solution obtained for various time steps sizes shows, that the numerical error due to time integration is several orders smaller that the errors due to spatial discretization. Therefore the time integration errors are not considered below in the text.

The numerical solutions obtained on the meshes $\bar{\Omega}_{nz=10}$, $\bar{\Omega}_{nz=20}$ and $\bar{\Omega}_{nz=40}$ are compared in the following way. The solution defined on a finer mesh is projected onto the coarser mesh. The numerical solutions for the total cell density, for the mature cell density and for the growth factor concentration are denoted, respectively, by $\vec{C}_{tot}^{nz=20}(t)$, $\vec{C}_{m}^{nz=20}(t)$ and $\vec{G}^{nz=20}(t)$, where the superscript $nz = 20$ refers to the resolution of the mesh, on which the present solution is defined, i.e. of the mesh $\bar{\Omega}_{nz=20}$ for the present notations. The solution on the mesh $\bar{\Omega}_{nz=20}$ can easily be projected onto the coarser mesh $\bar{\Omega}_{nz=10}$. Each control volume of $\bar{\Omega}_{nz=10}$ contains exactly two control volumes of the mesh $\bar{\Omega}_{nz=20}$. Hence the projected average value of some unknown (a cell density or the growth factor concentration) within a control volume of the mesh $\bar{\Omega}_{nz=10}$ is equal to the mean value of the (average) values of this unknown within two corresponding control volumes of the mesh $\bar{\Omega}_{nz=20}$. The solution $\vec{U}^{nz=40}(t)$, $U \in \{\vec{C}_m, \vec{C}_{tot}, \vec{G}\}$, is projected onto $\bar{\Omega}_{nz=10}$ in a similar way. The projected solutions are denoted, respectively, by $L_{nz=20}^{nz=10}U^{nz=20}(t)$ and $L_{nz=40}^{nz=10}U^{nz=40}(t)$, $U \in \{\vec{C}_m, \vec{C}_{tot}, \vec{G}\}$, where

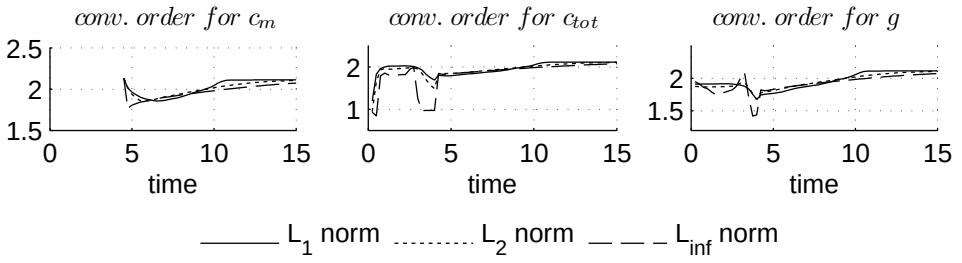

Figure 4.22: Plots of the estimated order of convergence with respect to the mesh resolution the z-direction against time, which is derived from the solutions obtained on the meshes $\bar{\Omega}_{nz=10}$, $\bar{\Omega}_{nz=20}$ and $\bar{\Omega}_{nz=40}$. Three types of vector norms are considered: L_1, L_2 and L_∞.

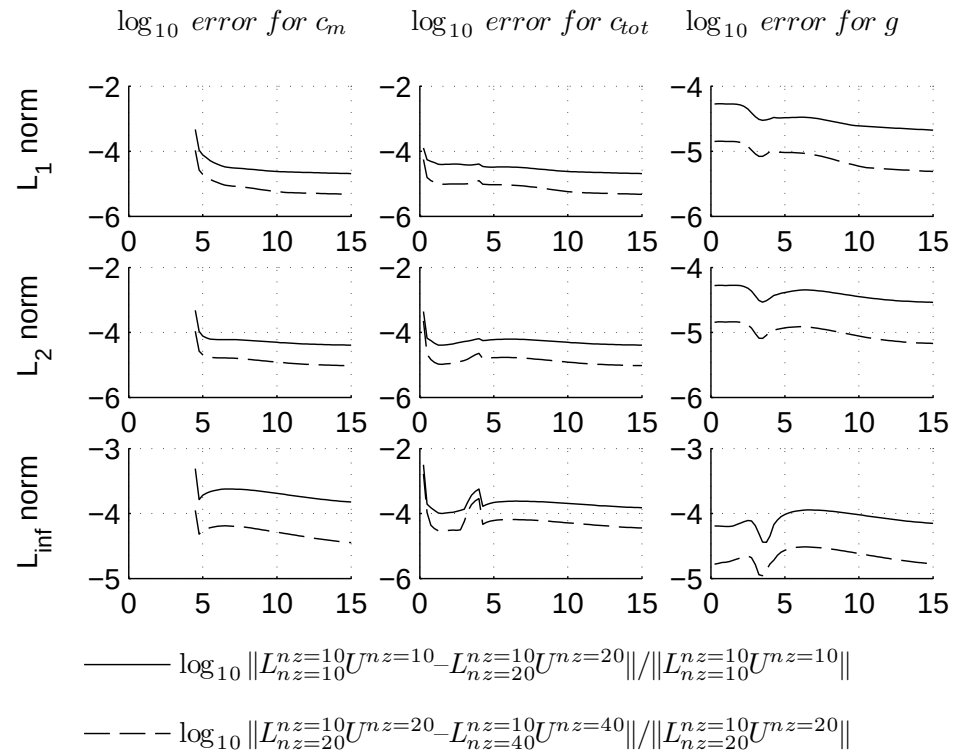

Figure 4.23: Plots of the order of relative errors between the numerical solutions obtained on the meshes $\bar{\Omega}_{nz=10}$ and $\bar{\Omega}_{nz=20}$ (blue curve) and $\bar{\Omega}_{nz=20}$ and $\bar{\Omega}_{nz=40}$ (green curve). Three types of vector norms are considered: L_1, L_2 and L_∞.

$L_{nz=N}^{nz=10}$ is the projection operator from the mesh $\bar{\Omega}_{nz=N}$, $N = \{20, 40\}$, onto the mesh $\bar{\Omega}_{nz=10}$. Note that $L_{nz=10}^{nz=10} U^{nz=10}(t) = U^{nz=10}(t)$. The convergence order is estimated by comparing the solutions for three consecutive mesh resolutions. For example, the convergence order, which is determined for the total cell density c_{tot} from the numerical solutions on the meshes $\bar{\Omega}_{nz=10}$, $\bar{\Omega}_{nz=20}$ and $\bar{\Omega}_{nz=40}$, is calculated as

$$p = \log_2 \frac{\| L_{nz=10}^{nz=10} C_{tot}^{nz=10} - L_{nz=20}^{nz=10} C_{tot}^{nz=20} \|}{\| L_{nz=20}^{nz=10} C_{tot}^{nz=20} - L_{nz=40}^{nz=10} C_{tot}^{nz=40} \|} \tag{4.21}$$

Derivation of equation (4.21) is based on the Richardson extrapolation and on the assumption that the numerical error obtained on the mesh with a cell size h is equal to Ch^p (see, for example, Vuik et al. [95]).

The order of convergence, which is calculated in different vector norms, is shown in Figure 4.22. From Figure 4.22, it follows that the estimated convergence order is close to two most of the time. However the order can decrease to values less than one at certain time moments. The most likely reason for such a fluctuation of the estimated convergence order is that the mesh sizes h_r and h_a along r- and a-axes are not sufficiently small. The error from the discretization in the r- and a-direction is combined with the error of discretization in the z-direction. This issue leads to jumps of the estimated order of convergence shown in Figure 4.22.

The difference between the numerical solutions, obtained on the considered consecutive meshes, can be used to assess the order of the total numerical error related to the current mesh resolution in the z-direction. The logarithm of the relative error between the numerical solutions, that is calculated in different vector norms, is plotted in Figure 4.23. In most of the plots in Figure 4.23, the relative errors are not larger than 10^{-4}. The maximum relative errors after time $t = 5$ *days* appear in the solution for c_m and c_{tot} and they are smaller than $10^{-3.5}$.

By analogy, the convergence of the numerical algorithm in the other two spatial directions is derived. The convergence against h_r is estimated from the numerical solutions obtained on the following meshes. The linear sizes h_z and h_a are equal to 0.035 *mm* and 1/160, respectively. Three values of the size h_r: 0.01 *mm*, 0.005 *mm* and 0.0025 *mm* are used for the meshes $\bar{\Omega}_{nr=44}$, $\bar{\Omega}_{nr=88}$ and $\bar{\Omega}_{nr=176}$.

The convergence of the algorithm in the a-direction is derived for the meshes $\bar{\Omega}_{na=40}$, $\bar{\Omega}_{na=80}$ and $\bar{\Omega}_{na=160}$, which have, respectively, 40, 80 and 160 elements along the a-axis. The sizes h_r and h_z are equal to 0.0025 *mm* and 0.035 *mm*, respectively.

The estimated order of convergence against the grid sizes h_r and h_a is plotted in Figures 4.24 and 4.25, respectively. The corresponding relative errors are shown in Figures 4.26 and 4.27.

The order of convergence in the r-direction is estimated between the values 2.2 and 2.6 after $t = 6$ *days*. It is larger than the actual order of

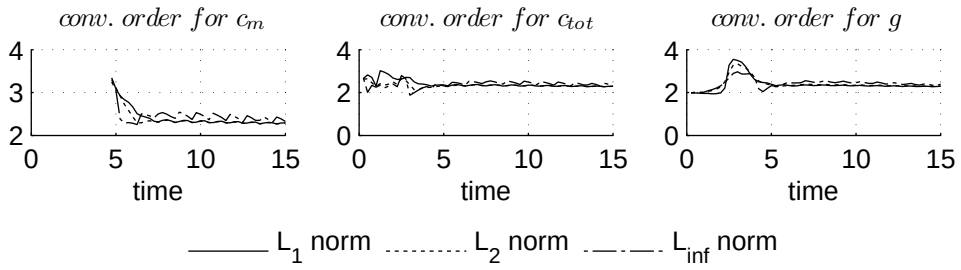

Figure 4.24: Plots of the estimated order of convergence with respect to the mesh resolution the r-direction against time, which is derived from the solutions obtained on the meshes $\bar{\Omega}_{nr=44}$, $\bar{\Omega}_{nr=88}$ and $\bar{\Omega}_{nr=176}$. Three types of vector norms are considered: L_1, L_2 and L_∞.

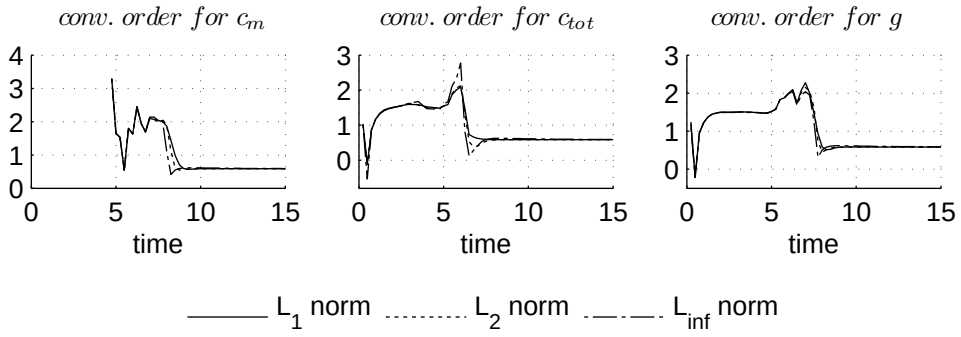

Figure 4.25: Plots of the estimated order of convergence with respect to the mesh resolution the a-direction against time, which is derived from the solutions obtained on the meshes $\bar{\Omega}_{na=40}$, $\bar{\Omega}_{na=80}$ and $\bar{\Omega}_{na=160}$. Three types of vector norms are considered: L_1, L_2 and L_∞.

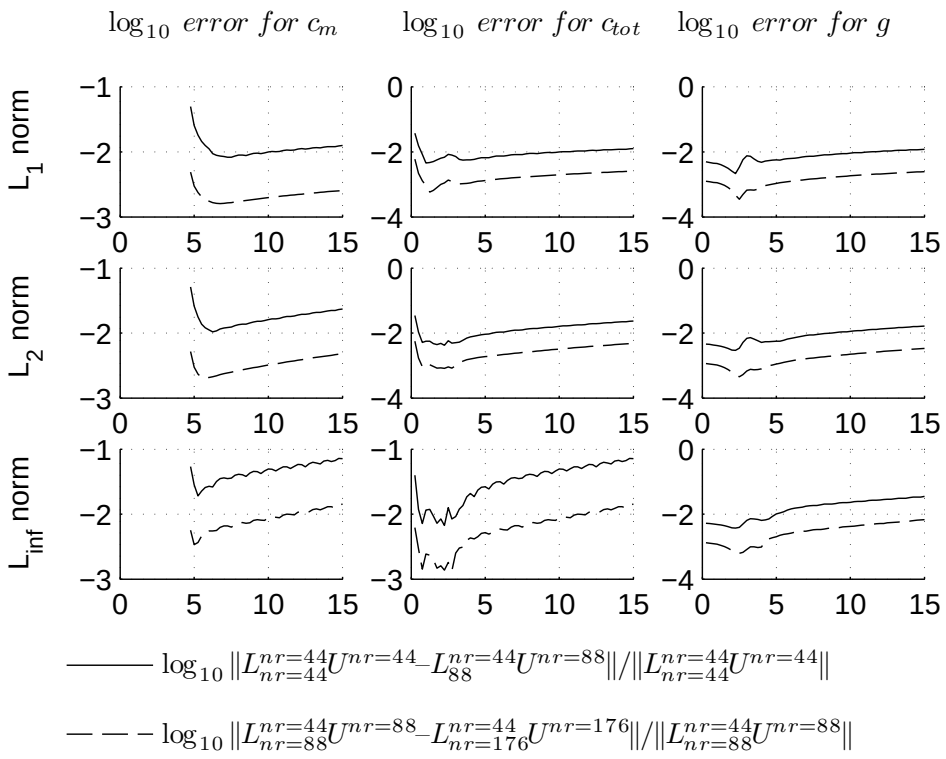

Figure 4.26: Plots of the order of relative errors between the numerical solutions obtained on the meshes $\bar{\Omega}_{nr=44}$ and $\bar{\Omega}_{nr=88}$ (blue curve) and $\bar{\Omega}_{nr=88}$ and $\bar{\Omega}_{nr=176}$ (green curve). Three types of vector norms are considered: L_1, L_2 and L_∞.

the accuracy of the numerical scheme, used for the spatial discretization of the model equations (4.1)–(4.3), which is equal to two on the uniform rectangular grid. The errors related to the variation of the mesh resolution in the r-direction (Figure 4.26) are much larger than those related to the sizes h_z and h_a (after time $t = 7$ *days*) plotted in Figures 4.23 and 4.27. The former errors prevail in the numerical solution for $t > 7$ *days* and have the most influence on the estimated convergence order. Due to a large computation time, it is not possible to estimate the convergence order for finer meshes with simultaneous refinement in all directions.

The convergence of the algorithm against the resolution in the a-direction is very poor (Figure 4.24). The first possible reason for this, is that a larger number of elements should be considered in the a-direction, in order to obtain better convergence estimates. The second potential reason, is that the errors due to discretization in r- and z- direction have a considerable influence on the behavior of the solution. Such a possibility follows from the order of the relative errors, plotted in Figures 4.23, 4.26 and 4.27. The estimated errors related to the discretization along the r-axis are comparable with the errors related to the discretization along the a-axis during the first week of simulation. The former errors become much larger than the latter ones for $t > 7$ *days*. Further increase of the mesh resolution is likely to yield a larger order of convergence of the numerical solution, which would approach the order of accuracy of the spatial discretization. However, it is not possible to get a solution for finer meshes due to limited computational resources.

Remark 4.9. It follows from the performed numerical simulations that the appearance of the wave-like patters of the high density- high concentration layer is influenced in general by the mesh size h_r. The slow convergence against the mesh resolution in the a-direction is not likely to influence such critical solution characteristics as the earlier mentioned wave-like patterns and splitting of the high density- high concentration layer.

An important conclusion, which should be drawn from the results of simulations, is that one should be very careful with choosing a mesh resolution when using the present numerical approach for the considered model. In some situations, it is not possible to assess the robustness of the solution based only on speculative conclusions about the biological relevance of the simulation results.

An analysis of the solution convergence against the mesh element size can reveal the hidden nature of large errors. Furthermore, a stability analysis of the mathematical model, as well as for the semi-discrete equations is of relevance.

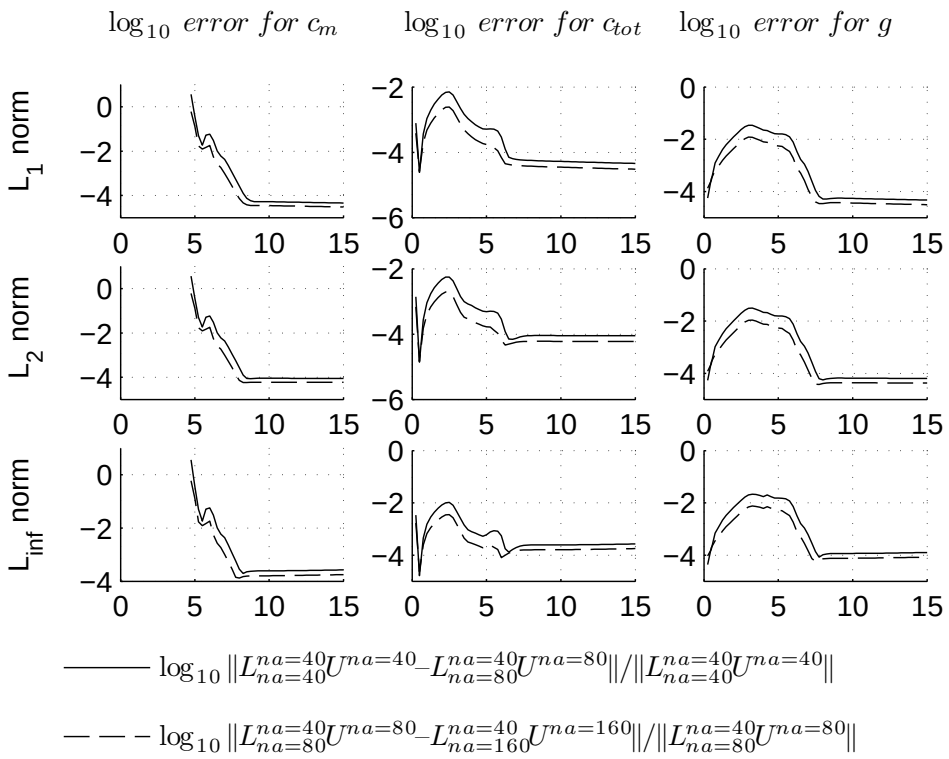

Figure 4.27: Plots of the order of relative errors between the numerical solutions obtained on the meshes $\bar{\Omega}_{na=40}$ and $\bar{\Omega}_{na=80}$ (blue curve) and $\bar{\Omega}_{na=80}$ and $\bar{\Omega}_{na=160}$ (green curve). Three types of vector norms are considered: L_1, L_2 and L_∞.

4.5 Results and discussion

We consider the solutions obtained for the reference values of the model parameters given in Tables 4.1 and 4.2 in more detail. Two types of implants are considered. The limit value $E_{pl}^{lim} = 0.32\ mm/days$ is assigned to the parameter E_{pl} in simulations for a turned implant.

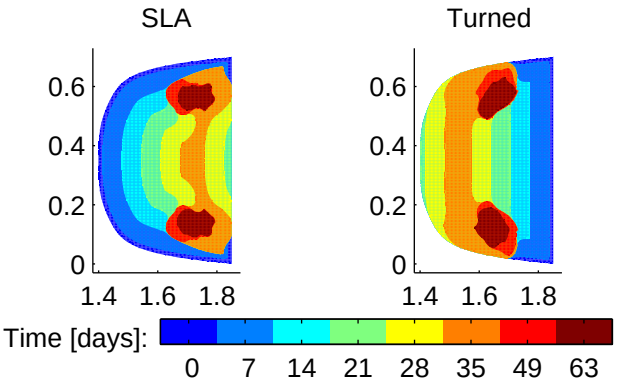

Figure 4.28: Evolution of the soft tissue region, due to formation of new bone near a micro-rough SLA implant and near a smooth turned implant. The contours correspond to the boundary of the soft tissue region, which shrinks, at time 0, 7, 14, 21, 28, 35, 49 and 63 days

Remark 4.10. It should be emphasized that the implant surface microstructure is not considered explicitly. The difference between turned and rough implants is modeled implicitly, by means of various values for the growth factor source at the implant surface. This feature is dealt with in a similar way in the recent models by Amor et al. [6] and Moreo et al. [67].

The evolution of the soft tissue region Ω_s for a smooth turned implant and a micro-rough SLA implant is shown in Figure 4.28. The contours represent the boundary of the soft tissue domain at time 0, 7, 14, 21, 28, 35, 49 and 63 days. The soft tissue region shrinks in both cases. However, the bone-forming surface moves in two different ways for a turned and SLA implant, respectively. The ossification front starts to move from the implant surface if the micro-rough implant is considered, whereas it moves from the old bone surface till day 26 in the case of the smooth turned implant. In other words, contact and distance osteogenesis are predicted for the rough and smooth implants, respectively. Contact osteogenesis leads to a slightly faster formation of new bone matrix, compared with distance osteogenesis. In Figure 4.29, the areas of newly formed bone for both implant types are plotted against time. The area of the healing site Ω is represented by the dotted line and the areas of newly formed bone near the SLA and turned implants are shown by the solid and dashed lines, respectively. From Figure 4.29, it follows that approximately a half of the entire healing site is

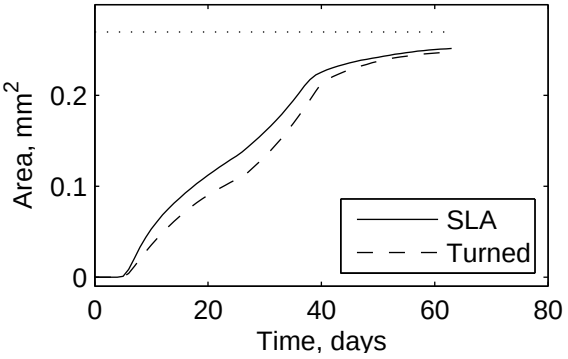

Figure 4.29: The area of newly formed bone against time for contact and distance osteogenesis, which are observed near the SLA and turned implants, respectively. The area of the healing site Ω is represented by the dotted line

filled by new bone matrix at the end of the fourth week near the rough implant and near the smooth implant. In the case of the SLA implant, the layer of a high concentration of growth factors and a high density of mature osteogenic cells, which is adjacent to the ossification front, reaches the old bone surface at day 25 (see Figures 4.15 and 4.28). Hence bone formation is initiated at the old bone surface at day 25 and the length of the bone forming surface increases rapidly. This issue leads to the increase of the amount of new bone released per unit of time, which is reflected by the increase of the slope of the solid line in Figure 4.29 at time $t = 25$ *days*. An analogous effect is observed for the turned implant at the day 27. The layer of a high cell density and of a high growth factor concentration reaches the implant body surface at this time (Figure 4.31). Hence bone starts forming at the implant surface and the rate of new bone formation increases rapidly.

The SLA implant is predicted to be in a direct contact with a newly formed bone at the end of the first week (Figure 4.28). It may be assumed that a direct bone-to-implant contact may provide an earlier and better anchorage of implants [1, 24, 32]. Almost the entire peri-implant region is predicted to be filled with new bone matrix after nine weeks of simulation for the both implant types.

Two different modes of bone formation are observed, because of two different sources of growth factors near the implant surfaces. Due to a strong source on the micro-rough SLA implant, a high concentration of growth factors near the implant surface (see the lower left plot in Figure 4.30) leads to active migration of osteogenic cells from the old bone surface to the implant, and, consequently, to active differentiation of immature cells into mature osteogenic cells near the implant, which release new bone matrix (see the upper left plot in Figure 4.30). Cells at a high maturation level release growth factors, hence the concentration of growth factors is maintained at a

high level near the micro-rough implant surface during the first four weeks (see Figure 4.15).

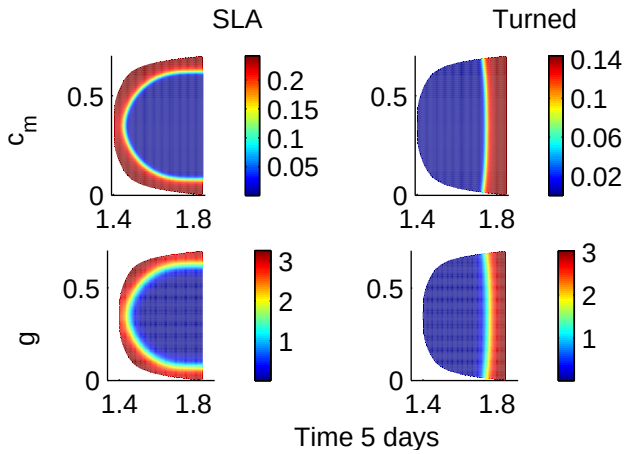

Figure 4.30: Distribution of the mature cell density c_m and of the growth factor concentration g in the soft tissue region at time 5 days near SLA and turned implants. High concentration of growth factors leads to differentiation of immature osteogenic cells into mature cells at the SLA implant surface. No growth factors and no mature cells are found near the turned implant

In experiments of Berglundh et al. [14] and Abrahamsson et al. [1], new bone formation was observed both on the SLA implant surface and on the old bone surface. However, the ossification front is predicted to move only from the SLA implant surface in the current simulations. The model parameter values providing a better correspondence of the model predictions with experimental results are not found. Adaptation of the treatment of diffusion and chemotaxis of the cells in the model, by introducing various functional dependencies of the corresponding coefficients on the cell densities and/or the growth factor concentration, is a potential direction of the improvement of the present model.

A weak source of growth factors is considered at the smooth implant surface, and the concentration of growth factors is very low in this region during the first days in the simulation (see the lower right plot in Figure 4.30). Due to a low growth factor concentration, cells are not attracted to the implant surface by a chemotaxis mechanism. The cells are concentrated at the old bone surface, due to a much larger source of growth factors in this area. A low concentration of growth factors yields a slow cell differentiation at the implant surface (see the dependence of the differentiation rate u_b on g in Table 4.1). Cells with low maturation level release growth factors at a low rate (see equation (5.3) and the expression for $\gamma(a)$ in Table 4.1). Due to the aforementioned factors and due to a high decay rate d_g, the concentra-

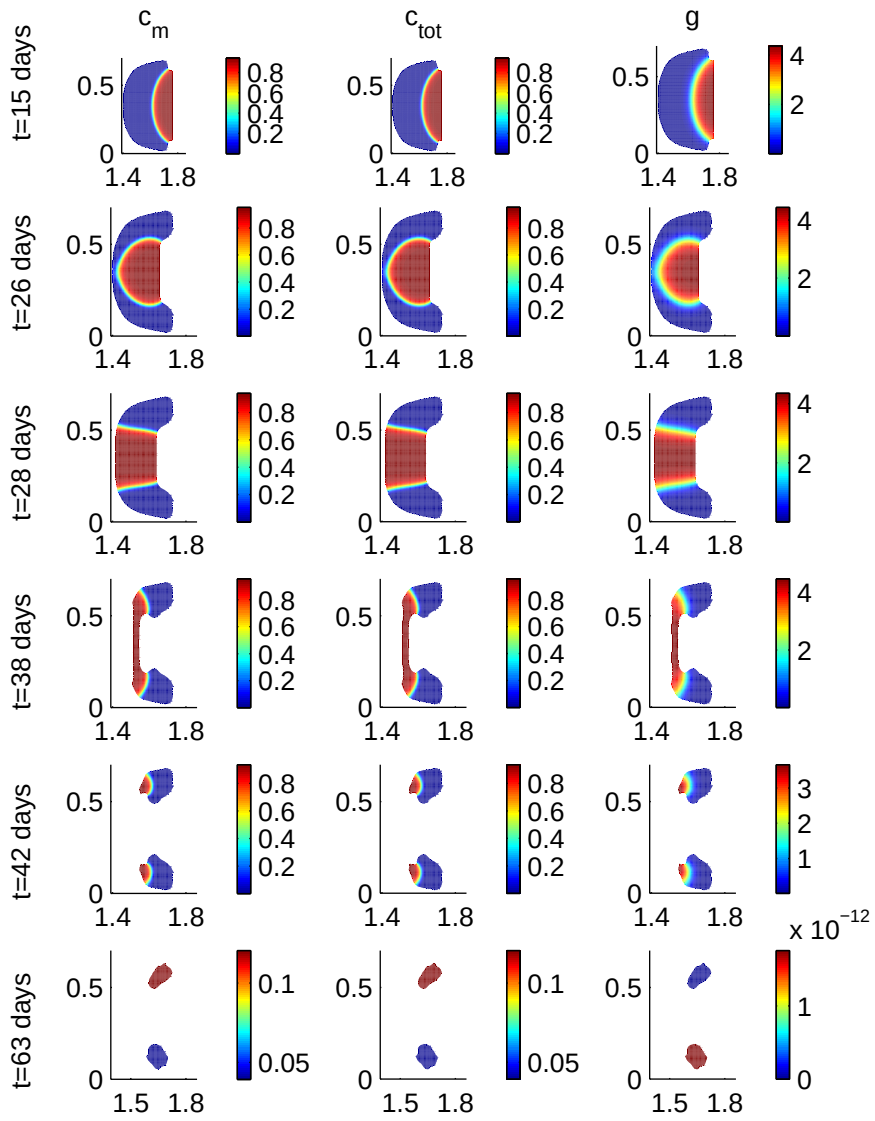

Figure 4.31: Plots of the mature cell density c_m, of the total cell density c_{tot} and of the growth factor concentration g at the time moments $t = 15$, 26, 28, 38, 42 and 63 *days* for the parameter values given in Tables 4.1 and 4.2 and for $E_{pl} = 0.1 \cdot 3.2$ $mm/days$, i.e. a turned implant considered. No growth factors and no mature cells are found near the turned implant till day 26. Hence distance osteogenesis is predicted by the numerical simulations

tion of growth factors and the density of mature osteogenic cells are close to zero near the implant surface till day 26. As a result, no bone forms at the surface of the smooth implant during this period (Figure 4.31).

4.6 Conclusions

A general mathematical model for peri-implant bone regeneration is formulated, which is able to capture some important features, that are observed in reality. The model is defined for the immature and mature osteogenic cell densities and for the growth factor concentration. Cell differentiation is considered as an evolutionary process, regulated by the presence of growth factors. Immature cells are distinguished with respect to the differentiation level, which is represented by the additional independent variable a, defined in the maturation space $[0, 1]$. Consequently, the differentiation path of individual cells can be considered.

During peri-implant osseointegration, new bone is produced by osteoblasts, attached to a rigid surface [1, 14, 65]. Bone formation takes place only through a direct apposition of new bone matrix on a pre-existing rigid surface [24]. That is, endosseous bone healing occurs in the form of intramembranous ossification, which can be considered as a moving boundary-type of bone formation. This effect is *directly* incorporated into the model, by the use of the concept of a bone-forming surface, which is defined as a moving boundary of a temporarily evolving computational domain. This is the *main innovation* of the current model, that distinguishes the current formalism from the recent models for the peri-implant bone regeneration. Cell processes, like migration, differentiation and proliferation, are considered within the region, filled with soft tissue and bounded by the bone-forming surface. Osteoblasts are represented by the mature cells, which are situated at the bone-forming surface. Bone formation is introduced through the movement of the boundary of the computational domain. Since bone is released by osteoblasts and boundary movement corresponds to the formation of new bone matrix, the velocity of the boundary movement is assumed to be proportional to the local osteoblast density. The model is composed of a system of partial differential equations, defined within the domain with a moving boundary, along with the set of initial and boundary conditions.

In experiments of Abrahamsson et al. [1], contact and distance osteogenesis are observed for micro-rough SLA implants and smooth turned implants, respectively. It is assumed that this switch in osseointegration mode is caused by different rates of growth factor release by activated platelets near the implant surfaces with different micro-structure [56, 71]. In the present model, the release of growth factor at the implant surface is represented by means of boundary conditions.

A number of the 2D simulations have been carried out. Two modes of

bone formation are predicted for the smooth and micro-rough implants. The micro-structure of the implant surface is modeled implicitly, by changing the source of growth factors at the implant surface. Contact and distance osteogenesis are modeled near the micro-rough SLA implant and the smooth turned implant, respectively. Two dimensional simulations allow to model various paths of the ossification front corresponding to different sources of growth factors at the implant surface.

CHAPTER 5

Numerical algorithm

5.1 Introduction

In this chapter, a numerical approach for the solution of the time-dependent advection-diffusion-reaction equations is described. The equations are defined for a model of bone healing near endosseous implants in Chapter 4. The model is constructed to simulate early stages of bone regeneration. The equations model migration of osteogenic cells from the old bone surface to the implant surface, cell differentiation and proliferation. These processes are assumed to be regulated by growth factors. Diffusion, decay and release of growth factors by osteogenic cells are also taken into account. The unknowns in the model are the densities of immature and mature osteogenic cells and the concentration of growth factors. New bone is formed through apposition on a pre-existing surface [24]. The advance of the ossification front, which was observed in experiments by Abrahamsson et al. [1], Berglundh et al. [14], Meyer et al. [65], is modeled by the movement of the boundary of the physical domain.

A robust method is constructed, which allows to get a numerical solution in case, when the physical domain is defined in 2D axisymmetric coordinates. First, an appropriate discretization in physical space, maturation space and time should be chosen, such that a stable nonnegative solution of the nonlinear advection-diffusion-reaction equations will be obtained. The movement of the domain boundary, determined from the internal solution, is tracked with use of the level set method. The embedded boundary method and some auxiliary interpolation techniques are elaborated in order to adapt the finite volume discretization, which is in general defined on the structured rectangular grid, to the evolving irregular physical domain.

Therefore, in Section 5.2, a short description of the model for peri-

implant osseointegration is given. The numerical algorithm, developed for the two dimensional physical domain is described in Section 5.3. The importance of positivity of the numerical solution is outlined in Section 5.3.1. In Section 5.3.2 the construction of the computational mesh within the irregular physical domain is presented. The level set function is used to track the temporal changes of the domain. The level set equation and the solution method are presented in Section 5.3.3. The equations for averaged quantities, derived from the initial governing equations, are constructed in Section 5.3.4. The discretization of the advection-diffusion terms is considered in Section 5.3.5, which demands the solution of the Riemann problem, defined for the system of hyperbolic equations. The Riemann solution is developed in Section 5.3.6. The approximation of the reaction terms, the boundary conditions and the time integration of the discretized ordinary differential equations are discussed in Sections 5.3.7, 5.3.8 and 5.3.9, respectively. Final conclusions are drawn in Section 5.4.

5.2 Mathematical model

For convenience, the model equations from Chapter 4 are summarized in this section. The model for bone regeneration, consists of three partial differential equations (PDE's), defined for the densities of immature and mature osteogenic cells, denoted as c_i and c_m, and for the concentration of growth factors g. The peri-implant interface Ω is divided into two subdomains Ω_s and Ω_b, which are occupied by soft connective tissue (fibrin network of blood clot) and new bone respectively. Osteogenic cells and growth factors are found within the soft tissue region. The boundary between subdomains Ω_s and Ω_b is the bone-forming surface. This interface moves in time and is denoted as $\Gamma(t)$.

The evolution of the unknown variables is determined by the following PDE's

$$\frac{\partial c_i}{\partial t} = -\nabla_s \cdot \left(-D_c \nabla_s c_i + \chi(g, c_{tot})\, c_i \nabla_s g\right) - \frac{\partial}{\partial a}\left(u_b(g) c_i\right) + A_c(g) c_i \left(1 - c_{tot}\right), \quad (5.1)$$

$$\frac{\partial c_m}{\partial t} = -\nabla_s \cdot \left(-D_c \nabla_s c_m + \chi(g, c_{tot})\, c_m \nabla_s g\right) + u_b(g) c_i(\vec{x}, 1, t) + A_c(g) c_m \left(1 - c_{tot}\right), \quad (5.2)$$

$$\frac{\partial g}{\partial t} = \nabla_s \cdot \left(D_g \nabla_s g\right) + E_c(g) \left(c_m + \int_0^1 \gamma(a) c_i \, da\right) - d_g g, \quad (5.3)$$

where $c_{tot} = \int_0^1 c_i da + c_m$ is the total density of osteogenic cells per unit of volume. Equation (5.1) is defined for $(\vec{x}, a, t) \in \Omega_s \times [0,1] \times \mathbb{R}^+$, and equations (5.2), (5.3) – for $(\vec{x}, t) \in \Omega_s \times \mathbb{R}^+$. Operator ∇_s is the nabla operator, defined in physical space, e.g. in cylindrical coordinates

$$\nabla_s = \vec{e_r}\frac{\partial}{\partial r} + \vec{e_\theta}\frac{\partial}{\partial \theta} + \vec{e_z}\frac{\partial}{\partial z}\,.$$

The movement of the boundary $\Gamma(t)$ of the physical domain Ω_s is determined by the following expressions for its initial location $\Gamma(0)$ and the normal velocity v_n:

$$\begin{cases} \Gamma(0) = \partial\Omega_b \cup \partial\Omega_i, \\ v_n(\vec{X}, t) = -P_b\, c_m(\vec{X}, t), \quad \vec{X} \in \Gamma(t),\ t > 0. \end{cases} \tag{5.4}$$

The initial cell densities and growth factor concentration are assumed to be zero:

$$c_i(\vec{x}, a, 0) = 0,\ c_m(\vec{x}, 0) = 0,\ g(\vec{x}, 0) = 0, \qquad \vec{x} \in \Omega_s,\ a \in [0,1]. \tag{5.5}$$

The natural boundary conditions are imposed, by equating the sources h_i, h_m and h_g to the normal fluxes of the variables c_i, c_m and g:

$$(-D_c \nabla_s c_i + \chi(g, c_{tot}) c_i \nabla_s g)\,(\vec{X}, a, t) \cdot \vec{n}(\vec{X}, t) = h_i(\vec{X}, a, t), \tag{5.6}$$

$$(-D_c \nabla_s c_m + \chi(g, c_{tot}) c_m \nabla_s g)\,(\vec{X}, t) \cdot \vec{n}(\vec{X}, t) = h_m(\vec{X}, t), \tag{5.7}$$

$$-D_g \nabla_s g(\vec{X}, t) \cdot \vec{n}(\vec{X}, t) = h_g(\vec{X}, t), \tag{5.8}$$

for $\vec{X} \in \Gamma(t)$, $a \in [0,1]$, $t > 0$ and

$$h_i(\vec{X}, a, t) = \begin{cases} 0, & a \in [0,1], \vec{X} \in \partial\Omega_i, t \le t_c, \\ -c_{bone} \cdot \frac{2}{\delta_a}(1 - \frac{a}{\delta_a}), & a \in [0, \delta_a], \vec{X} \in \partial\Omega_b, t \le t_c, \\ 0, & a \in [\delta_a, 1],\ \vec{X} \in \partial\Omega_b, t \le t_c, \\ c_i(\vec{X}, a, t)\ v_n(\vec{X}, t), & a \in [0,1], \vec{X} \in \Gamma(t), t > t_c, \end{cases} \tag{5.9}$$

$$h_m(\vec{X}, t) = 0, \quad \vec{X} \in \Gamma(t), t > 0 \tag{5.10}$$

$$h_g(\vec{X}, t) = \begin{cases} -\,g_{impl}(t), & \vec{X} \in \partial\Omega_i, t \le t_g, \\ -\,g_{bone}, & \vec{X} \in \partial\Omega_b, t \le t_g, \\ g(\vec{X}, t)\ v_n(\vec{X}, t), & \vec{X} \in \Gamma(t), t > t_g. \end{cases} \tag{5.11}$$

In the above formulas, $v_n(\vec{X}, t)$ is the normal velocity of the boundary $\Gamma(t)$ of subdomain Ω_s. The differentiation rate is assumed to be nonnegative.

Therefore, the following natural boundary condition is specified at the inflow boundary, in order to provide uniqueness of the solution:

$$u_b(g(\vec{X},t))\; c_i(\vec{X},a,t) = 0, \quad \vec{X} \in \Omega_s, a = 0, t > 0. \tag{5.12}$$

The expressions and the values for the model parameters are defined in Tables 4.1 and 4.2.

5.3 Numerical method

In this section a numerical method is described for a solution of the governing equations of the present osseointegration model in a 2D axisymmetric physical domain.

Consider the physical domain Ω_s, defined in the 2D axisymmetric coordinates (r, z). For the current problem statement, the physical domain is of irregular shape, and it evolves in time. In this case, the conventional finite volume discretization of the governing equations on the structured rectangular grid cannot be used in a straight-forward way. Therefore, irregular cells are used, in order to capture the irregular geometry. Further, the level set method is applied to track the evolution of the problem domain.

The method of lines forms the basis of the present numerical approach. First, the governing equations are discretized in the physical domain Ω_s and in the differentiation state domain $[0, 1]$, but not yet in time. The system of the PDE's is reduced to a system of ordinary differential equations (ODE's). Subsequently, a time integration technique is applied to solve the ODE's.

Remark 5.1. The governing equations (5.1)–(5.3) are solved within the soft tissue region Ω_s. No unknowns are defined in the subdomain Ω_b, and this region is never considered during the solution procedure. Therefore, for convenience, the terms *'physical domain'* and *'computational domain'* are used with respect to the soft tissue region Ω_s further in the text.

5.3.1 Positivity of the solution

The initial densities of cells and the initial growth factor concentration are zero (see equation (5.5)). The outflow of c_i, c_m and g at the boundaries given by the fluxes h_i, h_m and h_g in equations (5.9)–(5.11) is nonpositive, if c_i, c_m and g are nonnegative. Hence the boundary conditions model the influx of cells and of growth factors and they do not lead to negative solutions. Then it can be shown that the governing equations (5.1)–(5.3) have a nonnegative solution for the present initial and boundary conditions. Equation (5.1) can be rewritten in the following form:

$$\frac{\partial c_i}{\partial t} = D_c \nabla_s^2 c_i - \chi(g, c_{tot})\; \nabla_s g \cdot \nabla_s c_i - u_b(g) \frac{\partial c_i}{\partial a} \\ - c_i\; \nabla_s \cdot (\chi(g, c_{tot})\; \nabla_s g) + A_c(g) c_i\,(1 - c_{tot})\,, \tag{5.13}$$

The first term in the right-hand side is a diffusion term, the second and the third terms model advection in the physical space and in the maturation space with the velocities $\chi(g, c_{tot})\,\nabla_s g$ and $u_b(g)$, respectively. The last two terms in the right-hand side are the reaction terms, which become equal to zero, if $c_i = 0$. Therefore, neither of the terms in the right-hand side of equation (5.13) can lead to a sign-change over time and hence there is no appearance of negative values in the solution for c_i, if $c_i > 0$ on Ω_s at a certain time. The same conclusions can be drawn for equations (5.2), (5.3) providing a nonnegative solution for c_m and g for the present initial and boundary conditions.

Therewith, the exact solution of the considered problem should be nonnegative. However, it is quite common in practice, that numerical simulations give approximate solutions with negative values, even if an exact solution is known to be positive. This issue does not have any critical meaning, as long as numerical solutions converge to the exact solution.

A numerical algorithm described in this chapter provides nonnegative solutions for the present model. The requirement on the positivity of approximate solutions is essential in the current case due to the following reasons:

- Small negative values appearing in the numerical solutions may grow in magnitude fast due to nonlinearity of the fluxes of cells. The taxis term is divided into advection and reaction terms in equation (5.13). The reaction term (the fourth term in the right-hand side of equation (5.13)) is responsible for potential growth of negative values. More insight into the behavior of the system with nonlinear fluxes can be provided by considering a Riemann problem and by splitting the solution into a set of waves. The Riemann solution is described in Section 5.3.6. In Section 5.3.6.4, it is shown that nonclassical delta shock waves may form in the Riemann solution, if negative cell densities appear in the numerical solution at some time moment. Due to cell diffusion, delta shock waves are smoothed and look like peaks and troughs growing in magnitude. Large negative values in the approximate solution indicate that convergence to a nonnegative exact solution is not achieved.

- Furthermore, negative cell densities do not make any biological sense.

- According to the present model a negative local density of osteoblasts leads to a reverse movement of the bone-forming front, i.e. to bone resorption. That is another unphysical consequence of negative approximate solutions of the model.

Therefore, a numerical algorithm should provide nonnegative values for the cell densities in order to ensure a convergence and biological relevance of the numerical solution.

5.3.2 Definitions of cells and vertices in the grid

The physical domain Ω_s is defined in the 2D axisymmetric coordinate system (r, z). Let us consider some rectangular region $[R_0, R_1] \times [Z_0, Z_1]$, which contains region Ω_s. Within this rectangular region, the uniform rectangular $N_r \times N_z$ grid is constructed. The grid contains the set $\mathscr{W}$ of rectangular cells (or control volumes) $W_{j,k} \in \mathscr{W}$, $(j,k) \in \mathscr{I}_c = \{1, 2, .., N_r\} \times \{1, 2, .., N_z\}$, and the set Ψ_h of cell vertices $v_{j+\frac{1}{2},k+\frac{1}{2}} \in \Psi_h$, $(j,k) \in \mathscr{I}_v = \{0, 1, .., N_r\} \times \{0, 1, .., N_z\}$. The control volumes and the vertices are defined as $W_{j,k} = [r_{j-\frac{1}{2}}, r_{j+\frac{1}{2}}] \times [z_{k-\frac{1}{2}}, z_{k+\frac{1}{2}}]$, $(j,k) \in \mathscr{I}_c$ and $v_{j+\frac{1}{2},k+\frac{1}{2}} = (r_{j+\frac{1}{2}}, z_{k+\frac{1}{2}})$, $(j,k) \in \mathscr{I}_v$, where $r_{j+\frac{1}{2}} = R_0 + jh_r$, $z_{k+\frac{1}{2}} = Z_0 + kh_z$. Cell sizes along axes r and z are equal to $h_r = (R_1 - R_0)/N_r$ and $h_z = (Z_1 - Z_0)/N_z$. The vertices from set Ψ_h are the nodes of the rectangular volumes from set $\mathscr{W}$. Edges $\epsilon_{j+\frac{1}{2},k}$, $(j,k) \in \mathscr{I}_c = \{0, 1, .., N_r\} \times \{1, 2, .., N_z\}$ are defined as the line segments with end-points $v_{j+\frac{1}{2},k-\frac{1}{2}}$ and $v_{j+\frac{1}{2},k+\frac{1}{2}}$, and edges $\epsilon_{j,k+\frac{1}{2}}$, $(j,k) \in \{1, 2, .., N_r\} \times \{0, 1, .., N_z\}$ are the line segments with end-points $v_{j-\frac{1}{2},k+\frac{1}{2}}$ and $v_{j+\frac{1}{2},k+\frac{1}{2}}$.

In order to capture the irregular geometry of the problem domain, the Cartesian boundary, or the embedded boundary approach is used (see for example Colella et al. [20], Quirk [81]). The physical domain Ω_s is superimposed on the Cartesian grid $\mathscr{W}$, and the rectangular cells $W_{j,k} \in \mathscr{W}$ are divided into three types, depending on their location with respect to region Ω_s. The cells, which lie entirely within and outside region Ω_s, are called *inner cells* and *outer cells*, respectively. The cells, intersected by the boundary of region Ω_s, are defined as *cut cells*. For each cell, which is either an inner cell or a cut cell, the corresponding 'active' cell is constructed, within which the model equations are discretized. The indexes of active cells are the indexes of all inner and cut cells, and they are denoted as

$$\mathscr{I}_a = \{(j,k) \in \mathscr{I}_c, \text{ such that } \mu(W_{j,k} \cap \Omega_s) \neq 0\},$$

where $\mu(W)$ is the measure of a set W in the corresponding space, i.e. $\mu(W)$ denotes the volume, the area or the length of W, if the set W is defined in 3D, 2D or 1D space, respectively. The active cells are constructed in the following way:

$$V_{j,k} = W_{j,k} \cap \Omega_s, \ (j,k) \in \mathscr{I}_a, \tag{5.14}$$

and the set of the active cells is defined as

$$\mathscr{V} = \{V_{j,k}, \ (j,k) \in \mathscr{I}_a\}.$$

The edges of active cells, which lie on the grid lines, are defined as $e_{j,k+\frac{1}{2}} = \epsilon_{j,k+\frac{1}{2}} \cap \Omega_s$, and $e_{j+\frac{1}{2},k} = \epsilon_{j+\frac{1}{2},k} \cap \Omega_s$.

The differentiation state space $[0, 1]$ is divided into intervals $[a_{l-\frac{1}{2}}, a_{l+\frac{1}{2}}]$, $l = 1, 2, ..., N_a$, where $a_{l+\frac{1}{2}} = lh_a$, $l = 0, 1, ..., N_a$ and $h_a = 1/N_a$. The three-dimensional active cells are defined as $V^3_{j,k,l} = V_{j,k} \times [a_{l-\frac{1}{2}}, a_{l+\frac{1}{2}}]$, $(j,k) \in$

$\mathscr{I}_a,\ l = 1, 2, ..., N_a$. Hence cell $V_{i,k}$ is the orthogonal projection of cell $V^3_{i,k,l}$ onto the plane (r, z). The set of the three-dimensional active cells is denoted by $\mathscr{V}^3 = \{V^3_{j,k,l},\ (j,k,l) \in \mathscr{I}^3_a\}$, where $\mathscr{I}^3_a = \{(j,k,l),\ \text{s.t. } (j,k) \in \mathscr{I}_a,\ l = 1, 2, ..., N_a\}$. The faces of active cells $V^3_{j,k,l}$, which correspond to the edges $e_{j,k+\frac{1}{2}}$ and $e_{j+\frac{1}{2},k}$, are defined as $e^3_{j,k+\frac{1}{2},l} = e_{j,k+\frac{1}{2}} \times [a_{l-\frac{1}{2}}, a_{l+\frac{1}{2}}]$ and $e^3_{j+\frac{1}{2},k,l} = e_{j+\frac{1}{2},k} \times [a_{l-\frac{1}{2}}, a_{l+\frac{1}{2}}]$.

5.3.2.1 Domain evolution

For the present model, the evolution of the problem domain should be determined, according to relation (5.4). The level set method is used for this purpose, since it is very effective for those problems, where the temporal evolution of complex geometries should be determined, including changes in topology. Another advantage of the method, is that it can be applied on a fixed Cartesian grid [86], and that there is no need to update the mesh every time step. Further, it can be adapted for the embedded boundary method, which is used for the construction of irregular active cells near the boundary of the physical domain.

The boundary $\Gamma(t)$ of the domain Ω_s is found as the zero level of the level set function $\varphi(\vec{x}, t) : [R_0, R_1] \times [Z_0, Z_1] \to \mathbb{R}$, which is approximated in the nodes of the Cartesian grid Ψ_h. Within region Ω_s, the function φ is negative, and in Ω_b $\varphi > 0$.

The equation for φ is given in Section 5.3.3. Next, it is considered how the grid of the active cells is reconstructed, if the values of the level set function are known.

5.3.2.2 Treatment and reconstruction of active cells

The current geometry of the physical domain Ω_s is determined by the values of the level set function at the grid vertices. Assume that the level set function is approximated by the values $\varphi_{j+\frac{1}{2},k+\frac{1}{2}}$ at vertices $v_{j+\frac{1}{2},k+\frac{1}{2}} \in \Psi_h$ at some time moment t_n. A vertex $v_{j+\frac{1}{2},k+\frac{1}{2}} \in \Psi_h$ is referred to as an *inner, outer or boundary vertex*, if the level set function is *negative, positive or is zero* at this vertex, respectively.

A rectangular cell $W_{j,k} \in \mathscr{W}$ is assumed to be an *inner cell*, if all its vertices are either inner or boundary vertices. A cell $W_{j,k} \in \mathscr{W}$ is an *outer cell*, if all its vertices are either outer or boundary vertices, and at least one of them is an outer vertex. If a cell contains at least one outer vertex and at least one inner vertex, then it is a *cut cell* (Figure 5.1).

New boundary vertices are positioned on the edges of the cut cells, across which the level set function φ changes its sign. It is assumed, that the variable φ can be approximated by a linear function along a cell edge. From this assumption, the intersection of the cell edge with the zero level of function

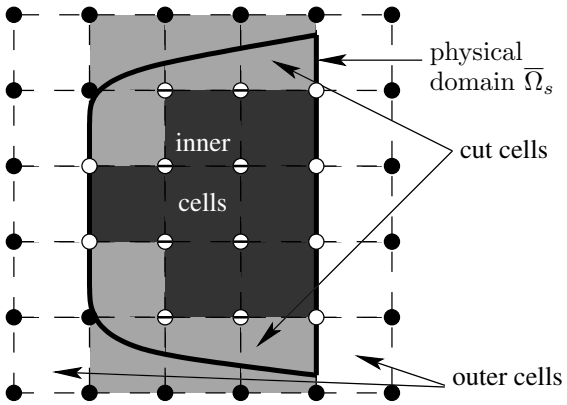

Figure 5.1: Sketch of the grid of the control volumes. Cell types are determined by the signs of the level set function φ at the cell vertices. At the vertices, denoted by the white circles with '-' sign, by the black circles and by the white circles, the function φ is negative, positive and equal to zero, respectively. Inner cells are the black squares within domain $\overline{\Omega}_s$, cut cells are the light gray squares, and outer cells are the white squares.

φ can be found. The new boundary vertices are defined at the intersection points. For the cut cell, shown in Figure 5.2, the level set function changes its sign across each cell edge. Hence four boundary vertices are added on the edges of the cell.

Each cut cell $W_{j,k} \in \mathscr{W}$ corresponds to the active cell $V_{j,k} \in \mathscr{V}$, which is defined as the intersection of cell $W_{j,k} \in \mathscr{W}$ with region Ω_s. The active cell $V_{j,k}$ is constructed as follows. Let us consider the new boundary points, defined at the intersection of the zero level of the function φ and the edges of the cut cell $W_{j,k}$ (vertices E, F, G, H in Figure 5.2), and the vertices of the cut cell $W_{j,k}$, at which the function φ is nonpositive (vertices B and D). These vertices lie on the boundary of the active cell $V_{j,k}$. The boundary of the cut cell $W_{j,k}$ is followed, for example, in a counterclockwise direction, and the considered points are connected by line segments in the corresponding order (vertices E, B, G, H, D, F in Figure 5.2). The active cell $V_{j,k}$ is defined as the area enclosed by the aforementioned line segments. The vertices, where the level set function is positive, are located outside the domain $\overline{\Omega}_s$. Hence they will lie outside the active cell $V_{j,k}$.

The computational domain, which represents the physical domain $\overline{\Omega}_s$, is determined by the set of all active cells. Several limitations are introduced during the reconstruction of active cells. For example, 1) new boundary vertices are found by means of *linear* interpolation of the level set function along cell edges, and 2) *line segments* are used to connect adjacent vertices of the active cell boundary. Thereby, the initial uniform Cartesian grid should be fine enough, so that the geometry of the domain Ω_s can be represented

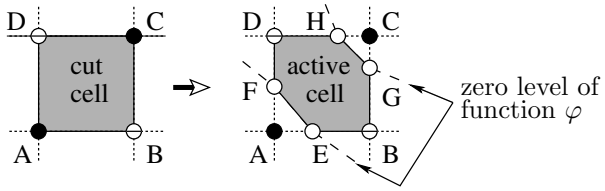

Figure 5.2: Construction of the active cell $EBGHDF$, corresponding to the rectangular cut cell $ABCD$. At the vertices, denoted by the white circles with '-' sign and by the black circles, the level set function φ is negative and positive, respectively. New boundary vertices E, F, G, H are the approximated intersection points of the cell edges with the zero level of function φ. The boundary of the cut cell $ABCD$ is followed, for example, in a counterclockwise direction, and the new boundary E, F, G, H and the vertices B and D, where function φ is nonpositive, are connected by line segments in the corresponding order. The active cell $EBGHDF$ is defined as the area enclosed by the aforementioned line segments.

correctly. It can be noted, for example, that any active cell, defined by us, will always be a simply-connected region. If the projection of the domain Ω_s on some rectangular cell is a multiply connected region, then the Cartesian grid should be refined, in order to provide a reasonable approximation of the problem domain by the set of active cells.

The vertices of active cells are either boundary or inner vertices. Then the edges of active cells are classified as follows. The edges, whose end-points are the boundary vertices, are assumed to coincide with the boundary of the physical domain Ω_s. Such edges are referred to as *boundary edges*. The rest of the edges has at least one inner vertex and lies within the computational domain. Hence these edges are called *inner edges*.

It should be noted here, that all inner edges are aligned with the coordinate axes r, z, and lie on the lines of the Cartesian grid. The cell edges, which are defined if the Cartesian control volumes are cut by the boundary of the physical domain Ω_s, and which may not lie on the lines of the Cartesian grid, will always correspond to the boundary of region Ω_s. These edges are considered as boundary edges.

5.3.3 Level set equation

The evolution of the level set function φ is determined by

$$\frac{\partial \varphi}{\partial t} + v_e |\nabla \varphi| = 0, \tag{5.15}$$

where v_e is equal to the normal velocity v_n, defined in equation (5.4), on the boundary $\Gamma(t)$, i.e.

$$v_e = v_n, \quad \text{for } \vec{X} \in \Gamma(t). \tag{5.16}$$

Out of the boundary $\Gamma(t)$, the value of the velocity v_e is obtained through a continuous extension. The velocity v_e is extrapolated in such a way, that

$$\nabla v_e \cdot \nabla \varphi = 0, \quad \vec{x} \in [R_0, R_1] \times [Z_0, Z_1]. \tag{5.17}$$

In this case, the surface, which represents the distribution of the level set function, is not distorted with time, and $|\nabla \varphi(t)| = 1$ for $t \geq 0$. This fact is important for the accuracy of the numerical solution of equation (5.15) [86].

In the current simulations the field of velocity v_e is constructed as follows. First, the values of the velocity v_e are found at the boundary vertices. According to equation (5.4), these values depend on the density of mature osteogenic cells c_m, which is found from the solution of system (5.1)–(5.3). The governing system (5.1)–(5.3) is solved with use of the finite volume method. Hence the internal solution for c_m is obtained in terms of the approximated average values $C_m^{j,k}$ within control volumes $V_{j,k}$, $(j,k) \in \mathscr{I}_a$. Cell averages $C_m^{j,k}$ can be considered, as the approximated (with second order accuracy) values of function c_m in the centers of the control volumes $V_{j,k}$. The value c_m^b of the cell density at the boundary vertex is approximated by the average cell densities in the control volumes, adjacent to the current vertex:

$$c_m^b = \sum_{(j,k) \in \vec{I}_{adj}} w_{j,k} C_m^{j,k},$$

where $\vec{I}_{adj}$ are the indexes of the active cells, adjacent to the considered boundary vertex. An inverse distance weighting method is used for the interpolation. Weights $w_{j,k}$ depend on the distances $d_{j,k}$ from the centers of the adjacent cells to the current boundary vertex in the following way:

$$w_{j,k} = \frac{\frac{1}{d_{j,k}}}{\sum_{(l,m) \in \vec{I}_{adj}} \frac{1}{d_{l,m}}}.$$

Given the values of the velocity v_e at the boundary vertices, the boundary value problem (5.16), (5.17) is solved. The Eikonal equation (5.17) is solved with use of the fast marching method [86].

5.3.4 PDE discretization in space

The governing equations (5.1)–(5.3) are discretized in space by means of the finite volume method. After the discretization, a system of ODE's is derived for the vectors of the average values in the control volumes of the unknown functions c_i, c_m and g.

The considered physical domain corresponds to the approximated geometry of the soft tissue region within the peri-implant interface, which is defined in the 2D axisymmetric coordinates. Consequently, the operator '$\nabla_s \cdot (\cdot)$', which appears in the governing equations (5.1)–(5.3), is the

divergence operator in the 2D axisymmetric coordinates. In Section 5.3.2 the construction of the grid of the active control volumes $V_{j,k} \in \mathscr{V}$ is described within the 2D axisymmetric physical domain. For convenience, in the presentation of the discretization procedure, the current grid of the finite volumes will be considered, as it were defined in the 2D Cartesian coordinates. For example, the calculation of the volumes of the computational cells and the lengths of the cell edges becomes much simpler in Cartesian coordinates. The axial symmetry of the bone-implant interface is taken into account through the changes, introduced in the governing equations. The axisymmetric spatial operators are expressed through the Cartesian operators plus some additional terms. Therefore, two different operator forms of the governing equations will be considered: one for the axisymmetric coordinate system and one for the Cartesian coordinate system, so that the solution, obtained in the 2D Cartesian coordinates satisfies the equations, which are defined for the 2D axisymmetric coordinates.

In the 2D axisymmetric coordinates the divergence operator '$\nabla_s \cdot (\cdot)$' is given by

$$\nabla_s \cdot \vec{u} = u_{r,r} + u_{z,z} + \frac{u_r}{r},$$

and it is equal to the divergence operator in the 2D Cartesian coordinates (r, z), plus term $\frac{u_r}{r}$. Therefore, the governing equations (5.1)-(5.3), which were defined initially in the 2D axisymmetric coordinates, will have the following form in the 2D Cartesian coordinates:

$$\frac{\partial c_i}{\partial t} = -\nabla_s^C \cdot \mathscr{F}_c(c_i, c_{tot}, g) - \frac{\partial}{\partial a}\left(u_b(g) c_i\right) + A_c(g) c_i \left(1 - c_{tot}\right) - \frac{\mathscr{F}_c^r(c_i, c_{tot}, g)}{r}, \quad (5.18)$$

$$\frac{\partial c_m}{\partial t} = -\nabla_s^C \cdot \mathscr{F}_c(c_m, c_{tot}, g) + u_b(g) c_i(\vec{x}, 1, t) + A_c(g) c_m \left(1 - c_{tot}\right) - \frac{\mathscr{F}_c^r(c_m, c_{tot}, g)}{r}, \quad (5.19)$$

$$\frac{\partial g}{\partial t} = \nabla_s^C \cdot (D_g \nabla_s g) + E_c(g) \left(c_m + \int_0^1 \gamma(a) c_i \, da\right) - d_g g + \frac{D_g}{r} \frac{\partial g}{\partial r}, \quad (5.20)$$

where the operator '$\nabla_s^C \cdot (\cdot)$' is the divergence operator, defined in the *2D Cartesian coordinates*. The gradient operator $\nabla_s(\cdot)$ is the same for the 2D axisymmetric and 2D Cartesian coordinates. Therefore, the gradient notation $\nabla_s(\cdot)$ is kept for the both coordinate systems. The cell flux is defined as:

$$\mathscr{F}_c(c_j, c_{tot}, g) = \begin{bmatrix} \mathscr{F}_c^r(c_j, c_{tot}, g) \\ \mathscr{F}_c^z(c_j, c_{tot}, g) \end{bmatrix} = -D_c \nabla_s c_j + \chi(g, c_{tot}) \, c_j \nabla_s g, \quad (5.21)$$

where $j = i, m$.

The average values of variables c_i, c_m and g are defined as follows:

$$\bar{c}_i^{j,k,l} = \frac{1}{\mu(V_{j,k,l}^3)} \int_{V_{j,k,l}^3} c_i dv, \tag{5.22}$$

$$\bar{c}_m^{j,k} = \frac{1}{\mu(V_{j,k})} \int_{V_{j,k}} c_m dv, \tag{5.23}$$

$$\bar{g}^{j,k} = \frac{1}{\mu(V_{j,k})} \int_{V_{j,k}} g dv, \tag{5.24}$$

where $(j,k) \in \mathscr{I}_a$, $l = 1, 2, .., N_a$. In formulas (5.22)–(5.24) and further in the text, the integration is performed over the cells $V_{j,k,l}^3$ and $V_{j,k}$, considered in the 3D Cartesian space (r, z, a) and in the 2D Cartesian space (r, z), respectively.

Let us denote by u some abstract unknown function, defined in space and in time. The time derivative of the average value $\bar{u}$ of function u in some volume V, which evolves in time, is determined by equation:

$$\frac{d\bar{u}}{dt} = \frac{d}{dt}\frac{\int_V u\, dv}{\mu(V)} = \frac{1}{\mu(V)}\left(\frac{d\int_V u\, dv}{dt} - \bar{u}\frac{d\mu(V)}{dt}\right). \tag{5.25}$$

The Leibniz integral rule is given by:

$$\frac{d}{dt}\int_V u\, dv = \int_V \frac{\partial u}{\partial t}\, dv + \int_{\partial V} u\, v_n\, ds. \tag{5.26}$$

The volumetric measure $\mu(V)$ can be determined from the equation $\mu(V) = \int_v dv$. Substitution of this relation and of formula (5.26) into equation (5.25) yields:

$$\frac{d\bar{u}}{dt} = \frac{1}{\mu(V)}\left(\int_V \frac{\partial u}{\partial t} dv + \int_{\partial V} (u - \bar{u}) v_n\, ds\right). \tag{5.27}$$

Equation (5.27) is used to derive the equations for the evolution of the averages of the cell densities and of the growth factor concentration. The variables c_i, c_m and g replace u into equation (5.27), and volume V is replaced with volumes $V_{j,k,l}^3$ and $V_{j,k}$, $(j,k) \in \mathscr{I}_a$, $l = \overline{1, N_a}$. The terms for c_i, c_m and g, corresponding to the first term in the brackets in equation (5.27), are replaced with the relations, which are obtained from integration of the right-hand sides of PDE's (5.18)-(5.20) over cells $V_{j,k,l}^3$ and $V_{j,k}$. Finally, the

following equations are obtained:

$$\frac{d\bar{c}_i^{j,k,l}}{dt} = \frac{1}{\mu(V^3_{j,k,l})}\left(-\int_{\partial V^{3I}_{j,k,l}} \mathscr{F}_c(c_i, c_{tot}, g)\cdot\vec{n}\; ds_3 \right.$$
$$- \int_{V_{j,k}} u_b(g)\left(c_i(\vec{\xi}, a_{l+\frac{1}{2}}, t) - c_i(\vec{\xi}, a_{l-\frac{1}{2}}, t)\right) dv_2$$
$$+ \int_{V^3_{j,k,l}} A_c(g)c_i(1-c_{tot}) - \frac{\mathscr{F}^r_c(c_i, c_{tot}, g)}{r}\; dv_3$$
$$\left. + \int_{\partial V^{3B}_{j,k,l}} (c_i - \bar{c}_i^{j,k,l})v_n - h_i\; ds_3\right) \quad (5.28)$$

$$\frac{d\bar{c}_m^{j,k}}{dt} = \frac{1}{\mu(V_{j,k})}\left(-\int_{\partial V^{I}_{j,k}} \mathscr{F}_c(c_m, c_{tot}, g)\cdot\vec{n}\; ds_2 \right.$$
$$+ \int_{V_{j,k}} u_b(g)c_i(\vec{\xi}, 1, t)\; dv_2$$
$$+ \int_{V_{j,k}} A_c(g)c_m(1-c_{tot}) - \frac{\mathscr{F}^r_c(c_m, c_{tot}, g)}{r}\; dv_2$$
$$\left. + \int_{\partial V^{B}_{j,k}} (c_m - \bar{c}_m^{j,k})v_n - h_m\; ds_2\right) \quad (5.29)$$

$$\frac{d\bar{g}^{j,k}}{dt} = \frac{1}{\mu(V_{j,k})}\left(\int_{\partial V^{I}_{j,k}} D_g\nabla_s g\cdot\vec{n}\; ds_2 \right.$$
$$+ \int_{V_{j,k}} E_c(g)\left(c_m + \int_0^1 \gamma(a)c_i\; da\right) - d_g g + \frac{D_g}{r}\frac{\partial g}{\partial r}\; dv_2$$
$$\left. + \int_{\partial V^{B}_{j,k}} (g - \bar{g}^{j,k})v_n - h_g\; ds_2\right) \quad (5.30)$$

The inner and boundary edges of cells $V_{j,k}$ are denoted as $\partial V^I_{j,k}$ and $\partial V^B_{j,k}$, respectively. The corresponding faces of the 3D cells $V_{j,k,l}$ are defined as

$$\partial V^{3J}_{j,k,l} = \partial V^J_{j,k} \times [a_{l-\frac{1}{2}}, a_{l+\frac{1}{2}}], \quad J = I, B. \quad (5.31)$$

Control volumes, which are situated in the middle of the computational domain Ω_s, do not have boundary edges. For these cells, the last terms in the RHS's of equations (5.28)–(5.30) are equal to zero. The vector $\vec{n}$ represents the outward unit normal at the edges (faces) of the control volumes. The variables dv_3, ds_3, dv_2 and ds_2, respectively, represent the differential elements of volumes $V^3_{j,k,l}$, of surfaces $\partial V^{3I}_{j,k,l}$ and $\partial V^{3B}_{j,k,l}$, of surfaces $V_{j,k}$, and

of line segments $\partial V^I_{j,k}$ and $\partial V^B_{j,k}$. Further, v_n is the normal velocity of the boundary edges or faces, which is defined in equation (5.4).

Further, the system of ODE's with respect to the average values of the cell densities and the growth factor concentration is derived, which approximates the exact equations (5.28)-(5.30). Let us denote the approximate average values of the unknown densities and concentration by the respective capital letters: $C_i^{j,k,l}$, $C_m^{j,k}$ and $G^{j,k}$. The vectors of the unknown averages are denoted as $\vec{C}_i = \{C_i^{\vec{i}^3}; \vec{i}^3 \in \mathscr{I}_a^3\}$, $\vec{C}_m = \{C_m^{\vec{i}}; \vec{i} \in \mathscr{I}_a\}$ and $\vec{G} = \{G^{\vec{i}}; \vec{i} \in \mathscr{I}_a\}$. The system of the approximated ODE's is written in the following general form:

$$\frac{dC_i^{\vec{i}^3}}{dt} = H_i^{M_I}(\vec{C}_i, \vec{C}_m, \vec{G}, \vec{i}^3) + H_i^D(\vec{C}_i, \vec{G}, \vec{i}^3) + H_i^R(\vec{C}_i, \vec{C}_m, \vec{G}, \vec{i}^3) + H_i^{M_B}(\vec{C}_i, \vec{C}_m, \vec{G}, \vec{i}^3), \quad (5.32)$$

$$\frac{dC_m^{\vec{i}}}{dt} = H_m^{M_I}(\vec{C}_i, \vec{C}_m, \vec{G}, \vec{i}) + H_m^D(\vec{C}_i, \vec{G}, \vec{i}) + H_m^R(\vec{C}_i, \vec{C}_m, \vec{G}, \vec{i}) + H_m^{M_B}(\vec{C}_i, \vec{C}_m, \vec{G}, \vec{i}), \quad (5.33)$$

$$\frac{dG^{\vec{i}}}{dt} = H_g^{M_I}(\vec{C}_i, \vec{C}_m, \vec{G}, \vec{i}) + H_g^R(\vec{C}_i, \vec{C}_m, \vec{G}, \vec{i}) + H_g^{M_B}(\vec{C}_i, \vec{C}_m, \vec{G}, \vec{i}). \quad (5.34)$$

The terms in the right-hand sides of equations (5.32)-(5.34) are the approximations of the respective terms in the right-hand sides of equations (5.28)-(5.30).

As it was mentioned before, the current numerical approach is based on the method of lines (MOL). The main feature of this method, which is often referred to as the "semi-discrete scheme", is that the spatial discretization is separated from the discretization in time. This allows to apply the principle of superposition to the discretization of the reaction, diffusion and advection terms in the governing equations. In other words, each term can be approximated independently of the others. Therefore, the complicated system of equations can be decomposed into a set of problems, that are easier to solve.

The semi-discrete schemes for the scalar time-dependent advection-diffusion-reaction equations are described in a very clear and detailed way in the book of Hundsdorfer and Verwer [48]. The authors put stress on equations with linear flux functions, and nonlinear conservation laws are not studied in detail in this work. The hyperbolic systems of nonlinear equations are considered thoroughly in the work of LeVeque [59], where the author describes the fully discrete Direct Space-Time schemes for various types of the hyperbolic partial differential equations. The current numerical algorithm is constructed in the framework of the principles and ideas, presented in these two works.

5.3.5 Advection-diffusion discretization

Let us consider the advection and diffusion terms in equations (5.18)–(5.20). The corresponding terms in the averaged equations (5.28)–(5.30) are given by the integrals of the fluxes of the unknown variables c_i, c_m and g over the inner faces $\partial V^{3I}_{j,k,l}$ and $V_{j,k} \times \{a_{l+\frac{1}{2}}\}$ and the inner edges $\partial V^{I}_{j,k}$. The considered integrals are approximated by the functions $H_i^{M_I}$, H_i^D, $H_m^{M_I}$ and $H_g^{M_I}$ from equations (5.32)–(5.34).

The integrals are approximated by the value of the integrand in the centers of the corresponding face or edge times its area or length, respectively. Therefore, the approximate values of the unknown functions c_i, c_m, g and of their normal derivatives should be derived at the centers of interfaces of control volumes from the averages of the cell densities $\vec{C}_i$, $\vec{C}_m$ and of the growth factor concentration $\vec{G}$.

5.3.5.1 Linear flux due to cell differentiation

The general procedure of the discretization of hyperbolic equations in space with semi-discrete schemes involves two stages. First, piece-wise polynomial approximations of the unknown functions are reconstructed from their average values. The reconstructed piece-wise polynomial functions usually have jumps at the interfaces of the computational cells. This means, that there are two states (values) of each reconstructed function at each inner interface of the control volumes. The reconstruction technique should be total variation diminishing (TVD), in order to provide the numerical solution without spurious oscillations, which can also lead to negative values of the unknown variables.

At the second stage, the reconstructed unknown functions are used to determine the values of the fluxes at the interfaces of the control volumes. In order to obtain a stable numerical approximation, the Riemann problem has to be solved exactly, or with use of some approximate solver in the case of large complex systems of equations.

In the discretization of the multidimensional hyperbolic equations on regular Cartesian grids, the dimensions of the physical space can be split. That means, that the techniques, used to solve one-dimensional problems, can be applied for the spatial discretization in each individual coordinate direction. Such a splitting can be applied due to the possibility of the superposition of spatial discretizations, when the method of lines is used [48].

The current finite volume grid contains irregular active cells near the boundary of the physical domain Ω_s. This irregularity requires a special solution reconstruction technique within the irregular cells and cells adjacent to them. This technique will be introduced in Section 5.3.5.2.

Let us first consider the flux of immature cells due to differentiation. This

flux should be approximated on the faces $(\vec{X}, a) \in V_{j,k} \times \{a_{l-\frac{1}{2}}\}$, $(\vec{X}, a) \in V_{j,k} \times \{a_{l+\frac{1}{2}}\}$ of cells $V^3_{j,k,l}$, $(j,k,l) \in \mathscr{I}^3_a$. The flux vector is parallel to the a-axis. The finite volume grid is uniform along the a coordinate axis. Hence the method of the reconstruction of the solution on a 1D uniform grid can be applied. The integral over the face of the control volume is approximated by the values of the integrated functions in the center of the face. Hence it is not necessary to reconstruct the numerical solution for density c_i within the whole cell. It is sufficient to approximate its value in the center of the considered cell interfaces.

In order to justify the 1D reconstruction, applied in the considered situation, function $\tilde{c}_i^{j,k}(a,t)$ is defined, which depends only on a coordinate and time, and which is equal to the average value of the function c_i over the transverse sections $\{(\vec{\xi}, a),\ \text{s.t.}\ \ \vec{\xi} \in V_{j,k},\ a = const\}$ of the cells $V^3_{j,k,l}$, i.e.

$$\tilde{c}_i^{j,k}(a,t) = \frac{1}{\mu(V_{j,k})} \iint_{V_{j,k}} c_i(r,z,a,t) dr\ dz.$$

Sections $a = a_{l+\frac{1}{2}}$ and $a = a_{l-\frac{1}{2}}$ coincide with the faces of cell $V^3_{j,k,l}$. The average values can be considered as the second order approximations of the function values in the face centers. Hence the "one-dimensional" function $\tilde{c}_i^{j,k}(a,t)$ can be reconstructed, in order to determine the approximate states of the immature cell density at the centers of the considered cell faces.

Note, that

$$\frac{1}{h_a} \int_{a_{l-\frac{1}{2}}}^{a_{l+\frac{1}{2}}} \tilde{c}_i^{j,k}\ da = \frac{1}{h_a\ \mu(V_{j,k})} \int_{a_{l-\frac{1}{2}}}^{a_{l+\frac{1}{2}}} \iint_{V_{j,k}} c_i\ dr\ dz\ da = \bar{c}_i^{j,k,l}.$$

That is, the average value of the function $\tilde{c}_i^{j,k}$ over the interval $[a_{l-\frac{1}{2}}, a_{l+\frac{1}{2}}]$ is equal to the cell average of function c_i over cell $V^3_{j,k,l}$. Hence the piece-wise polynomial approximation of $\tilde{c}_i^{j,k}$ is reconstructed from its average values on the 1D uniform grid $[a_{l-\frac{1}{2}}, a_{l+\frac{1}{2}}]$, $l = 1, .., N_a$, given by $\vec{C}_i$.

The value of the function $u_b(g)$ on the midpoint of the considered cell faces is approximated by value $u_b(G^{j,k})$.

The Riemann solution is straightforward in the considered case, since the flux is linear and it only depends on the unknown c_i. The value of the coefficient $u_b(g)$ does not vary along a-axis, and it can be considered as constant, when the flux is evaluated on faces $V_{j,k} \times \{a_{l+\frac{1}{2}}\}$. It is assumed in the current model, that the differentiation rate u_b is nonnegative (see Tables 4.1, 4.2). Hence the left state of $\tilde{c}_i^{j,k}$ is chosen at each interface, i.e. the value of the reconstructed function $\tilde{c}_i^{j,k}(a,t)$ for $a \to a_{l+\frac{1}{2}} - 0$.

Therefore, the terms, which represent the flux of immature cells due to differentiation, are approximated as follows:

$$H_i^D(\vec{C}_i, \vec{G}, (j,k,l)) = -\frac{1}{h_a} u_b(G^{j,k}) \left(C_i^{j,k,l+\frac{1}{2}} - C_i^{j,k,l-\frac{1}{2}} \right), \qquad (5.35)$$

where the states $C_i^{j,k,l+\frac{1}{2}}$, $l = 2, ..., N_a$ are determined as

$$C_i^{j,k,l+\frac{1}{2}} = C_i^{j,k.l} + \psi\left(\frac{C_i^{j,k,l} - C_i^{j,k,l-1}}{C_i^{j,k,l+1} - C_i^{j,k,l}}\right)\left(C_i^{j,k,l+1} - C_i^{j,k,l}\right), \tag{5.36}$$

for $l = 1, .., N_a$. Function $\psi(\theta)$ is a "limiter function". It is responsible for the TVD property of the reconstruction method. The choice of the limiter function determines the order of the reconstruction of the unknown function from its average values. If $\psi \equiv 0$, then the order of approximation of $C_i^{j,k,l+\frac{1}{2}}$ is one. By choosing the Koren limiter for a uniform grid,

$$\psi(\theta) = \max\left(0, \min\left(\frac{1}{3} + \frac{1}{6}\theta, \theta, 1\right)\right), \tag{5.37}$$

a higher order approximation is obtained [48]. In fact, the Koren limiter provides a third order of accuracy in the regions, where the function is smooth and where it does not have any extremes. Otherwise, a first order accuracy is achieved. However, since the surface integrals are evaluated at the center points, and the values at the surface centers are approximated with the average values, the order of accuracy cannot be larger than two.

Boundary condition (5.12) is used to define the flux at faces $V_{j,k} \times \{0\}$. Then

$$H_i^D(\vec{C}_i, \vec{C}_m, \vec{G}, (j,k,1)) = -\frac{1}{h_a} u_b(G^{j,k}) C_i^{j,k,\frac{3}{2}}.$$

In order, to find the values $C_i^{j,k,\frac{3}{2}}$ and $C_i^{j,k,N_a+\frac{1}{2}}$, the 'ghost cells' are defined, such that

$$C_i^{j,k,0} = C_i^{j,k,1}, \quad C_i^{j,k,N_a+1} = C_i^{j,k,N_a}, \quad (j,k) \in \mathscr{I}_a.$$

Constant extrapolation at the boundaries $a = 0$ and $a = 1$ is chosen, since it provides nonnegative solutions. Furthermore, it leads to the first order accuracy in the approximations of the states $C_i^{j,k,\frac{3}{2}}$ and $C_i^{j,k,N_a+\frac{1}{2}}$.

The function H_m^D in equation (5.29) approximates the inflow of mature cells due to differentiation of immature cells. The cell density conservation is maintained, if this inflow is equal to the flux of the density c_i through interface $(\vec{X}, a) \in V_{j,k} \times \{a_{N_a+\frac{1}{2}}\}$. That is,

$$H_m^D(\vec{C}_i, \vec{C}_m, \vec{G}, (j,k)) = u_b(G^{j,k}) C_i^{j,k,N_a+\frac{1}{2}}, \tag{5.38}$$

where the average cell density $C_i^{j,k,N_a+\frac{1}{2}}$ is obtained from equations (5.36)–(5.37).

5.3.5.2 Fluxes due to cell migration

In order to approximate the terms, which correspond to the fluxes of the cell densities due to migration, the values of the immature and mature cell densities, the values of the growth factor concentration and the normal derivatives of the cell densities and of the growth factor concentration have to be determined at the centers of the inner edges and faces of the control volumes. The method, used to determine the values of the growth factor concentration and the normal derivatives of the model variables is defined in Section 5.3.5.3. The approach, used to find the left and right states (values) of the cell densities at the centers of the inner edges and faces, is described in this section.

Consider first the density of mature osteogenic cells, defined within the two dimensional physical domain. In analogy to Section 5.3.5.1, function $\tilde{c}_m^k(r,t)$ can be defined as the average value of the cell density c_m over the sections $S(r,k) = \{(r,z),\ \text{s.t. } (r,z) \in V_{j,k},\ (j,k) \in \mathscr{I}_a\}$, where r and k are considered as fixed parameters, which characterize each section $S(r,k)$. Therefore,

$$\tilde{c}_m^k(r,t) = \frac{1}{\mu(S(r,k))} \int_{S(r,k)} c_m(r,z,t)\, dz. \tag{5.39}$$

If cell $V_{j,k}$ is a regular rectangular cell, then the average of $\tilde{c}_m^k$ is given by

$$\begin{aligned} \frac{1}{h_r} \int_{r_{j-\frac{1}{2}}}^{r_{j+\frac{1}{2}}} \tilde{c}_m^k\, dr &= \frac{1}{h_r} \int_{r_{j-\frac{1}{2}}}^{r_{j+\frac{1}{2}}} \frac{1}{\mu(S(r,k))} \int_{S(r,k)} c_m\, dz\, dr \\ &= \frac{1}{h_r \mu(S(r,k))} \int_{V_{j,k}} c_m dv = \frac{1}{\mu(V_{j,k})} \int_{V_{j,k}} c_m dv = \bar{c}_m^{j,k}. \end{aligned} \tag{5.40}$$

This means, that the averages of the functions $\tilde{c}_m$ and c_m on regular rectangular cells are equal.

Remark 5.2. Note, that equation (5.40) is valid, if and only if $\mu(S(r,k)) = const$ for $r \in [r_{j-\frac{1}{2}}, r_{j+\frac{1}{2}}]$.

Let us consider an inner edge $e_{j+\frac{1}{2},k}$. Assume that this edge is located far away from the boundary of the physical domain, and that there exist active inner (i.e. regular rectangular) cells $V_{j-1,k}$, $V_{j,k}$, $V_{j,k+1}$. Then the function $\tilde{c}_m$ has average values $\bar{c}_m^{j-1,k}$, $\bar{c}_m^{j,k}$, $\bar{c}_m^{j+1,k}$ on uniform intervals $[r_{n-\frac{1}{2}}, r_{n+\frac{1}{2}}]$, $n \in \{j-1, j, j+1\}$, and the conventional one-dimensional TVD reconstruction can be applied, so that the left state at the center of the edge $e_{j+\frac{1}{2},k}$ is given by:

$$C_{m\,(L)}^{j+\frac{1}{2},k} = C_m^{j,k} + \psi\left(\frac{C_m^{j,k} - C_m^{j-1,k}}{C_m^{j+1,k} - C_m^{j,k}}\right)\left(C_m^{j+1,k} - C_m^{j,k}\right), \tag{5.41}$$

where the function ψ is a Koren limiter again, defined in equation (5.37). If cell $V_{j+2,k}$ is also a regular inner cell, then the right state is determined as:

$$C_{m\,(R)}^{j+\frac{1}{2},k} = C_m^{j+1,k} + \psi\left(\frac{C_m^{j+2,k} - C_m^{j+1,k}}{C_m^{j+1,k} - C_m^{j,k}}\right)\left(C_m^{j,k} - C_m^{j+1,k}\right). \tag{5.42}$$

The situation is more complicated, if some of the cells in the three-cell stencil, which is used to approximate the left state or the right state at the edge center, are irregular or do not exist at all (Figure 5.3). Consider, for example, the situation shown in Figure 5.3a. Assume that there exists

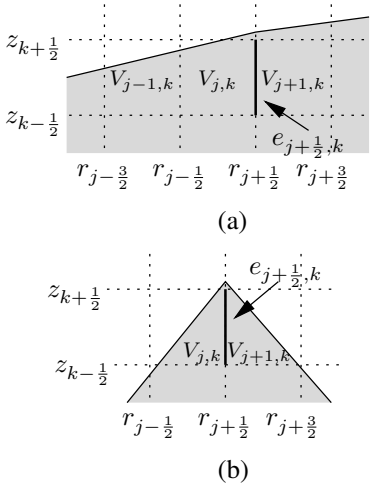

Figure 5.3: Situations, when the conventional one-dimensional reconstruction for the uniform grid cannot be applied to approximate the solution at the edge $e_{j+\frac{1}{2},k}$. Active cells are plotted in gray color.

an irregular active cell $V_{j-1,k}$, which has a common inner edge $e_{j-\frac{1}{2},k}$ with the cell $V_{j,k}$. On irregular cells, the length of the section $\mu(S(r,k))$ may not be constant, hence, according to Remark 5.2, equality (5.40) does not hold in general. The value of $\tilde{c}_m$ at point $r_{j+\frac{1}{2}}$ is found with an approach, which is similar to the 1D reconstruction on a cell-centered nonuniform grid, defined in Hundsdorfer and Verwer [48]. First $\tilde{c}_m$ is approximated with a quadratic polynomial, and then a limiter is applied, in order to get a TVD reconstruction, which prevent spurious oscillations in the numerical solution.

Note, that

$$C_m^{j,k} \approx \bar{c}_m^{j,k} = \frac{1}{\mu(V_{j,k})} \int_{r_{j-\frac{1}{2}}}^{r_{j+\frac{1}{2}}} \int_{S(r,k)} c_m \, dz \, dr$$
$$= \frac{1}{\mu(V_{j,k})} \int_{r_{j-\frac{1}{2}}}^{r_{j+\frac{1}{2}}} \mu(S(r,k)) \tilde{c}_m^k \, dr$$
$$= \frac{1}{\mu(V_{j,k})} \int_{r_{j-\frac{1}{2}}}^{r_{j+\frac{1}{2}}} \tilde{c}_m^k \int_{S(r,k)} dz \, dr = \frac{1}{\mu(V_{j,k})} \int_{V_{j,k}} \tilde{c}_m^k \, dv. \quad (5.43)$$

Let a_0, a_1, a_2 be the coefficients of the quadratic polynomial, which is used to approximate $\tilde{c}_m^k$:

$$\tilde{c}_m^k \approx a_0 + a_1 r + a_2 r^2.$$

From integration of this polynomial over the cells $V_{n,k}$, $n \in \{j-1, j, j+1\}$ and from equation (5.43), three linear equations are derived, which can be used to determine the coefficients a_i, $i \in \{0, 1, 2\}$:

$$a_0 + a_1 r_c^{n,k} + a_2 I_{zz}^{n,k} = C_m^{n,k}, \quad n \in \{j-1, j, j+1\}, \quad (5.44)$$

where $r_c^{n,k}$ is the r coordinate of the center of cell $V_{n,k}$, and $I_{zz}^{n,k}$ is the second moment of area of cell $V_{n,k}$ about z-axis, i.e. $I_{zz}^{n,k} = \frac{1}{\mu(V_{n,k})} \int_{V_{n,k}} r^2 dv$. The determinant of the matrix of system (5.44) is not equal to zero (see B.1), hence coefficients a_i, can always be uniquely expressed in terms of the geometric characteristics $r_c^{n,k}$, $I_{zz}^{n,k}$ of the control volumes, and approximate average values $C_m^{n,k}$. Evaluating the quadratic polynomial at point $r_{j+\frac{1}{2}}$ for the values of coefficients a_0, a_1 and a_2, obtained from the solution of the linear system (5.44), the following expression is obtained:

$$\tilde{c}_m^k(r_{j+\frac{1}{2}}, t) \approx C_m^{j,k}$$
$$+ \psi_0^r \left(\frac{C_m^{j,k} - C_m^{j-1,k}}{C_m^{j+1,k} - C_m^{j,k}}, r_{j+\frac{1}{2}}, j-1, j, j+1, k \right) \left(C_m^{j+1,k} - C_m^{j,k} \right), \quad (5.45)$$

where

$$\psi_0^r(\theta, r_e, j_1, j_2, j_3, k) = \Big((r_c^{j_1,k} - r_c^{j_2,k}) r_e + (I_{zz}^{j_2,k} - I_{zz}^{j_1,k}) r_e^2$$
$$+ I_{zz}^{j_1,k} r_c^{j_2,k} - I_{zz}^{j_2,k} r_c^{j_1,k} + \theta \Big((r_c^{j_3,k} - r_c^{j_2,k}) r_e$$
$$+ (I_{zz}^{j_2,k} - I_{zz}^{j_3,k}) r_e^2 + I_{zz}^{j_3,k} r_c^{j_2,k} - I_{zz}^{j_2,k} r_c^{j_3,k} \Big) \Big)$$
$$/ \Big((I_{zz}^{j_2,k} - I_{zz}^{j_1,k})(r_c^{j_3,k} - r_c^{j_2,k}) + (I_{zz}^{j_3,k} - I_{zz}^{j_2,k})(r_c^{j_1,k} - r_c^{j_2,k}) \Big). \quad (5.46)$$

The quadratic approximation, given by formula (5.45), provides a third order of accuracy for smooth solutions. Since a TVD approximation is needed,

the function ψ_0^r has to be limited in the regions, where $\tilde{c}_m$ changes rapidly. A limiter function is given by:

$$\psi_{irr}^r(\theta,\cdot,\cdot,\cdot,\cdot,\cdot) = \max(0, \min(\psi_0^r(\theta,\cdot,\cdot,\cdot,\cdot,\cdot), \theta, 1)),$$

so that $0 < \psi_{irr}^r < 1$, and $0 < \frac{1}{\theta}\psi_{irr}^r(\theta,\cdot,\cdot,\cdot,\cdot,\cdot) < 1$. This means, that the limiter ψ_{irr}^r provides a TVD reconstruction of the solution [48]. Note, that the limiter function ψ_{irr}^r, which is defined for irregular cells, is equivalent to the Koren limiter function (5.37), if the geometric characteristics $r_c^{j,k}$, $I_{zz}^{j,k}$ of uniform regular rectangular cells are substituted into expression (5.46). Therefore, for the present case, the left state of the mature cell density c_m at the edge $e_{j+\frac{1}{2},k}$ is approximated as

$$C_{m(L)}^{j+\frac{1}{2},k} = C_m^{j,k} + \psi_{irr}^r\left(\frac{C_m^{j,k} - C_m^{j-1,k}}{C_m^{j+1,k} - C_m^{j,k}}, r_{j+\frac{1}{2}}, j-1, j, j+1, k\right)\left(C_m^{j+1,k} - C_m^{j,k}\right). \quad (5.47)$$

By analogy, the right state is determined as

$$C_{m\,(R)}^{j+\frac{1}{2},k} = C_m^{j+1,k} + \psi_{irr}^r\left(\frac{C_m^{j+2,k} - C_m^{j+1,k}}{C_m^{j+1,k} - C_m^{j,k}}, r_{j+\frac{1}{2}}, j+2, j+1, j, k\right)\left(C_m^{j,k} - C_m^{j+1,k}\right). \quad (5.48)$$

If the inner edge $e_{j+\frac{1}{2},k}$ is very close to the boundary, then, for example, the active cell $V_{j-1,k}$ and/or the active cell $V_{j+2,k}$ may not exist (Figure 5.3b). In this case, the first order piece-wise constant reconstruction of the solution for the density c_m is used and its left and/or right states are defined as:

$$C_{m(L)}^{j+\frac{1}{2},k} = C_m^{j,k}, \quad C_{m(R)}^{j+\frac{1}{2},k} = C_m^{j+1,k}. \quad (5.49)$$

This is equivalent to the constant extrapolation for the 'ghost' cells, outlined in Section 5.3.5.1.

Each inner edge $e_{j+\frac{1}{2},k}$ corresponds to n_a inner faces $e^3_{j+\frac{1}{2},k,l}$, $l = 1, ..., n_a$. The derivation of the formulas for the left and right values of the density c_i at the centers of these inner faces is very similar to the derivation of the formulas for the states $C_{m(L)}^{j,k}$, $C_{m(R)}^{j,k}$. The only difference is that integration in the a-direction from $a_{l-\frac{1}{2}}$ to $a_{l+\frac{1}{2}}$ is performed additionally. Due to a homogeneity of the mesh in the a-direction, this integration does not lead to any modifications in the derived formulas. Six different situations of the mutual location of regular and irregular active cells and inner edge $e_{j,k}$ are represented by the formulas (5.41), (5.42), (5.47), (5.48) and (5.49). For each situation, the following equations for the values of the immature cell

density in the centers of faces $e^3_{j+\frac{1}{2},k,l}$, $l = 1, ..., n_a$ are given, respectively, by:

$$C_{i\,(L)}^{j+\frac{1}{2},k,l} = C_i^{j,k,l} + \psi\left(\frac{C_i^{j,k,l} - C_i^{j-1,k,l}}{C_i^{j+1,k,l} - C_i^{j,k,l}}\right)\left(C_i^{j+1,k,l} - C_i^{j,k,l}\right), \tag{5.50}$$

$$C_{i\,(R)}^{j+\frac{1}{2},k,l} = C_i^{j+1,k,l} + \psi\left(\frac{C_i^{j+2,k,l} - C_i^{j+1,k,l}}{C_i^{j+1,k,l} - C_i^{j,k,l}}\right)\left(C_i^{j,k,l} - C_i^{j+1,k,l}\right), \tag{5.51}$$

$$\begin{aligned} C_{i(L)}^{j+\frac{1}{2},k,l} &= C_i^{j,k,l} \\ &+ \psi_{irr}^r\left(\frac{C_i^{j,k,l} - C_i^{j-1,k,l}}{C_i^{j+1,k,l} - C_i^{j,k,l}}, r_{j+\frac{1}{2}}, j-1, j, j+1, k\right)\left(C_i^{j+1,k,l} - C_i^{j,k,l}\right), \end{aligned} \tag{5.52}$$

$$\begin{aligned} C_{i\,(R)}^{j+\frac{1}{2},k,l} &= C_i^{j+1,k,l} \\ &+ \psi_{irr}^r\left(\frac{C_i^{j+2,k,l} - C_i^{j+1,k,l}}{C_i^{j+1,k,l} - C_i^{j,k,l}}, r_{j+\frac{1}{2}}, j+2, j+1, j, k\right)\left(C_i^{j,k,l} - C_i^{j+1,k,l}\right), \end{aligned} \tag{5.53}$$

$$C_{i(L)}^{j+\frac{1}{2},k,l} = C_i^{j,k,l}, \quad C_{i(R)}^{j+\frac{1}{2},k,l} = C_i^{j+1,k,l}. \tag{5.54}$$

The values of c_m and c_i at the horizontal inner cells edges $e_{j,k+\frac{1}{2}}$ and faces $e^3_{j,k+\frac{1}{2},l}$ are determined with use of limiters ψ and ψ^z_{irr} in the same way as for the vertical edges and faces. The only difference is that the cells $V_{j,n}$, $V^3_{j,n,l}$, $n \in \{k-1, k, k+1, k+2\}$, are considered instead of the cells $V_{m,k}$, $V^3_{m,k,l}$, $m \in \{j-1, j, j+1, j+2\}$ in the stencil, used in the computation of the states of the variables. Further, the limiter ψ^z_{irr} is used instead of the limiter ψ^r_{irr}, which is defined as follows:

$$\psi^z_{irr}(\theta, \cdot, \cdot, \cdot, \cdot, \cdot) = \max(0, \min(\psi^z_0(\theta, \cdot, \cdot, \cdot, \cdot, \cdot), \theta, 1)),$$

$$\begin{aligned} \psi_0^z(\theta, z_e, k_1, k_2, k_3, j) = \Big((z_c^{j,k_1} - z_c^{j,k_2})z_e + (I_{rr}^{j,k_2} - I_{rr}^{j,k_1})z_e^2 \\ + I_{rr}^{j,k_1} z_c^{j,k_2} - I_{rr}^{j,k_2} z_c^{j,k_1} + \theta\left((z_c^{j,k_3} - z_c^{j,k_2})z_e\right. \\ \left. + (I_{rr}^{j,k_2} - I_{rr}^{j,k_3})z_e^2 + I_{rr}^{j,k_3} z_c^{j,k_2} - I_{rr}^{j,k_2} z_c^{j,k_3}\right)\Big) \\ \Big/\left((I_{rr}^{j,k_2} - I_{rr}^{j,k_1})(z_c^{j,k_3} - z_c^{j,k_2}) + (I_{rr}^{j,k_3} - I_{rr}^{j,k_2})(z_c^{j,k_1} - z_c^{j,k_2})\right), \end{aligned}$$

where $z_c^{j,k}$ is the z coordinate of the center of the cell $V_{j,k}$, and $I_{rr}^{j,k}$ is the second moment of area of the cell $V_{j,k}$ about the r-axis, i.e. $I_{rr}^{j,k} = \frac{1}{\mu(V_{j,k})} \int_{V_{j,k}} z^2 dv$. The left and right states of the unknown variables are, in fact, the lower and upper states, respectively.

5.3.5.3 Gradient approximation at cell edges

In this section, the approach is described to approximate the normal derivatives of the densities of immature and mature cells and of the growth factor concentration and the value of the growth factor concentration in the centers of the inner edges and faces of the control volumes.

First, the expressions for the normal derivative and the value of the growth factor concentration g at the centers of the inner edges are derived. Consider a vertical inner edge $e_{j+\frac{1}{2},k}$. The normal derivative is equal to partial derivative $\frac{\partial g}{\partial r}$. Since the edge is inner, the cells $V_{j,k}$, $V_{j+1,k}$, which are adjacent to it, are active cells. If these cells are regular rectangular cells, then their centers and the center of the edge $e_{j+\frac{1}{2},k}$ have the same z-coordinate, equal to $\left(z_{k-\frac{1}{2}} + z_{k+\frac{1}{2}}\right)/2$, which is denoted as $z_e^{j+\frac{1}{2},k}$. The edge center lies at the middle of the line segment, which connects the cell centers. From a Taylor series expansion, it follows that

$$\frac{\partial g}{\partial r}(r_{j+\frac{1}{2}}, z_e^{j+\frac{1}{2},k}) = \frac{g(r_c^{j+1,k}, z_c^{j+1,k}) - g(r_c^{j,k}, z_c^{j,k})}{r_c^{j+1,k} - r_c^{j,k}} + O(h_r^2),$$

and

$$g(r_{j+\frac{1}{2}}, z_e^{j+\frac{1}{2},k}) = \frac{g(r_c^{j+1,k}, z_c^{j+1,k}) + g(r_c^{j,k}, z_c^{j,k})}{2} + O(h_r^2).$$

Hence the approximate normal derivative $\frac{\partial g}{\partial r}^{j+\frac{1}{2},k}$ and the state $G^{j+\frac{1}{2},k}$ of the function g at the center of the edge $e_{j+\frac{1}{2},k}$ are determined as

$$\frac{\partial G}{\partial r}^{j+\frac{1}{2},k} = \frac{G^{j+1,k} - G^{j,k}}{r_c^{j+1,k} - r_c^{j,k}}, \tag{5.55}$$

$$G^{j+\frac{1}{2},k} = \frac{G^{j+1,k} + G^{j,k}}{2}. \tag{5.56}$$

The equation for the evolution of the growth factor concentration is a diffusion-reaction equation. The flux function for the growth factor concentration only depends on the normal derivative of the growth factor concentration. Equation (5.56) is not a TVD approximation, in contrast to the reconstruction of the cell densities at the inner edges and faces. However, due to the presence of the purely diffusive flux of the growth factor concentration, the TVD property is not needed for the considered approximation.

The value of the growth factor concentration on the inner edges is considered as fixed during the solution of the Riemann problem for the fluxes of the cell densities, which is presented in Section 5.3.6. Despite the reconstruction of the solution for function g does not contain a TVD property, this will not lead to the appearance of spurious oscillations in the numerical solution.

The right-hand side of equation (5.55) approximates the directional derivative along the vector, which connects the centers of the cells $V_{j,k}$, $V_{j+1,k}$. If this vector is parallel to the r-axis, then this directional derivative coincides with the normal derivative at the inner edge. If the considered vector is not parallel to the r-axis, then the directional derivative along one more vector, is needed, which is not parallel to the first one, in order to obtain at least a first order of accuracy for the normal derivative at the considered edge. To accomplish this, a third point is defined, on which the value of the function is known. The third point is chosen among the centers of the active cells, adjacent to the end-points of the edge $e_{j+\frac{1}{2},k}$, excluding the cells $V_{j,k}$, $V_{j+1,k}$. There can be from four to one such cells. This statement follows from the definition of inner edges and active cells in Section 5.3.2.2 (see a detailed proof in B.2). If there are some adjacent active cells besides cells $V_{j,k}$, $V_{j+1,k}$, then such a cell is chosen, that the perimeter of the triangle with vertices at the centers of the considered cell and cells $V_{j,k}$, $V_{j+1,k}$ is the smallest among all adjacent cells. Suppose, that the third point is chosen. The general formula for the average value of the gradient over some arbitrary volume V is defined as

$$\frac{1}{\mu(V)}\int_V \nabla g \, dv = \frac{1}{\mu(V)}\int_S g\vec{n} \, ds,$$

where S is the boundary surface of the volume V with the outer unit normal $\vec{n}$. This formula is applied for the triangle with the vertices at the centers of the three chosen cells. If the cell averages of the function g within the three chosen cells are denoted by G^1, G^2, G^3 , and the r- and z- coordinates of the cell centers are denoted by r^1, r^2, r^3, z^1, z^2 and z^3, then the normal derivative $\frac{\partial g}{\partial r}(r_{j+\frac{1}{2}}, z_e^{j+\frac{1}{2},k})$ is approximated as:

$$\frac{\partial G}{\partial r}^{j+\frac{1}{2},k} = \frac{(G^1+G^2)(z^2-z^1)+(G^2+G^3)(z^3-z^2)+(G^3+G^1)(z^1-z^3)}{(r^2-r^1)(z^3-z^1)-(z^2-z^1)(r^3-r^1)}. \quad (5.57)$$

The partial derivative with respect to z coordinate is determined as follows

$$\frac{\partial G}{\partial z}^{j+\frac{1}{2},k} = -\frac{(G^1+G^2)(r^2-r^1)+(G^2+G^3)(r^3-r^2)+(G^3+G^1)(r^1-r^3)}{(r^2-r^1)(z^3-z^1)-(z^2-z^1)(r^3-r^1)}. \tag{5.58}$$

Then the value of the growth factor concentration g in the center of edge $e_{j+\frac{1}{2},k}$ is determined from linear interpolation:

$$G^{j+\frac{1}{2},k} = G^1 + \frac{\partial G}{\partial r}^{j+\frac{1}{2},k}(r_e^{j+\frac{1}{2},k}-r^1) + \frac{\partial G}{\partial z}^{j+\frac{1}{2},k}(z_e^{j+\frac{1}{2},k}-z^1), \tag{5.59}$$

where $(r_e^{j+\frac{1}{2},k}, z_e^{j+\frac{1}{2},k})$ are the coordinates of the center of edge $e_{j+\frac{1}{2},k}$.

If a horizontal edge $e_{j,k+\frac{1}{2}}$ is adjacent to regular rectangular cells $V_{j,k}$, $V_{j,k+1}$, then the following formulas are used:

$$\frac{\partial G}{\partial z}^{j,k+\frac{1}{2}} = \frac{G^{j,k+1}-G^{j,k}}{z_c^{j,k+1}-z_c^{j,k}}, \qquad G^{j,k+\frac{1}{2}} = \frac{G^{j,k+1}+G^{j,k}}{2}. \tag{5.60}$$

If at least one of the cells $V_{j,k}$, $V_{j,k+1}$ is irregular, then the third adjacent cell is chosen in the way, as it is done for the vertical edges. The partial derivatives $\frac{\partial G}{\partial r}^{j,k+\frac{1}{2}}$, $\frac{\partial G}{\partial z}^{j,k+\frac{1}{2}}$ are approximated with the right-hand sides of equations (5.57), (5.58), in which variables G^1, G^2, G^3, r^1, r^2, r^3, z^1, z^2 and z^3 are defined in the same way. The value of g at the edge center $(r_e^{j,k+\frac{1}{2}}, z_e^{j,k+\frac{1}{2}})$ is determined as

$$G^{j,k+\frac{1}{2}} = G^1 + \frac{\partial G}{\partial r}^{j,k+\frac{1}{2}}(r_e^{j,k+\frac{1}{2}}-r^1) + \frac{\partial G}{\partial z}^{j,k+\frac{1}{2}}(z_e^{j,k+\frac{1}{2}}-z^1), \tag{5.61}$$

The derivation of the normal derivatives of the immature and mature cell densities is analogous to the approach for the derivatives of the growth factor concentration. If a horizontal edge $e_{j,k+\frac{1}{2}}$ and faces $e^3_{j,k+\frac{1}{2},l}$ or a vertical edge $e_{j+\frac{1}{2},k}$ and corresponding faces $e^3_{j+\frac{1}{2},k,l}$, $l = 1, 2, ..., N_a$, are adjacent to regular rectangular cells, then the following formulas are used, respectively:

$$\frac{\partial C_i}{\partial z}^{j,k+\frac{1}{2},l} = \frac{C_i^{j,k+1,l}-C_i^{j,k,l}}{z_c^{j,k+1}-z_c^{j,k}}, \qquad \frac{\partial C_m}{\partial z}^{j,k+\frac{1}{2}} = \frac{C_m^{j,k+1}-C_i^{j,k}}{z_c^{j,k+1}-z_c^{j,k}}, \tag{5.62}$$

$$\frac{\partial C_i}{\partial r}^{j+\frac{1}{2},k,l} = \frac{C_i^{j+1,k,l}-C_i^{j,k,l}}{r_c^{j+1,k}-r_c^{j,k}}, \qquad \frac{\partial C_m}{\partial r}^{j+\frac{1}{2},k} = \frac{C_m^{j+1,k}-C_i^{j,k}}{r_c^{j+1,k}-r_c^{j,k}}, \tag{5.63}$$

If at least one of the cells adjacent to the considered edge is irregular, then the third adjacent cell is chosen in the way, as it was described above. If the cell averages of the functions c_i and c_m within the chosen cells are denoted by $C_i^{1,l}$, $C_i^{2,l}$, $C_i^{3,l}$, and C_m^1, C_m^2, C_m^3, respectively, and the r- and z- coordinates of the cell centers are denoted by r^1, r^2, r^3, z^1, z^2 and z^3, respectively, then the linear approximations of the normal derivatives $\frac{\partial c_i}{\partial r}(r_{j+\frac{1}{2}}, z_e^{j+\frac{1}{2},k}, a_l)$, $\frac{\partial c_m}{\partial r}(r_{j+\frac{1}{2}}, z_e^{j+\frac{1}{2},k})$, $\frac{\partial c_i}{\partial z}(r_e^{j,k+\frac{1}{2}}, z_{k+\frac{1}{2}}, a_l)$ and $\frac{\partial c_m}{\partial z}(r_e^{j,k+\frac{1}{2}}, z_{k+\frac{1}{2}})$ are given by:

$$\frac{\partial \widehat{C}_i}{\partial r}^{j+\frac{1}{2},k,l} = \big((C_i^{1,l} + C_i^{2,l})(z^2 - z^1) + (C_i^{2,l} + C_i^{3,l})(z^3 - z^2) + (C_i^{3,l} + C_i^{1,l})(z^1 - z^3)\big) / \big((r^2 - r^1)(z^3 - z^1) - (z^2 - z^1)(r^3 - r^1)\big), \tag{5.64}$$

$$\frac{\partial \widehat{C}_m}{\partial r}^{j+\frac{1}{2},k} = \big((C_m^1 + C_m^2)(z^2 - z^1) + (C_m^2 + C_m^3)(z^3 - z^2) + (C_m^3 + C_m^1)(z^1 - z^3)\big) / \big((r^2 - r^1)(z^3 - z^1) - (z^2 - z^1)(r^3 - r^1)\big), \tag{5.65}$$

$$\frac{\partial \widehat{C}_i}{\partial z}^{j,k+\frac{1}{2},l} = -\big((C_i^{1,l} + C_i^{2,l})(r^2 - r^1) + (C_i^{2,l} + C_i^{3,l})(r^3 - r^2) + (C_i^{3,l} + C_i^{1,l})(r^1 - r^3)\big) / \big((r^2 - r^1)(z^3 - z^1) - (z^2 - z^1)(r^3 - r^1)\big), \tag{5.66}$$

$$\frac{\partial \widehat{C}_m}{\partial z}^{j,k+\frac{1}{2}} = -\big((C_m^1 + C_m^2)(r^2 - r^1) + (C_m^2 + C_m^3)(r^3 - r^2) + (C_m^3 + C_m^1)(r^1 - r^3)\big) / \big((r^2 - r^1)(z^3 - z^1) - (z^2 - z^1)(r^3 - r^1)\big). \tag{5.67}$$

The linear approximations of the normal derivatives on the unstructured mesh may yield negative values in the numerical solutions for the cell densities in the regions, where the cell densities have values close to zero and where the gradients of the densities are high. As it is mentioned in Section 5.3.1, the current model is very sensitive with respect to negative values of the cell densities. Hence the present numerical approach should provide nonnegative approximate solutions for the densities. Therefore, the linear approximations in equations (5.64)–(5.67) should be limited in the following way:

$$\frac{\partial C_i}{\partial r}^{j+\frac{1}{2},k,l} = \max\left(\min\left(\frac{\partial \widehat{C}_i}{\partial r}^{j+\frac{1}{2},k,l}, \frac{C_i^{j+1,k,l}}{r_c^{j+1,k,l} - r_c^{j,k,l}}\right), -\frac{C_i^{j,k,l}}{r_c^{j+1,k,l} - r_c^{j,k,l}}\right), \tag{5.68}$$

$$\frac{\partial C_m}{\partial r}^{j+\frac{1}{2},k} = \max\left(\min\left(\frac{\partial \widehat{C}_m}{\partial r}^{j+\frac{1}{2},k}, \frac{C_m^{j+1,k}}{r_c^{j+1,k} - r_c^{j,k}}\right), -\frac{C_m^{j,k}}{r_c^{j+1,k} - r_c^{j,k}}\right), \tag{5.69}$$

$$\frac{\partial C_i}{\partial z}^{j,k+\frac{1}{2},l} = \max\left(\min\left(\frac{\partial \widehat{C}_i}{\partial z}^{j,k+\frac{1}{2},l}, \frac{C_i^{j,k+1,l}}{z_c^{j,k+1,l} - z_c^{j,k,l}}\right), -\frac{C_i^{j,k,l}}{z_c^{j,k+1,l} - z_c^{j,k,l}}\right), \tag{5.70}$$

$$\frac{\partial C_m}{\partial z}^{j,k+\frac{1}{2}} = \max\left(\min\left(\frac{\partial \widehat{C}_m}{\partial z}^{j,k+\frac{1}{2}}, \frac{C_m^{j,k+1}}{z_c^{j,k+1} - z_c^{j,k}}\right), -\frac{C_m^{j,k}}{z_c^{j,k+1} - z_c^{j,k}}\right). \tag{5.71}$$

The limiting procedure introduced above is equivalent to the assumption, that the outflow of the cell density caused by random walk and taking place through the boundaries of control volumes is bounded from above. If the outflow is bounded by some limit value, an appropriate time step size providing nonnegative numerical solutions can be chosen as described in Section 5.3.9. The upper boundary for the outflow of the cell density per unit length is determined in a straightforward way for a uniform rectangular mesh. The outflow caused by random walk is equal to $D_c\frac{C-C_{adj}}{h}$, where C is the average density over the considered control volume, C_{adj} is the average density in the adjacent control volume and h is the linear mesh size. Then the outflow is less than or equal to $D_c\frac{C}{h}$ if the solution is nonnegative. The limiting formulas (5.68) – (5.71) provide the values of the outflow of the cell densities on the unstructured mesh, which are bounded from above by some limit value related to the average cell densities within the considered control volumes. The limit value is determined in an analogous way as the value $D_c\frac{C}{h}$ for a uniform mesh. The linear gradient approximation given by formulas (5.64)–(5.67) for the unstructured mesh can yield a nonzero outflow from the control volumes with zero average cell densities. In this case, negative values of the cell densities can appear in the numerical solution at any time step. Therefore, the limiting of the linear flux approximation is crucial for the positivity of the numerical solution.

The first stage of the derivation of the fluxes at the inner edges and faces, which are represented by the terms $H_i^{M_I}$, $H_m^{M_I}$ and $H_g^{M_I}$ in equations (5.32)–(5.34), is outlined in Sections 5.3.5.2 and 5.3.5.3. At this stage, the two states of the cell densities, the values of the growth factor concentration and the normal derivatives of the cell densities and of the growth factor concentration at the centers of the inner edges and faces are derived. These quantities are used for the initialization of the Riemann problem at each

inner edge or face. As it was mentioned earlier, the Riemann problem is solved at the second stage, in order to provide a stable discretization of the advection-diffusion terms. Therefore, the exact Riemann solution for the considered flux functions is obtained in Section 5.3.6. This Riemann solution provides the fluxes at the inner edges and faces.

5.3.6 Nonlinear system of conservation laws

At the first stage of the approximation of the fluxes of the cell densities at the inner edges $e_{\vec{j}}$ and faces $e^3_{\vec{j}^3}$, the left and right states of the cell densities $C^{\vec{j}}_{m(L)}$, $C^{\vec{j}^3}_{i(L)}$, $C^{\vec{j}}_{m(R)}$, $C^{\vec{j}^3}_{i(R)}$, the values of normal derivatives $\frac{\partial C_i}{\partial x}^{\vec{j}^3}$, $\frac{\partial C_m}{\partial x}^{\vec{j}}$ and $\frac{\partial G}{\partial x}^{\vec{j}}$ and the values of the growth factor concentration $G^{\vec{j}}$ were determined at the centers of the considered edges and faces. The vectors $\vec{j}$ and $\vec{j}^3$ are the indices of the considered inner edge and of the corresponding inner faces, respectively. The variable x is used to denote the independent coordinate r or z, which corresponds to the normal direction at the considered edge or face. For the horizontal edges and faces, $x = z$ is used, and for the vertical edges and faces, $x = r$ is employed.

At the second stage of the approximation, a one-dimensional Riemann problem is solved. The problem is defined by one-dimensional equations, which are derived from the governing equations (5.18)–(5.19). The solution of the Riemann problem for the system of hyperbolic PDE's provides a stable discretization of the initial governing system. The diffusive parabolic terms $-D_c\frac{\partial^2 c_i}{\partial x^2}$, $-D_c\frac{\partial^2 c_m}{\partial x^2}$ and the reactive terms from equations (5.18)–(5.19) do not contribute to a wave-like behavior of the solution. Such a behavior is the main characteristic of the hyperbolic equations. Therefore, these terms are skipped in the present analysis. The flux of cells is considered only in the normal direction with respect to the considered inner edges or faces. The following equations are obtained:

$$\frac{\partial c_i}{\partial t} + \frac{\partial}{\partial x}\left(\chi(g, c_{tot})\; c_i \frac{\partial g}{\partial x}\right) = 0, \tag{5.72}$$

$$\frac{\partial c_m}{\partial t} + \frac{\partial}{\partial x}\left(\chi(g, c_{tot})\; c_m \frac{\partial g}{\partial x}\right) = 0, \tag{5.73}$$

Recall that the total osteogenic cell density is defined as $c_{tot} = \int_0^1 c_i\, da + c_m$. If equation (5.72) is integrated over the interval $a \in [0, 1]$, and equation (5.73) is added to it, then the equation for the total cell density is obtained:

$$\frac{\partial c_{tot}}{\partial t} + \frac{\partial}{\partial x}\left(\chi(g, c_{tot})\; c_{tot} \frac{\partial g}{\partial x}\right) = 0. \tag{5.74}$$

Instead of obtaining a Riemann solution for system (5.72), (5.73), which is defined for the unknowns c_i, c_m, two systems can be considered. The

present systems consist of either equations (5.74), (5.72) or equations (5.74), (5.73), which are defined with respect to the unknown variables c_{tot}, c_i and c_{tot}, c_m, respectively. The new systems are more convenient to solve and to analyse than the initial system (5.72), (5.73). A solution for the unknown c_{tot} is easily obtained from equation (5.74), which is a nonlinear scalar conservation law similar to Burger's equation for $c_{tot} \in [0,1]$. The solution procedure for the two new systems (5.74), (5.72) and (5.74), (5.73) is the same. Equation (5.72) becomes identical to equation (5.73), if the variable c_m is substituted in place of the variable c_i.

Therefore, a Riemann problem is solved for system (5.74), (5.73), with the initial conditions:

$$c_{tot} = \begin{cases} c_{tot}^L, & x < 0, \\ c_{tot}^R, & x > 0, \end{cases} \quad c_m = \begin{cases} c_m^L, & x < 0, \\ c_m^R, & x > 0, \end{cases} \tag{5.75}$$

where c_{tot}^L, c_m^L and c_{tot}^R, c_m^R are the left and right states of the variables at the considered inner edge. The normal derivatives of the growth factor concentration and the value of the growth factor concentration in equations (5.73), (5.74), are assumed to be constant and equal to their values at the inner edge, which are denoted as $\frac{\partial g}{\partial x}^{\downarrow}$ and $g^{\downarrow}$, respectively. If, for example, a vertical inner edge $e_{j+\frac{1}{2},k}$ is considered, then

$$\begin{aligned} c_{tot}^L &= h_a \sum_{l=1}^{N_a} C_{i(L)}^{j+\frac{1}{2},k,l} + C_{m(L)}^{j+\frac{1}{2},k}, \\ c_{tot}^R &= h_a \sum_{l=1}^{N_a} C_{i(R)}^{j+\frac{1}{2},k,l} + C_{m(R)}^{j+\frac{1}{2},k}, \\ c_m^L &= C_{m(L)}^{j+\frac{1}{2},k}, \; c_m^R = C_{m(R)}^{j+\frac{1}{2},k}, \\ \frac{\partial g}{\partial x}^{\downarrow} &= \frac{\partial G}{\partial r}^{j+\frac{1}{2},k}, \; g^{\downarrow} = G^{j+\frac{1}{2},k}. \end{aligned}$$

The variables $C_{i(L)}^{j+\frac{1}{2},k,l}$, $C_{i(R)}^{j+\frac{1}{2},k,l}$, $C_{m(L)}^{j+\frac{1}{2},k}$, $C_{m(R)}^{j+\frac{1}{2},k}$, $\frac{\partial G}{\partial r}^{j+\frac{1}{2},k}$, $G^{j+\frac{1}{2},k}$, which are used in the current formulas, are defined in Sections 5.3.5.2, 5.3.5.3. System (5.74), (5.73) can be rewritten in the form:

$$\frac{\partial \vec{q}}{\partial t} + \frac{\partial}{\partial x}\vec{f}(\vec{q}) = \vec{0}, \tag{5.76}$$

where

$$\vec{q} = \begin{bmatrix} q_1 \\ q_2 \end{bmatrix} = \begin{bmatrix} c_{tot} \\ c_m \end{bmatrix},$$

$$\vec{f}(\vec{q}) = \begin{bmatrix} f_1(q_1) \\ f_2(q_1, q_2) \end{bmatrix} = \begin{bmatrix} \chi(g^{\downarrow}, q_1)\; q_1 \dfrac{\partial g}{\partial x}^{\downarrow} \\ \chi(g^{\downarrow}, q_1)\; q_2 \dfrac{\partial g}{\partial x}^{\downarrow} \end{bmatrix}.$$

Let us assume first, that $c_{tot} \in (0, 1]$. This assumption is taken into account from here up to Section 5.3.6.1 inclusive. The situation $c_{tot} \in [0, \infty)$ is considered in Sections 5.3.6.2–5.3.6.4.

The Jacobian of the flux function $\vec{f}(\vec{q})$ is equal to

$$J = \begin{bmatrix} \chi^{\downarrow}(1 - 2q_1) & 0 \\ -\chi^{\downarrow} q_2 & \chi^{\downarrow}(1 - q_1) \end{bmatrix},$$

where $\chi^{\downarrow} = \frac{\chi_0 \, g^{\downarrow}}{K_{ch}^2 + g^{\downarrow 2}} \frac{\partial g}{\partial x}^{\downarrow}$. Its eigenvalues and the corresponding eigenvectors are

$$\lambda_1 = \chi^{\downarrow}(1 - 2q_1), \quad \lambda_2 = \chi^{\downarrow}(1 - q_1), \tag{5.77}$$

$$\vec{r^1} = \begin{bmatrix} q_1 \\ q_2 \end{bmatrix}, \quad \vec{r^2} = \begin{bmatrix} 0 \\ 1 \end{bmatrix}.$$

The Hugoniot-locus and the integral curve [59] for the waves from the first family coincide. These curves are the straight lines

$$\frac{q_2}{q_1} = const. \tag{5.78}$$

The Hugoniot locus is the location of all states $\vec{q}^*$, which can be connected to some fixed state $\vec{q}$ by a shock wave from the corresponding wave family. It is determined from equation

$$\vec{f}(\vec{q}^*) - \vec{f}(\vec{q}) = s(\vec{q}^* - \vec{q}), \tag{5.79}$$

where s is an arbitrary scalar value, denoting the shock wave speed. For two states $\vec{q}$ and $\vec{q}^*$, which lie on the line (5.78), the following relation holds

$$f(\vec{q}^*) - f(\vec{q}) = \begin{bmatrix} \chi^{\downarrow} \left(q_1^*(1 - q_1^*) - q_1(1 - q_1) \right) \\ \chi^{\downarrow} \frac{q_2}{q_1} \left(q_1^*(1 - q_1^*) - q_1(1 - q_1) \right) \end{bmatrix}$$

$$= \chi^{\downarrow} \left(1 - q_1^* - q_1\right) \begin{bmatrix} q_1^* - q_1 \\ q_2^* - q_2 \end{bmatrix}.$$

Hence the speed of the shock waves from the first family is equal to

$$s = \chi^{\downarrow} \left(1 - q_1^* - q_1\right). \tag{5.80}$$

The integral curve is the location of all states, which can be connected with a given state by a rarefaction wave. It is defined as a curve, which is tangent to the eigenvector from the corresponding family at each point. In equation (5.78), the integral curves are defined as contours of the function $\xi(\vec{q}) = \frac{q_2}{q_1}$. Since the gradient of ξ is orthogonal to eigenvector $\vec{r^1}$, equation (5.78) is the correct definition for the corresponding integral curves.

Hence the mature cell density can be considered as the total density times a weight function w_m:

$$c_m = c_{tot} w_m.$$

Then equation (5.78) is equivalent to $w_m = const.$ This means, that waves from the first family connect the states of the variables with a constant weight. The density of mature cells changes along lines (5.78), for example from state c_m to c_m^*, only as a result of variation of the total cell density from c_{tot} to c_{tot}^*. The weight fraction remains constant, that is $c_m = w_m c_{tot}$ and $c_m^* = w_m c_{tot}^*$. In Figure 5.4, the lines of the first family are plotted as the radial lines.

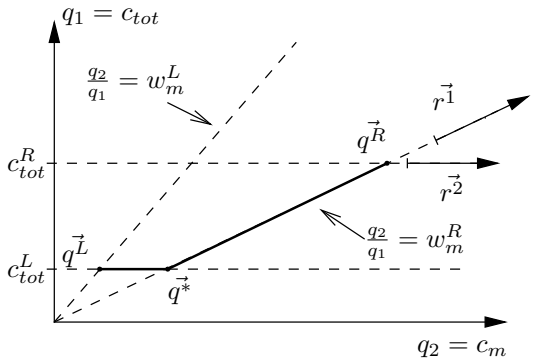

Figure 5.4: Hugoniot loci and integral curves for system (5.74), (5.73), which are represented by the straight dashed lines

For the second wave family, referred to as the 2-waves, it can be derived that

$$\nabla \lambda_2 \cdot \vec{r^2} = (\lambda_2)'_{q_1} \cdot 0 + 0 \cdot 1 = 0.$$

This means that the characteristics from the second family have a constant slope λ_2 along a simple wave from this family, and this field is linearly degenerate [59]. The 2-waves are the contact waves, i.e. they do not show any nonlinear behavior (formation of shocks and rarefaction waves). The Hugoniot loci for the contact waves are defined as straight lines, which are parallel to the corresponding eigenvector (in the current case to vector $\vec{r^2}$). The equation for these lines is

$$q_1 = const.$$

The two states, connected by a 2-wave have the same total cell density $c_{tot} = c_{tot}^*$. The density of mature cells varies due to a variation of their weight fraction, i.e. $c_m = w_m c_{tot}$ and $c_m^* = w_m^* c_{tot}$.

The first field is genuinely nonlinear, if

$$\nabla \lambda_1 \cdot \vec{r^1} = -2\chi^{\downarrow} q_1 \neq 0.$$

The genuine nonlinearity implies, that the waves in the considered family propagate as shock waves or as rarefaction waves. If $\chi^{\downarrow} = 0$, then the flux of cells due to chemotaxis is zero. In this trivial situation, a Riemann solution is not needed, since the hyperbolic terms in the governing equations are equal to zero. Further, it is assumed, that $\chi^{\downarrow} \neq 0$. Note, that from assumptions $c_{tot} \in (0, 1]$ and $\chi^{\downarrow} \neq 0$ it follows, that the 1-wave, associated with the eigenvector $\vec{r^1}$, is genuinely nonlinear.

5.3.6.1 The strictly hyperbolic case

From equation (5.77), it follows that the eigenvalues λ_1 and λ_2 are equal, if and only if $q_1 = 0$. Hence the eigenvalues λ_1 and λ_2 are distinct and system (5.74), (5.73) is strictly hyperbolic, if $c_{tot} \in (0, 1]$. For a general strictly hyperbolic system, if the left and right states $\vec{q}^L$ and $\vec{q}^R$ are situated sufficiently close to each other in the phase plane, then they can be connected by the intersecting Hugoniot loci and integral curves, as it is shown in Figure 5.4 for the present system of two equations. In this case, the Riemann solution consists of classical nonlinear and/or linear waves. The qualitative structure of the solution is determined in a simple way, which is described, for example, in LeVeque [59].

However, if $\vec{q}^L$ and $\vec{q}^R$ are located far away from each other, then they may not be connected by intersecting Hugoniot loci and integral curves. In this case, a Riemann solution cannot be represented as a set of classical nonlinear and/or linear waves. Instead of classical shock waves, which are also referred to as Lax shocks, nonclassical delta shocks or singular shocks can form [see, for example, 23, 90]. Delta shocks waves are characterized by appearance of singularities in the solutions, which are expressed through the Dirac delta function. Classical Lax shocks are always intersected by the characteristics from other wave families. This feature distinguishes Lax shocks from nonclassical shocks. For a particular system of two nonlinear hyperbolic equations, which was considered in Tan et al. [90], the characteristics of the second family go into the 1-delta shock from the left and from the right. A situation, when system (5.74), (5.73) is weakly hyperbolic and when delta shock waves appear in the Riemann solution, is considered in Section 5.3.6.4.

Under the current assumption $c_{tot} \in (0, 1]$, Hugoniot loci and integral curves of the first family always intersect any integral curve from the second family. Hence any two states $\vec{q}^L$ and $\vec{q}^R$, such that $c_{tot}^L \in (0, 1]$ and $c_{tot}^R \in (0, 1]$, can be connected by Hugoniot loci and integral curves in the phase plane (Figure 5.4). A Riemann solution is composed of a 1-shock or a 1-rarefaction wave and a 2-contact wave. It is easy to demonstrate, that the 1-shock wave is a Lax shock.

A nonlinear wave in the solution of scalar equation (5.74) for the total cell density c_{tot} coincides with a 1-wave in the Riemann solution of system

(5.74), (5.73). Therefore, the shock wave of the first family (if it appears) splits the $x-t$ plane in two parts, so that the total cell density is equal to c_{tot}^L and to c_{tot}^R to the left and to the right from the shock wave, respectively. The shock wave speed s is equal to $\chi^{\downarrow}(1-c_{tot}^L-c_{tot}^R)$. The 2-characteristics have the slopes $\lambda_2(c_{tot}^L)=\chi^{\downarrow}c_m^L(1-c_{tot}^L)$ and $\lambda_2(c_{tot}^R)=\chi^{\downarrow}c_m^R(1-c_{tot}^R)$ to the left and to the right from the shock, respectively. Hence

$$(\lambda_2(c_{tot}^L)-s)(\lambda_2(c_{tot}^R)-s)=\chi^{\downarrow 2}c_{tot}^Lc_{tot}^R>0. \tag{5.81}$$

Inequality (5.81) implies, that the 2-characteristics always enter the 1-shock from one side and leave the shock from the other side, that is they intersect the shock. Hence the 1-shock wave is a Lax shock, if $c_{tot}\in(0,1]$ and $\chi^{\downarrow}\neq 0$. The number of characteristics, which impinge on a 1-shock will be equal to three: two characteristics of the first family from the left and from the right of the shock and one set of 2-characteristics at some side from the shock.

Assume that

$$\lambda_1>\lambda_2. \tag{5.82}$$

Consider a 1-shock wave, which has a speed s. It follows from the entropy condition [59], that $\lambda_1(c_{tot}^R)<s$. Hence $\lambda_2(c_{tot}^R)<\lambda_1(c_{tot}^R)<s$. Inequality (5.81) yields that $\lambda_2(c_{tot}^L)<s$. Therefore, 2-characteristics intersect a 1-shock wave from right to left. It follows from condition (5.82) that the 2-characteristics intersect a 1-rarefaction wave from right to left (Figure 5.5). Hence the 2-contact wave always lies to the left from the nonlinear shock or rarefaction wave from the first family, if inequality (5.82) holds. The intermediate state $\vec{q^*}$ lies between the first and second waves (Figure 5.5c, d). The left state $\vec{q^L}=[c_{tot}^L,w_m^Lc_{tot}^L]^T$ is connected to $\vec{q^*}$ by the 2-wave. Hence the state $\vec{q^*}$ should lie on the same integral curve from the second family with the state $\vec{q^L}$. By analogy, the state $\vec{q^*}$ lies on the 1-integral curve (or 1-Hugoniot locus, since they coincide), which passes through the right state $\vec{q^R}=[c_{tot}^R,w_m^Rc_{tot}^R]^T$. In the phase plane, shown in Figure 5.4, such a structure of the solution looks like a thick poly-line, which connects the states $\vec{q^L}$, $\vec{q^*}$ and $\vec{q^R}$. It follows, that $q_1^*=c_{tot}^L$ and $q_2^*=w_m^Rc_{tot}^L$. Our aim is to determine the value of the flux function $f_2(\vec{q})=\chi^{\downarrow}(1-q_1)q_2$ at the edge between two control volumes. The flux function is evaluated for the state $\vec{q^{\downarrow}}=[q_1^{\downarrow},q_2^{\downarrow}]^T$ on the considered edge, which is found from the solution of the Riemann problem. The values $q_1^{\downarrow}$, $q_2^{\downarrow}$ can be determined from the characteristic portrait of the solution in the $x-t$ plane, which is shown in Figure 5.5. For the considered Riemann problem, the location of the edge between the control volumes corresponds to the ray $\frac{x}{t}=0$ for $t>0$ in the $x-t$ plane.

Remark 5.3. If rays $\frac{x}{t}=const$ are mentioned further in the text, it is implied that $t>0$.

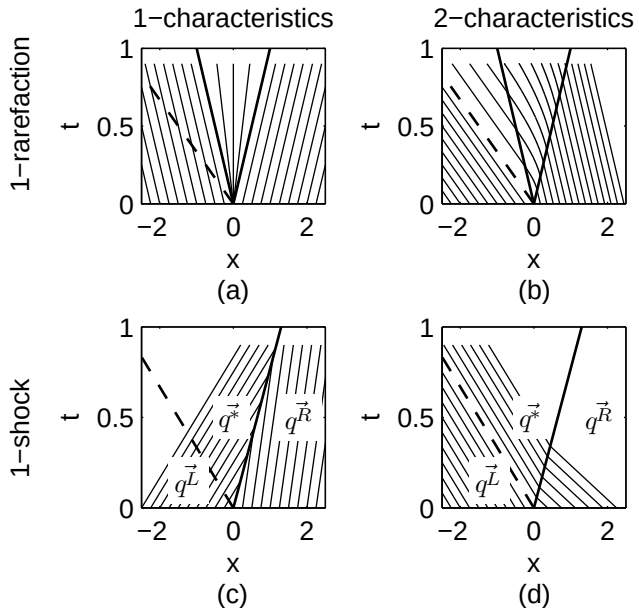

Figure 5.5: Solution structure in the $x - t$ plane for a strictly hyperbolic system. The thick lines denote the edges of the 1-rarefaction wave or the 1-shock wave and the thick dashed lines denote the 2-contact wave. The thin lines are the characteristics of the first (a), (c) and second families (b),(d). The 2-contact wave lies to the left from the nonlinear 1-wave, since it is assumed that $\lambda_2 < \lambda_1$ everywhere

For the present system it is possible to derive simple general formulas, which provide the values of c_{tot} and c_m at $\frac{x}{t} = 0$. The discontinuities of the variables c_{tot} and w_m are considered separately, since they are carried by two separate waves. The 1-wave carries the discontinuity in c_{tot}. The state $c_{tot}^{\downarrow}$ at the ray $\frac{x}{t} = 0$, corresponding to the considered inner edge, can be determined from the Riemann solution for the scalar nonlinear equation (5.74) [59]:

$$c_{tot}^{\downarrow} = \begin{cases} \arg \min\limits_{c_{tot}^L \le c_{tot} \le c_{tot}^R} f_1(c_{tot}), & \text{if } c_{tot}^L \le c_{tot}^R, \\ \arg \max\limits_{c_{tot}^R \le c_{tot} \le c_{tot}^L} f_1(c_{tot}), & \text{if } c_{tot}^R \le c_{tot}^L. \end{cases} \tag{5.83}$$

The 2-contact wave carries the discontinuity in the weight fraction w_m. For the considered case $\lambda_1 > \lambda_2$, the speed of this wave is equal to $\lambda_2(c_{tot}^L)$. Then the state $w_m^{\downarrow}$ at the ray $\frac{x}{t} = 0$ is equal to w_m^L or to w_m^R, if the eigenvalue $\lambda_2(c_{tot}^L)$ is positive or negative, respectively. If the 2-wave speed is zero, i.e. $\lambda_2(c_{tot}^L) = 0$, then according to the current assumption, the 1-wave will lie to the right from the 2-wave and, hence, from the ray $\frac{x}{t} = 0$. This means, that $c_{tot}^{\downarrow} = c_{tot}^L$, and that the 2-wave speed coincides with eigenvalue $\lambda_2(c_{tot}^{\downarrow})$. Note, that $f_2(c_{tot}, c_m) = c_m \lambda_2(c_{tot}) = w_m c_{tot} \lambda_2(c_{tot})$. Hence if the second eigenvalue $\lambda_2(c_{tot}^L)$ is zero, then irrespectively of the states w_m^L or w_m^R assigned to $w_m^{\downarrow}$, the flux function on the inner edge will be zero: $f_2(c_{tot}^{\downarrow}, w_m^{\downarrow} c_{tot}^{\downarrow}) = f_2(c_{tot}^L, w_m^{\downarrow} c_{tot}^L) = w_m^{\downarrow} c_{tot}^L \lambda_2(c_{tot}^L) = 0$.

Further, the following general formula for the state $w_m^{\downarrow}$ will be used:

$$w_m^{\downarrow} = \begin{cases} w_m^L, & \text{if } \lambda_2(c_{tot}^{\downarrow}) \ge 0, \\ w_m^R, & \text{if } \lambda_2(c_{tot}^{\downarrow}) < 0. \end{cases} \tag{5.84}$$

To justify equation (5.84) for the case $\lambda_1 > \lambda_2$, it should be shown that the eigenvalues $\lambda_2(c_{tot}^L)$ and $\lambda_2(c_{tot}^{\downarrow})$ have the same sign or are equal to zero simultaneously. For conciseness, the following notations are introduced

$$\lambda_i^L = \lambda_i(c_{tot}^L), \quad \lambda_i^R = \lambda_i(c_{tot}^R), \quad \lambda_i^{\downarrow} = \lambda_i(c_{tot}^{\downarrow}), \quad i = 1, 2.$$

Suppose that a 1-shock wave has a speed $s > 0$ and lies to the right from the ray $\frac{x}{t} = 0$. Then $c_{tot}^{\downarrow} = c_{tot}^L$ and $\lambda_2^L = \lambda_2^{\downarrow}$.

Assume that the 1-shock has a speed $s \le 0$. Condition (5.82) yields that 2-characteristics intersect the 1-shock wave from right to left. This means that $\lambda_2^L < s \le 0$ and $\lambda_2^R < s \le 0$. The eigenvalue λ_2 is negative everywhere. Hence $\lambda_2^L < 0$ and $\lambda_2^{\downarrow} < 0$, irrespectively of the states c_{tot}^L or c_{tot}^R assigned to $c_{tot}^{\downarrow}$.

It should be mentioned that a zero shock speed $s = 0$ leads to an ambiguity in the definition of $c_{tot}^{\downarrow}$. The total cell density is discontinuous at the ray $\frac{x}{t} = 0$. Formula (5.83) provides two values c_{tot}^L and c_{tot}^R for $c_{tot}^{\downarrow}$, since

$$f_1(c_{tot}^L) = f_1(c_{tot}^R). \tag{5.85}$$

Note that

$$f_2(c_{tot}, c_m) = \chi^{\downarrow} \frac{c_m}{c_{tot}} c_{tot}(1 - c_{tot}) = \chi^{\downarrow} w_m c_{tot}(1 - c_{tot}) = w_m f_1(c_{tot}).$$

The value of the flux $f_2^{\downarrow}$ is defined uniquely in this case, since the weight fraction w_m does not change through the 1-shock wave and since equality (5.85) holds.

For a 1-rarefaction wave, it follows from the entropy condition that $\lambda_1^L < \lambda_1^R$. If $\lambda_1^L > 0$, then the rarefaction fan lies to the right from the ray $\frac{x}{t} = 0$, and $c_{tot}^L = c_{tot}^{\downarrow}$. Consequently, $\lambda_2^L = \lambda_2^{\downarrow}$.

If $\lambda_1^R \leq 0$, then $c_{tot}^{\downarrow} = c_{tot}^R$. Further, $\lambda_2^L < \lambda_1^L < \lambda_1^R \leq 0$, and $\lambda_2^{\downarrow} = \lambda_2^R < \lambda_1^R \leq 0$.

Consider the case of a transonic rarefaction: $\lambda_1^L < 0 < \lambda_1^R$. In the rarefaction fan, there exists a characteristic line with slope $\lambda_1 = 0$, which coincides with the ray $\frac{x}{t} = 0$. Hence the state $c_{tot}^{\downarrow}$ is the value of the total cell density along the characteristic $\lambda_1 = 0$. That means that $\lambda_1^{\downarrow} = 0$ (and also that $c_{tot}^{\downarrow} = 0.5$). Then $\lambda_2^{\downarrow} < \lambda_1^{\downarrow} = 0$, and $\lambda_2^L < \lambda_1^L < 0$.

It was proved that λ_2^L and $\lambda_2^{\downarrow}$ have the same sign or are equal to zero simultaneously, if $\lambda_1 > \lambda_2$. Alternatively, if $\lambda_1 < \lambda_2$, then a 2-wave will be faster than a 1-wave. Hence the speed of the contact wave, which carries the discontinuity in the weight fraction w_m is equal to λ_2^R. By analogy, it can be proved that the eigenvalues λ_2^R and $\lambda_2^{\downarrow}$ have the same sign or are equal to zero simultaneously, if $\lambda_1 < \lambda_2$. This proof will justify formula (5.84).

5.3.6.2 Nonconvex flux function

In a more general case $c_{tot} \in (0, \infty)$, the solution structure becomes more complicated. The flux of the total cell density

$$f_1(c_{tot}) = \begin{cases} \chi^{\downarrow} c_{tot}(1 - c_{tot}), & c_{tot} \leq 1, \\ 0, & c_{tot} > 1, \end{cases} \tag{5.86}$$

is not a convex or a concave function in this case. The Riemann solution of the scalar equation (5.74) for the total cell concentration Riemann problem has the form of the compound wave, i.e. the wave, which is composed of a number of shocks, rarefactions and/or traveling waves. The structure of the solution is determined from the boundary of the convex hull, constructed for the given flux function [59]. If the left and right states in the Riemann problem are such that $c_{tot}^L < c_{tot}^R$, then the convex hull is constructed for the set $\{(x, y) : c_{tot}^L \leq x \leq c_{tot}^R, y \geq f_1(x)\}$, and if $c_{tot}^L > c_{tot}^R$, then the convex hull is constructed for the set $\{(x, y) : c_{tot}^R \leq x \leq c_{tot}^L, y \leq f_1(x)\}$.

Remark 5.4. The flux of the mature cell density is defined as:

$$f_2(c_{tot}, c_m) = \begin{cases} \chi^{\downarrow} c_m(1 - c_{tot}), & c_{tot} \leq 1, \\ 0, & c_{tot} > 1. \end{cases} \tag{5.87}$$

Let us consider the case $c_{tot}^L < c_{tot}^R$. Suppose, that $c_{tot}^R > 1$. Otherwise, due to the monotonicity of the entropy solution of the Riemann problem, the solution will be in the interval $(0, 1]$, and this situation was considered before. If $c_{tot}^L \geq 1$, then the Riemann solution will be constant in time, since $f_1 \equiv 0$ everywhere. That is the jump between c_{tot}^L and c_{tot}^R will not move.

Therefore, it is supposed that $0 < c_{tot}^L < 1 < c_{tot}^R$. Then the convex hulls can have three possible configurations, which are shown in Figure 5.6. For the situation illustrated in Figure 5.6a, the compound wave consists of

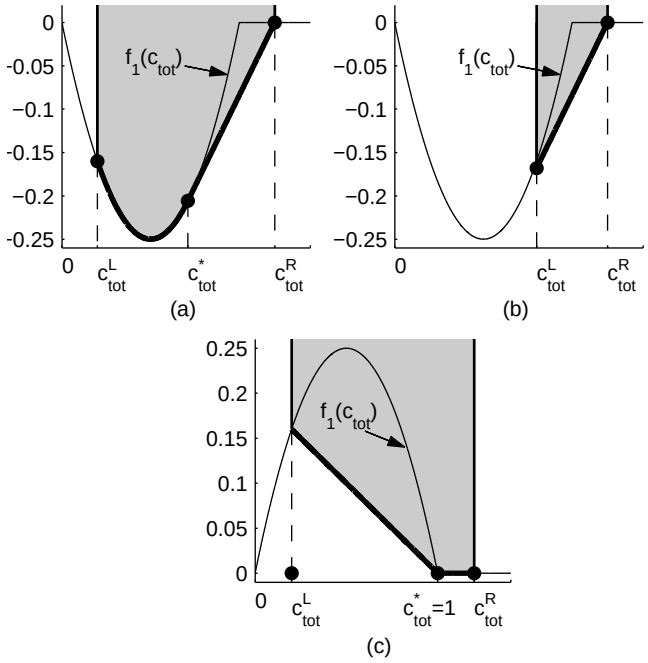

Figure 5.6: Three possible configurations of the convex hull, if $c_{tot}^L < 1 < c_{tot}^R$. The convex hull is constructed for the set $\{(x, y) : c_{tot}^L \leq x \leq c_{tot}^R, y \geq f_1(x)\}$. It is denoted by the filled area, with the boundary shown in the solid line.

the rarefaction wave, which connects the left state c_{tot}^L to an intermediate state c_{tot}^*, and of the shock wave, connecting the states c_{tot}^* and c_{tot}^R. The intermediate state is determined from the condition

$$f_1(c_{tot}^*)' = \frac{f_1(c_{tot}^R) - f_1(c_{tot}^*)}{c_{tot}^R - c_{tot}^*}. \tag{5.88}$$

The convex hull boundaries, which are shown in Figures 5.6b, c, correspond to the single shock wave between states c_{tot}^L and c_{tot}^R and to the compound wave, which consists of the shock and the linear contact wave, respectively.

The state $c_{tot}^{\downarrow}$ on the inner edge of the control volumes can be found from the general formula (5.83), which is also applicable for the case of a

nonconvex flux function [59]. Subsequently, it is proved that equation (5.84) for the weight fraction $w_m^{\downarrow}$ is correct in the current case.

Consider a single shock wave between the states $0 < c_{tot}^L < 1 < c_{tot}^R$ (Figure 5.6b), which appears if $\chi^{\downarrow} < 0$. Then the shock speed is given by:

$$s = \frac{f_1(c_{tot}^R) - f_1(c_{tot}^L)}{c_{tot}^R - c_{tot}^L} = -\chi^{\downarrow} \frac{c_{tot}^L(1 - c_{tot}^L)}{c_{tot}^R - c_{tot}^L} > 0,$$

and

$$\lambda_2^L - s = \chi^{\downarrow} \frac{c_{tot}^R(1 - c_{tot}^L)}{c_{tot}^R - c_{tot}^L} < 0, \qquad \lambda_2^R - s = \chi^{\downarrow} \frac{c_{tot}^L(1 - c_{tot}^L)}{c_{tot}^R - c_{tot}^L} < 0. \quad (5.89)$$

It follows from condition (5.89) that the characteristics of the 2-nd family intersect the 1-shock from right to left. Hence the 2-wave speed is equal to $\lambda_2(c_{tot}^L) = \chi^{\downarrow}(1 - c_{tot}^L) < 0$ and lies to the left of the ray $\frac{x}{t} = 0$. It follows that $w_m^{\downarrow} = w_m^R$. Since the shock speed is positive, the 1-shock lies to the right of the ray $\frac{x}{t} = 0$, and $c_{tot}^{\downarrow} = c_{tot}^L$. Therefore, formula (5.84) provides the correct value of $w_m^{\downarrow}$, since $\lambda_2(c_{tot}^{\downarrow}) = \lambda_2(c_{tot}^L)$.

Consider the compound wave, which consists of the rarefaction and shock waves (Figure 5.6a). This wave corresponds to the situation, when $c_{tot}^L < c_{tot}^R$ and $\chi^{\downarrow} < 0$. Therefore, $\lambda_2 - \lambda_1 = \chi^{\downarrow} c_{tot} < 0$ for $c_{tot} \in (0, 1]$. The rarefaction wave connects the states c_{tot}^L and c_{tot}^*, which lie in the interval $(0, 1]$. Hence the 2-characteristics intersect the 1-rarefaction wave from right to left. The characteristic portrait of the present Riemann solution is shown in Figure 5.7. The shock wave front coincides with the right edge of the rarefaction

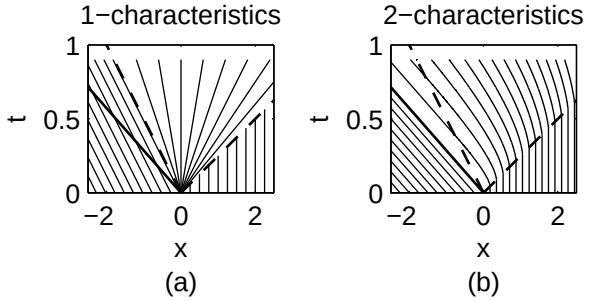

Figure 5.7: Characteristics of the first family and of the second family in the $x-t$ plane are shown in thin unbroken lines in plots (a) and (b), respectively. The wedges of the rarefaction fan are shown in solid dashed lines. The 2-contact wave front is denoted by a solid unbroken line. The 1-shock wave coincides with the right edge of 1-rarefaction wave. The 2-wave front lies to the left from the compound 1-wave

fan (see equation (5.88)). Then the 2-characteristics also intersect the shock

wave between the states c^*_{tot} and c^R_{tot} from right to left, since

$$\lambda_2(c^*_{tot}) - s = \chi^{\downarrow}\frac{c^R_{tot}(1-c^*_{tot})}{c^R_{tot}-c^*_{tot}} < 0, \qquad \lambda^R_2 - s = \chi^{\downarrow}\frac{c^*_{tot}(1-c^*_{tot})}{c^R_{tot}-c^*_{tot}} < 0.$$

This means that the 2-contact wave lies to the left of the compound 1-wave. The speed of the 2-wave is equal to λ^L_2. To justify formula (5.84) for the present case, it is necessary to show, that the eigenvalues λ^L_2 and $\lambda^{\downarrow}_2$ have the same sign or are equal to zero simultaneously. This is proved as follows. Since $\chi^{\downarrow} < 0$, the right edge of the rarefaction fan has the slope $\lambda_1(c^*_{tot}) = s = \chi^{\downarrow}(1 - c^*_{tot} - c^R_{tot}) > 0$. If $\lambda^L_1 > 0$, then $c^{\downarrow}_{tot} = c^L_{tot}$. If $\lambda^L_1 \le 0$, then $\lambda^{\downarrow}_1 = 0$ and $c^{\downarrow}_{tot} = 0.5$. Further, $\lambda^{\downarrow}_2 < \lambda^{\downarrow}_1 = 0$ and $\lambda^L_2 < \lambda^L_1 \le 0$.

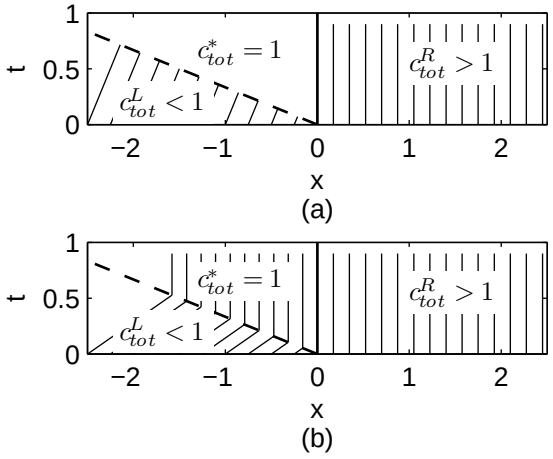

Figure 5.8: The solution to the Riemann problem, which consists of the shock wave (dashed line) and the stationary wave (thick solid line), includes three states: c^L_{tot}, $c^*_{tot} = 1$ and $c^R_{tot} > 1$. The 1- and 2-characteristics are shown in thin solid lines in plots (a) and (b), respectively. The derivative of the flux function $f_1(c_{tot})$ is discontinuous at the point $c_{tot} = 1$. As a result, the 1-characteristic lines are not defined in the wedge between the shock wave front and the contact wave front. The 2-characteristics intersect the 1-shock wave. The 2-contact wave is stationary and coincides with the stationary 1-contact wave

The third situation appears, if the compound wave consists of the shock wave between the states c^L_{tot} and $c^*_{tot} = 1$ and of the linear contact wave, which connects the states $c^*_{tot} = 1$ and $c^R_{tot} > 1$ (Figure 5.6c). The present type of the 1-wave appears for $0 < c^L_{tot} < 1 < c^R_{tot}$, if $\chi > 0$. The linear wave is stationary, since $\lambda_1 = f'_1 = 0$ for $c_{tot} \in (1, c^R_{tot})$, where $f_1(c_{tot})$ is given in equation (5.86). The derivative of the flux function $f_1(c_{tot})$ is discontinuous at the point $c_{tot} = 1$. Consequently, the 1-characteristic lines are not defined in the wedge between the fronts of the 1-shock wave and of the 1-contact

wave. The solution of the Riemann problem in the $x-t$ plane for the considered case is plotted in Figure 5.8. The 2-characteristics intersect the 1-shock wave, since $s = \chi^{\downarrow}(1 - c^L_{tot} - c^*_{tot}) < 0$, $\lambda^L_2 = \chi^{\downarrow}(1 - c^L_{tot}) > 0$ and $\lambda^L_2(c^*_{tot}) = 0$. The discontinuity of the weight fraction w_m propagates along the ray $\frac{x}{t} = 0$. The general formula (5.83) for the total cell density at the inner edge of the control volumes provides multiple solutions $c_{tot} \in [1, c^R_{tot}]$, which corresponds to the stationary discontinuity between states $c^*_{tot} = 1$ and $c^R_{tot} > 1$ in the solution for the total cell density at the inner edge (see Figure 5.8). This does not give us any problem, since the flux of mature cells is approximated, and $f_2(c_m, c_{tot}) = 0$ for $c_{tot} \in [1, c^R_{tot}]$.

The situation when $c^L_{tot} > c^R_{tot}$ is symmetrical to the case $c^L_{tot} < c^R_{tot}$. Conclusions, which can be made in this case, are analogous to the conclusions, which were stated for the case $c^L_{tot} < c^R_{tot}$.

5.3.6.3 Nonstrictly hyperbolic system

It was assumed in Section 5.3.6.2, that $c_{tot} \in (0, \infty)$. For $c_{tot} \in (1, \infty)$ the Jacobian is a zero matrix and the eigenvalues λ_1 and λ_2 are both equal to zero. Hence the considered system is not strictly hyperbolic for $c_{tot} \in (1, \infty)$. The zero eigenvalues have a two dimensional eigenspace. Therefore, the algebraic multiplicity of the eigenvalues is equal to their geometric multiplicity. Systems with this property are referred to as nonstrictly hyperbolic systems. At the points of the phase plane, where the system becomes nonstrictly hyperbolic, there exists an infinite number of eigendirections. The Riemann solution for the nonstrictly hyperbolic system may be more complicated, compared to a strictly hyperbolic case [59]. For $c_{tot} \in (1, \infty)$ the first and second fields are linearly degenerate. The waves in these fields are stationary contact waves. That is, the 1-wave and the 2-wave coincide in the regions, where $c_{tot} \in (1, \infty)$. This leads to the structure of the Riemann solution as described in Section 5.3.6.2.

Another point of the phase plane, where system (5.73)–(5.74) is nonstrictly hyperbolic, is $(c_{tot}, c_m) = (0, 0)$. The eigenvalues λ_1 and λ_2 are equal to $\chi^{\downarrow}$ and have a two dimensional eigenspace. An infinite number of the integral curves of the first family passes through the point $(0, 0)$, and any state $(c_{tot}, c_m) \in (0, \infty) \times \mathbb{R}$ can be connected to the state $(0, 0)$ by a 1-wave. Assume that the left state $\vec{q}^L$ is $[0, 0]^T$. Depending on the sign of $\chi^{\downarrow}$ and on the value of c^R_{tot}, the 1-wave, which connects $\vec{q}^L$ and $\vec{q}^R$ can have four configurations shown in Figure 5.9. Formula (5.83), which determines the value of c_{tot} at the ray $\frac{x}{t} = 0$, is valid in all considered cases, since this identity is derived for a scalar equation (5.74).

The 1-wave is a rarefaction wave if $\chi^{\downarrow} < 0$ and $c^R_{tot} \leq 1$ (Figure 5.9a). It is shown in Section 5.3.6, that the weight fraction is constant along a 1-wave in the region $c_{tot} \leq 1$. Hence the value of $c^{\downarrow}_m$ is determined by the expression

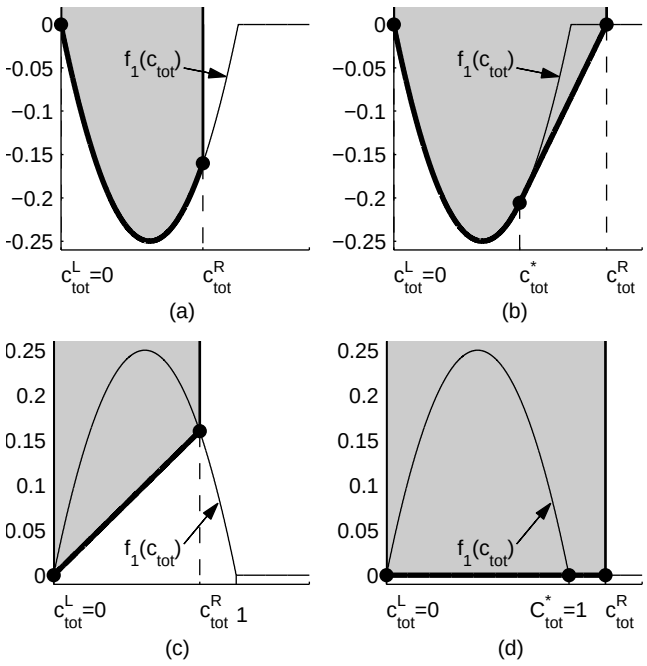

Figure 5.9: The structure of the 1-wave in the case $0 = c_{tot}^L < c_{tot}^R$, which is determined from the convex hull reconstruction. The convex hull is constructed for the set $\{(x, y) : c_{tot}^L \leq x \leq c_{tot}^R, y \geq f_1(x)\}$. It is denoted by the filled area, with the boundary shown by the solid line.

$$c_m^{\downarrow} = c_{tot}^{\downarrow} \frac{c_m^R}{c_{tot}^R}. \tag{5.90}$$

If $\chi^{\downarrow} < 0$ and $c_{tot}^R > 1$, then the 1-wave consist of a rarefaction wave and a shock, which connect the states $\vec{q}^*$ and $\vec{q}^R$ (Figure 5.9b). From the Rankine-Hugoniot condition

$$\vec{f}(\vec{q}^R) - \vec{f}(\vec{q}^*) = s(\vec{q}^R - \vec{q}^*),$$

it is derived, that $\frac{c_m^*}{c_{tot}^*} = \frac{c_m^R}{c_{tot}^R}$. Therefore, the weight fraction is constant through a shock and rarefaction part of the compound 1-wave, and $c_m^{\downarrow}$ is determined by equation (5.90). The 1-wave is a pure shock, if $\chi^{\downarrow} > 0$ and $c_{tot}^R \leq 1$ (Figure 5.9c). Then $\vec{q} = \vec{q}^L = [0,0]^T$ to the left of the shock front and $\vec{q} = \vec{q}^R$ to the right of the shock. If $\chi^{\downarrow} > 0$ and $c_{tot}^R > 1$, then the 1-wave is a compound wave, consisting of a stationary non-moving shock and a stationary contact wave (Figure 5.9d). In this case, $\vec{q} = \vec{q}^L = [0,0]^T$ for $\frac{x}{t} < 0$ and $\vec{q} = \vec{q}^R$ for $\frac{x}{t} > 0$. At the ray $\frac{x}{t} = 0$, the total cell density is discontinuous. The flux function f_2 is equal to zero, if it is evaluated at the both sides of the discontinuity. Formula (5.83) provides multiple values for $c_{tot}^{\downarrow}$: $c_{tot} \in \{0\} \cup [1, c_{tot}^R)$. Any of these values provide a zero flux f_2, if $c_m^{\downarrow}$ is bounded. Therefore, equations (5.83) and (5.90) give a correct value of the flux f_2 at the inner edge.

The 1-wave structure is analogous in the symmetric case $c_{tot}^L > c_{tot}^R = 0$, $c_m^R = 0$ for the opposite signs of $\chi^{\downarrow}$. The state c_{tot} is determined from expression (5.83), and $c_m^{\downarrow}$ is given by:

$$c_m^{\downarrow} = c_{tot}^{\downarrow} \frac{c_m^L}{c_{tot}^L}. \tag{5.91}$$

5.3.6.4 Weakly hyperbolic system

According to Section 5.3.1, the present numerical algorithm should provide nonnegative solutions for the cells densities. In this case, the total cell density c_{tot} is equal to zero, if and only if $c_i = 0$ and $c_m = 0$. The definition of the states $c_{tot}^{\downarrow}$ and $c_m^{\downarrow}$ given in Sections 5.3.6.1–5.3.6.3 is sufficient to determine the flux f_2 at the cell boundaries if a numerical solution for the cell densities is nonnegative. Nonnegativity of the solution is crucially important for the current model, since negative values of the cell densities may grow in magnitude, leading to divergence of the numerical solution. This phenomenon is discussed further in this section.

Assume that the cell densities can take negative values. In this case, a zero total cell density does not imply zero densities of immature and mature osteogenic cells. Therefore, the states $c_{tot} = 0$ and $c_m \neq 0$ can be considered.

At these states, the eigenvalues λ_1 and λ_2 are equal to $\chi^{\downarrow}$ and have just one eigenvector $[0,1]^T$. Therefore, the algebraic multiplicity is larger than geometric multiplicity. The Jacobian matrix is defective and the system is weakly hyperbolic. One of the characteristics of a weakly hyperbolic system, is that the Riemann solution may not be represented as a set of classical rarefaction, shock and/or contact waves. In some situations nonclassical shock waves, which are referred to as delta shock waves or singular shocks, can appear in the solution.

The delta shocks can arise in various hyperbolic systems under certain initial and boundary conditions. These waves contain singularities, which can be expressed by the Dirac delta function. If delta shocks appear, the solutions of the hyperbolic systems are defined in a generalized form. Various authors [23, 55, 59, 70, 90] propose multiple approaches to construct generalized solutions for different hyperbolic systems. Most often the generalized solution is derived as a limit of some set of regularized viscous solutions.

For the present hyperbolic system, a delta shock wave appears, for example, if $\chi^{\downarrow} > 0$ and $c^L_{tot} = 0$, $c^L_m \neq 0$ and $c^R_{tot} > 0$. To understand the nature of this delta shock wave, let us consider a Riemann problem for $c^L_{tot} = \varepsilon$, $c^L_m \neq 0$, $0 < c^R_{tot} \leq 1$. Let us look at the solution behavior for $\varepsilon \to 0$. The solution consists of a shock wave, connecting the state $\vec{q}^L$ to an intermediate state $\vec{q}^* = [c^R_{tot}, c^R_{tot}\frac{c^L_m}{\varepsilon}]^T$. The contact wave connecting the states $\vec{q}^*$ and $\vec{q}^R$ lies to the right of the shock wave and propagates along the ray $\frac{x}{t} = \chi^{\downarrow}(1 - c^R_{tot})$ (Figure 5.10). The shock speed is equal to $\chi^{\downarrow}(1 - c^R_{tot} - \varepsilon)$. Therefore, if $\varepsilon \to +0$, then the shock wave approaches the contact wave, and the density c^*_m between these waves tends to infinity.

Therefore, the 1-characteristics impinge on the delta shock from the left and from the right. The 2-characteristics impinge on the delta shock from the left and are parallel to it from the right. According to [23], the Riemann solution for c_m for the present case is defined in the distributional form:

$$c_m = c^L_m + (c^R_m - c^L_m)H(x - st) + \chi^{\downarrow} t \left(c^R_{tot} c^L_m - c^L_{tot} c^R_m\right) \delta(x - st),$$

where $H(\cdot)$ is the Heaviside step function, $\delta(\cdot)$ is the Dirac delta function and s is the shock speed, which is equal to $\chi^{\downarrow}(1 - c^L_{tot} - c^R_{tot})$. If $\chi^{\downarrow} > 0$, $c^L_{tot} = 0$, $c^L_m < 0$ and $0 < c^R_{tot} < 1$, then the mature cell density tends to minus infinity on the ray $\frac{x}{t} = \chi^{\downarrow}(1 - c^R_{tot})$. Due to a random walk of cells, represented by the diffusive terms in the governing equations, the singularity of the delta shock is smoothed in the solution of the full system. A negative density grows in magnitude in time. This issue can be demonstrated explicitly for the following simplified problem.

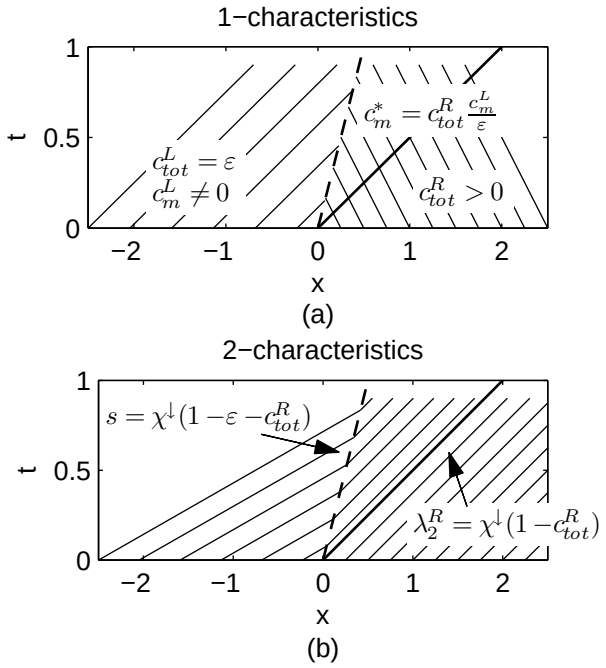

Figure 5.10: The solution to the Riemann problem, which consists of the 1-shock wave (dashed line) and the 2-contact wave (thick solid line), includes the left state $c^L_{tot} = \varepsilon$, $c^L_m \neq 0$, the right state $c^R_{tot} > 0$ and c^R_m and the intermediate state $c^*_{tot} = c^R_{tot}$, $c^*_m = c^R_{tot}\frac{c^L_m}{\varepsilon}$. The 1- and 2-characteristics are shown in thin solid lines in plots (a) and (b), respectively. The 2-characteristics intersect the 1-shock wave. The difference between the speeds of the 1-shock and the 2-contact wave is equal to $\chi^{\downarrow}\varepsilon$

Large negative solutions Consider the following simplified equations describing the migration of cells in the 1D physical space $x \in \mathbb{R}$:

$$\frac{\partial c_{tot}}{\partial t} + \frac{\partial}{\partial x}\left(-D_c \frac{\partial c_{tot}}{\partial x} + \frac{\chi_0\, g^{\downarrow}}{K_{ch}^2 + g^{\downarrow 2}} \frac{\partial g}{\partial x}(1 - c_{tot})c_{tot}\right) = 0 \tag{5.92}$$

$$\frac{\partial c_m}{\partial t} + \frac{\partial}{\partial x}\left(-D_c \frac{\partial c_m}{\partial x} + \frac{\chi_0\, g^{\downarrow}}{K_{ch}^2 + g^{\downarrow 2}} \frac{\partial g}{\partial x}(1 - c_{tot})c_m\right) = 0 \tag{5.93}$$

Assume that $\frac{\chi_0\, g^{\downarrow}}{K_{ch}^2 + g^{\downarrow 2}} \frac{\partial g}{\partial x} \equiv const = \hat{\chi} > 0$. The function

$$\hat{c}_{tot}(x) = \frac{1}{\exp\{-\frac{\hat{\chi}}{D_c}x\} + 1}$$

is the stationary solution of equation (5.92), such that $\hat{c}_{tot} \to 0$ if $x \to -\infty$, $\hat{c}_{tot} \to 1$ if $x \to \infty$ and $\hat{c}_{tot}(0) = \frac{1}{2}$. The derivative of the stationary solution is given by

$$\frac{d\hat{c}_{tot}}{dx} = \frac{\hat{\chi}}{D_c}\hat{c}_{tot}(1 - \hat{c}_{tot}).$$

If $\hat{c}_{tot}$ is substituted into equation (5.93), then the equation for the mature cell density becomes the linear diffusion-advection-reaction equation:

$$\frac{\partial c_m}{\partial t} + \hat{\chi}(1 - \hat{c}_{tot})\frac{\partial c_m}{\partial x} = D_c \frac{\partial^2 c_m}{\partial x^2} + \frac{\hat{\chi}^2}{D_c}\hat{c}_{tot}(1 - \hat{c}_{tot})c_m, \tag{5.94}$$

which can be easily solved numerically. Suppose that chemotaxis prevails over random walk of cells, that is $\frac{\hat{\chi}}{D_c} >> 1$. The stationary solution $\hat{c}_{tot}$ for the case $\frac{\hat{\chi}}{D_c} = 30$ is plotted in Figure 5.11a. The derivative $\frac{d\hat{c}_{tot}}{dx}$ is large near $x = 0$ and its maximal value is $\frac{d\hat{c}_{tot}}{dx}(0) = \frac{\hat{\chi}}{4D_c}$. Hence the reaction term in the right-hand side of equation (5.94) is large near $x = 0$, and negative values of c_m grow in magnitude in this region, since $\hat{c}_{tot} \in (0, 1)$ and in particular for $\hat{c}_{tot} = \frac{1}{2}$. In Figure 5.11b, the numerical solution of equation (5.93) is plotted for different time moments. The solution is obtained for the spatial domain $x \in [-1, 1]$ and for the following initial and boundary conditions: $c_m(x, 0) = \hat{c}_{tot}(x)/2 - 0.1$, $c_m(-1, 0) = \hat{c}_{tot}(-1)/2 - 0.1$ and $c_m(1, 0) = \hat{c}_{tot}(1)/2 - 0.1$. The minimal value of c_m grows in magnitude from -0.1 at $t = 0$ to -0.56 at $t = 1$. The point of minimum lies to the right from $x = 0$ due to the advection term in the left-hand side of equation (5.94).

Therefore, this example shows how small negative values of the cell density can grow significantly in magnitude in time, due to a nonlinearity of the flux function. Hence negative values of the cell densities should be avoided during simulations at all times in order to get a convergence of the numerical solution.

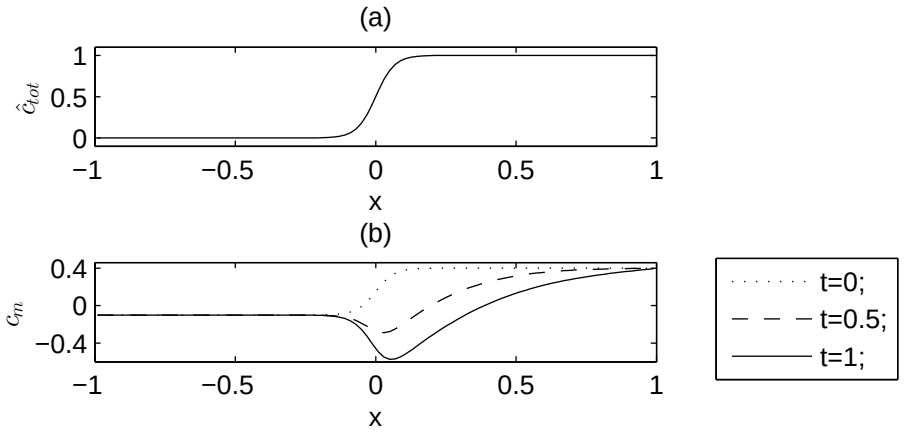

Figure 5.11: (a) Plot of the stationary solution $\hat{c}_{tot}$ of equation (5.92) for the case $\frac{\hat{\chi}}{D_c} = 30$; (b) Plots of the solution c_m of equation (5.94) for the time moments 0, 0.5 and 1 days. Negative values of c_m grow in magnitude in time near the point $x = 0$, where the derivative of $\hat{c}_{tot}$ is large

5.3.6.5 Summary

To summarize, the fluxes due to cell migration are approximated as follows. First, the left and right states of the immature and mature cell densities are found at the inner edges of the 2D control volumes and at the faces of the 3D control volumes, corresponding to these edges, as it is described in Section 5.3.5.2. The left and right states of the total cell concentration are obtained by adding the total density of immature cells and the density of mature osteogenic cells. The considered states of the immature, mature and total cell densities are denoted as $c^L_{i,l}$, $c^R_{i,l}$, c^L_m, c^R_m, c^L_{tot} and c^R_{tot}, respectively. The index l ranges from 1 to N_a. It is used to denote the states of the immature cell density at N_a inner faces of the 3D control volumes, corresponding to each inner edge of the 2D control volumes.

The normal derivatives of the immature and mature cell densities and the normal derivative and the value of the growth factor concentration at the inner edges and at the corresponding inner faces are determined in Section 5.3.5.3. These quantities are denoted as $\frac{\partial c_{i,l}}{\partial x}^{\downarrow}$, $\frac{\partial c_m}{\partial x}^{\downarrow}$, $\frac{\partial g}{\partial x}^{\downarrow}$ and $g^{\downarrow}$, respectively.

Then the variables $c^{\downarrow}_{tot}$, $c^{\downarrow}_m$, $c^{\downarrow}_{i,l}$ are defined from the Riemann solution,

which is determined by formula (5.83) and by equations:

$$c_m^{\downarrow} = \begin{cases} c_{tot}^{\downarrow} w_m^{\downarrow}, & \text{if } c_{tot}^L \neq 0, c_{tot}^R \neq 0, \\ c_{tot}^{\downarrow} \dfrac{c_m^R}{c_{tot}^R}, & \text{if } c_{tot}^L = 0, c_{tot}^R \neq 0, \\ c_{tot}^{\downarrow} \dfrac{c_m^L}{c_{tot}^L}, & \text{if } c_{tot}^L \neq 0, c_{tot}^R = 0, \\ 0, & \text{if } c_{tot}^L = 0, c_{tot}^R = 0, \end{cases}$$

$$c_{i,l}^{\downarrow} = \begin{cases} c_{tot}^{\downarrow} w_{i,l}^{\downarrow}, & \text{if } c_{tot}^L \neq 0, c_{tot}^R \neq 0, \\ c_{tot}^{\downarrow} \dfrac{c_{i,l}^R}{c_{tot}^R}, & \text{if } c_{tot}^L = 0, c_{tot}^R \neq 0, \\ c_{tot}^{\downarrow} \dfrac{c_{i,l}^L}{c_{tot}^L}, & \text{if } c_{tot}^L \neq 0, c_{tot}^R = 0, \\ 0, & \text{if } c_{tot}^L = 0, c_{tot}^R = 0. \end{cases}$$

The weight fraction $w_m^{\downarrow}$ is given by equation (5.84), and $w_{i,l}$ is defined in a similar way:

$$w_{i,l}^{\downarrow} = \begin{cases} w_{i,l}^L, & \text{if } \lambda_2(c_{tot}^{\downarrow}) \geq 0, \\ w_{i,l}^R, & \text{if } \lambda_2(c_{tot}^{\downarrow}) \leq 0, \end{cases}$$

where the left and right states of the weight fractions are determined in the following way:

$$w_m^S = \frac{c_m^S}{c_{tot}^S}, \qquad w_{i,l}^S = \frac{c_{i,l}^S}{c_{tot}^S}, \quad S \in \{L, R\}.$$

The functions f_1 and λ_2, which are included in the mentioned equations, are defined in equations (5.86) and (5.95):

$$\lambda_2(c_{tot}) = \begin{cases} \chi^{\downarrow}(1 - c_{tot}), & c_{tot} < 1, \\ 0, & c_{tot} \geq 1, \end{cases} \tag{5.95}$$

where $\chi^{\downarrow} = \frac{\chi_0 g^{\downarrow}}{K_{ch}^2 + g^{\downarrow 2}} \frac{\partial g}{\partial x}^{\downarrow}$.

Finally the flux of mature osteogenic cells at the inner edge, and the flux of immature cells at the corresponding inner faces are approximated as follows:

$$\mathscr{F}_m^{\downarrow} = -D_c \frac{\partial c_m}{\partial x}^{\downarrow} + f_2(c_{tot}^{\downarrow}, c_m^{\downarrow}), \qquad \mathscr{F}_{i,l}^{\downarrow} = -D_c \frac{\partial c_{i,l}}{\partial x}^{\downarrow} + f_2(c_{tot}^{\downarrow}, c_{i,l}^{\downarrow}),$$

where the flux function $f_2(\cdot, \cdot)$ is given by equation (5.87).

The present formulas are valid only if solutions for the cell densities are nonnegative. For negative cell densities, singular delta shock waves

can appear in the solution to the Riemann problem, from which the given relations are derived. One of the situations, when delta shocks form, is described in Section 5.3.6.4. Although the equations describe some of the qualitative nature of the solutions, the present formulas are not justified and hence they may give wrong approximation of the fluxes, if negative values of the cell densities are admitted.

5.3.7 Treatment of the reaction term

The reaction terms in equations (5.28)–(5.30) are approximated by functions H_i^R, H_m^R and H_g^R, respectively. The integrals over the control volumes $V_{j,k,l}^3$ and $V_{j,k}$ are substituted by the values of the integrated functions at the centers of the control volumes. The fluxes of the cell densities c_i and c_m and of the growth factor concentration g depend on the gradients of these functions, which are approximated at the inner edges and faces of the control volumes. Hence the values of the r-components of the fluxes at the centers of control volumes are obtained through the interpolation of the normal flux values, determined at the centers of the inner edges of the 2D control volumes $V_{j,k}$, $\{j,k\} \in \mathscr{I}_a$, which are parallel to the z-axis, and at the centers of the corresponding faces of the 3D control volumes $V_{j,k,l}^3$, $\{j,k\} \in \mathscr{I}_a^3$. The considered normal fluxes were approximated using the principles outlined in Sections 5.3.5 and 5.3.6.

The following interpolation technique is applied. Each regular rectangular cell $V_{j,k}$ has two vertical, i.e. parallel to the z-axis, edges $e_{j-\frac{1}{2},k}$ and $e_{j+\frac{1}{2},k}$. The center of the cell $V_{j,k}$ lies in the middle of the line segment, which connects the centers of the considered edges. Hence the approximate values $F_i^{j,k,l}$, $F_m^{j,k}$, $F_g^{j,k}$ of the r-components of the fluxes corresponding to the variables c_i, c_m and g in the centers of cells $V_{j,k,l}^3$ and $V_{j,k}$ are defined as:

$$\begin{aligned} F_i^{j,k,l} &= \frac{F_i^{j-\frac{1}{2},k,l} + F_i^{j+\frac{1}{2},k,l}}{2}, \\ F_p^{j,k} &= \frac{F_i^{j-\frac{1}{2},k} + F_i^{j+\frac{1}{2},k}}{2}, \quad p \in \{m,g\}, \end{aligned} \tag{5.96}$$

where $F_i^{j-\frac{1}{2},k,l}$, $F_m^{j-\frac{1}{2},k}$, $F_g^{j-\frac{1}{2},k}$ and $F_i^{j+\frac{1}{2},k,l}$, $F_m^{j+\frac{1}{2},k}$, $F_g^{j+\frac{1}{2},k}$ are the normal fluxes of variables c_i, c_m and g at the corresponding vertical faces and edges of control volumes $V_{j,k,l}^3$ and $V_{j,k}$.

An irregular cell $V_{j,k}$ can have either one or two vertical edges. If the cell $V_{j,k}$ has one vertical inner edge, for example edge $e_{j-\frac{1}{2},k}$, then the flux at the cell center is determined through the following extension:

$$\begin{aligned} F_i^{j,k,l} &= F_i^{j-\frac{1}{2},k,l}, \\ F_p^{j,k} &= F_i^{j-\frac{1}{2},k}, \quad p \in \{m,g\}, \end{aligned} \tag{5.97}$$

If there are two inner vertical edges $e_{j-\frac{1}{2},k}$ and $e_{j+\frac{1}{2},k}$, adjacent to the active irregular cell $V_{j,k}$, then the inverse distance weighting interpolation is used:

$$\begin{aligned} F_i^{j,k,l} &= w_1^{j,k} F_i^{j-\frac{1}{2},k,l} + w_2^{j,k} F_i^{j+\frac{1}{2},k,l}, \\ F_p^{j,k} &= w_1^{j,k} F_p^{j-\frac{1}{2},k} + w_2^{j,k} F_p^{j+\frac{1}{2},k}, \quad p \in \{m, g\}, \\ w_1^{j,k} &= \frac{d_2^{j,k}}{d_1^{j,k} + d_2^{j,k}}, \quad w_2^{j,k} = \frac{d_1^{j,k}}{d_1^{j,k} + d_2^{j,k}}, \end{aligned} \tag{5.98}$$

where $d_1^{j,k}$ and $d_2^{j,k}$ are the distances from the center of cell $V_{j,k}$ to its vertical inner edges $e_{j-\frac{1}{2},k}$ and $e_{j+\frac{1}{2},k}$, respectively.

Therefore, the following expressions for the reaction terms are defined:

$$H_i^R(\vec{C}_i, \vec{C}_m, \vec{G}, (j,k,l)) = A_c(G^{j,k}) C_i^{j,k,l}(1 - C_{tot}^{j,k}) - \frac{F_i^{j,k,l}}{r_c^{j,k}}, \tag{5.99}$$

$$H_m^R(\vec{C}_i, \vec{C}_m, \vec{G}, (j,k)) = A_c(G^{j,k}) C_m^{j,k}(1 - C_{tot}^{j,k}) - \frac{F_m^{j,k}}{r_c^{j,k}}, \tag{5.100}$$

$$H_g^R(\vec{C}_i, \vec{C}_m, \vec{G}, (j,k)) = E_c(G^{j,k}) \left(C_m^{j,k} + h_a \sum_{l=1}^{N_a} \frac{a_{l-\frac{1}{2}} + a_{l+\frac{1}{2}}}{2} C_i^{j,k,l} \right) - \frac{F_g^{j,k}}{r_c^{j,k}}, \tag{5.101}$$

where $A_c(g)$ and $E_c(g)$ are defined in Table 4.1, and the averages of the total cell concentration are determined as follows

$$C_{tot}^{j,k} = C_m^{j,k} + h_a \sum_{l=1}^{N_a} C_i^{j,k,l}, \quad (j,k) \in \mathscr{I}_a.$$

5.3.8 Boundary conditions

The fluxes of the immature and mature cell densities c_i and c_m and of the growth factor concentration g at the boundary $\Gamma(t)$ of the physical domain Ω_s and at the corresponding boundary $\Gamma^3(t) = \Gamma \times [0,1]$ of the 3D domain, which includes the maturation space, are represented by the integrals over interfaces $\partial V_{j,k,l}^{3B}$ and $\partial V_{j,k}^{B}$ in equations (5.28)–(5.30). The integrals are approximated by functions $H_i^{M_b}$, $H_m^{M_b}$ and $H_g^{M_b}$ in equations (5.32)–(5.34) through the values of the integrands at the centers of the boundary faces and edges. Each boundary face and edge is adjacent to exactly one active control volume, otherwise they will lie between active control volumes and, hence, they will not lie on the boundary of the physical domain. The values of the unknown cell densities and of the growth factor concentration are

approximated at the centers of the boundary edges and faces by their average values in the adjacent control volumes. The velocity at the center of the boundary edge and at the centers of all corresponding 2D faces is defined as the mean value of the normal velocities at the vertices of the considered edge, which were determined in Section 5.3.3.

5.3.9 Time integration

Ordinary differential equations (5.32)–(5.34) are integrated with the use of the explicit modified Euler method (also called explicit trapezoidal rule). It is a two stage method. The grid of control volumes is updated at each stage.

Since an explicit time integration is used for the advection-diffusion-reaction equations, the time step size should be chosen correctly. Due to the presence of the parabolic diffusion terms, severe restrictions on the time step size should be set, in order to provide a stable numerical scheme. The reason, why an implicit time integration method is not used, is that implicit methods are not efficient for the solution of the equations of the considered hyperbolic type, if no dominance of the diffusion terms is observed, and if a positivity of the solution should be kept. An explicit time integration is usually more efficient than implicit methods, if a nonnegative numerical solution of hyperbolic equations has to be obtained. Another advantage of the explicit scheme, is that it is much more convenient for the implementation into the computer code and for its verification, especially if nonlinearly coupled equations defined within the evolving in time physical domain are considered.

Let us first estimate the order of the time step size, determined by the stability restrictions. Such an estimate can be derived for the linear 1D advection-diffusion equation

$$\frac{\partial u}{\partial t} + a\frac{\partial u}{\partial x} = d\frac{\partial^2 u}{\partial x^2}$$

with constant coefficients d, a, in the following way. The eigenvalues of the matrix obtained from the discretization of the advection-diffusion terms times the time step should lie within the stability region of the considered time integration scheme. If the modified Euler method for the time discretization, the third order upwind biased discretization for the advection term, and the second order central scheme for the diffusion term are considered, then the following restrictions are obtained for the time step τ

$$\nu = \frac{\tau|a|}{h} < 0.874, \quad \mu = \frac{\tau d}{h^2} < 0.209, \tag{5.102}$$

where h is the size of uniform 1D control volumes. The given conditions are sufficient, but not necessary. That is, the time step size is underestimated

by inequalities (5.102). The preliminary estimates for the considered nonlinear multidimensional problem are obtained, if the diffusion coefficient of osteogenic cells D_c is substituted for the parameter d, and the parameter a is replaced with the derivative of the total cell flux, caused by chemotaxis, with respect to the total cell density, which can be estimated in the following way:

$$| (\chi(c_{tot}, g)c_{tot}\nabla_s g)'_{c_{tot}} | = \left| \frac{\chi_0(1-2c_{tot})g\nabla_s g}{K_{ch}^2 + g^2} \right| \sim \frac{\chi_0}{h}.$$

Then inequalities (5.102) yield:

$$\tau < 0.874\frac{h^2}{\chi_0}, \quad \tau < 0.209\frac{h^2}{D_c}, \tag{5.103}$$

where h is the characteristic linear size of the mesh.

Another restriction on the time step size is applied in order to keep nonnegativeness of the numerical solution. If regular rectangular 2D control volumes in the center of the physical domain are considered, then the following constraint on the time step size can be derived:

$$\tau < \frac{h}{4\left(D_c/h + \chi_0/h\right)}. \tag{5.104}$$

Stability and positivity restrictions for the time step size, which follows from the equation for the growth factor evolution, can be reduced to the inequality:

$$\tau \leq \frac{1}{4}\frac{h^2}{D_g}. \tag{5.105}$$

The reaction terms from the governing equations are neglected in derivation of time step restrictions. This simplification is justified by the fact, that for the characteristic mesh size h, which is used in the numerical simulations, the magnitude of the corresponding discretized terms is much smaller than the magnitude of the discretized advection-reaction terms, which are proportional to $1/h^2$.

Inequalities (5.102), (5.104) and (5.105) can be reduced to the following condition:

$$\tau < h^2 \min\left\{ \frac{1}{4\left(D_c + \chi_0\right)}, \frac{0.209}{D_c}, \frac{1}{4D_g} \right\}. \tag{5.106}$$

Due to the movement of the domain boundary, the control volumes, located at the boundary, contract in time. Hence at some time moment, very small control volumes can appear in the mesh, with the characteristic linear size $h \to 0$, which yields, that $\tau \to 0$. In order to prevent this, small control volumes are united with the adjacent control volumes and *combined* control volumes are constructed, so that an acceptable time step τ can be used.

The combined control volumes are constructed in the following way. The characteristic linear size of an irregular computational cell is defined as the minimal ratio of its volume to the length of the inner edges. The approximations $H_i^{M_I}$, $H_m^{M_I}$, $H_g^{M_I}$ of the advection-diffusion terms are inversely proportional to this characteristic linear size. If the considered ratio becomes too small, then very small time step should be chosen in order to provide stability and positivity of the numerical solution. Hence the considered linear size of the irregular cell is used to determine, whether the cell should be united with its neighbors.

Let us consider some irregular active control volume $V_{j,k}$ at the boundary of the physical domain. It is united with some of its neighbors, if the minimal ratio of its volume to the length of its inner edges is smaller than limit h_{irr}. If the neighbor, with which the considered control volume is united, is part of another combined cell, then that combined cell is included in the combined control volume, which is constructed around cell $V_{j,k}$ (see Figure 5.12).

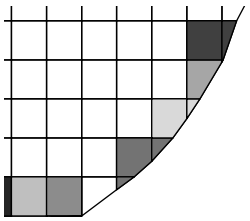

Figure 5.12: Sketch of the combined cells, which are constructed near the boundary of the physical domain. Each combined cell consists of several active control volumes, which are shown in one color

The value of the limit h_{irr} is chosen to be equal to $0.4h$, where h is the minimal linear size of the regular rectangular control volumes in the middle of the computational domain. From constraint (5.106), it follows that the time step should be proportional to the square of the linear size of the mesh. Due to the presence of small irregular cells near the boundary of the physical domain, the following time step size

$$\tau = h_{irr} h \tau_c \min\left\{\frac{1}{4\left(D_c + \chi_0\right)}, \frac{0.209}{D_c}, \frac{1}{4D_g}\right\} \tag{5.107}$$

is chosen, where τ_c is some constant parameter. For the parameter values defined in Table 4.2, we obtain:

$$\min\left\{\frac{1}{4\left(D_c + \chi_0\right)}, \frac{0.209}{D_c}, \frac{1}{4D_g}\right\} = 0.590 \ \left[\frac{days}{mm^2}\right].$$

For the current problem statement, the numerical simulations, carried out for the parameter value $\tau_c = 0.9$ and for the different mesh resolutions,

provided nonnegative solutions for the cell densities and the growth factor concentration, in which no spurious oscillations were recognized. The numerical solutions, obtained for the parameters $\tau_c = 1$ and $\tau_c = 0.5$, were close to each other. Hence we assumed, that the chosen time-step size is small enough for stability and positiveness of the numerical solution.

5.4 Discussion and conclusions

The aim of the current work is to develop the algorithm, which allows to obtain the numerical solution in a two dimensional physical domain for the peri-implant osseointegration model, defined in Chapter 4. The considered model is formulated in terms of three coupled nonlinear time-dependent advection-diffusion-reaction equations, which are defined within the evolving in time domain.

The method of lines is used as a basis of the current numerical approach. The discretizations in time and space are separated. This allows to apply superposition in the discretization of the advection, diffusion and reaction terms. Since a moving boundary problem is considered, the efficiency of the method, which is used to construct the computational mesh, is of great importance. In order to avoid a complete remeshing at every time step, the embedded boundary method is applied on the initial regular rectangular grid. This means, that only the control volumes, adjacent to the boundary of the domain, change their shape. The evolution of the domain is tracked with the level set method, which is easily implemented on the initial rectangular grid. The irregular geometry of the physical domain is determined from the values of the level set function at the nodes of the rectangular grid. The computational mesh consists of the regular rectangular control volumes in the middle and of the irregular computational cells near the boundary of the domain.

Special attention should be paid to the discretization of the hyperbolic terms from the governing partial differential equations. The finite volume method is known to be efficient for this type of problems. With this method, a Riemann problem should be solved at the inner edges of the control volumes. The Riemann problem is defined for the nonstrictly hyperbolic system of equations without genuine nonlinearity, which is analogous to nonconvex flux functions in scalar hyperbolic equations [59]. In this chapter, the exact Riemann solution is defined in the simple form.

For the discretization of the advection-diffusion terms, the values of the gradients of the total cell density and of the growth factor concentration should be approximated at the inner edges of the control volumes. Since the control volumes, which are located near the boundary of the domain, can be of an irregular shape, the approach for the gradient approximation on the irregular grid is constructed.

The explicit trapezoidal method is used for the time integration of the ordinary differential equations, which are obtained after the discretization of the PDE's in the physical and maturation spaces. The explicit method is chosen, since the positivity of the solution is very important for the current model. First of all, negative densities and concentration do not make any sense from biological point of view. Second, it is shown that negative values of the cell densities can grow in magnitude due to nonlinearity of the flux functions. Hence even small negative values of the cell densities can cause bad convergence of an approximate solution to the exact solution. Another advantage of the explicit methods, is that they are easy to implement and that they are more convenient on the stage of the verification of the solution of the complex numerical model. A disadvantage of the explicit methods is that we have to use very small time steps, in order to obtain positive and stable numerical solutions. This leads to large computation times, especially when a fine mesh in the physical domain is considered.

A weak point of the current algorithm is the large computation time, needed to obtain the numerical solution, when a fine mesh resolution is used. In future, the development of an efficient time integration method, which will reduce the time of computations, could improve the approach, proposed in the present work. An operator splitting method can be useful in this case as discussed in Section 6.2.

CHAPTER 6

Conclusions and outlook

6.1 Conclusions

Extended and deep knowledge of the main processes occurring in a real system, which can be obtained, for example, from experiments and observations, are of great importance on the stage of construction of a theoretical model for the considered system. It is also critically important to know the characteristics of the developed mathematical model in order to justify that the initial assumptions incorporated in the model are represented by the current mathematical formalism in a correct way. It can happen that solutions of the mathematical model have some features, which were not expected initially. Such a situation is considered in Chapter 2. It is found that biologically irrelevant wave-like patterns appear in the solution for a continuous bone regeneration model. A stability analysis allows to determine the relation between the parameter values and a characteristic behavior of the solution. It is demonstrated by combining analytical and numerical approaches that for a certain range of the parameter values the solution for the cell densities and the growth factor concentration converges to unphysical wave-like profiles. However, if the parameter values are within a stability region, then biologically irrelevant characteristics of the solution disappear, and a final homogeneous distribution of cells and growth factors is predicted.

Modeling can be considered as a representation of complex phenomena in a rather simple form by taking certain assumptions and focusing on those aspects, that are supposed to have the most significant impact on a process that is considered. Therefore, the main processes occurring in bone regeneration are modeled by a number of various mathematical formalisms. Different theoretical approaches yield different results and allow to study bone

regeneration from various perspectives. In Chapters 3 and 4, the models for cell differentiation and bone formation, which are conceptually different from classical approaches, are proposed. Several new features of bone regeneration are represented with these approaches, which cannot be simulated with the already existing models.

The evolutionary differentiation model described in Chapter 3 allows to incorporate a history of cell differentiation, so that the current state of cells depends on how the cells evolved before. In contrast to an immediate differentiation formalism, which is commonly used in classical models, the new approach assigns a finite, bounded, time of differentiation to each cell. The finite time of differentiation corresponds to a gradual gaining of new properties by cells in the course of time, which is in line with experimental observations. Another advantage of the evolutionary differentiation model, is that bone formation within the peri-implant region can be predicted to start only after some time from the implant placement, as it happens in reality.

Due to its advanced characteristics, the evolutionary approach is an essential part of a moving boundary problem for endosseous bone healing, which is presented in Chapter 4. A moving boundary-type of bone formation around endosseous implants, which is well observed in experiments, is directly incorporated into the present model. The ossification front is modeled by the moving boundary of the computational domain, which corresponds to a soft tissue region. An explicit representation of the bone-forming surface is the main innovation of the proposed model, which distinguishes the current formalism from the recent models for peri-implant osseointegration.

The robust numerical algorithm for the solution of a complex mathematical problem is developed and presented in Chapter 5. The main challenges were to capture the irregular and time-evolving geometry of the problem domain, and to construct a stable and positivity preserving discretization of the nonlinearly coupled system of time dependent taxis-diffusion-reaction equations for this domain. Such approaches based on the method of lines, the finite volume method, the level set method and the embedded boundary method are incorporated in the present elaborate numerical algorithm.

6.2 Recommendations

A general comment, which concerns most of the recent models of bone regeneration and, in particular, the two models presented in this work, is that further model validation is necessary in order to assess an applicability and a robustness of the proposed theoretical approaches. This can be done by comparing observation data obtained for various experimental settings with the corresponding simulation results performed for the current continuous models.

For a validation of the evolutionary differentiation approach, the present approach is incorporated into a mechanoregulatory model. Mechanoregulatory expressions for differentiation rates are derived from numerical simulations and based on the educated guesses. In order to verify and to evaluate the expressions for the differentiation rates directly, corresponding experimental studies should be done. One of the potential research directions, related to the present study, is an experimental and theoretical investigation of how cells gain properties of some phenotype in time under influence of various factors (for example, mechanical loading or an influence of growth factors and other chemicals). The mechanoregulatory model, which is described in Chapter 3, is derived in a rather simple form, since it is used mainly to check the performance of the evolutionary differentiation approach. Therefore, there is a lot of space for further improvement of the model. For example, an additional unknown for the growth factor concentration can be incorporated into the formalism, in order to consider bioregulatory effects occurring during bone regeneration. A mechanical stimulus can be adapted to a dynamical loading of the healing tissue, which then can be modeled as a poro-elastic medium. Considering cell differentiation as a partly stochastic process can be a following step in extending the present model. Based on the model for cell differentiation, a similar evolutionary approach for cell proliferation is another potential line of the research.

The aforementioned directions for future research can be also considered for the improvement of the moving boundary model presented in Chapter 4. A further justification and adjustment of the model parameters and formalisms, which are used to model cellular and biochemical processes, can be made by comparing paths of the ossification front during endosseous bone healing for various experimental settings. Making a diffusion coefficient dependent on the local cell density and on the growth factor concentration and analogous modification of the rest of the parameters can deliver new interesting results, which were not observed at the present moment. A disadvantage of all these extensions is the increase of the model complexity and of the number of parameters that are barely known, or very hard to determine or to estimate.

The numerical algorithm, developed for the solution of the moving boundary problem is based on an explicit time integration scheme, which yields an enormous calculation time, especially if the control volumes used for the spatial discretization are small. In this situation, an operator splitting method can be useful. Applying an implicit time integration for diffusion and reaction terms and an explicit integration scheme for hyperbolic taxis and differentiation terms will allow the use of larger time steps, such that the stability of the numerical solution will be maintained. However, an implicit integration can violate a positivity of the solution, which is critical for the considered problem. Therefore, further research on the efficient and robust time integration method for the present continuous model is needed.

An interesting behavior of the numerical solutions was obtained on the meshes with various resolution in Chapter 4. The high density- high concentration layer, which was located at the old bone surface, had a wave-like pattern on coarse meshes. The aforementioned pattern disappeared with the increase of the mesh resolution. The issue of the pattern appearance in the numerical solution, which is dependent on the sizes of the mesh elements and on the model parameters, can be a subject of a theoretical research. An elaborated stability analysis may unravel the reasons of such a behavior of the solution and provide some guidelines on the choice of mesh resolution and of the parameter values.

The current numerical scheme operates on a uniform initial rectangular mesh. It was concluded in Chapter 4, that it is necessary to use very fine meshes within the physical domain in order to get convergent numerical solutions. Small element sizes lead to a large number of time steps, to abnormal amount of the required memory and hence to a huge CPU time. In fact, an enhanced mesh resolution is only necessary in the regions, where the gradients of the cell densities and/or of the growth factor concentration are high. Therefore, small mesh elements are only needed within a small part of the physical domain: at the boundary between the high density - high concentration layer located near the ossification front and the rest of the physical domain, where the cell densities and the growth factor concentration are close to zero. In such a situation, adaptive mesh refinement can significantly reduce the computational time and required computer resources. Therewith, an incorporation of the adaptive mesh refinement technique into the present numerical algorithm is a potential direction for the following studies. We also think that spectral or discontinuous Galerkin methods may be worth investigating with respect to accuracy issues. We remark that the use of limiters will probably still be necessary in order to grant positivity of the numerical solution.

APPENDIX A

Notes to the moving boundary model for endosseous healing

A.1 Cell source at the old bone surface

The parameter t_{cbone} denotes the time period, during which the influx of immature non-differentiated cells takes place near the old bone. In Abrahamsson et al. [1] new bone formation is recognized at the end of the first week after the implant placement. Therefore, the value $t_{cbone} = 1\ day$ is estimated from numerical simulations, so that new bone formation is observed at the old bone surface at time $t = 7\ days$, if no growth factor source is considered at the smooth implant surface.

Decrease of t_{cbone} to value 0.5 $days$, leads to the issue, that fewer cells are recruited from the old bone surface. Bone formation starts in the corners, formed by the old bone surface and by the tread of the implant. No bone forms in the middle of the old bone surface (Figure A.1).

On the other hand, for the value 2 $days$ of the parameter t_{cbone}, new bone does not form. This happens, due to the extensive source of non-differentiated cells at the old bone surface. The differentiating osteogenic cells are squeezed from the old bone surface by non-differentiated cells. Cells with low level of differentiation release little growth factor (see equation (4.3)). A low concentration of growth factor near the old bone surface leads to a slow cell differentiation in this region (see the expression for $u_b(g)$ in Table 4.1). Therefore, the density of mature osteogenic cells is zero, and no new bone forms near the old bone surface within the considered time frame.

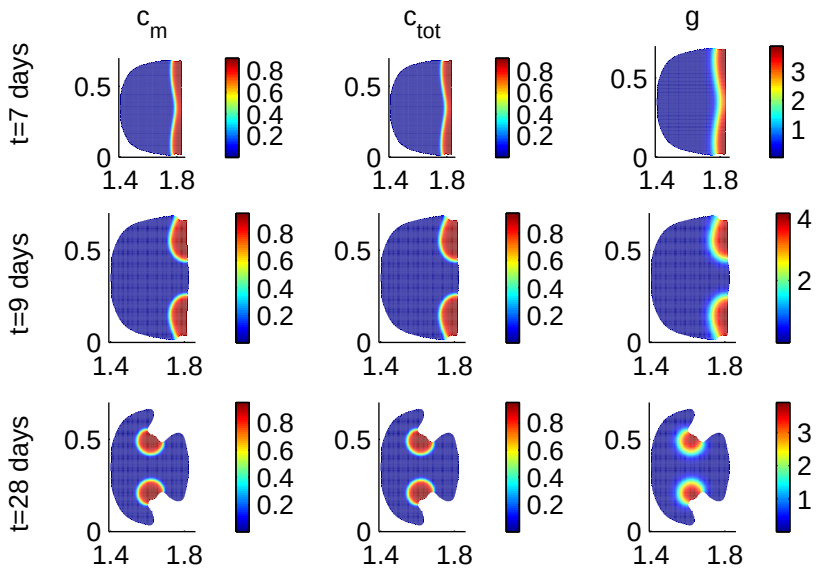

Figure A.1: Plots of the mature cell density c_m, of the total cell density c_{tot} and of the growth factor concentration g at the time moments $t = 7$, 9 and 28 *days* for the parameter values given in Tables 4.1 and 4.2 and for $t_{cbone} = 0.5$ *days*. The bone-forming surface moves from the the corners, formed by the old bone surface and by the tread of the implant

A.2 Fluxes at the moving boundary

Next, the flux of some quantity is considered, which can be, for example, cell density, which is denoted as c, near the moving boundary. Cellular processes, like differentiation and proliferation, are disregarded. Let the density be defined within some region $\Omega_c(t)$, which evolves in time and has the moving boundary $\partial\Omega_c(t)$. The movement of the domain boundary is determined by the velocity field $\vec{v}(\vec{X}, t)$, $\vec{X} \in \partial\Omega_c(t)$, $t > 0$. Since the flux of cell density is studied, assume, that the evolution of the density is determined only by cell migration. Then, the cell dynamics can be described by the conservation law:

$$\frac{\partial c}{\partial t}(\vec{x}, t) + \nabla \cdot \vec{F}(c, \vec{x}, t) = 0, \quad \vec{x} \in \Omega_c, t > 0, \tag{A.1}$$

where $F(c, \vec{x}, t)$ is the flux density vector field. From application of the Leibniz integral rule to equation (A.1) and from the divergence theorem, it

follows:

$$\frac{d}{dt}\int_{\Omega_c} c\,dV = \int_{\Omega_c}\frac{\partial c}{\partial t}dV + \int_{\partial\Omega_c(t)} c\,\vec{v}\cdot\vec{n}\,dS = -\int_{\Omega_c}\nabla\cdot\vec{F}\,dV$$
$$+\int_{\partial\Omega_c(t)} c\,\vec{v}\cdot\vec{n}\,dS = -\int_{\partial\Omega_c(t)}\vec{F}\cdot\vec{n}\,dS + \int_{\partial\Omega_c(t)} c\,\vec{v}\cdot\vec{n}\,dS. \quad \text{(A.2)}$$

Let us denote the projection of the velocity $\vec{v}$ on the normal $\vec{n}$ as

$$v_n(\vec{X},t) = \vec{v}(\vec{X},t)\cdot\vec{n}(\vec{X},t),$$

where $\vec{X}\in\partial\Omega_c(t)$, $t>0$ and $\vec{n}$ is the outward unit normal to the surface $\partial\Omega_s$.

Assume first, that cells are pushed by the moving boundary in a piston-like way. In this case, the total number of cells within the domain will not change, i.e.

$$\frac{d}{dt}\int_{\Omega_c(t)} c\,dV = 0. \quad \text{(A.3)}$$

The velocity of cells at the moving boundary $\partial\Omega_s$, projected on the normal to the boundary, will be equal to the normal velocity of the boundary v_n. Hence, the flux through the surface element $\vec{n}\,dS$ will be equal to the local cell density times the velocity in direction $\vec{n}$ times the area of the surface dS:

$$\vec{F}(c,\vec{X},t)\cdot\vec{n}(\vec{X},t)\,dS = c(\vec{X},t)\,v_n(\vec{X},t)dS,$$

or

$$\vec{F}(c,\vec{X},t)\cdot\vec{n}(\vec{X},t) = c(\vec{X},t)\,v_n(\vec{X},t), \quad \text{(A.4)}$$

where $\vec{X}\in\partial\Omega_c(t)$, $t>0$, $\vec{n}$ is the outward unit normal to the surface $\partial\Omega_c(t)$. Equation (A.4) is the natural boundary condition for the cell density under interfacial movement. Further, from the equations (A.2) and (A.4) it follows, that the condition (A.3) is satisfied.

Suppose now, that the cells, adjacent to the boundary, attach to it and become immobile. They do not move together with boundary, but they are trapped by it. Hence, it is assumed, that they do not change their position, i.e. their velocity and, consequently, their flux, with respect to the coordinates of the physical space, become equal to zero, after the cells are attached to the domain boundary:

$$\vec{F}(c,X,t) = \vec{0}, \qquad \vec{X}\in\partial\Omega_c(t), t>0. \quad \text{(A.5)}$$

If the cells are trapped by the moving boundary, then the total cell number within the domain Ω_s will decrease. This fact can be derived from equations (A.2), (A.5) and from equation (4.4), where the normal velocity v_n is defined as non-positive variable, i.e.

$$\vec{v}\cdot\vec{n} = v_n \le 0,$$

where $\vec{n}$ is the outward normal. This means, that the boundary moves inwards the domain (domain shrinks). Consequently,

$$\frac{d}{dt}\int_{\Omega_c} c\, dV = \int_{\partial\Omega_c(t)} c\, \vec{v}\cdot\vec{n}\, dS \leq 0. \tag{A.6}$$

Neumann boundary conditions are formulated for the flux *through* the boundary surface. Thus, condition (A.5) should be rewritten in the form:

$$\vec{F}(c, X, t)\cdot\vec{n}(X, t) = 0, \qquad \vec{X}\in\partial\Omega_c(t), t > 0, \tag{A.7}$$

where $\vec{n}$ is the outward unit normal to the surface $\partial\Omega_c(t)$.

The boundary conditions, formulated in Section 4.3.2, are derived from the equations (A.4) and (A.7) and from the assumptions, made in Section 4.3.2. The flux density field $\vec{F}$ is substituted by expressions

$$\left(-D_c\nabla_s c_j + \chi(g, c_{tot})c_j\nabla_s g\right), \quad j = i, m,$$

for immature and mature cell densities, and by the expression $-D_g\nabla_s g$, for growth factor concentration, respectively.

Relation (A.7), used as a boundary condition for the mature cell density, is derived from a rather rough assumption, that these cells do not change their position in physical space, after they attach to the moving boundary. In reality, some osteoblasts move simultaneously with the bone-forming surface, and a part of them becomes completely surrounded by the new bone matrix [63]. The mechanism of movement of the osteoblasts, which attach to the solid surface and which release new bone matrix, seems to be complicated and not well studied in the literature. In future, the present model can be improved by a more accurate representation of the relative movement of the mature osteogenic cells and the bone-forming surface.

APPENDIX B

Notes to the numerical algorithm

B.1 Determinant of the linear system

Linear equations (5.44) can be written in the matrix form:

$$A\,\vec{a} = \vec{C},$$

where

$$A = \begin{bmatrix} 1 & r_c^{j-1,k} & I_{zz}^{j-1,k} \\ 1 & r_c^{j,k} & I_{zz}^{j,k} \\ 1 & r_c^{j+1,k} & I_{zz}^{j+1,k} \end{bmatrix}.$$

The determinant of matrix A is equal to:

$$det(A) = (I_{zz}^{j,k} - I_{zz}^{j-1,k})(r_c^{j+1,k} - r_c^{j,k}) + (I_{zz}^{j+1,k} - I_{zz}^{j,k})(r_c^{j-1,k} - r_c^{j,k}). \quad \text{(B.1)}$$

In this appendix, it is proved that $det(A) \neq 0$.

Let us define a new coordinate system (r', z'), such that $r' = r - r_0$ and $z' = z - z_0$, where r_0, z_0 are some real numbers. The r'-coordinate of the center of any area V is equal to

$$r'_c = r_c - r_0, \quad \text{(B.2)}$$

where r_c is the r-coordinate of the center in the old coordinates. The second moment of the area is modified in the new coordinate system in the following way

$$I'_{zz} = \frac{1}{\mu(V)} \int_V r'^2 dv = \frac{1}{\mu(V)} \int_V (r - r_0)^2 dv = I_{zz} - 2r_0 r_c + r_0^2, \quad \text{(B.3)}$$

where I_{zz} is the corresponding moment in the old coordinates.

Remark B.1. Since the second moment of area is non-negative, then $I'_{zz} \geq 0$ for any real r_0. If it is assumed, that $r_0 = r_c$, then from equation (B.3) it follows, that

$$I_{zz} = I'_{zz} + r_c^2 \geq r_c^2,$$

i.e. the second moment of area is greater or equal to the square of the corresponding coordinate of its center.

From relations (B.2), (B.3), it follows that the determinant of the matrix A is invariant with respect to the parallel shift of the coordinate system. Hence, without loss of generality, it can be assumed, that the coordinate origin is situated in the middle of the line segment, which connects the centers of cells $V_{j-1,k}$ and $V_{j+1,k}$, i.e. $\frac{r_c^{j-1,k}+r_c^{j+1,k}}{2} = 0$ or $-r_c^{j-1,k} = r_c^{j+1,k} = R > 0$. Further, the following parameters are introduced:

$$r_{max}^{m,k} = \max_{(r,z)\in V_{m,k}} r,\ r_{min}^{m,k} = \min_{(r,z)\in V_{m,k}} r,\ r_{|max|}^{m,k} = \max_{(r,z)\in V_{m,k}} |r|,$$
$$m \in \{j-1, j, j+1\}. \quad \text{(B.4)}$$

From Figure 5.3a it follows, that

$$-R = r_c^{j-1,k} < r_{min}^{j,k} < r_c^{j,k} < r_{max}^{j,k} < r_c^{j+1,k} = R, \quad \text{(B.5)}$$

hence $r_{|max|}^{j,k} < R$. Then,

$$I_{zz}^{j,k} = \frac{1}{\mu(V_{j,k})} \int_{V_{j,k}} r^2 dv \leq (r_{|max|}^{j,k})^2 < R^2.$$

From Remark B.1 it follows, that

$$I_{zz}^{m,k} \geq (r_c^{m,k})^2 = R^2 > I_{zz}^{j,k}, \quad m \in \{j-1, j+1\}. \quad \text{(B.6)}$$

Inequalities (B.5) and (B.6) yield, that the determinant of matrix A is less than zero. Hence, there exists a unique solution for linear system (5.44).

B.2 Number of adjacent cells

Consider for example an inner vertical edge $e_{j+\frac{1}{2},k}$, which lies within the physical domain Ω_s. Hence, rectangular cells of the initial mesh $W_{j,k}$, $W_{j+1,k}$ lie within the domain, at least partially. Then, there exist active cells $V_{m,k} = W_{m,k} \cap \Omega_s$, $m \in \{j, j+1\}$. Further, all possible situations of the location of the vertices of the inner edge $e_{j+\frac{1}{2},k}$ with respect to domain Ω_s will be determined, and the number N_c of active cells, exclusive cells $V_{j,k}$, $V_{j+1,k}$, adjacent to these vertices will be found in each case. The vertices of edge $e_{j+\frac{1}{2},k}$ can have at most 4 adjacent active cells, exclusive cells $V_{j,k}$, $V_{j+1,k}$

(see for example Figure B.1a), hence $N_c \leq 4$. It will be proved, that this number is also greater than zero.

Case 1a. Assume, that one of the vertices of the edge $e_{j+\frac{1}{2},k}$, for example vertex $v_{j+\frac{1}{2},k-\frac{1}{2}}$, is inner, i.e. the level set function is negative at this vertex. Then, besides cells $V_{j,k}$, $V_{j+1,k}$, there exist two active cells $V_{j,k-1}$, $V_{j+1,k-1}$, adjacent to vertex $v_{j+\frac{1}{2},k-\frac{1}{2}}$. If vertex $v_{j+\frac{1}{2},k+\frac{1}{2}}$ is also an inner vertex, then there exist two active adjacent cells $V_{j,k+1}$, $V_{j+1,k+1}$, and $N_c = 4$ (Figure B.1a).

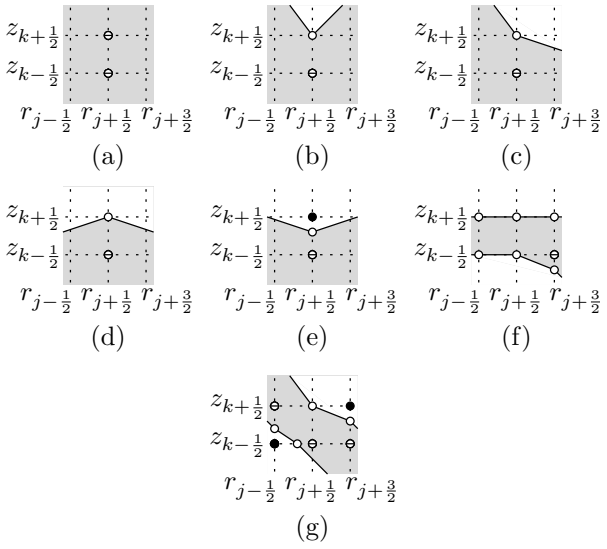

Figure B.1: Possible locations of the inner edge $e_{j+\frac{1}{2},k}$ and of the adjacent cells $V_{j,k}$, $V_{j+1,k}$ with respect to the physical domain Ω_s

Case 1b. In case, when vertex $v_{j+\frac{1}{2},k+\frac{1}{2}}$ is a boundary vertex, then, besides cells $V_{j,k}$, $V_{j+1,k}$, there may exist from zero to two active cells, adjacent to this vertex (see for example Figures B.1b–d). The number N_c ranges from two to four.

Case 1c. If vertex $v_{j+\frac{1}{2},k+\frac{1}{2}}$ is an outer vertex, then the additional boundary vertex is defined between vertices $v_{j+\frac{1}{2},k+\frac{1}{2}}$ and $v_{j+\frac{1}{2},k-\frac{1}{2}}$. This new vertex is the second vertex of the inner edge $e_{j+\frac{1}{2},k}$. Only cells $V_{j,k}$, $V_{j+1,k}$ are adjacent to the new boundary vertex (Figure B.1e). Hence, $N_c = 2$.

Case 2. Suppose, that vertex $v_{j+\frac{1}{2},k-\frac{1}{2}}$ is outer. Since, edge $e_{j+\frac{1}{2},k}$ is inner, then vertex $v_{j+\frac{1}{2},k+\frac{1}{2}}$ has to be an inner vertex. This situation is symmetrical to Case 1c.

Case 3a. Assume, that vertex $v_{j+\frac{1}{2},k-\frac{1}{2}}$ is a boundary vertex. Then vertex $v_{j+\frac{1}{2},k+\frac{1}{2}}$ cannot be an outer vertex, since the considered edge $e_{j+\frac{1}{2},k}$ is inner. If vertex $v_{j+\frac{1}{2},k+\frac{1}{2}}$ is an inner vertex, then the conclusions from

Case 1b are valid.

Case 3b. Suppose, that vertex $v_{j+\frac{1}{2},k+\frac{1}{2}}$ is also a boundary vertex. Let us now consider vertices $v_{j-\frac{1}{2},k+\frac{1}{2}}$ and $v_{j+\frac{3}{2},k+\frac{1}{2}}$. If they are boundary vertices, then vertices $v_{j-\frac{1}{2},k-\frac{1}{2}}$ and $v_{j+\frac{3}{2},k-\frac{1}{2}}$ cannot be outer vertices. Otherwise, cells $W_{j,k}$, $W_{j+1,k}$ would be outer cells, and there would not exist active cells $V_{j,k}$, $V_{j+1,k}$. This contradicts to the initial assumption. Hence, the considered cells $V_{j,k}$, $V_{j+1,k}$ are regular rectangular cells (Figure B.1f). In this situation, the normal derivatives and the value of the growth factor concentration are obtained with formulas (5.55), (5.56). Further, it is not necessary to define one more adjacent cell to approximate the gradients of the unknown functions.

Case 3c. Assume, that at least one of the vertices $v_{j-\frac{1}{2},k+\frac{1}{2}}$ and $v_{j+\frac{3}{2},k+\frac{1}{2}}$, is not a boundary vertex. If, for example, vertex $v_{j-\frac{1}{2},k+\frac{1}{2}}$ is inner (Figure B.1g), then cell $V_{j,k+1}$ will be an active cell. Hence, $N_c \geq 1$.

Case 3d. If, for example, vertex $v_{j+\frac{3}{2},k+\frac{1}{2}}$ is outer (Figure B.1g), then vertex $v_{j+\frac{3}{2},k-\frac{1}{2}}$ should be an inner vertex. Otherwise, there would not exist active cell $V_{j+1,k}$. It follows then, that cell $V_{j+1,k-1}$ is active, and $N_c \geq 1$.

Therefore, it has been proved for all possible situations, when at least one of cells $V_{j,k}$, $V_{j+1,k}$ is irregular, that $1 \leq N_C \leq 4$. The proof for the horizontal inner edges is analogous.

Acknowledgment

At the end of my four year research at Delft University of Technology, I would like to acknowledge the people who helped me a lot in various aspects of my work and made my stay in Delft an exciting experience.

First of all, I would like to thank my supervisor Prof. Kees Vuik for giving me an opportunity to work on the present project in the Group of Numerical Analysis at Delft Institute of Applied Mathematics, and for his wise guidance and valuable suggestions during our meetings. Thank you Kees, for your support and understanding from my first days in Delft till the end of my project. It was an honor for me to do a research under your supervision.

It was a great pleasure to me to work with Dr. Fred Vermolen, my daily supervisor. Fred, informal and trusting relations and the confidence that I can rely on you were extremely important for me to adapt fast in the Netherlands and to feel comfortable at my new job at the Delft University. Your support, coaching and encouragement have helped me to remain optimistic in several complicated situations concerning my research and to progress in my work. I enjoyed our talks during out weekly meetings and during a number of formal and informal events in Delft and Amsterdam. The trips to Zaragoza, Madrid and Edinburgh were exciting. It was a fun to walk in these cites accompanied by you and to go to bars in the evenings.

The present research was done together with Prof. José Manuel García-Aznar from the University of Zaragoza, Spain. Our cooperation was extremely valuable for me and resulted into a number of interesting research achievements published in several journal articles and in the present thesis. Manu, I appreciate a friendly atmosphere your created during our meetings, your enthusiasm and willingness to help with various complicated aspects in the research. I am happy that I had a possibility to work with you.

I would like to acknowledge the financial support of my stay and work in Delft provided by the Delft Institute of Applied Mathematics. I would like to thank Agentschap NL for the sponsored collaboration between Delft University of Technology and the University of Zaragoza.

Theda Olsder has managed with a huge amount of formal procedures related to my arrival and stay in the Netherlands. I appreciate her support and readiness to find a way out of any complicated situation.

I am also grateful to Dr. Wim van Horssen for his help with several administrative questions.

I am grateful to my first supervisor at the Belarusian State University Prof. Michail Zhuravkov. He played an important role for my decision to continue study at the PhD level.

I am thankful to Dr. Valery Gaiko, who actually told me about the open PhD position at Delft University of Technology when I was in Minsk considering various places to continue my education.

It was a fun and pleasure to share the office with the cheerful, friendly and enthusiastic guys Tijmen and Reijer, and then Xiaozhou and Gido. During my study in Delft I met a lot of pleasant and interesting people whom I would like to express my gratitude: the former and present PhD students Denis, Elwin, Rohid, Paulien, Liangyue, Bowen, Jing, Miranda, Fahim, Abdul, Ibrahim, Joost, Lech, Miriam, Alexandr, Timofiy, the post doc fellow Sergey, the permanent staff members of the the Numerical Analysis group Jenifer, Domenico, Duncan, Martin van Gijzen, Prof. Kees Oosterlee, Guus Segal, Niel Budko, Fons Daalderop, Peter Sonneveld, our secretaries Deborah and Mechteld, Prof. Sybrand van der Zwaag from the aerospace faculty, Etelvina Javierre from Centro Universitario de la Defensa in Zaragoza.

I am thankful to Maxim Molokov and to Masha for their help with design of the cover for the present thesis.

I would like to acknowledge my friends in Belarus and in the Netherlands who added colors to my life and with whom I had a lot of fun during my free time.

I express my deepest gratitude to all my large family and in particular to my parents. Despite a large distance to home I always experienced their support and encouragement during these four years. Masha and Paulinka are the source of inspiration in my work. I thank them for their patience and care which were of enormous importance to me.

Curriculum vitae

- September 2008 - 2012: Delft University of Technology, The Netherlands, PhD student in Numerical Analysis, supported by Delft Institute of Applied Mathematics, subject: *Modeling bone regeneration around endosseous implants*, supervisor: Prof.dr.ir. Kees Vuik, daily supervisor: Dr.ir. Fred Vermolen, Department of Applied Mathematics, Faculty of Electrical Engineering, Mathematics and Computer Science
- July 2007- July 2008: Engineer, Belgorkhimprom, Minsk, Belarus
- 2002- July 2007: Belarusian State University, Minsk, Belarus, Diploma with honors in Applied Mathematics and Mechanics
- 1991-2002: Gymnasium #4, Minsk, Belarus
- Born on 01-09-1984 in Mahiliou, Belarus

BIBLIOGRAPHY

[1] I. Abrahamsson, T. Berglundh, E. Linder, N. P. Lang, and J. Lindhe. Early bone formation adjacent to rough and turned endosseous implant surfaces. an experimental study in the dog. *Clin. Oral Implants Res.*, 15(4):381 – 392, 2004.

[2] J. A. Adam. A simplified model of wound healing (with particular reference to the critical size defect). *Math. Comput. Model.*, 30:23 – 32, 1999.

[3] J. A. Adam. A simplified model of wound healing ii: the critical size defect in two dimensions. *Math. Comput. Model.*, 30:47 – 60, 1999.

[4] C. Ament and E. P. Hofer. A fuzzy logic model of fracture healing. *J. Biomech.*, 33:961 – 968, 2000.

[5] N. Amor, L. Geris, J. Vander Sloten, and H. Van Oosterwyck. Modelling the early phases of bone regeneration around an endosseous oral implant. *Comput. Methods Biomech. Biomed. Eng.*, 12(4):459 – 468, 2009.

[6] N. Amor, L. Geris, J. Vander Sloten, and H. Van Oosterwyck. Computational modelling of biomaterial surface interactions with blood platelets and osteoblastic cells for the prediction of contact osteogenesis. *Acta Biomater.*, 7:779 – 790, 2011.

[7] A. Andreykiv. *Simulation of bone ingrowth.* PhD thesis, Delft University of Technology, 2006.

[8] A. Andreykiv, P. J. Prendergast, F. van Keulen, W. Swieszkowski, and P. M. Rozing. Bone ingrowth simulation for a concept glenoid component design. *J. Biomech.*, 38:1023 – 1033, 2005.

[9] A. Andreykiv, F. van Keulen, and P. J. Prendergast. Simulation of fracture healing incorporating mechanoregulation of tissue differentiation and dispersal/proliferation of cells. *Biomech. Model. Mechanobiol.*, 7: 443 – 461, 2007. doi: 10.1007/s10237-007-0108-8.

[10] L. Audigé, D. Griffin, M. Bhandari, J. Kellam, and Rüedi T. P. Path analysis of factors for delayed healing and nonunion in 416 operatively treated tibial shaft fractures. *Clin. Orthop Relat Res.*, 438:221 – 232, 2005.

[11] A. Bailon-Plaza and M. C. H. van der Meulen. A mathematical framework to study the effects of growth factor influences on fracture healing. *J. Theor. Biol.*, 212:191 – 209, 2001.

[12] A. Bailon-Plaza and M. C. H. van der Meulen. Beneficial effects of moderate, early loading and adverse effects of delayed or excessive loading on bone healing. *J. Biomech.*, 36:1069 – 1077, 2003. doi: 0.1016/S0021-9290(03)00117-9.

[13] G. R. Beck, B. Zerler, and E. Moran. Gene array analysis of osteoblast differentiation. *Cell Growth Differ.*, 12:61 – 83, 2001.

[14] T. Berglundh, I. Abrahamsson, N. P. Lang, and J. Lindhe. De novo alveolar bone formation adjacent to endosseous implants. *Clin Oral Implants Res.*, 14(3):251 – 262, 2003.

[15] P. R. Blenman, D. R. Carter, and G. S. Beaupré. Role of mechanical loading in the progressive ossification of a fracture callus. *J. Orthop. Res.*, 7:398 – 407, 1989.

[16] D. Buser, N. Broggini, M. Wireland, R. K. Schenk, A. J. Denzer, D. L. Cochran, B. Hoffmann, A. Lussi, and S. G. Steinemann. Enhanced bone apposition to a chemically modified slasurface. *J Dent Res.*, 83 (7):529 – 533, 2004.

[17] D. R. Carter, P. R. Blenman, and Beaupré. Correlations between mechanical stress history and tissue differentiation in initial fracture healing. *J Orthop. Res.*, 6:736 – 748, 1988.

[18] D. R. Carter, G. S. Beaupré, N. J. Giori, and J. A. Helms. Mechanobiology of skeletal regeneration. *Clin. Orthop. Relat. Res.*, 355S:S41 – S55, 1998.

[19] L. E. Claes and C. A. Heigele. Magnitudes of local stress and strain along bony surfaces predict the course and type of fracture healing. *J. Biomech.*, 32(3):255 – 266, 1999.

[20] P. Colella, D. T. Graves, B. J. Keen, and D. Modiano. A cartesian grid embedded boundary method for hyperbolic conservation laws. *J. Comput. Phys.*, 211:347 – 366, 2006.

[21] C. Colnot, D. M. Romero, S. Huang, J. Rahman, J. A. Currey, A. Nanci, J. B. Brunski, and J. A. Helms. Molecular analysis of healing at a bone-implant interface. *J Dent Res.*, 86(9):862 – 867, 2007.

[22] J. Crank. *Free and Moving Boundary Problems*. The Oxford University Press, 1987.

[23] V. G. Danilov and V. M. Shelkovich. Delta-shock wave type solution of hyperbolic systems of conservation laws. *Quart. Appl. Math.*, 63: 401–427, 2005.

[24] J. E. Davies. Understanding peri-implant endosseous healing. *J Dent. Educ.*, 67(8):932 – 949, 2003.

[25] R. Dimitriou, E. Tsiridis, and P. V. Giannoudis. Current concepts of molecular aspects of bone healing. *Injury*, 36:1392 – 1404, 2005.

[26] R. Dimitriou, E. Jones, D. McGonagle, and Giannoudis P. V. Bone regeneration: current concepts and future directions. *BMC Med.*, 9 (66), 2011.

[27] M. Doblaré and J.M. García-Aznar. Anisotropic bone remodelling model based on a continuum damage-repair theory. *Journal of Biomechanics*, 35(1):1 – 17, 2002. ISSN 0021-9290. doi: 10.1016/S0021-9290(01)00178-6. URL `http://www.sciencedirect.com/science/article/pii/S0021929001001786`.

[28] J. Duyck, K. Vandamme, L. Geris, H. Van Oosterwyck, M. De Cooman, J. Vandersloten, R. Puers, and I. Naert. The influence of micro-motion on the tissue differentiation around immediately loaded cylindrical turned titanium implants. *Arch Oral Biol.*, 51:1 – 9, 2006.

[29] J. Duyck, E. Slaets, K. Sasaguri, K. Vandamme, and I. Naert. Effect of intermittent loading and surface roughness on peri-implant bone formation in a bone chamber model. *J Clin Periodontol*, 34:998 – 1006, 2007.

[30] T. A. Einhorn. Enhancement of fracture-healing. *J Bone Joint Surg Am.*, 77(6):940 – 956, 1995.

[31] D. R. Epari, G. N. Duda, and M. S. Thompson. Mechanobiology of bone healing and regeneration: in vivo models. *Proc Inst Mech Eng H.*, 224(12):1543 – 1553, 2010.

[32] M. Franchi, M. Fini, D. Martini, E. Orsini, L. Leonardi, A. Ruggeri, G. Giavaresi, and V. Ottani. Biological fixation of endosseous implants. *Micron*, 36:665 – 671, 2005.

[33] J. S. Gabbay, P. A. Zuk, A. Tahernia, M. Askari, C. M. O'Hara, T. Karthikeyan, K. Azari, J. O. Hollinger, and J. P. Bradley. In vitro microdistraction of preosteoblasts: distraction promotes proliferation and oscillation promotes differentiation. *Tissue Eng.*, 12(11):3055 – 3065, 2006.

[34] J. M. García-Aznar, T. Rueberg, and M. Doblaré. A bone remodelling model coupling micro-damage growth and repair by 3d bmu-activity. *Biomech Model Mechanobiol*, 4(2-3):147 – 167, 2005.

[35] J. M. García-Aznar, , J. H. Kuiper, M. J. Gómez-Benito, M. Doblaré, and J.B. Richardson. Computational simulation of fracture healing: influence of interfragmentary movement on the callus growth. *J. Biomech.*, 40:1467 – 1476, 2007.

[36] M. J. Gardner, M. C. van der Meulen, D. Demetrakopoulos, T. M. Wright, E. R. Myers, and M. P. Bostrom. In vivo cyclic axial compression affects bone healing in the mouse tibia. *J. Orthop. Res.*, 24:1679 – 1686, 2006.

[37] L. Geris, H. Van Oosterwyck, J. Vander Sloten, J. Duyck, and I. Naert. Assessment of mechanobiological models for the numerical simulation of tissue differentiation around immediately loaded implants. *Comp. Methods Biomech. Biomed. Eng.*, 6:277 – 288, 2003.

[38] L. Geris, A. Andreykiv, H. Van Oosterwyck, J. Vander Sloten, F. van Keulen, J. Duyck, and I. Naert. Numerical simulation of tissue differentiation around loaded titanium implants in a bone chamber. *J. Biomech.*, 37:763 – 769, 2004.

[39] L. Geris, K. Vandamme, I. Naert, J. Vander Sloten, J. Duyck, and H. Van Oosterwyck. Application of mechanoregulatory models to simulate peri-implant tissue formation in an in vivo bone chamber. *J. Biomech.*, 41:145 – 154, 2008.

[40] L. Geris, A. Gerisch, J. Vander Sloten, R. Weiner, and H. Van Oosterwyck. Angiogenesis in bone fracture healing: a bioregulatory model. *J. Theor. Biol.*, 251:137 – 158, 2008a.

[41] L. Geris, J. Vander Sloten, and H. Van Oosterwyck. Mathematical modelling of bone regeneration including angiogenesis: design of treatment strategies for atrophic nonunions. In *Transactions of the 54th Annual Meeting of the Orthopaedic Research Society*. New Orleans, 2008c.

[42] L. Geris, J. Vander Sloten, and H. Van Oosterwyck. In silico biology of bone modelling and remodelling: regeneration. *Philos Transact A Math Phys Eng Sci.*, 367:2031 – 2053, 2009.

[43] L. Geris, J. Sloten, and H. Oosterwyck. Connecting biology and mechanics in fracture healing: an integrated mathematical modeling framework for the study of nonunions. *Biomech Model Mechanobiol*, 9: 713–724, 2010a. ISSN 1617-7959. doi: 10.1007/s10237-010-0208-8.

[44] L. Geris, A. Gerisch, and R. C. Schugart. Mathematical modeling in wound healing, bone regeneration and tissue engineering. *Acta Biotheor.*, 58(4):355 – 367, 2010b.

[45] L. Geris, A. A. C. Reed, J. Vander Sloten, A. H. R. W. Simpson, and H. Van Oosterwyck. Occurrence and treatment of bone atrophic nonunions investigated by an integrative approach. *PLoS Comput. Biol.*, 6 (9):e1000915, 2010c.

[46] M. J. Gómez-Benito, J. M. García-Aznar, J. H. Kuiper, and M. Doblaré. Influence of fracture gap size on the pattern of long bone healing: a computational study. *J. Theor. Biol.*, 235:105 – 119, 2005.

[47] R. Huiskes, W. D. Vandriel, P. J. Prendergast, and K. Søballe. A biomechanical regulatory model of peri-prosthetic tissue differentiation. *J. Mater. Sci. Mater. Med.*, 8:785 – 788, 1997.

[48] W. Hundsdorfer and J. G. Verwer. *Numerical Solution of Time-Dependent Advection-Diffusion-Reaction Equations*. Springer, 2003.

[49] S. Idelsohn, J. A. Planell, F. J. Gil, and D. Lacroix. Development of a dynamic mechanoregulation model based on shear strain and fluid flow to optimize distraction osteogenesis. *J. Biomech.*, 39(Suppl. 1):S9 – S10, 2006.

[50] H. Isaksson, W. Wilson, C. C. van Donkelaar, R. Huiskes, and I. Keita. Comparison of biophysical stimuli for mechano-regulation of tissue differentiation during fracture healing. *J. Biomech.*, 39:1507 – 1516, 2006a.

[51] H. Isaksson, C. C. van Donkelaar, R. Huiskes, and K. Ito. Corroboration of mechanoregulatory algorithms for tissue differentiation during fracture healing: comparison with in vivo results. *J. Orthop. Res.*, 24: 898 – 907, 2006b.

[52] H. Isaksson, O. Comas, C. C. van Donkelaar, J. Mediavilla, W. Wilson, R. Huiskes, and I. Keita. Bone regeneration during distraction osteogenesis: Mechano-regulation by shear strain and fluid velocity. *J. Biomech.*, 40:2002 – 2011, 2007.

[53] H. Isaksson, C. C. van Donkelaar, , R. Huiskes, and K. Ito. A mechano-regulatory bone-healing model incorporating cell-phenotype specific activity. *J. Theor. Biol.*, 252:230 – 246, 2008a. doi: 10.1016/j.jtbi.2008.01.030.

[54] G. Kasper, N. Dankert, J. Tuischer, M. Hoeft, T. Gaber, J. D. Glaeser, D. Zander, M. Tschirschmann, M. Thompson, G. Matziolis, and G. N. Duda. Mesenchymal stem cells regulate angiogenesis according to their mechanical environment. *Stem Cells*, 25(4):903 – 910, 2007. ISSN 1549-4918. doi: 10.1634/stemcells.2006-0432.

[55] B.L. Keyfitz and H.C. Kranzer. Spaces of weighted measures for conservation laws with singular shock solutions. *Journal of Differential Equations*, 118(2):420 – 451, 1995. doi: 10.1006/jdeq.1995.1080. URL `http://www.sciencedirect.com/science/article/pii/S0022039685710807`.

[56] L. Kikuchi, J. Y. Park, C. Victor, and J. E. Davies. Platelet interactions with calcium-phosphate-coated surfaces. *Biomaterials*, 26(26):5285 – 5295, 2005.

[57] D. Lacroix and P. J. Prendergast. A mechano-regulation model for tissue differentiation during fracture healing: analysis of gap size and loading. *J. Biomech.*, 35(10.1016/S0021-9290(02)00086-6):1163 – 1171, 2002b.

[58] D. Lacroix, P. J. Prendergast, G. Li, and D. Marsh. Biomechanical model to simulate tissue differentiation and bone regeneration: application to fracture healing. *Med. Biol. Eng. Comput.*, 40:14 – 21, 2002a.

[59] R. J. LeVeque. *Finite-Volume Methods for Hyperbolic Problems*. Cambridge University Press, 2002.

[60] J. B. Lian and G. S. Stein. Development of the osteoblast phenotype: molecular mechanisms mediating osteoblast growth and differentiation. *Iowa Orthop J.*, 15:118 – 140, 1995.

[61] M. Lind. Growth factors: possible new clinical tools. a review. *Acta Orthop Scand.*, 67(4):407 – 417, 1996.

[62] T. A. Linkhart, S. Mohan, and D. J. Baylink. Growth factors for bone growth and repair: Igf, tgf-beta and bmp. *Bone*, 19:1S – 12S, 1996.

[63] A. F. Mavrogenis, R. Dimitriou, J. Parvizi, and G. C. Babis. Biology of implant osseointegration. *J Musculoskelet. Neuronal. Interact.*, 9(2):61 – 71, 2009.

[64] P. Mayer-Kuckuk and A. L. Boskey. Molecular imaging promotes progress in orthopedic research. *Bone*, 39(5):965 – 977, 2006. ISSN 8756-3282. doi: 10.1016/j.bone.2006.05.009.

[65] U. Meyer, U. Joos, J. Mythili, T. Stamm, A. Hohoff, T. Fillies, U. Stratmann, and H. P. Wiesmann. Ultrastructural characterization of the implant/bone interface of immediately loaded dental implants. *Biomaterials*, 25(10):1959 – 1967, 2004.

[66] S. Miyata and T. Sasaki. Asymptotic analysis of a chemotactic model of bacteria colonies. *Math. Biosci.*, 201:184 – 194, 2006.

[67] P. Moreo, J. M. García-Aznar, and M. Doblaré. Bone ingrowth on the surface of endosseous implants. part 1: Mathematical model. *J. Theor. Biol.*, 260(1):1 – 12, 2009.

[68] E. F. Morgan, M. T. Longaker, and D. R. Carter. Relationships between tissue dilatation and differentiation in distraction osteogenesis. *Matrix Biol.*, 25(2):94 – 103, 2006.

[69] M. Myerscough and J. Murray. Analysis of propagating pattern in a chemotaxis system. *Bulletin of Mathematical Biology*, 54:77–94, 1992. ISSN 0092-8240. doi: 10.1007/BF02458621.

[70] Michael Oberguggenberger and Ya-Guang Wang. Delta-waves for semilinear hyperbolic cauchy problems. *Math. Nachr.*, 166(1):317–327, 1994. ISSN 1522-2616. doi: 10.1002/mana.19941660124. URL `http://dx.doi.org/10.1002/mana.19941660124`.

[71] J. Y. Park, C. H. Gemmell, and J. E. Davies. Platelet interactions with titanium: modulation of platelet activity by surface topography. *Biomaterials*, 22(19):2671 – 2682, 2001.

[72] F. Pauwels. Eine neue theorie über den einflußmechanischer reize auf die differenzierung der stützgewebe. *Z. Anat. Entwicklungsgeschichte*, 121:478 – 515, 1960. doi: 10.1007/BF00523401.

[73] S. M. Perren. Physical and biological aspects of fracture healing with special reference to internal fixation. *Clin. Orthop. Relat. Res.*, 138:175 – 195, 1979.

[74] S. M. Perren and J. Cordey. Concepts of interfragmentary strain. In H. K. Uhthoff, editor, *Current concepts of internal fixation of fractures*, volume 138, pages 63 – 77. N.Y. Springer, 1980.

[75] P. Pivonka, J. Zimak, D. W. Smith, B. S. Gardiner, C. R. Dunstan, N. A. Sims, T. J. Martin, and G. R. Mundy. Model structure and control of bone remodeling: a theoretical study. *Bone*, 43(2):249 – 263, 2008.

[76] A. Praemer, S. Furner, and D. P. Rice. *Musculoskeletal conditions in the United States*. Amer Acad of Orthopaedic Surgeons, 1992.

[77] P. J. Prendergast, R. Huiskes, and K. Søballe. Biophysical stimuli on cells during tissue differentiation at implant interfaces. *J. Biomech.*, 30: 539 – 548, 1997.

[78] P. Prokharau and F. Vermolen. Stability analysis for a peri-implant osseointegration model. *J Math Biol*, pages 1 – 32, 2012. ISSN 0303-6812. doi: 10.1007/s00285-012-0513-1.

[79] P. Prokharau, F. Vermolen, and J. M. García-Aznar. Evolutionary cell differentiation approach in a peri-implant osseointegration model. In *Proceedings of II International Conference on Tissue Engineering*, pages 149–156. 2011.

[80] D. A. Puleo and A. Nanci. Understanding and controlling the bone-implant interface. *Biomaterials*, 20(23-24):2311 – 2321, 1999.

[81] J. J. Quirk. An alternative to unstructured grids for computing gas dynamic flows around arbitrary complex two-dimensional bodies. *Comput. Fluids*, 23(1):125 – 142, 1994.

[82] J. Y. Reginster and Burlet N. Osteoporosis: a still increasing prevalence. *Bone*, 38:S4 – 9, 2006.

[83] E. Reina-Romo, M. J. Gómez-Benito, J. M. García-Aznar, J. Domínquez, and M. Doblaré. Modeling distraction osteogenesis: analysis of the distraction rate. *Biomech. Model. Mechanobiol.*, 8:323 – 335, 2009.

[84] I. Röder. *Dynamical modeling of hematopoietic stem cell organization*. PhD thesis, University of Leipzig, 2003.

[85] M. D. Ryser, N. Nigam, and S. V. Komarova. Mathematical modeling of spatio-temporal dynamics of a single bone multicellular unit. *J. Bone Miner. Res.*, 24(5):860 – 870, 2009.

[86] J. A. Sethian. *Level Set Methods and Fast Marching Methods: evolving interfaces in computational geometry, fluid mechanics, computer vision, and materials science*. Cambridge University Press, 1999.

[87] F. Shapiro. Bone development and its relation to fracture repair. the role of mesenchymal osteoblasts and surface osteoblasts. *Eur Cell Mater.*, 1(15):53 – 76, 2008.

[88] S. J. Shefelbine, P. Augat, L. Claes, and U. Simon. Trabecular bone fracture healing simulation with finite element analysis and fuzzy logic. *J. Biomech.*, 38:2440 – 2450, 2005. doi: 10.1016/j.jbiomech.2004.10.019.

[89] U. Simon, P. Augat, M. Utz, and L. Claes. Simulation of tissue development and vascularisation in the callus healing process. New Orleans, 2003.

[90] D.C. Tan, T. Zhang, T. Chang, and Y.X. Zheng. Delta-shock waves as limits of vanishing viscosity for hyperbolic systems of conservation laws. *Journal of Differential Equations*, 112(1):1 – 32, 1994. doi: 10.1006/jdeq.1994.1093. URL `http://www.sciencedirect.com/science/article/pii/S002203968471093X`.

[91] R. Tyson, S. R. Lubkin, and J. D. Murray. Model and analysis of chemotactic bacterial patterns in a liquid medium. *J. Math. Biol.*, 38: 359 – 375, 1999.

[92] K. Vandamme, I. Naert, L. Geris, J. Vander Sloten, R. Puers, and J. Duyck. Histodynamics of bone tissue formation around immediately loaded cylindrical implants in the rabbit. *Clin. Oral Implants Res.*, 18: 471 – 480, 2007a.

[93] K. Vandamme, I. Naert, L. Geris, J. Vander Sloten, R. Puers, and J. Duyck. Influence of controlled immediate loading and implant design on peri-implant bone formation. *J. Clin. Periodontol.*, 34:172 – 181, 2007b.

[94] K. Vandamme, I. Naert, L. Geris, J. Vander Sloten, R. Puers, and J. Duyck. The effect of micro-motion on the tissue response around immediately loaded roughened titanium implants in the rabbit. *Eur J Oral Sci*, 115:21 – 29, 2007c.

[95] C. Vuik, P. van Beek, F. Vermolen, and J. van Kan. *Numerical Methods for Ordinary Differential Equations*. VSSD, 2007.

[96] C. Weinand, I. Pomerantseva, C. M. Neville, R. Gupta, E. Weinberg, I. Madisch, F. Shapiro, H. Abukawa, M. J. Troulis, and Vacanti J. P. Hydrogel-beta-tcp scaffolds and stem cells for tissue engineering bone. *Bone*, 38(4):555 – 563, 2006.

[97] A. Yamaguchi, T. Komori, and T. Suda. Regulation of osteoblast differentiation mediated by bone morphogenetic proteins, hedgehogs, and cbfa1. *Endocr Rev*, 21(4):393 – 411, 2000.

[98] L. You, S. C. Cowin, M. B. Schaffler, and S. Weinbaum. A model for strain amplification in the actin cytoskeleton of osteocytes due to fluid drag on pericellular matrix. *Journal of Biomechanics*, 34(11): 1375 – 1386, 2001. ISSN 0021-9290. doi: 10.1016/S0021-9290(01)00107-5. URL `http://www.sciencedirect.com/science/article/pii/S0021929001001075`.

List of publications

- P. Prokharau and F. Vermolen. Stability analysis for a peri-implant osseointegration model. *J Math Biol*, pages 1 – 32, 2012. ISSN 0303-6812. doi: 10.1007/s00285-012-0513-1

- P. Prokharau, F. Vermolen, and J. M. García-Aznar. Evolutionary cell differentiation approach in a peri-implant osseointegration model. In *Proceedings of II International Conference on Tissue Engineering*, pages 149–156, 2011.

- P. A. Prokharau, F. J. Vermolen, J. M. García-Aznar. Model for direct bone apposition on pre-existing surfaces, during peri-implant osseointegration. *J Theor. Biol.* 304: 131–142, 2012. ISSN 0022-5193. doi: 10.1016/j.jtbi.2012.03.025

- P. A. Prokharau, F. J. Vermolen, J. M. García-Aznar. A mathematical model for cell differentiation, as an evolutionary and regulated process. *Accepted for publication in Comput. Meth. Biomech. Biomed. Eng.*

- P. A. Prokharau, F. J. Vermolen, J. M. García-Aznar. Numerical method for the bone regeneration model, defined within the evolving 2D axisymmetric physical domain. *Accepted for publication in Comput. Meth. Appl. Mech. Eng.*